University of California Santa Barbara

Additively Manufactured Alloy Characterization with Resonant Ultrasound Spectroscopy

A dissertation submitted in partial satisfaction
of the requirements for the degree

Doctor of Philosophy
in
Materials

by

Jeffrey Oliver Rossin

Committee in charge:
Professor Tresa M. Pollock, Co-Chair
Professor Samantha H. Daly, Co-Chair
Professor Matthew R. Begley
Professor Irene J. Beyerlein

September 2022

The dissertation of Jeffrey Oliver Rossin is approved.

Professor Irene J. Beyerlein

Professor Matthew R. Begley

Professor Samantha H. Daly, Committee Co-Chair

Professor Tresa M. Pollock, Committee Co-Chair

August 2022

Additively Manufactured Alloy Characterization with Resonant Ultrasound Spectroscopy

by

Jeffrey Oliver Rossin

Acknowledgements

Firstly, thank you to all those that have made this PhD possible. It is difficult to succintly describe everyone, but I first want to thank my advisors, Sam Daly and Tresa Pollock, for their support and guidance to attack the relevant problems. They have both been excellent role-models to navigate the last few years.

I want to acknowledge Patrick Leser at NASA Langley, as none of my work could have happened in time for a single PhD without his help in coding, his own code SMCPy, and his ability to pull apart some of my issues. Thank you for listening to my problems over the years, and for all the advice on managing work-from-home/ COVID hurdles during the pandemic. Thank you to Stephen Smith as well, as my NASA advisor you were essential to open the doors to progress. Thank you to the NASA Space Technology Research Fellowship for funding my work and allowing me to connect with the wider NASA community. It has been an amazing experience.

Dr. Richard Otis and Dr. R. Peter Dillon at NASA Jet Propulsion Laboratories were immensely supportive and understanding, making my experience at JPL both possible and beneficial despite needing to complete it remotely. Pete's willingness to provide his time was crucial to many of my successful research efforts.

I want to thank Brent Goodlet immensely, as he taught me everything I knew about resonance ultrasound spectroscopy, our experimental setup, and initial computational framework. He was absolutely critical in helping to identifying and analyze the the early problem stages, and I appreciate all the long conversations about life that I never realized I would have in the lab. Thank you to Ben Bales for his work on the computational side of the RUS problem, as it was critical for my understanding of the RUS forward/ inverse problem. Chris Torbet is and always will be the cornerstone of the Pollock group, and

without his aid in specimen preparation, experimental setup, and general know-how, none of my work would have happened in time. His mentorship and calm demeanor was invaluable and cannot be appreciated enough.

Andrew Polonsky and James Lamb exposed me to the Tribeam, and their patience in teaching me about it is much appreciated. Along with Neal Brodnik, the exposure to 3D techniques and machine learning has been critical to my push forward.

Thank you to Bhavana Swaminathan and the Daly research group for creating a support structure for my first few years. Without some colleagues to survive and push through those overnight experiments, classes would have been much more challenging. To Zhe Chen, our years sharing 'the concentration zone' office were very special to me, and I will not forget all those 3am work sessions.

The Materials front office staff: Alexandria Huddleston, Jocelyn Guzman, Tawny Hernandez, Max Mccumber and Dawn Holden cannot be overappreciated for their aid in figuring out my fellowship funding and constant overhead issues. Additionally I want to thank the MMF, Materials, and ME support staff enough for all their help with training, equipment use, and scheduling.

The group of friends I have in Santa Barbara has been absolutely amazing, and have prompted many impromptu kiteboarding, diving, and mountain biking trips that have made living here the most special time of my life. My partner, Samantha, has been an incredibly supportive advocate throughout my graduate studies, and I cannot express my gratitude for being there for me.

Curriculum Vitae

Jeffrey Oliver Rossin

Education

University of California Santa Barbara PhD in Materials
August 2022

University of Florida BS in Materials Science & Engineering
May 2017

Publications

In Preparation: **Rossin, J.**, Leser, P., Torbet, C., Smith, S., Daly, S., & Pollock, T. M. (2022). Non-destructive quantification of single crystal elasticity in additively manufactured aerospace alloys.

Rossin, J., Leser, P., Pusch, K., Frey, C., Vogel, S., Saville, A.I., Torbet, C., Clarke A.J., Daly, S., & Pollock, T. M. (2022). Single crystal elastic constants of additively manufactured components determined by resonant ultrasound spectroscopy. *Materials Characterization, 192*. 112244. HTTPS://DOI.ORG/10.1016/J.MATCHAR.2022.112244

Rossin, J., Leser, P., Pusch, K., Frey, C., Murray, S., Torbet, C., Smith, S., Daly, S., & Pollock, T. M. (2021). Bayesian inference of elastic constants and texture coefficients in additively manufactured cobalt-nickel superalloys using resonant ultrasound spectroscopy. *Acta Materialia, 220* 117287. HTTPS://DOI.ORG/10.1016/J.ACTAMAT.2021.117287

Goodlet, B. R., Murray, S. P., Bales, B., **Rossin, J.**, Torbet, C. J., & Pollock, T. M. (2021). Temperature dependence of single crystal elastic constants in a CoNi-Base alloy: A new methodology. *Materials Science and Engineering: A, 803*, 140507. HTTPS://DOI.ORG/10.1016/J.MSEA.2020.140507

Rossin, J., Goodlet, B., Torbet, C., Musinski, W., Cox, M., Miller, J., ... & Pollock, T. (2020). Assessment of grain structure evolution with resonant ultrasound spectroscopy in additively manufactured nickel alloys. *Materials Characterization, 167*, 110501. HTTPS://DOI.ORG/10.1016/J.MATCHAR.2020.110501

Abstract

Additively Manufactured Alloy Characterization with Resonant Ultrasound Spectroscopy

by

Jeffrey Oliver Rossin

Additive manufacturing (AM) of metallic components has become a full-fledged manufacturing technique as the space and aerospace industries require reduced weight, increased design and property control, and reduced lead times. The advantages of additive manufacturing directly correlate to challenges in characterization, property prediction, and component reliability, as printed parts display remarkable variability compared to traditionally qualified components. Regarding characterization, additively manufactured components represent a departure from traditional assumptions such as isotropic (same in all directions) material properties. Particularly for properties such as crystallographic texture, the variable solidification conditions of AM require consideration of arbitrary anisotropy and symmetry on the bulk scale.

This work focuses on advancing the quantification of the properties of additively manufactured components with the bulk ultrasonic technique, resonant ultrasound spectroscopy (RUS). Critically, this technique is non-destructive, low-cost, and can be performed in a matter of minutes. However, existing frameworks to characterize properties such as the elastic constants from ultrasonic data only account for either isotropic or single crystalline compounds, with assumptions made to simplify the elastic symmetry of polycrystalline textures. To account for arbitrarily textured microstructures, a novel framework is developed to quantify texture directly from the resonant frequencies, with

a novel cobalt-nickel-base superalloy (SB-CoNi-10C) specimen used to demonstrate the effectiveness of the technique. The determination of elastic constants from the resonant frequencies requires inverse problem solving to iteratively calculate the resonant frequencies and compare them to those measured in the laboratory. Given the complexity of the solution space and a need for robust parameter estimates on the independently determined texture, a CPU-parallelizable Bayesian inference technique, Sequential Monte Carlo (SMC) is employed to reduce computational costs to under 24h on a 10-core system. Looking toward crystal scale property prediction, the single crystal elastic constants are critical to understand the behavior of novel AM alloys. Therefore, a framework is developed to determine the single crystal elastic constants from the resonant frequencies of textured AM specimens, provided their texture is known by EBSD or neutron diffraction measurements. Agreement with reported single crystal constants measured on grown single crystal specimens is demonstrated, circumventing the need to grow single crystals. This framework provides an end-to-end determination of the single crystal elastic constants that quantifies error directly from the measured resonant frequency measurements.

The determination of single crystal elastic constants from AM specimens has been extended to the lab scale, with 2 mm x 2 mm EBSD scans demonstrated as sufficient to inform the texture within a specimen, in contrast to the prior need for neutron diffraction or large-scale EBSD data. The incorporation of texture coefficient variability from an EBSD measurement in the model enables the single crystal elastic constants to be determined much more accurately. The single crystal elastic constants are determined with EBSD and RUS data of additively manufactured SB-CoNi-10C, Inconel 625, and Ti-6Al-4V, demonstrating agreement with previously reported literature values for each material. Finally, RUS is extended to arbitrary geometry specimens of AM Inconel 625,

demonstrating the capability of RUS to quantify microstructure variability by leveraging finite-element forward models of the resonant frequencies and correlating to experimental frequencies. Insightful examples are provided to demonstrate the limitations and constraints of determining the single crystal elastic constants and texture coefficients from resonant frequencies.

Contents

List of figures

List of Tables

List of Tables

List of Symbols

C_{ijkl}	Elastic stiffness tensor (units GPa)
S_{ijkl}	Elastic compliance tensor (units GPa^{-1})
A	Zener anisotropy ratio for cubic materials
C_{mn}^{l}	Fourier coefficients at l order of ODF
R	Rietveld refinement R_{wp}-factor for neutron diffraction data
$y_{obs,i}$	Neutron diffraction i^{th} measured intensity value
V_{pqrs}	Tensorial representation (4th-order) of ODF coefficients
$f(Q)$	Orientation distribution function f over orientations Q
P_0	4th-order Polarization tensor
a_1, a_2, a_3	ellipsoidal inclusion semi-axis lengths
C^{SC}	Single crystal elastic stiffness tensor
C_0	Stiffness tensor of calculated equivalent isotropic medium
C^{self}	Self consistent solution of stiffness tensor with texture
C_0^{self}	Self consistent solution of stiffness tensor with no texture
C_0	Stiffness tensor of calculated equivalent isotropic medium
λ_k	k eigenvalues of isotropic stiffness tensor of medium
ω_n	List of n resonance frequencies
K	Stiffness matrix for eigenvalue frequency equation
M	Mass matrix for eigenvalue frequency equation
u	Displacement vector (3D)
N	Polynomial order of Rayleigh Ritz approximation
Θ_j	j independent parameters for Bayesian inference
$\pi(\Theta\|\omega_n)$	Posterior probability density function for Θ
$\pi(\omega_n\|\Theta)$	Likelihood function of observing ω_n given Θ
$\pi(\Theta)$	Prior knowledge of Θ parameter distributions
σ	Standard deviation of Bayesian-estimated measurement errors

List of Abbreviations

AM	Additive Manufacturing
LPBF	Laser Powder Bed Fusion
EBM	Electron Beam Melting
BD	AM Build Direction
SB-CoNi-10	Cobalt-Nickel-base superalloy
IN625	Nickel-base alloy Inconel625
Ti64	Titanium6V4Al Alloy
SEM	Scanning Electron Microscopy
EBSD	Electron Backscatter Diffraction
CI	Confidence index
XRD	X-ray diffraction
ND	Neutron Diffraction
HIPPO	High-Pressure Preferred Orientation diffractometer
MAUD	Material Analysis using Diffraction software
ODF	Orientation Distribution Function
MTEX	Matlab toolbox for quantitative texture analysis
BCC	Body Centered Cubic crystal structure
FCC	Face Centered Cubic crystal structure
HCP	Hexagonal Close Packed crystal structure
TOF	Time of Flight
RUS	Resonance Ultrasound Spectroscopy
RS	Residual Stress
AB	As-built
HIP	Hot Isostatic Press
HT	Heat treatment
SR	Stress relief
MCMC	Markov Chain Monte Carlo
HMC	Hamiltonian Monte Carlo
SMC	Sequential Monte Carlo
SMCPy	Sequential Monte Carlo with Python Package
ESS	Effective Sample Size
EDM	Electrical Discharge Machining

Chapter 1
Additive Manufacturing, Ultrasonics, and Characterization

Additive manufacturing (AM), often referred to as 3D printing, has the potential to revolutionize traditional manufacturing of structural components, and has already proven to be a disruptive technology [1, 2, 3]. Fundamentally, AM defines any layer by layer generation of a component, rather than the subtractive process of removing material from a larger volume of the desired material. This chapter seeks to introduce the metal AM process, the fundamental advantages and associated limitations, the control and variability of material properties, and the state of qualification/ non-destructive evaluation techniques for AM materials. Special attention is given to the anisotropic behavior of AM materials, characterizing anisotropic materials with ultrasonics, and the assumptions made in traditional materials characterization.

1.1 Metal Additive Manufacturing

Additive manufacturing has historically been used as a rapid prototyping technique, with the intent of iterating through designs of a component before investing in the tooling and process to fabricate a final part geometry. Initial commercial development centered on polymers in the early 1980s [4], but metal powders were quickly explored with a laser heat source for AM [5]. Early systems involved polymer-coated metal powders for sintering [6] and led to the metallic powder/ wire feedstock machines used today. Given the localized melting of AM and departure from the controlled thermal gradients of traditional methods, the need for computer control became paramount to the development of commercial systems. Correspondingly, the initial adoption period primarily involved refinement of the additive equipment, with repeatability and process control rapidly ad-

vancing.

With increasing design, weight, and performance needs, the design freedom of AM has incentivized adoption for low yield parts over the traditional casting/ forging, joining, and machining processes [7]. While public successes such as GE Aviation's fuel injectors [8] demonstrate the performance advantages in service, AM is often implemented for cost and lead-time advantages alone [9]. With these novel performance and cost advantages, AM parts are no longer defined by comparison to their traditionally fabricated counterparts.

1.1.1 AM techniques

Metal AM techniques can be divided by feedstock, feedstock delivery, and heat source, with a variety of different naming conventions used for similar systems depending on the supplier. Broadly, there are powder bed fusion techniques or deposited powder/wire feedstock techniques [3], used with either laser or electron heat sources. Sheet lamination and binder jetting techniques are of interest in particular applications, but will not be considered in this work. Separating AM techniques by feedstock delivery, there are directed energy deposition (DED) and powder bed fusion (PBF) techniques.

DED methods involve one or more nozzles that feed wire or powder feedstock into the path of a heat source as it arrives at the component. A significant advantage of DED systems over PBF is the capability for component repair or addition to existing components [10], as well as the generation of large build volumes with high deposition rates. Wire-fed DED is useful for the production of large scale structures, but the range of alloys that are readily available in wire form is more limited than those available as powders, with many desirable alloys prohibitively difficult to produce in wire form. Powder-fed DED systems can leverage both elemental and alloy powders, in some cases enabling tuning of composition at the melt pool with multiple feedstock powders to generate complex gradients such as in functionally graded materials [11].

Powder bed fusion (PBF) processes are the most prevalent metal AM technique, involving the iterative movement of a heat source across layers of a precursor powder bed to build up the net-shape component. A given thickness of the metal powder is evenly spread by a coater or raking system after each completed layer, ensuring a consistent layer thickness of the powder on the order of 30 - 80 μm. The relatively small layer thickness limits the build volume and speed at the advantage of a low surface roughness and high geometric accuracy. PBF processes generally involve remelting the material below the 'fresh' powder layer, resulting in consistent part density. Powder-bed systems utilize either a laser heat source, referred to as laser powder bed fusion (LPBF), or an electron beam heat source, referred to as electron beam melting (EBM). EBM requires a vacuum environment to operate and has the inherent advantage of higher scanning speeds enabled by the lack of moving parts to control the beam. EBM also enables significantly higher powder bed preheat temperatures (1000°C or more), enabling a reduction in thermal gradient throughout the part that consequently reduces part distortion, contaminant pickup, and residual stresses in the part [12]. LPBF systems are more common than EBM systems due to the difficulty and expense of maintaining an electron beam/ vacuum environment. LPBF is typically conducted under an argon atmosphere [13], with finer powders ($\sim$ 15 - 45 μm [14]) than those used in the EBM process. The powder bed preheat temperature is presently limited in LPBF, but the process can be performed at ambient pressures. Laser heat sources enable greater control of the beam, with options for multiple lasers and different beam shapes enabling greater flexibility in the printing process [15].

This dissertation will only involve PBF techniques, as all of the material under study in this work was fabricated by EBM or LPBF.

1.1.2 Printing, microstructure, and properties of AM components

AM is capable of leveraging complex microstructural processing paths and spatial control over properties through the inherent high cooling rates, localized melting, and related tunability of the processing parameters [16]. In fact, the fast solidification velocities often lead to finer microstructures with increased strength at the cost of ductility [17]. For example, a wide range of tensile properties have been demonstrated between the different AM techniques or print orientations relative to the build direction (BD) [2]. Variations in effective process parameters and build conditions are not entirely user specified, as differences in AM equipment/ optics, powder quality, and heat treatments can alter the final properties. Thermal treatments such as stress-relief (SR) and hot isostatic pressing (HIP) have become standard to attempt to normalize residual stress levels or reduce the anisotropic behavior of the grain structure [18], respectively.

While point to point microstructural control [19] is advantageous to tailor part performance and properties [2], the relationship between the microstructure and processing parameters are ideally known prior to printing. The anisotropic behavior of AM microstructures is primarily a result of the preferential orientation of crystalline grains, known as texture, and related alterations of the grain shape/ morphology [20]. Large columnar grain morphologies are common for PBF materials due to the significant remelting of prior layers and epitaxial solidification relative to the heat extraction direction (build plate) [21]. The path, speed, and intensity of the heat source as it traverses each layer will be collectively referred to as the 'scan strategy', and is primarily responsible for controlling the solidification and overall component texture. Changes in heat source intensity, movement speed, or scan path result in large and often discontinuous changes in the grain structure, grain morphology, and residual stress levels [22, 23]. The sensitivity of the properties to variations in process parameters, component geometry, and build

chamber environmental conditions results in significant variability between built components [24], capable of inducing unacceptable variability in critical end-use properties. Even differences between the default scan strategies provided by different AM equipment manufacturers can produce unacceptable variability in properties.

The variability in crystallographic texture and consequent mechanical properties motivates efforts to qualify AM components with high resolution characterization techniques [25, 26]. Consequently, methods that can capture phenomena on the macroscopic (bulk specimen) scale, such as large-scale EBSD, have proven critical to adequately characterize AM textures and their corresponding effect on the final-part properties [27]. Phenomena such as surface-induced microstructure heterogeneity [24, 28] require bulk scale, yet precise, characterization techniques, resulting in drastic increases in the quantity and time expense of data collection. As a result, low-cost, rapid, and high-resolution qualification efforts to validate AM parts for critical component use have been identified as a key factor for wider implementation of AM [25, 29].

1.1.3 Qualification of AM components

Because of the inherent flexibility of AM, the traditional method to qualify each combination of alloy, property, and process quickly becomes intractable [17]. Qualification topics for AM components can be broadly classified into non-destructive evaluation/ testing (NDE) [25], print process parameter control and tuning [30], in-situ process feedback and monitoring [31], and post-process characterization and property measurements to generate process-property maps [32].

Print process parameter tuning and the generation of process-property maps are both time-intensive and dependent on testing at each parameter combination. Modeling efforts have naturally risen to reduce the need for extensive testing, but the complex physics needed to quantify melt-track interactions result in prohibitive computation times [33].

As introduced in Section 1.1.2, post-process approaches to normalize the property differences between AM parts have involved designing heat treatments and printing standards that seek to reduce the unintentional property differences. Unfortunately, post-processes such as heat treatments significantly increase the expense and time to generate end-use parts, and reduce some property advantages of as-printed AM parts. As a result, low cost, high throughput, and high resolution Non-Destructive Evaluation (NDE) techniques are of interest. Recent AM NDE approaches seek to quantify fracture critical and process induced defects, namely residual stresses, defect populations, secondary phases, and surface roughness effects [34]. While techniques such as μ-computed tomography (μCT) may be capable of supplanting a slower method such as serial sectioning, the expense of completing μCT on each printed part is limiting [35].

Techniques such as thermography [36] have been proven capable of in-process print monitoring, but are not suitable to characterize components after printing, as with a conventionally fabricated component [37]. Established NDE techniques that are rapid enough to interrogate large quantities of parts, either prior to service or in service, are therefore focused on here [38, 39]. Ultrasonics and acoustics fulfill these requirements, providing a range of capabilities for defect detection and property quantification depending on wavelength, experimental setup, and intended use [37]. Ultrasonics traditionally allow for the measurement of elastic properties, which is relatively unexplored for textured polycrystalline materials and anisotropic materials in general. The application of ultrasonics to AM components, particularly with regard to their elasticity, is focused on in this work with the goal of automating and furthering the capability of the ultrasonic measurements.

1.2 Nondestructive characterization of materials with ultrasound

Following scientific theory on wave propagation, ultrasonic characterization techniques were developed in the early 1900s following the development of technologies such as sonar. Ultrasound can be simply defined as a sound wave propagating at a frequency above the threshold of human hearing (∼20 kHz), with acoustics alternatively laying within the limit of human hearing. Although many fields of ultrasonic study involve couplings between solid and fluid or solid and gas, this work will only concern ultrasonics in solid matter. Neglecting the effects of coupling is a safe assumption for the technique of interest here, Resonant Ultrasound Spectroscopy (RUS), which will be further discussed in Section 1.2.1.

Ultrasonic waves are generated by an incident pulse of energy into the medium, which perturbs equilibrium positions as it propagates. The 3D wave equation of motion governs the speed and behavior of the wave as it propagates with time [40]. So long as the incident energy does not exceed the elastic limit of the material, ultrasound is non-destructive [41].

With Sokolov's work to detect metal flaws in objects via wave propagation [42, 43] and Firestone's patent and publication on the 'supersonic reflectoscope' [44], the field of imaging via ultrasound was established. Both the medical and non-destructive evaluation communities contributed to advancements in the mid 1900s, with the development of piezoelectric crystals enabling significantly more reliable excitation and detection capabilities [45, 46]. All of the early methods involved time-of-flight type measurements, often referred to as 'pulse' methods, where the time of travel of the reflected or transmitted wave was measured relative to the incident excitation event. These methods enabled a wide range of frequencies to be used for the incident wave, enabling the study of a variety of wavelengths with consequent length scales across a broad range of materials [47]. The basic principles of wave propagation also enabled the study of elastic properties,

attenuation losses, and the temperature dependence of these properties [48].

Resonant frequency based analysis methods were introduced by Fraser [49], where analytical methods to calculate the natural resonant frequencies of a perfect isotropic sphere [50] enabled the determination of Q-factors (ratio of resonance frequency to detected frequency width at half of frequency peak amplitude) and elastic behavior. Basic mechanical resonance involves the constructive interference of opposite directionally travelling waves in the object, resulting in a standing wave [51]. The natural resonant frequencies of a volume of material are also referred to as resonant modes, and are always listed beginning with the first (fundamental) resonant mode and counted increasing in frequency. Resonance methods involve exciting/ measuring the mechanical resonances of a given specimen, to interrogate the properties that induce the frequency values of those resonant frequencies.

Given the initial analytical models required fabrication of a perfectly spherical specimen [49], the analytical calculation of resonant frequencies rather than the measurement of them was the limiting factor in measuring elastic constants. Variational techniques enabled the analytical model to be generalized to calculate the resonant frequencies of a rectangular specimen [52, 53]. The calculation of resonant frequencies was solved as an eigenvalue equation with Rayleigh-Ritz numerical methods, with the development of the Rectangular Parallelepiped Resonance (RPR) [54] method enabling the expansion of the technique to different symmetry classes of materials [55]. These greater degrees of freedom complicated solving the optimization problem of the elastic constants, due to the required identification of mode types [55, 56].

1.2.1 Resonant ultrasound spectroscopy

Resonant Ultrasound Spectroscopy (RUS), as it is known today, was developed to quantify the elastic properties and phase transitions of ceramics that were difficult to

grow as large single crystals [57, 58]. Broadly, modern RUS has been used to define any measurement setup to determine the resonances of an object, though the range of the frequencies over which the term 'RUS' is applicable is not consistent. Though both time-of-flight (TOF) and resonant methods leverage higher inherent accuracy in characterizing elastic media [59], RUS has distinct advantages over TOF methods such as pulse-echo measurements. First, RUS does not rely on a plane-wave assumption, which incorporates the requirement that the specimen face be significantly larger than the transducer [60]. RUS therefore enables the use of small specimens, < 1 mm^3. Secondly, the full elastic tensor of the given object is probed by the resonance frequencies, where TOF ultrasound methods often require multiple measurements. As the symmetry of the material decreases (increasing anisotropy), the number of independent wave velocities that must be measured increases [61]. This is a critical factor when considering textured polycrystals, as arbitrary anisotropy can occur.

As discussed in Section 1.2, much of the practical development of RUS involved the construction of models to calculate resonant frequencies, and then inversely solve these models. The development of RUS as a broader technique employed novel basis functions [58] that expanded the analytical models to calculate the resonant frequencies of a greater number of shapes. With these forward model developments, the elastic constants of a wider range of materials could be precisely determined, provided the resonant frequencies could be measured. Briefly, measurement of the resonant frequencies enables the calculation of elastic constants through an inverse calculation [51, 57], such as an optimization. The need for inverse solving stems from the fundamental issue that no direct solution of the elastic constants can be determined from the resonant frequencies [62], while the resonant frequencies can be calculated from the shape and elastic constants of a specimen. Simply, the purpose of the inverse calculation is to iteratively calculate

the resonant frequencies from 'guessed' values of the elastic constants and compare to the experimentally measured frequencies. The calculated resonant frequencies are compared to experimentally-measured frequencies at each iteration, with the elastic constants being varied to minimize the difference, often using a cost function [57]. Despite the expansion of the calculation of resonant frequencies to arbitrary shapes, simple shapes such as parallelepipeds or spheres are preferred for computational efficiency [63] and prediction of mode shapes.

While the measurement of the resonant frequencies has become more reliable by implementing techniques such as contactless laser-RUS (LRUS) [64], the fundamental significance (dependence on elasticity, shape, and density of the component) of a complete set of resonant frequencies has remained constant. Supplementing the resonance frequencies with mode shape information (LRUS), x-ray/ strain information [65, 66], or directional pulse-echo measurements [67] has been proven to provide additional quantitative value, but the largest steps forward for analyzing RUS data have been computational in nature [68].

1.2.2 Elastic properties of AM components

RUS, as well as RUS inversion, provides a promising framework for the NDE of metal AM components. As mentioned in Section 1.1.2, the detection of AM grain structure variability, geometry, and defects is a significant challenge, with RUS an exciting avenue. While the concurrent sensitivity of RUS to various properties through the bulk of the specimen leaves the possibility for uncontrolled experimental errors, the sensitivity also enables the detection of variability between AM parts.

RUS is traditionally couched in the quantification of bulk elastic properties, i.e. the elastic constants are quantified relative to the reference frame of the specimen of interest. For single crystalline specimens, the single crystal elastic constants are quantified as they

align with the specimens principal axes, or for an isotropic polycrystalline specimen the isotropic elastic tensor is calculated from the Young's modulus (E) and Poisson's ratio (ν). Though research has addressed experimental symmetry breaking operations such as mis-aligned single crystal specimens [68], invariant solutions under triclinic specimen symmetry polycrystals [67], and basic relations between texture and bulk elasticity [69, 70], no framework exists to determine the elastic constants of an arbitrarily anisotropic polycrystalline aggregate.

Within ultrasonics and elasticity in general, the characterization of anisotropic polycrystals is rare [69, 70, 71, 72]. Given that very few materials are perfectly isotropic or single crystalline, the use of AM materials precludes the use of isotropic elasticity assumptions. The vast majority of the literature conducting research on textured polycrystals has employed orthotropic, cubic, or hexagonal specimen symmetries that may or may not match a given specimen's observed texture symmetry [69]. Alternatively, studies that examine the arbitrary anisotropy of the bulk specimen elasticity give little regard to the microscopic mechanisms at play [73, 74].

1.3 Motivation and structure

This thesis will focus on developing and quantifying AM components and microstructures with RUS, through novel quantitative connections between the predicted and measured resonant frequencies. Both forward modeling frameworks as well as inverse modeling frameworks are developed to enable significantly more robust and automated analyses of the properties of AM components without the existing symmetry limitations.

The mathematical concepts, terms, theory, and models used to define wave propagation, elasticity, texture representation, and symmetry are presented in Chapter 2. Additionally, the computational methods/ framework for the bulk and single crystal elastic constants are described in detail. Chapter 3 describes the development of an RUS frame-

work to determine the texture of AM components directly from the resonant frequencies. This approach leverages sequential Monte Carlo to robustly solve the inverse model in a highly parallel manner, resulting in an order of magnitude reduction in computation time.

Chapter 4 describes a novel method to determine the single crystal elastic constants from AM polycrystalline specimens, using only the resonant frequencies and texture data. This approach utilizes an end-to-end propagation of error from the resonant frequencies to the determined single crystal elastic constants, enabling robustly determined Bayesian uncertainties to capture the true convergence of the independent parameters from the base frequency data. Neutron diffraction and EBSD are utilized to inform the texture of the simulation, with resultant alterations in the determined single crystal elastic constants quantified. The determination of single crystal elastic constants is further expanded in Chapter 5, demonstrating that EBSD data in small quantities can be used to robustly determine the single crystal elastic constants of three alloys produced by AM: a novel cobalt-nickel-base alloy SB-CoNi-10C, nickel-base Inconel 625 alloy, and Ti-6Al-4V. The texture is calculated alongside the single crystal elastic constants, and is informed and bounded by the measured EBSD data.

Recommendations and limitations for the implementation of RUS on AM and polycrystalline specimens is given in Chapter 7, with examples to demonstrate the effect of isotropic texture, second phases, and inelastic effects such as residual stresses. The future outlook for the RUS technique with regard to rapid qualification of AM components is also discussed.

Chapter 2
Theory, Computations, Experimental Methods

This chapter defines the constitutive laws and theory used in this work, the related computations, and the overarching experimental methodologies. All of the theory will be presented with relevance toward the AM materials of interest, with special attention toward the differentiation of isotropic and anisotropic properties. The connections between these properties and wave propagation will be presented in order to explain their relevance for determining the relevant properties of AM materials.

2.1 Theory

2.1.1 Elasticity

Constitutive relations define the response of materials to external phenomena as the relation between physical quantities [75], most of which have been established empirically. Hooke's law is the constitutive relation between stress (σ) and strain (ϵ) on a material, through the material property, the elastic modulus (E) [76]. Elastic deformations in the material solely refer to changes in the shape that do not remain after the removal of the external stress. Equation 2.1 is a simplified scalar representation of these quantities, though importantly stress, strain, and the modulus are tensorial in nature (i.e. having magnitudes defined relative to the dimensions of a vector space). Note that this definition of elasticity, stress, and strain is defined for a simplified uniaxial loading condition.

$$E = \frac{\sigma}{\epsilon}$$
$$\sigma = \frac{F_N}{A_0} \tag{2.1}$$
$$\epsilon = \frac{\Delta l}{l_0}$$

Stress can be defined in this context as a force normal (F_N) to a nominal cross sectional area (A_0), with strain defined as the change in length (Δl) of the material along the direction of the applied force divided by the original length (l_0) of the material in that direction. Strain is a unitless quantity, with the units of stress and modulus consequently in Pa (N/m^2). The relation between stress and strain can be observed in Figure 2.1, remembering that the change in shape is purely elastic and that the material will return to its original shape after the removal of the force.

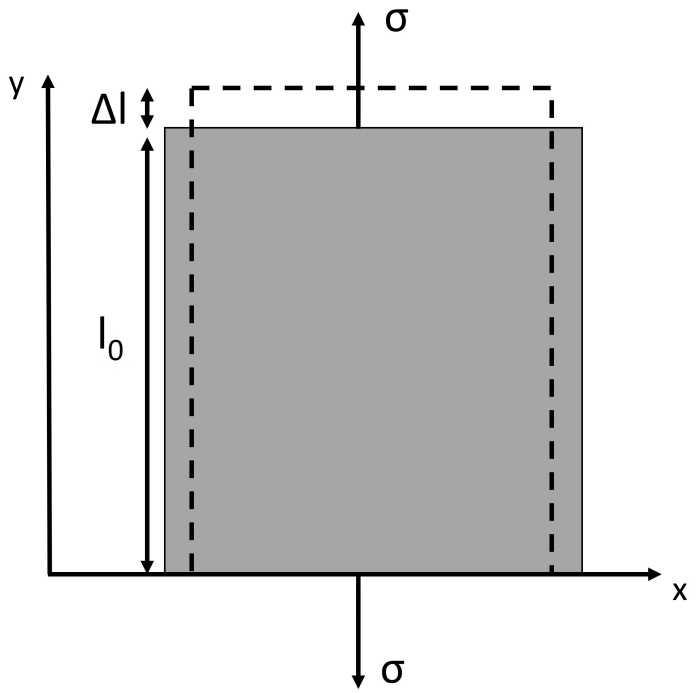

Figure 2.1: Simple stress and strain defined on a 2D block of elastic material. The dashed line shows the shape of the material after application of the applied stress.

The elastic modulus (E) is hereafter used to refer only to the Young's modulus [76], where the term elastic moduli, elastic tensor, and stiffness tensor will be interchangeably used to refer to the rank-4 elastic stiffness tensor (C_{ijkl}) relating stress and strain in three dimensions. The Young's modulus is denoted a 'directional' modulus here, meaning that it is a magnitude representing a stiffness of the material under specific directions, relative to some specific applied stresses/ strains in the material. There are a variety of different 'directional' moduli that are commonly reported, typically for isotropic materials given the moduli are not directionally dependent under those conditions. These include the shear modulus relating shear stresses (typically denoted τ) and shear strains (γ). These 'directional' moduli are less useful as a reportable value when the medium does not have isotropic properties, as the value of the modulus (e.g. Young' modulus) will change depending on the orientation of the medium, despite identical stresses being applied. Therefore, instead of stating all the different terminology and names of these different moduli, the tensorial notation of three-dimensional stress is introduced in Equation 2.2 and Figure 2.2 with an orthogonal basis e_1, e_2, e_3.

$$\sigma_{ij} = \begin{bmatrix} \sigma_{11} & \sigma_{12} & \sigma_{13} \\ \sigma_{21} & \sigma_{22} & \sigma_{23} \\ \sigma_{31} & \sigma_{32} & \sigma_{33} \end{bmatrix} = \begin{bmatrix} \sigma_{11} & \tau_{12} & \tau_{13} \\ \tau_{21} & \sigma_{22} & \tau_{23} \\ \tau_{31} & \tau_{32} & \sigma_{33} \end{bmatrix} \tag{2.2}$$

The choice of orthogonal basis as $1, 2, 3$ could be expressed as x, y, z for an analogue to Figure 2.1, with the importance of the indices simply indicating the normal direction of the material unto which the stress is applied and the direction that the stress is applied, respectively. Following this notation for strain, the three dimensional representation can be succinctly written as $\epsilon_{ij} = \frac{1}{2}(u_{i,j}+u_{j,i})$, with $u_{i,j}$ denoting Einstein summation notation of $\frac{\partial u_i}{\partial x_j}$. This notation is shown for the traditional strain and shear strain notation (γ) in

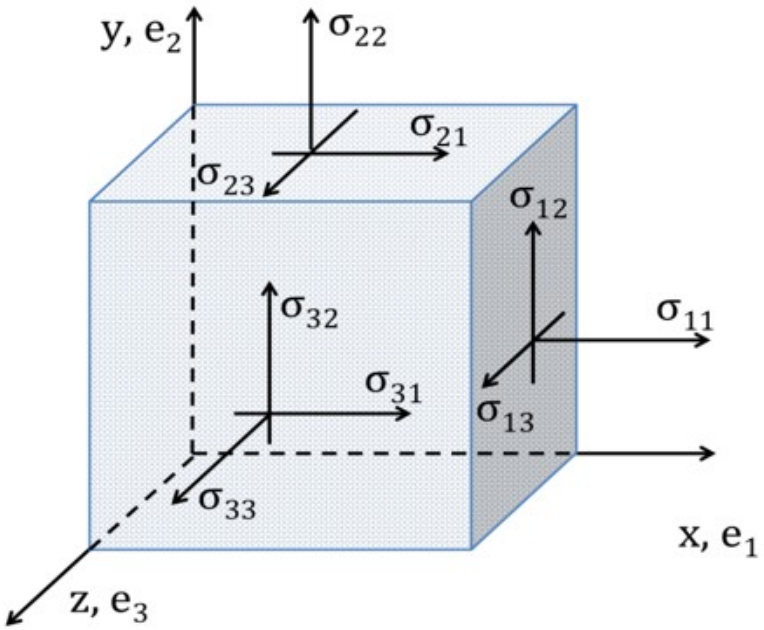

Figure 2.2: 3D stresses on a cube of material. Reprinted from [77] with permission from the author.

Equation 2.3.

$$\epsilon_{ij} = \begin{bmatrix} \frac{\partial u_1}{\partial x_1} & \frac{1}{2}(\frac{\partial u_1}{\partial x_2} + \frac{\partial u_2}{\partial x_1}) & \frac{1}{2}(\frac{\partial u_1}{\partial x_3} + \frac{\partial u_3}{\partial x_1}) \\ \frac{1}{2}(\frac{\partial u_2}{\partial x_1} + \frac{\partial u_1}{\partial x_2}) & \frac{\partial u_2}{\partial x_2} & \frac{1}{2}(\frac{\partial u_2}{\partial x_3} + \frac{\partial u_3}{\partial x_2}) \\ \frac{1}{2}(\frac{\partial u_3}{\partial x_1} + \frac{\partial u_1}{\partial x_3}) & \frac{1}{2}(\frac{\partial u_3}{\partial x_2} + \frac{\partial u_2}{\partial x_3}) & \frac{\partial u_3}{\partial x_3} \end{bmatrix} \tag{2.3}$$

$$\epsilon_{ij} = \begin{bmatrix} \epsilon_{11} & \epsilon_{12} & \epsilon_{13} \\ \epsilon_{21} & \epsilon_{22} & \epsilon_{23} \\ \epsilon_{31} & \epsilon_{32} & \epsilon_{33} \end{bmatrix} = \begin{bmatrix} \epsilon_{11} & \gamma_{12}/2 & \gamma_{13}/2 \\ \gamma_{21}/2 & \epsilon_{22} & \gamma_{23}/2 \\ \gamma_{31}/2 & \gamma_{32}/2 & \epsilon_{33} \end{bmatrix}$$

This notation introduces the fully anisotropic form of Hooke's law in three dimensions, as shown for the rank-4 stiffness tensor C_{ijkl}, rank-2 stress tensor σ_{ij}, and rank-2 strain tensor ϵ_{kl} in Equation 2.4.

$$\sigma_{ij} = C_{ijkl}\epsilon_{kl} \tag{2.4}$$

In contrast to the isotropic elastic tensor described up until this point, anisotropic elasticity involves describing all the elements of C_{ijkl}, and identifying symmetries between said elements [78]. Corresponding to the orthogonal coordinate system, the C_{ijkl} tensor has 3^4=81 components. Luckily, the diagonal symmetry of stress and strain ($\epsilon_{kl} = \epsilon_{lk}$, $\sigma_{ij} = \epsilon_{ji}$) results in $C_{ijkl} = C_{jikl}$ and $C_{ijkl} = C_{ijlk}$, meaning there are only 6 independent components of stress and strain and therefore 36 independent components of C_{ijkl}. The 36 components can therefore be represented relative to the stress and strain as shown in Equation 2.5.

$$\begin{bmatrix} \sigma_{11} \\ \sigma_{22} \\ \sigma_{33} \\ \sigma_{23} \\ \sigma_{13} \\ \sigma_{12} \end{bmatrix} = \begin{bmatrix} C_{1111} & C_{1122} & C_{1133} & C_{1123} & C_{1113} & C_{1112} \\ C_{2211} & C_{2222} & C_{2233} & C_{2223} & C_{2213} & C_{2212} \\ C_{3311} & C_{3322} & C_{3333} & C_{3323} & C_{3313} & C_{3312} \\ C_{2311} & C_{2322} & C_{2333} & C_{2323} & C_{2313} & C_{2312} \\ C_{1311} & C_{1322} & C_{1333} & C_{1323} & C_{1313} & C_{1312} \\ C_{1211} & C_{1222} & C_{1233} & C_{1223} & C_{1213} & C_{1212} \end{bmatrix} \begin{bmatrix} \epsilon_{11} \\ \epsilon_{22} \\ \epsilon_{33} \\ 2\epsilon_{23} \\ 2\epsilon_{13} \\ 2\epsilon_{12} \end{bmatrix} \tag{2.5}$$

Shortening the 2-index notation of stress and strain in Equation 2.5 to Voigt notation [41] by the ordering 11→1, 22→2, 33→3, 23→4, 13→5, 12→6 simplifies the representation significantly, as shown in Equation 2.6. Diagonal symmetry, e.g. $C_{ij} = C_{ji}$ then reduces the number of independent elastic constants to a maximum of 21. The notation given in Equation 2.6 is what will be used for the remainder of this work, and represents an arbitrary crystalline state.

$$\begin{bmatrix} C_{11} & C_{12} & C_{13} & C_{14} & C_{15} & C_{16} \\ C_{21} & C_{22} & C_{23} & C_{24} & C_{25} & C_{26} \\ C_{31} & C_{32} & C_{33} & C_{34} & C_{35} & C_{36} \\ C_{41} & C_{42} & C_{43} & C_{44} & C_{45} & C_{46} \\ C_{51} & C_{52} & C_{53} & C_{54} & C_{55} & C_{56} \\ C_{61} & C_{62} & C_{63} & C_{64} & C_{65} & C_{66} \end{bmatrix} \rightarrow \begin{bmatrix} C_{11} & C_{12} & C_{13} & C_{14} & C_{15} & C_{16} \\ C_{12} & C_{22} & C_{23} & C_{24} & C_{25} & C_{26} \\ C_{13} & C_{23} & C_{33} & C_{34} & C_{35} & C_{36} \\ C_{14} & C_{24} & C_{34} & C_{44} & C_{45} & C_{46} \\ C_{15} & C_{25} & C_{35} & C_{45} & C_{55} & C_{56} \\ C_{16} & C_{26} & C_{36} & C_{46} & C_{56} & C_{66} \end{bmatrix} \tag{2.6}$$

Single crystal elasticity

In the context of this work, single crystal elasticity is considered a simplification of general elasticity as many symmetry and specimen assumptions must be made to ensure the stiffness tensor of an object is identical to that of the single crystalline form. For example, by applying three mutually orthogonal planes of reflection symmetry to the arbitrary elastic tensor in Equation 2.6, the 9 independent stiffness terms of an orthotropic symmetry are obtained on the left side of Equation 2.7. Orthotropic is the general symmetry class, while orthorhombic refers to a single crystal symmetry of the same form. Then, if the three directions e_1, e_2, e_3 are assumed equal in length for the crystal axes, a cubic symmetry (3 independent parameters) is obtained on the right side of Equation 2.7.

$$\begin{bmatrix} C_{11} & C_{12} & C_{13} & 0 & 0 & 0 \\ C_{12} & C_{22} & C_{23} & 0 & 0 & 0 \\ C_{13} & C_{23} & C_{33} & 0 & 0 & 0 \\ 0 & 0 & 0 & C_{44} & 0 & 0 \\ 0 & 0 & 0 & 0 & C_{55} & 0 \\ 0 & 0 & 0 & 0 & 0 & C_{66} \end{bmatrix} \rightarrow \begin{bmatrix} C_{11} & C_{12} & C_{12} & 0 & 0 & 0 \\ C_{12} & C_{11} & C_{12} & 0 & 0 & 0 \\ C_{12} & C_{12} & C_{11} & 0 & 0 & 0 \\ 0 & 0 & 0 & C_{44} & 0 & 0 \\ 0 & 0 & 0 & 0 & C_{44} & 0 \\ 0 & 0 & 0 & 0 & 0 & C_{44} \end{bmatrix} \tag{2.7}$$

Hexagonal materials can be similarly reduced from an orthorhombic symmetry state, with axial symmetry around the c-axis (height), taken to be the e_3 axis traditionally. In this case, a state of 'transverse isotropy' is implied, meaning that there are 5 independent elastic moduli in Equation 2.8.

$$\begin{bmatrix} C_{11} & C_{12} & C_{13} & 0 & 0 & 0 \\ C_{12} & C_{11} & C_{13} & 0 & 0 & 0 \\ C_{13} & C_{13} & C_{33} & 0 & 0 & 0 \\ 0 & 0 & 0 & C_{44} & 0 & 0 \\ 0 & 0 & 0 & 0 & C_{44} & 0 \\ 0 & 0 & 0 & 0 & 0 & \frac{C_{11}-C_{12}}{2} \end{bmatrix} \tag{2.8}$$

Isotropic elasticity

Isotropic symmetry is a special case of cubic symmetry, where $C_{44} = \frac{C_{11}-C_{12}}{2}$ in Equation 2.9.

$$\begin{bmatrix} C_{11} & C_{12} & C_{12} & 0 & 0 & 0 \\ C_{12} & C_{11} & C_{12} & 0 & 0 & 0 \\ C_{12} & C_{12} & C_{11} & 0 & 0 & 0 \\ 0 & 0 & 0 & \frac{C_{11}-C_{12}}{2} & 0 & 0 \\ 0 & 0 & 0 & 0 & \frac{C_{11}-C_{12}}{2} & 0 \\ 0 & 0 & 0 & 0 & 0 & \frac{C_{11}-C_{12}}{2} \end{bmatrix} \tag{2.9}$$

The assumption of isotropic elasticity can be further simplified in Equations 2.10, where $\nu = \frac{-\epsilon_T}{\epsilon_N}$ is the known Poisson's ratio describing the material's strain in the transverse direction relative to the direction of uniaxial applied stress.

$$\begin{bmatrix} \sigma_{11} \\ \sigma_{22} \\ \sigma_{33} \\ \sigma_{23} \\ \sigma_{13} \\ \sigma_{12} \end{bmatrix} = E/(1+\nu)(1-2\nu) \begin{bmatrix} 1-\nu & \nu & \nu & 0 & 0 & 0 \\ \nu & 1-\nu & \nu & 0 & 0 & 0 \\ \nu & \nu & 1-\nu & 0 & 0 & 0 \\ 0 & 0 & 0 & 1-2\nu & 0 & 0 \\ 0 & 0 & 0 & 0 & 1-2\nu & 0 \\ 0 & 0 & 0 & 0 & 0 & 1-2\nu \end{bmatrix} \begin{bmatrix} \epsilon_{11} \\ \epsilon_{22} \\ \epsilon_{33} \\ 2\epsilon_{23} \\ 2\epsilon_{13} \\ 2\epsilon_{12} \end{bmatrix} \tag{2.10}$$

Following Equation 2.10, the method to determine the Young's modulus from a uniaxial tensile test can be observed when $\sigma_{11} \neq 0$, ϵ_{11} is measured, and all other stresses are zero. Again, the requisite assumptions when measuring complete isotropy are assumed, not implied, by the result of the form of the tensor.

2.1.2 Additive manufacturing texture and solidification

At the most basic level, solidification describes the phase change upon cooling from liquid to solid, where the free energy of each phase are equal to one another (assuming

equilibrium conditions). The driving forces behind fundamental solidification are well studied and will not be restated here, rather this section serves to describe the AM solidification process necessary to understand the resultant microstructures and morphologies.

Solidification morphology of AM microstructures

Though AM components are subject to localized melting and specific thermal gradients as a result of the AM process, it is important to note that the solidification of the liquid to solid in AM is subject to standard solidification theory. Despite this, the kinetics of solidification in AM tend to occur in shorter times and with more complex gradients than a more controlled solidification process such as casting. As a result, traditional assumptions and simplifications about phenomena such as fluid flow and convection must be abandoned in favor of more complex, physics-based models [79].

After overcoming the energy barrier to nucleate the solid phase [80], the morphology of the solidified structure is dependent on the crystal growth conditions at the liquid/solid surface, known as the growth front. There is limited diffusion of the solute in the molten liquid, generating gradients of the chemical concentrations in the liquid in addition to the partitioning of solute as a result of the Schiel-Gulliver relationship [81]. The stability of the growing solid involves a flow of heat normal to that surface, which can be represented by a thermal gradient. The thermal gradient (G) relative to a standard cartesian reference frame can be described by Equation 2.11, where T represents temperature and x, y, z represent standard cartesian directions.

$$G = ||\nabla T|| = \sqrt{(\frac{\partial T}{\partial x})^2 + (\frac{\partial T}{\partial y})^2 + (\frac{\partial T}{\partial z})^2} \tag{2.11}$$

At the growth interface, the conditions to maintain growth are affected by the curvature of the interface, which also affects the melting temperature of the system. Stability

criteria for a planar front growth (no curvature) or spherical growth have been developed, with the thermal gradient heavily affecting these estimates. The stability criteria for planar growth are provided in Equation 2.12 [82], with G representing the thermal gradient, R representing the interface velocity, ΔT_0 as the freezing temperature range, and D_l as the liquid diffusivity.

$$\frac{G}{R} \geq \frac{\Delta T_0}{D_l} \tag{2.12}$$

The commonly observed growth morphologies such as cellular and dendritic are determined by the undercooling (ΔT), with varying sizes of and cells and dendrites representing the transition between the two states. Dendrite solidification is a result of the anisotropy of interfacial energy between crystallographic orientations [83] and will vary within the AM melt pool.

Given the prevalence of materials with cubic crystalline nature (face/ body centered cubic), cubic materials will be focused on in this section to elucidate the solidification structures of AM materials. When cubic materials solidify in dendritic morphologies, they solidify along <001> crystallographic directions (faces of the cubic unit cell) [84]. The growth direction is then dependent on the direction of heat flow during solidification, resulting in phenomena such as the 'alignment' of an AM microstructure with the build direction. The overall build direction in an AM build represents the direction that heat must travel through the part and back to the build plate, the heat conduction path. As a result, well-aligned, dendritic grain morphologies are often observed in AM components as constrained, columnar microstructures.

Elasticity dependent on texture

Polycrystalline aggregates of crystallite grains, called polycrystals, compose the vast majority of in-service metal components. Even for crystalline aggregates with chemical and phase homogeneity, the distribution of the crystallography of grains will certainly differ relative to their orientation in a printed object. Given that perfectly isotropic single phase materials are rare, each individual crystallite is typically anisotropic in its physical properties. As a result, an aggregate of these crystal grains will also be anisotropic, unless the orientations of all the crystallites are perfectly random.

Elasticity is a 4th order tensor, and hence captures the directional dependence of elasticity [20]. However, because the orientations of the individual anisotropic crystallites are capable being completely anisotropic as an aggregate, or completely isotropic, the bulk elastic symmetry exhibited by an unknown polycrystalline specimen is unknown. The bulk elastic symmetries (as opposed to the intrinsic single crystal symmetry) can range anywhere between isotropic (Figure 2.10, and triclinic (Figure 2.5). Figure 2.3 displays this relationship with an electron backscatter diffraction (EBSD) map of grain orientations for an additively manufactured specimen later presented in Chapter 3.

EBSD involves point by point orientation mapping, with each pixel colorized by their orientation relative to the build direction, indicated. As demonstrated, the grains grow aligned with the build direction regardless of the specimen orientation, meaning the rotation of the specimen axes relative to the build direction results in a change in bulk symmetry, despite identical texture relative to the build itself.

As a result, classifying textured polycrystalline specimens by their bulk symmetry, analogous to how a single crystal symmetry would be described (elastically), is limiting when considering a technique such as additive manufacturing. Luckily, because the elasticity of the macro-scale is dependent on the texture (and single crystal elastic constants),

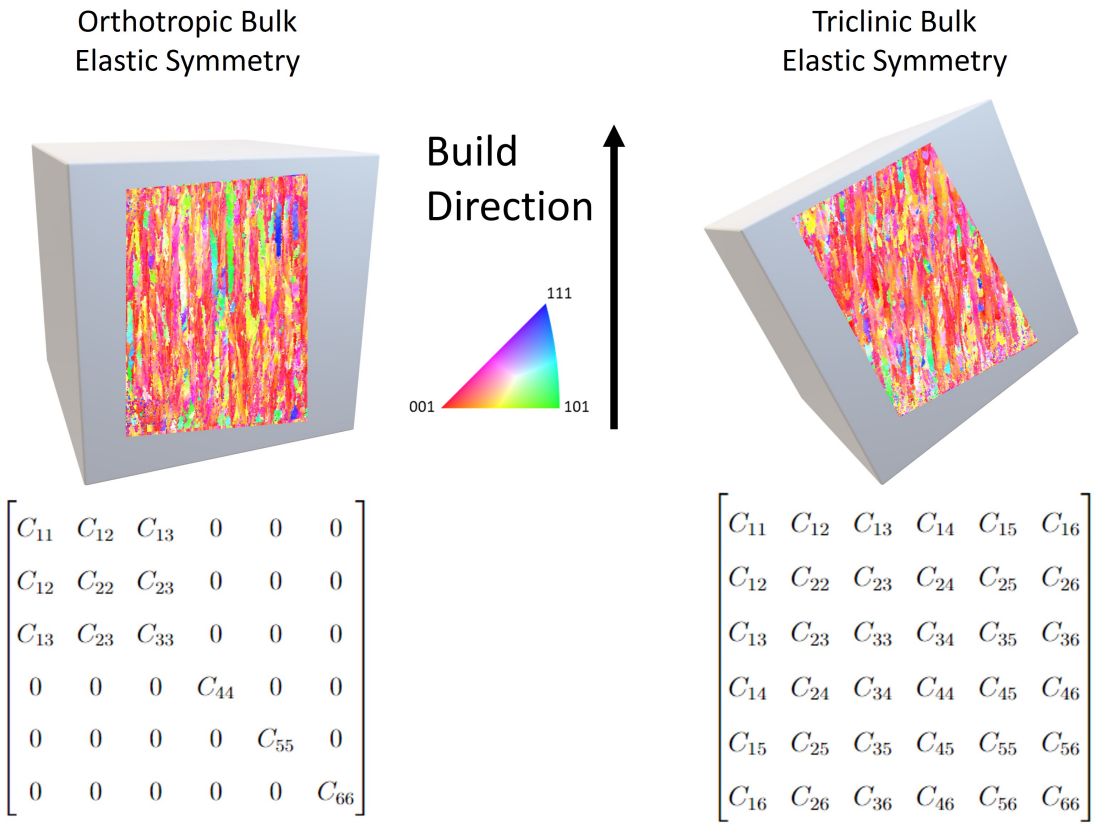

Figure 2.3: Change in bulk elastic symmetry with texture orientation of an additively manufactured cobalt-nickel superalloy specimen (Chapter 3). EBSD data/ grain size is not to scale.

the macroscale properties such as elasticity can be calculated.

With knowledge of the single crystal elastic symmetry, relations between the observed orientations of the crystallites and the bulk elastic constants can be determined. Generally, the measured orientations are used to calculate functions that represent the observed distribution of orientations across all the measurements of interest. These functions are termed orientation distribution functions (ODF). The representation of texture for the purposes of determining the physical properties of materials is critical to the understanding and in-service-application of anisotropic materials [20].

2.1.3 Texture representation

The field of quantitative texture representation was initiated by Roe [85, 86], with the goal of efficiently representing and accounting for the most basic representation of the orientation properties, inducing alterations in physical behavior. This field has spread to connect metallurgy, geology, polymer science, and many others.

Following [20], the representation of texture includes an inherent assumption that the (generally large number of) individual orientations are known. This distribution of points can be considered as existing in three-dimensional space. The goal of texture representation is to distill the raw data of individual orientations into a continuous distribution in orientation space, such that the entire space is concretely described. This defines a traditional orientation distribution function (ODF). The ODF is represented by the symbol $f(g)$, with the symbol g representing orientation.

$$\frac{\Delta V}{V} = \frac{\int_{\Delta\Omega} f(g)dg}{\int_{\Omega_0} f(g)dg} \tag{2.13}$$

Equation 2.13 represents the ODF, $\frac{\Delta V}{V}$ denoting a volume fraction and $\Delta\Omega$ representing a region of the total volume of orientation space Ω_0. Ω_0 is either the full $8\pi^2$ or a symmetry reduced fraction of that. Orientation densities are often referred to in multiples of random distribution (MRD), by setting f(g)=1 for a uniform density (perfect isotropy). The orientations dg (or for finite increments Δg) are most often represented by Euler angles, with Θ referring to the pole distance in Equation 2.14.

$$\begin{aligned} dg &= sin\Theta d\Theta d\Psi d\phi \\ \Delta g &= \Delta(cos\Theta) d\Theta d\Psi d\phi \end{aligned} \tag{2.14}$$

Because the ODF is effectively a distribution of vectors across the surface of a sphere,

the use of 'generalized spherical harmonics' has enabled application to a variety of problems [85, 87].

Aggregate elastic constants calculated with the ODF

The elastic constants of an aggregate of grains begins with a volume average of a tensorial quantity, in this case represented by $\langle t \rangle$. For tensors such as elasticity that can be assumed constant within a single crystal grain, the volume integral can be expressed as a summation over the crystals and transformed into an integral over orientation space.

$$\begin{aligned} \langle t \rangle &= \frac{1}{V} \int_V t(x) dV \\ \langle t \rangle &= \int t(g) f(g) dg \end{aligned} \tag{2.15}$$

The representation of the ODF in terms of the generalized spherical harmonics is expressed as Equation 2.16.

$$f(\Theta, \Psi, \phi) = \sum_{l}^{L} \sum_{m=-l}^{l} \sum_{n=-l}^{l} W_{lmn} Z_{lmn} (cos\Theta) e^{im\Psi} e^{in\phi} \tag{2.16}$$

Where L represents the order and consequent number of terms of the approximation, based on the property of interest. W_{lmn} are the coefficients of the expansion depending on the texture of the polycrystal, with specific micro and macroscopic symmetries containing different numbers of independent coefficients [87]. The tensor property of interest can also be expressed by spherical harmonics, as follows for the tensor t in Equation 2.17. The volume average can then be expressed by the sum of the expansion coefficient products.

$$t(g) = \sum_{l}^{L'} \sum_{m=-l}^{l} \sum_{n=-l}^{l} t_{lmn} Z_{lmn}(cos\Theta) e^{im\Psi} e^{in\phi}$$
$$\langle t \rangle = 4\pi^2 \sum_{l}^{L''} \sum_{m=-l}^{l} \sum_{n=-l}^{l} t_{lmn} W_{lmn} \tag{2.17}$$

The tensor t can now be considered as the bulk elastic tensor for relation back to a calculation of the average polycrystalline properties. The standard Voigt and Reuss (upper/ lower) bounds on the bulk elastic constants are derived by considering a state of uniform strain or uniform stress, respectively. The Voigt [88] and Reuss [89] bounds are denoted C^V and C^R (in the context of linearized Hooke's law) in Equation 2.18, where C^{SC} denotes the single crystal elastic constants.

$$C^V = \langle C^{SC} \rangle$$
$$C^R = \langle (C^{SC})^{-1} \rangle^{-1} \tag{2.18}$$

Tighter upper and lower elastic bounds are obtained through the Hashin Shtrikman bounds [90], which incorporates 2-point statistics of the microstructure shapes, as well as phase-fractions for multiple phases. This more precise treatment of bulk elasticity was quickly iterated on with self-consistent solutions of the elastic constants (inspired by Eshelby's inclusion in an isotropic medium [91]) by Kroner [92]. The theory behind the Hashin-Strikman and self-consistent elastic solutions with regard to the ODF are provided in the computations of Section 2.2.1, with the critical point that the representation of texture by an ODF is identical for each estimate.

2.1.4 3D wave propagation and resonance

The governing laws of acoustics and ultrasonics come from the same basic laws of physics as those of continuum mechanics. The wave equation of motion, given in Equation

2.19, is the connection between elastic behavior and wave propagation properties. Body forces are assumed to be zero, the stress (σ_{ij}) is assumed homogeneous throughout the assumed volume, and the symbols ρ, u, x, t represent the density, displacement, position, and time in the ith direction, respectively.

$$\frac{\partial \sigma_{ij}}{\partial x_i} = \rho \frac{\partial^2 u_i}{\partial t^2} \tag{2.19}$$

Replacing σ_{ij} with the anisotropic representation of elasticity (Eq 2.4) into Equation 2.19 yields 2.20.

$$\frac{C_{ijkl}\partial^2 u_k}{\partial x_i \partial x_j} = \rho \frac{\partial^2 u_i}{\partial t^2} \tag{2.20}$$

While isotropic materials only have two fundamental wave velocities (c_0) corresponding to the shear and longitudinal wave velocities, arbitrarily anisotropic materials are capable of a greater number of independent wave velocities, which can be determined according to the Christoffel determinant [93] given in Equation 2.21.

$$|C^*_{ijkl} n_j n_k - \rho c_0^2 \delta_{il}| = 0 \tag{2.21}$$

Note that $n = [cos(\phi_j)sin(\theta_i), sin(\theta_j)sin(\theta_i), cos(\theta_i)]$ and δ_{il} the Kronecker delta.

Resonance frequency solution

Solving the wave equation in the context of resonance frequencies involves formulation of the mechanical Lagrangian ($\mathcal{L}$) [40, 94]. In Equation 2.22, the kinetic energy (KE) and potential energy (PE) of the specimen are integrated relative to the volume (V) of the specimen. The PE and KE obtain their form from a simple harmonic oscillator (time dependence $e^{i\omega t}$ [57]), with ω representing the angular resonance frequencies and

the consequent resonance frequencies $f_r = \omega/2\pi$.

$$\begin{aligned} \mathcal{L} &= \int_V (KE - PE) dV \\ PE &= \frac{1}{2} \sum_{i,j,k,l} C_{ijkl} \frac{\partial u_i}{\partial x_j} \frac{\partial u_k}{\partial x_l} \\ KE &= \frac{1}{2} \sum_i \rho \omega^2 u_i^2 \end{aligned} \tag{2.22}$$

In order to find the stationary solution of $\mathcal{L}$, a variational approach of Hamilton's principle is employed [57] in Equation 2.23. The displacements (u_i) vary arbitrarily in the volume V and surface S to calculate the variation of the Lagrangian.

$$\begin{aligned} u_i \to u_i + \delta u_i, \mathcal{L} \to \mathcal{L} + \delta \mathcal{L} \\ \mathcal{L} + \delta \mathcal{L} = 1/2 \int_V \sum_i \rho \omega^2 (u_i + \delta u_i)^2 - \sum_{i,j,k,l} C_{ijkl} \frac{\partial (u_i + \delta u_i)}{\partial x_j} \frac{\partial u_k}{\partial x_l} dV \end{aligned} \tag{2.23}$$

Neglecting higher order terms in δu_i, applying integration by parts and the divergence theorem, and leveraging n_i as the unit outer normal to S:

$$\delta \mathcal{L} = \int_V \sum_i [\rho \omega^2 u_i + \sum_{j,k,l} C_{ijkl} \frac{\partial^2 (u_k)}{\partial x_j \partial x_l}] \delta u_i dV - \int_S [\sum_i (\sum_{j,k,l} C_{ijkl} n_j \frac{\partial u_k}{\partial x_l}) \delta u_i] dS \tag{2.24}$$

This solution, combined with the arbitrariness of δu_i in the volume V and surface S, implies that the u_i corresponding to $\delta \mathcal{L} = 0$ result in each term equaling zero. Therefore, the u_i enabling each side to equal zero are the same where ω^2 are the discrete set of eigenvalues equal to the resonant frequencies.

While solutions to the wave equation can describe both standing waves (i.e. resonance) and traveling waves, only the basics of standing waves will be covered here. A

standing wave involves the overlap of two opposite traveling waves with identical wavelength. The mechanical normal mode vibrations (resonance frequencies) of an elastic body are these same constructively interfering waves, trapped in a finite distance [59]. Equation 2.25 demonstrates a simplified description of the resonant frequencies (f_r). The resonance mode order number is denoted n and specimen wave propagation distance L.

$$\begin{aligned} f_r &= \frac{c_0}{\lambda} \\ \lambda &= \frac{2\pi}{k} \\ L &= \frac{n\lambda}{\pi} \end{aligned} \tag{2.25}$$

The given resonance frequency is dependent on the wavespeed (c_0) and wavelength (λ), where the wavespeed is dependent on the effective elastic stiffness (C^*_{ijkl}) through Equation 2.21. (C^*_{ijkl}) is the effective directional modulus calculated through a linear combination of the components of the full elastic tensor (C_{ijkl}).

2.2 Computations

This section will describe the computations, based on the theory laid out in Sections 2.1.3 and 2.1.4, necessary to make quantitative determinations from measured resonant frequency data. This section will be split into two parts, the calculation of resonant frequencies which is referred to as the *forward model* in Section 2.2.1, and the *inverse model* in Section 2.2.2 which is comprised of iteratively calculating the forward model and comparing it to the measured frequencies.

2.2.1 Forward model of resonant frequencies

The forward model describes a single evaluation of the theoretical resonant frequencies. As remarked in Section 1.2.2, the resonance frequencies are sensitive to a variety of quantities such as the specimen shape, elastic constants, and density, with the distinction

to the inverse model being that variations in these properties are not considered within the forward model. The result of the forward model is therefore a list of the n resonance frequencies, denoted ω_n.

The calculation of resonant frequencies in this work is discretized into two parts. The first is the classical calculation of resonant frequencies [58] from the elastic constants of a given specimen shape in Section 2.2.1, and the second is the calculation of the effective (aggregate) elastic constants of a given specimen from the specimen's microstructural texture and single crystal elastic constants in Section 2.2.1. By combining these two models, the single crystal elastic constants and microstructural texture can be directly used to calculate the resonant frequencies, with no preset determination of the polycrystalline elastic symmetry. The complete forward model is therefore denoted the *combined forward model*.

Calculating resonant frequencies from elasticity

Following Section 2.1.4, the left side of equation 2.24 can be restated as Equation 2.26 due to $\delta\mathcal{L} = 0$.

$$\rho\omega^2 u_i + \sum_{j,k,l} C_{ijkl} \frac{\partial^2(u_k)}{\partial x_j \partial x_l} = 0 \tag{2.26}$$

This equation takes the form of a generalized eigenvalue equation, which is approached by first expanding the displacements u_i as the sum of a finite number of J basis functions with $3J$ coefficients $a_{i\lambda}$ [57]. Writing the u_i in terms of their basis functions ϕ_λ results in Equation 2.27 following the Rayleigh-Ritz prescription.

$$a_i = a_{i\lambda}\phi_\lambda(x_1, x_2, x_3) \tag{2.27}$$

The variational "xyz" method was used for the basis polynomials [58], where the x, y, z are denoted x_1, x_2, x_3 here as the Cartesian coordinates. Note that Legendre polynomials,

consisting of an orthonormal basis, might be used in the case of specimen geometries such as a rectangular parallelepiped and could enable quicker computations [53, 55]. However, the use of the "xyz" method is more easily extendable to other specimen geometries and is thus implemented here. The basis polynomial representation is summarized in Equation 2.28, with P representing the polynomial order and l, m, n representing non-negative integers.

$$\begin{aligned} \phi(x_1, x_2, x_3) &= x_1^l x_2^m x_3^n \\ l + m + n &\leq P \\ J &= \frac{(P+1)(P+2)(P+3)}{6} \end{aligned} \tag{2.28}$$

With the basis in context, it can be substituted back into Equation 2.22 to obtain Equation 2.29.

$$\mathcal{L} = \frac{1}{2} \int_V [\sum_{i,i',\lambda,\lambda'} \delta_{ii'} \rho \omega^2 a_{i\lambda} a_{i'\lambda'} \phi_\lambda \phi_{\lambda'} - \sum_{i,i',j,k,l,\lambda,\lambda'} C_{ijkl} a_{i\lambda} a_{i'\lambda'} \frac{\partial \phi_\lambda}{\partial x_j} \frac{\partial \phi_{\lambda'}}{\partial x_l}] dV \tag{2.29}$$

i' and λ' indicate the second substitution of u_i, where summing over λ' and λ are each the J permutations of the non-negative integer sets $\lambda = (l, m, n)$. Condensing in terms of i, k, λ, λ' corresponding to [68], the Equation can be restated as a stiffness matrix K and a mass matrix M, with δ being the Kronecker delta. This terminology is then substituted into Equation 2.29, as shown in Equation 2.30.

$$\begin{aligned} K = K_{i\lambda k\lambda'} &= \sum_{j,l} C_{ijkl} \int_V [\frac{\partial \phi_\lambda}{\partial x_j} \frac{\partial \phi_{\lambda'}}{\partial x_l}] dV \\ M = M_{i\lambda k\lambda'} &= \rho \delta_{ik} \int_V [\phi_\lambda \phi_{\lambda'}] dV \\ \mathcal{L} &= \frac{1}{2}[\omega^2 a^T M a - a^T K a] \end{aligned} \tag{2.30}$$

a_i is therefore a vector, with the stationary condition fulfilled by setting $\frac{\partial \mathcal{L}}{\partial a_{i\lambda}} = 0$ when $\partial \mathcal{L} = 0$ to obtain the generalized eigenvalue Equation 2.31.

$$Ka = \omega^2 M a \tag{2.31}$$

Given the connection between the coefficients a and u, the eigenvalue problem is succinctly restated as Equation 2.32, with the resonant frequencies ω determinable by easily accessible eigenvalue solvers.

$$Ku = \omega^2 M u \tag{2.32}$$

This relationship can be further summarized in Figure 2.4, where the elasticity, dimensions, density, and polynomial order are used to determine the parameters in Equation 2.32 and calculate the resonant frequencies.

Calculation of aggregate polycrystalline elasticity from texture

To define the effect of preferred grain orientation (texture) on the elastic constants of the specimen, the ODF $f(Q)$ is defined to represent the relative amount of grains with orientation Q over $Q \in SO(3)$. $SO(3)$ denotes the standard special orthogonal group of $\mathbb{R}^3$. The ODF is given in terms of the tensorial texture coefficients $V_{\langle\alpha\rangle\beta}$, the basis tensors $F_{\langle\alpha\rangle\beta}$ fixed by the microscopic symmetry, and the tensor order α (as given in [95]). The tensorial texture coefficients can be determined from the coefficients C_{lmn}

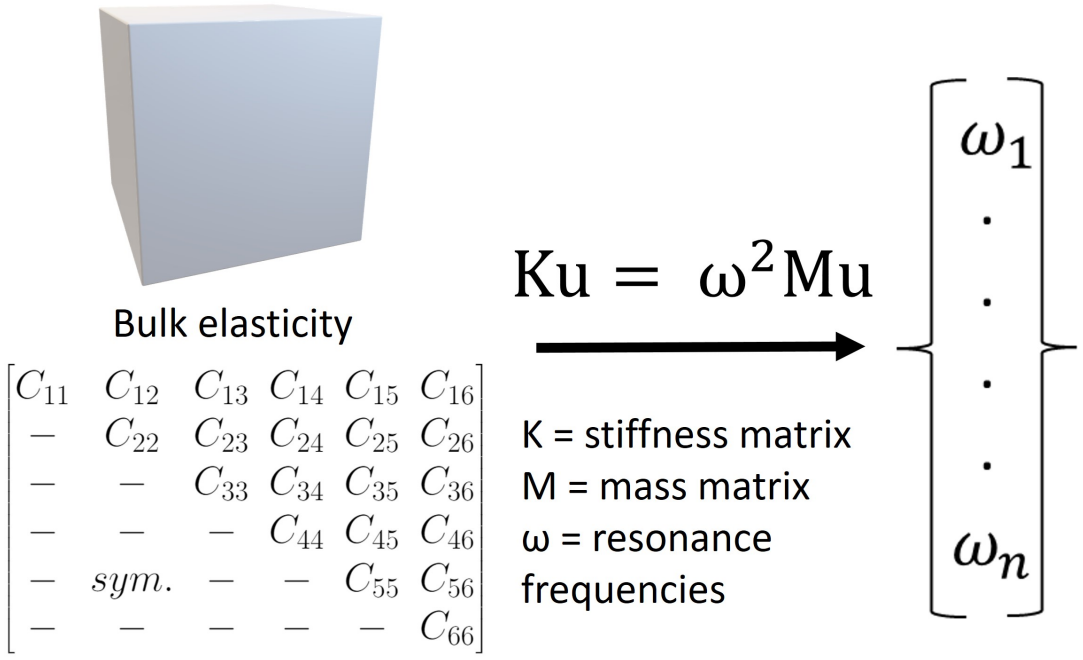

Figure 2.4: Forward model calculation of resonant frequencies from arbitrarily elasticity of a parallelepiped specimen.

traditionally utilized for quantitative texture analysis [87] by using the spherical harmonic functions T_{lmn} (Euler angle parameterization). The translation from tensorial $V_{\langle\alpha\rangle\beta}$ to C_{lmn} coefficients is provided in Equation 2.33 [95]. Note that brackets $\langle\rangle$ indicate an orientation average over $SO(3)$, α indicates order, and m, n correspond to the indices at that order.

$$\begin{aligned} f(Q) &= \sum_{\alpha=0}^{4} \sum_{\beta=1}^{n_\alpha^H} (1+2\alpha) V_{\langle\alpha\rangle\beta} \cdot F_{\langle\alpha\rangle\beta}(Q) \\ C_{lmn} &= (1+2\alpha)\langle f, T_{lmn}\rangle = (1+2l)^2 \sum_{\beta=1}^{n_\alpha^H} \langle V_{\langle l\rangle\beta} \cdot F_{\langle l\rangle\beta}, T_{lmn}\rangle \end{aligned} \tag{2.33}$$

β is the index of each independent basis tensor, omitted in further representations given n_α^H=1 for materials with cubic (at α=4) or hexagonal (at α=2,4) single crystal symmetry, constituting all the materials studied here. ODF coefficients up to order 4 ($\alpha \leq 4$) fully

define the effect of grain orientations on the aggregate elastic tensor [69, 93, 96], with alternate numbers of independent ODF coefficients necessary at each order α to define the aggregate elasticity relative to the macroscopic symmetry.

For arbitrary anisotropy on the bulk scale, triclinic symmetry must be assumed, and is therefore assumed throughout the remainder of this work. The texture coefficients (C_{lmn}) can be calculated from ODFs in the MATLAB package MTEX, in order to translate to $V_{\langle\alpha\rangle pqrs}$ using Equation 2.33. The orientation average of a reference 4th order tensor L can be parameterized in terms of a harmonic decomposition (hd) of that reference tensor, as given below in Equation 2.34. The constants $h_{I1}, h_{I2}, H_{2,1}, H_{2,2}, H_{4,1}$ are determined by the harmonic decomposition (hd) of L, with P_1 and P_2 as isotropic projectors, consistent with [95].

$$\begin{gathered} hd(L) \rightarrow h_{I1}, h_{I2}, H_{2,1}, H_{2,2}, H_4 \\ \langle f, L\rangle = h_{I1}P_1 + h_{I2}P_2 + H_{2,1} * V_{\langle 2\rangle ij} + H_{2,2} * V_{\langle 2\rangle ij} + H_{4,1} * V_{\langle 4\rangle pqrs} \end{gathered} \tag{2.34}$$

The texture coefficients that affect the specimen elasticity at a given tensor order are dependent on the number of independent harmonic basis tensors H for the given single crystal elastic constant symmetry, as given in [95]. The number of independent texture coefficients within each texture tensor is then dependent on the specimen symmetry, again taken to be arbitrarily anisotropic (triclinic) in this work. For microscopically cubic materials, $H_{2,1} = 0$ and $H_{2,2} = 0$, meaning only the fourth order texture tensor $V_{\langle 4\rangle pqrs}$ with nine independent terms is needed (Equation 2.35) to define an arbitrary macroscopic symmetry.

$$V_{\langle 4\rangle pqrs} = \begin{bmatrix} V_{1111} & V_{1122} & V'_{1133} & V_{1123} & V_{1113} & V_{1112} \\ - & V_{2222} & V'_{2233} & V_{2223} & V'_{2213} & V_{2212} \\ - & - & V'_{3333} & V'_{3323} & V'_{3313} & V'_{3312} \\ - & - & - & V'_{2323} & V'_{2313} & V_{1223} \\ - & sym. & - & - & V'_{1313} & V'_{1312} \\ - & - & - & - & - & V'_{1212} \end{bmatrix} \tag{2.35}$$

Note that the parameters denoted with $'$ in Equation 2.35 are determined through linear combinations of the other parameters. For hexagonal materials, the second order texture tensor with five independent terms is also considered (Equation 2.36), given a single second order basis tensor exists ($H_{2,1} \neq 0$ and $H_{2,2} \neq 0$).

$$V_{\langle 2\rangle ij} = \begin{bmatrix} V_{11} & V_{12} & V_{13} \\ - & V_{22} & V_{23} \\ sym. & - & V_{11} - V_{22} \end{bmatrix} \tag{2.36}$$

Again, an arbitrarily anisotropic polycrystal is fully defined by the triclinic macrosymmetry here, with the second and fourth order texture tensors containing five and nine independent terms respectively.

The self-consistent elastic constants (specimen reference frame) [91], assuming isotropic grain shapes, are generated at each iteration of the forward model using the single crystal elastic constants and a tensorial representation of the ODF coefficients [95]. The self-consistent elastic constant calculation considers arbitrary (triclinic) anisotropy on the macroscopic scale with nine independent 4th-order texture components of $V_{\langle 4\rangle pqrs}$. Equation 2.37 details the construction of the self-consistent elastic constants with isotropic grain-shapes ($C^{self,iso}$) in terms of the zeroth-order reference elastic tensor $C_0^{self,iso}$, the

inverse of the isotropic polarization tensor P_0 (calculated with $C_0^{self,iso}$), and the inverse of the orientation average $\langle f, L\rangle$ as calculated from the harmonic decomposition of Equation 2.34. The reference tensor L is defined in place of the traditional single crystal elastic constants C^{SC} in the orientation average, as the self-consistent solution here is defined consistent with the Hashin-Shtrikman-type bounds in [95]. L inherits the cubic symmetry of C^{SC}, as it is calculated as the linear combination of the single crystal elastic constants C^{SC}, the zeroth-order reference stiffness $C_0^{self,iso}$, and the polarization tensor P_0. As a result of the assumption of isotropic grain shape statistics in [95], the self-consistent solution is fully defined by the same texture coefficients used to generate the Hashin-Shtrikman upper/lower bounds and the Voigt/Reuss bounds. The polarization tensor assumes isotropic grain statistics, allowing the polarization to be analytically determined with the calculated reference stiffness $C_0^{self,iso}$.

$$\begin{aligned} C^{self,iso} &= C_0^{self,iso} - [P_0(C_0^{self,iso})]^{-1} + [\langle f, L\rangle]^{-1} \\ L &= [C^{SC} - C_0^{self,iso} + [P_0(C_0^{self,iso})]^{-1}]^{-1} \end{aligned} \tag{2.37}$$

The forward model to determine the effective elasticity ($C^{self,iso}$) of a given arbitrarily textured AM specimen is schematically shown in Figure 2.5, with a cubic microsymmetry material used as an example.

Under the assumption of spherical grain shapes (semi-axes parameters $a_1 = a_2 = a_3 = 1$), the polarization tensor for ellipsoidal inclusions is determined analytically [95]. However, the non-isotropic calculation of P_0 requires the reference stiffness ($C_0^{self,iso}$/ C_0) to be defined, meaning an assumption of the stiffness of the medium would still be necessary to determine the polycrystalline stiffness and the resonant frequencies. Because the reference stiffness is calculated from the independently determined single crystal constants, there is a relationship between these parameters that is not well studied in the

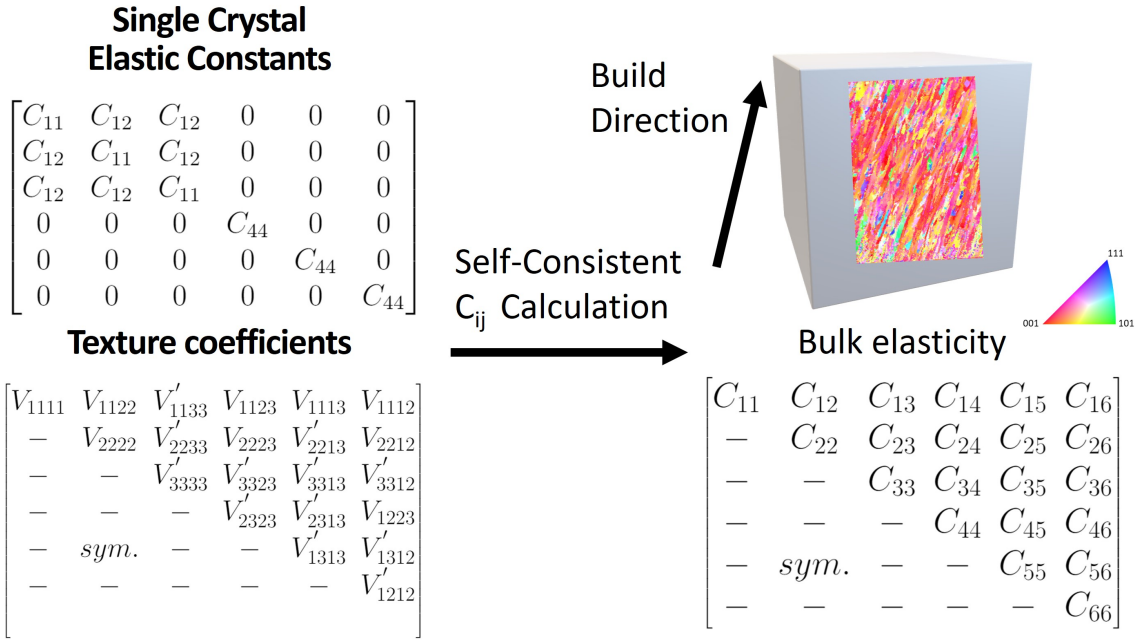

Figure 2.5: Forward model calculation of effective macroscopic elastic properties from texture coefficients and single crystal elastic constants of a parallelepiped specimen.

context of inversely solving this model [97]. Consequently, the analytical determination of isotropic P_0 is used, as given in Equation 2.38. P_1 and P_2 are same isotropic projectors as in Equation 2.37, c_1 and c_2 are constants, and λ_1 and λ_2 are the eigenvalues of the isotropic stiffness tensor C_0.

$$\begin{aligned} P_0 &= c_1 * P_1 + c_2 * P_2 \\ c_1 &= \frac{1}{\lambda_1 + 2\lambda_2}, c_2 = \frac{2}{5\lambda_2} * \frac{\lambda_1 + 3\lambda_2}{\lambda_1 + 2\lambda_2} \end{aligned} \tag{2.38}$$

The zeroth-order elastic tensor ($C_0^{self,iso}$) is determined analytically by generating the self-consistent elastic solution (Equation 2.37) where the reference stiffness of the medium C_0 is identical to its self consistent solution, i.e. an untextured aggregate of spherical (isotropic) grains with single crystal elasticity C^{SC}. Isotropic projectors (P_1 and P_2) are again utilized to generate the isotropic reference stiffness of the medium ($C_0^{self,iso}$) by

supplying the single-crystal elastic tensor C^{SC} as detailed in Equation 2.39 [95, 98]. The zero-order bounds therefore do not contain grain shape or orientation information, and are used in Equation 2.37.

$$\begin{aligned} C_0^{self,iso} &= C_0 - [P_0(C_0)]^{-1} + \langle f^{iso}, L \rangle^{-1} \\ L &= [C^{SC} - C_0 + [P_0(C_0)]^{-1}]^{-1} \\ C_0 &= C_0^{self,iso} \end{aligned} \tag{2.39}$$

Combined forward model

The combined forward model therefore consists of the calculation of resonant frequencies from the bulk elastic constants (Section 2.2.1) with a self-consistent calculation of those bulk elastic constants from the texture and single crystal elastic constants (Section 2.2.1). This construction is demonstrated in Figure 2.6.

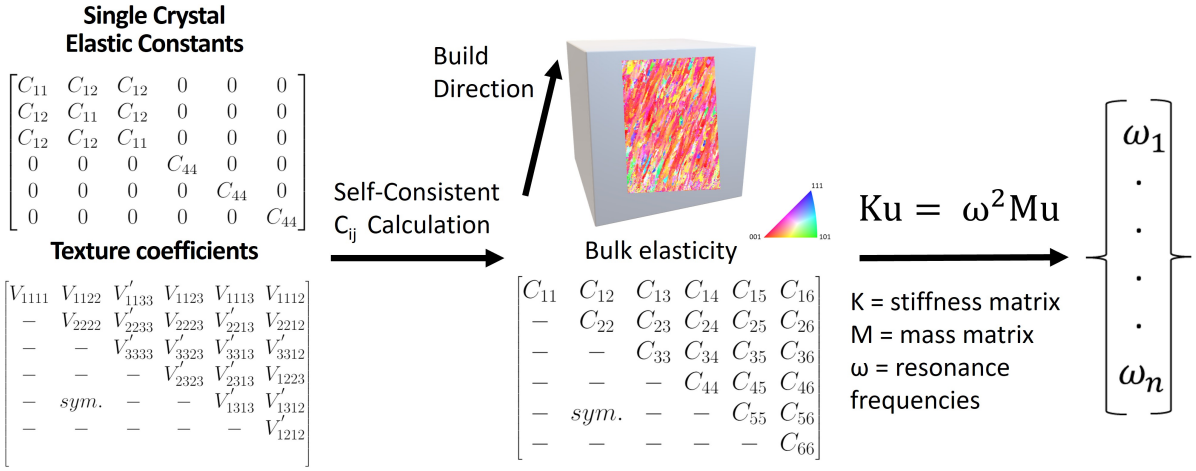

Figure 2.6: Combined forward model calculation of resonant frequencies from the single crystal elastic constants and microstructural texture. A self-consistent elastic constant calculation is used to determine the bulk elastic constants, which are then used to calculate the theoretical resonant frequencies. EBSD is not to scale, but demonstrates that any symmetry microstructure is permissible so long as it is homogeneous through the bulk.

Following the combined construction of the forward model, it is important to note that

the bulk elastic constants are calculated on the way to calculate the resonant frequencies. Therefore, the symmetry of the bulk elastic constants is completely divorced from the solution, as the arbitrary form of the texture coefficients will control the values and symmetry of the bulk elastic constants. As a result, the simulation can be thought of as a calculation of the resonant frequencies directly from the texture and single crystal elastic constants as in Figure 2.7.

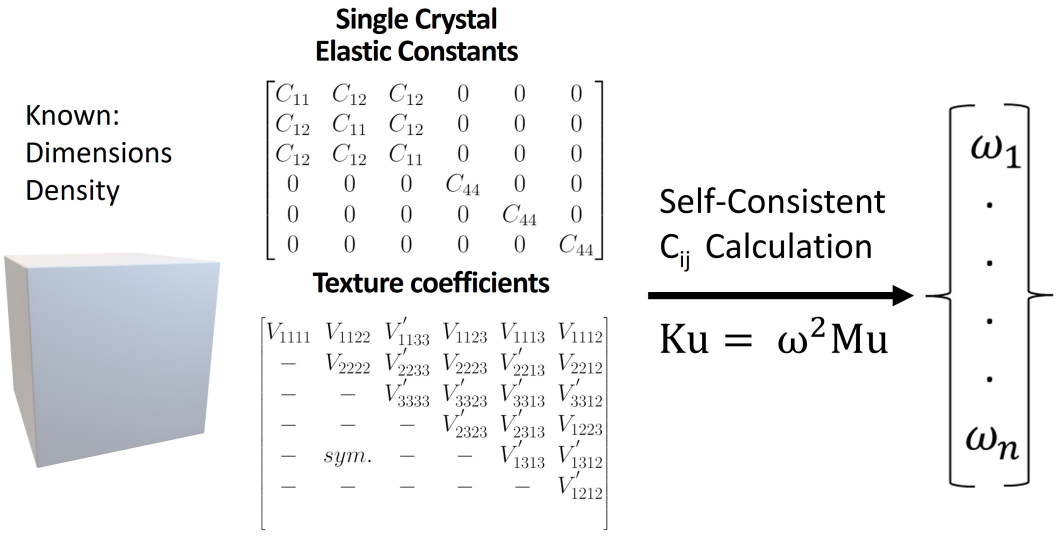

Figure 2.7: Combined forward model calculation of resonant frequencies from the single crystal elastic constants and microstructural texture does not require any information about the symmetry of the bulk microstructure.

2.2.2 Bayesian inference with sequential Monte Carlo

Bayesian inference is a powerful technique for solving the RUS inverse problem [68]. Bayesian techniques are more robust to local minima solutions than deterministic optimizations [57, 58], and yield estimates of forward model parameter uncertainty as well as measurement uncertainty. Bayes' Theorem provides a mechanism to update prior knowledge of the RUS model parameters with new resonant frequency observations. The updated knowledge is the solution of the inverse problem and is represented by the pos-

terior probability density function,

$$\pi(\Theta|\omega_n) = \frac{\pi(\omega_n|\Theta)\pi(\Theta)}{\int_\Omega \pi(\omega_n|\Theta)\pi(\Theta)d\Theta} \tag{2.40}$$

where Θ is the vector of the independent parameters.

The numerator of the right hand side of Equation 2.40 comprises the likelihood function $\pi(\omega_n|\Theta)$ (which represents the likelihood of observing the measured resonant frequencies given Θ) and the prior $\pi(\Theta)$ (which represents prior knowledge of the model parameters). The prior distribution can be defined by physical bounds (e.g., strictly positive) or more subjectively through domain knowledge and previously conducted experiments. The denominator is the marginal likelihood and involves integration over the entire parameter support, $\Omega = \{\Theta \in \mathbb{R}^n\}$. The marginal likelihood is a normalizing constant and is typically intractable, precluding the solution to the inverse problem through analytical means. However, by assuming that the measurement errors are independently and identically distributed as zero-mean Gaussian distributions with variance σ^2, a closed form expression is obtained for the likelihood,

$$\pi(\omega_n|\Theta) = \frac{1}{(2\pi\sigma^2)^{-n/2}} \exp\left(-\frac{\text{SSE}}{2\sigma^2}\right) \tag{2.41}$$

where SSE is the sum of squared error between the n measured resonant frequencies and those predicted by the forward model. Given Equation 2.41, the posterior probability density function for a given Θ is known up to some proportionality, $\pi(\Theta|\omega_n) \propto \pi(\omega_n|\Theta)\pi(\Theta)$. Thus, sampling methods can be used to approximate the solution to Equation 2.40.

A number of techniques have been developed to sample from the posterior distribution based on point-wise evaluations of the likelihood and prior densities [99]. Arguably the most ubiquitous of these is Markov Chain Monte Carlo (MCMC). While a large number

of specific algorithms exist, MCMC generally involves the construction of a Markov chain via a random walk through the parameter space with well-defined acceptance/rejection probabilities based on the proportional posterior density function. In this way, MCMC is inherently serial. As each proposed sample requires a model evaluation to compute SSE, MCMC can be computationally expensive, particularly as the number of samples required to meet a desired accuracy are often on the order of thousands or even millions. Efficiency is thus key, which has given rise to smarter methods for exploring the parameter space such as Hamiltonian Monte Carlo (HMC). HMC was used previously for RUS [68] but, given the modifications to the forward model proposed herein, HMC was too computationally intensive to be practical.

To alleviate the computational burden associated with approximating a solution to Equation 2.40, sequential Monte Carlo (SMC) [100] was adopted. SMC is capable of generating samples from a static target distribution and enables construction of unbiased estimators of the target distribution statistics. As a result, it is a drop-in replacement for HMC/MCMC. Expressions for the asymptotic variances of SMC samplers are provided in [100, 101]. While still a sampling-based approach, SMC achieves speedup by parallelizing model evaluations and is generally more robust than single-chain MCMC methods when estimating multimodal posterior distributions. SMC works by generating a series of target distributions based on tempering of the likelihood function in Equation 2.40. The series starts with the known prior distribution, which is presumably easy to sample from directly, and gradually transitions to the full posterior distribution. The target distributions are estimated by evolving a population of particles, or weighted parameter vectors, through a sequential importance sampling algorithm. The particles are mutated at each step to avoid degeneracy by passing each through an arbitrary MCMC kernel. A comparison of the SMC and MCMC sampling processes is illustrated in Figure 2.8.

The key advantage of SMC is its significant speedup, achieved by passing each particle through the MCMC kernel independently and in a highly parallel fashion. In contrast, MCMC requires an initial burn-in period followed by strictly serial sampling from the posterior until the desired number of samples has been reached.

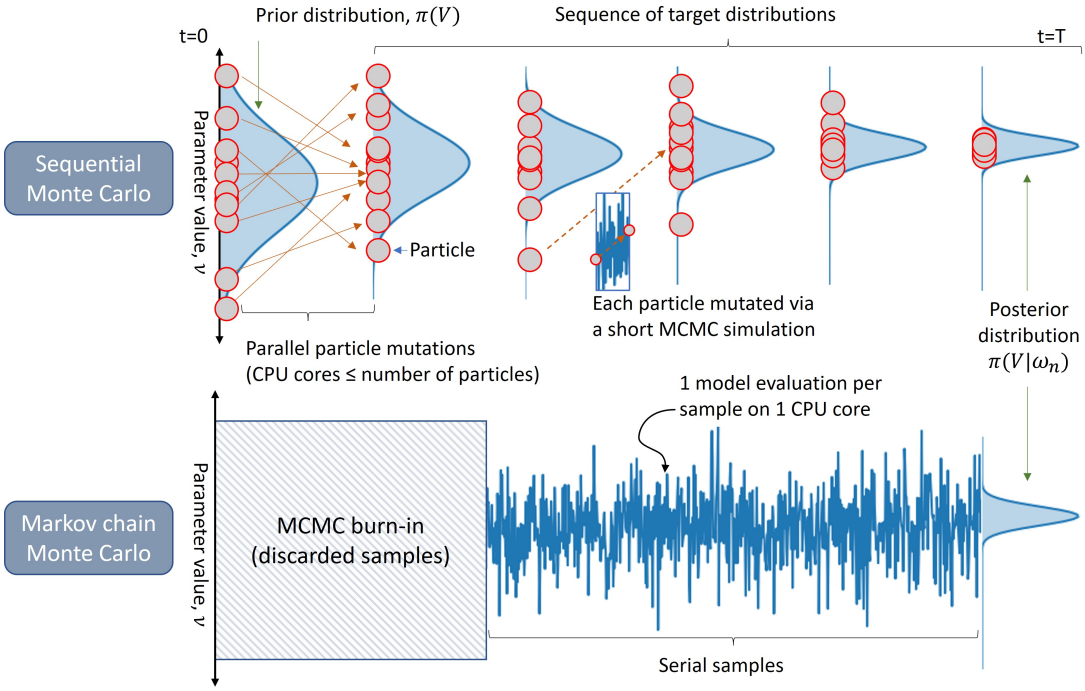

Figure 2.8: Illustration of SMC and MCMC sampling methods. Posterior distribution is obtained at the final timestep, t=T. Traditional MCMC sampling (lower figure) consists of a burn-in period of discarded samples and is followed by samples generated from the posterior in a serial fashion until a desired number has been reached. For SMC (upper figure), a MCMC mutation chain migrates each particle to its new value at the next timestep.

To achieve robust Bayesian parameter estimates and uncertainties in a highly parallel fashion, an open-source Python implementation of Sequential Monte Carlo, `SMCPy`[1], was used to estimate the posterior distribution of single crystal constants. `SMCPy` is based on the algorithm presented in [100]. The parallel particle evaluations in `SMCPy` are vectorized using `numpy` to achieve single-core speedup, but `SMCPy` is also Message Passing Interface (MPI)-enabled to allow parallel computation on distributed memory systems as in this

[1]SMCPy Python package available open-source at https://github.com/nasa/SMCPy.

work.

Hyperparameter tuning

Selecting polynomial order

Following Equation 2.28 in Section 2.2.1, the polynomial order P must be user-defined for the forward model to determine resonant frequencies. As noted in [57], the choice of P determines the J number of basis functions exponentially, resulting in substantial increases in the computation time of the resonant frequency eigenvalues for each increase in P. Given the eigenvalue calculation generally consists of $\sim$90% or more of each calculation of the resonant frequencies, judicious choice of P is critical for solving the inverse problem with computationally expensive Bayesian approaches. Typical values of P are 8,10,12,14 depending on the necessary precision of each calculated resonant mode. Research in [77, 102] demonstrates that values of $P = 10$ and $P = 12$ correspond to computation times of 20.3 h and 60.9 h respectively for 40 modes each, with the precision of the highest modes substantially lower than the lowest frequency modes. Importantly, the precision of each calculated resonant mode is independent of the constituent material symmetry and therefore can be calculated based on resonant mode number alone.

Though the computational code and development of this methodology is reviewed in Chapter 3, the selection of polynomial order in this work is given here in the context of inverse solving with SMCPy. Within each inverse model, a set number of experimentally measured resonant frequencies must be supplied. This number of frequencies is generally selected based on the number of independent parameters to be determined, though reliable experimental measurement of high frequency modes may limit the number that may be measured as discussed in Section 2.3.

Therefore, the desired precision of the calculated resonant modes can be set at the beginning of the inverse calculation, depending on the number of n resonant modes.

A polynomial order of $P = 20$ is used to calculate a 'convergent' set of the n resonant frequencies with the initial set of guessed elastic constants from the Bayesian prior and the specimen dimensions. This calculation is then carried out for the n resonant frequencies at increasing polynomial orders starting with $P = 6$, and increasing by 2 at each iteration. Each set of N frequencies is compared to the frequencies calculated with $P = 20$ ($\omega_{n,20}$), with the maximum allowable difference set as 0.1%. Once none of the resonant frequencies at a given P, $\omega_{n,P}$, differs from $\omega_{n,20}$ by $\geq 0.1\%$ in Equation 2.42, that value of P is selected for the inversion.

$$\frac{|\omega_{n,P} - \omega_{n,20}|}{\omega_{n,20}} \leq 0.1 \tag{2.42}$$

Looking at a few different polynomial orders using a cobalt-nickel-base superalloy specimen in Chapter 3, a polynomial order of 12 exhibited a calculated maximum deviation of 0.05 % (kHz) up to mode 45, compared to a polynomial order of 20. The polynomial order of 14 exhibited a calculated maximum deviation of 0.03 % (kHz) for any single resonant frequency up to mode 70, compared to a polynomial order of 20. These results indicate that for these relative numbers of modes, a choice of either 12 or 14 polynomial order should produce more than sufficient precision.

Symmetry considerations in inverse solving

As noted in [67], when the arbitrary (21 component) elastic tensor is considered, the resonant frequencies are invariant under the reflection of the elastic tensor about each of the specimen axes (180° rotation around each axis).

Correspondingly, for any set of resonant frequencies, there are 4 representations of the elastic tensor that produce the given set of resonant frequencies. This can result in sampling errors when utilizing inversion techniques. Despite the potential for inversion

error, directly reducing the solution space would result in a loss of generality for higher symmetry samples, and thus all permutations of the elastic tensor exist within the inverse solver. Instead, post-processing code is available in Appendix A to automatically apply the 180° rotations, negating the effect of multimodal distributions on the final estimates. The rotations are applied directly to the texture coefficient tensor, then propagated to a final set of elastic constants and resonant frequencies.

2.3 Experimental resonant ultrasound spectroscopy

The resonant ultrasound setup used to measure resonant frequencies in this work consisted of three piezoelectric transducers, transceivers, and a computer control unit. The piezoelectric transducers, transceiver, and computer control used for the measurement of resonant frequencies were provided by Vibrant Corporation[2], though equipment can be fabricated or purchased at relatively low cost [61]. The omni-directional piezoelectric transducers were mounted to a vibration damping platform with optical table hardware as shown in Figure 2.9, enabling precise positioning of the contact points between the specimen and transducers.

The piezoelectric transducers are each identical in Figure 2.9, being used for both the excitation of elastic waves ('Drive' transducer) and measurement of the amplitude response ('Rec 1/2'). Both round-tip piezoelectric transducers and flat tip transducers were used, depending on the specimen shape and contact area of interest. Regardless of the tip shape, the tip was constructed of silicon carbide, with the piezoelectric element housed beneath it in a casing of brass and steel. Coaxial cables connect each piezoelectric transducer to the computer control unit, upon which an instance of Vibrant Corp.'s Galaxy© software is used to instantiate and control the sinusoidal frequency sweeps, record data, and identify resonant frequency peaks.

[2]Vibrant Corporation, 8916 Adams St NE, Albuquerque, NM 87113

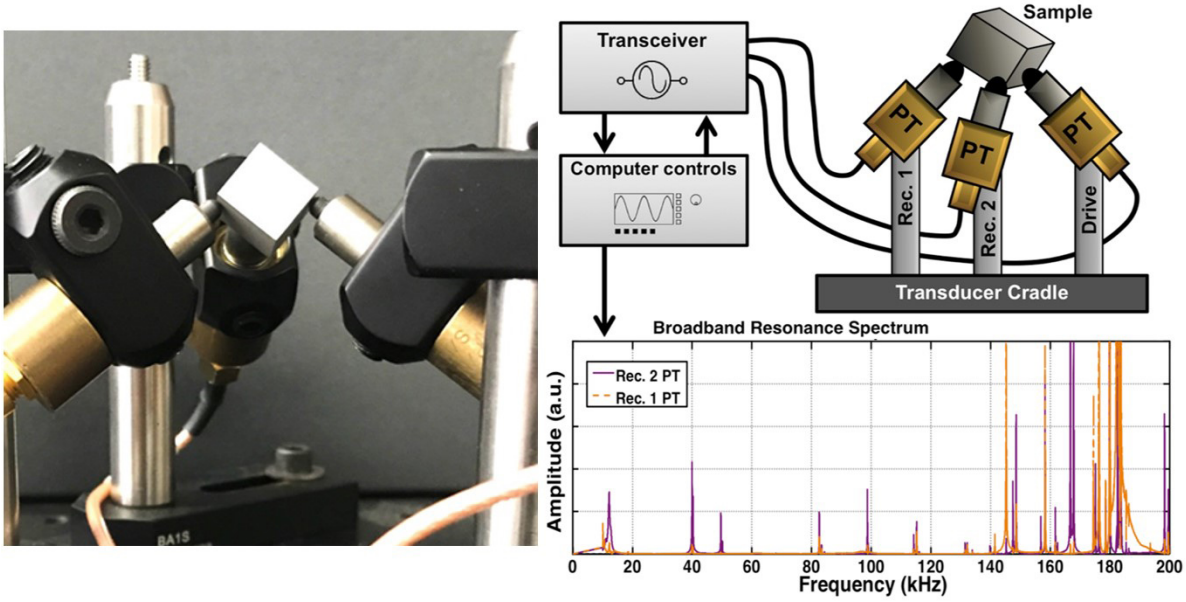

Figure 2.9: Resonant ultrasound spectroscopy experimental setup with parallelepiped specimen (left). The specimen rests on the piezoelectric transducers by its own weight. Figure reproduced from [68] with permission of the authors.

Depending on specimen size and quality, step sizes 1-5 Hz and dwell times of 1-5 μs were chosen to conduct the resonant frequency sweeps. The goal of the sinusoidal sweep is to capture the first 50-75 natural resonant modes of the specimen. The first mode is often identified prior to the full sweep, either through forward modeling of the frequencies, often with finite element modeling (FEM), or an initially coarse search of the first 100/200 kHz. Due to the fundamentals of resonance, the displacement response during the excitation of a resonant mode is hundreds or thousands times greater than the excitation displacement, resulting in the trivial detection of most modes [103].

The reliable measurement of the resonant modes, without missing any modes, is critical to the accuracy of any property determined from them [104]. While the RUS setup here has proven robust to measure the frequencies of a variety of specimen sizes, weights, and shapes, high damping materials provide significant challenges in the measurement of the resonant frequencies as they reduce the amplitude response of the frequencies. This can be expressed in terms of a Q-factor ($Q = f_r/\Delta f$), where Δf is width of the resonance

peak at half the amplitude height. When the displacement and resultant amplitude response of the frequencies are reduced beneath the level of the background signal noise, frequencies are often missed. Low amplitude mode detection requires contactless, and therefore substantially more expensive, excitation techniques such as laser-RUS (LRUS) [64] and alternative data analysis techniques [105].

Reliable resonant mode measurements

The use of two receiving transducers significantly reduces the chance of a mode being 'missed' during any one scan, for example due to the transducer contacting the specimen at a zero-displacement point for that particular resonant mode. The transducers are generally placed near corners of a specimen to increase the likelihood of large displacements and consistent measurements. The transducers are not placed directly against the corner edges of a specimen, as some force is required to hold the transducer against the sharp point of the specimen, leading to inconsistency and shifts in the resonant modes, damage to the transducers, and a higher signal to noise ratio [106].

Therefore, all of the tests are completed with the specimen freely resting on the piezoelectric transducers to ensure that no externally induced contact forces violate the free-resonance conditions. Additionally, the resonant frequencies are gathered for each specimen 3-5 times, altering the position of the specimen, transducers, and cradle between each frequency scan. The frequencies are then aligned and averaged across all scans, generally resulting in $\pm 0.02\%$ precision of each frequency [68].

Chapter 3
Determination of Texture from AM Components with RUS

Bayesian inference with sequential Monte Carlo is used to quantify the orientation distribution function coefficients and to calculate the fully anisotropic elastic constants of additively manufactured specimens from only the experimentally-measured resonant frequencies. The parallelizable and open-source SMCPy Python package enabled Bayesian inference within this new modeling framework, resulting in an order of magnitude reduction of the computation time for an 8-core machine. Residual stress-induced shifts on the resonant frequencies were explicitly accounted for during the Bayesian inference, enabling the estimation of their effect on the resonant frequencies without a stress-relief heat treatment.

Additively manufactured cobalt-nickel-base superalloy (SB-CoNi-10C)[1] specimens were sectioned at multiple inclinations relative to the build direction and scanned with resonant ultrasound spectroscopy to demonstrate characterization of any arbitrarily textured cubic microstructure through the resonant frequencies. The orientation distribution function coefficients of the textured polycrystalline microstructure were estimated in tensorial form to calculate both the 2nd order Hashin-Shtrikman bounds and the self-consistent estimate of the elastic constants, enabling accurate determination of all 21 possible independent elastic constants through the convergence constraints of the texture. Pole figures generated directly from the calculated texture coefficients showed good agreement with experimentally measured textures.

[1] Commercially available at Carpenter Technologies as Gamma Print 700™

3.1 Introduction

Unlike single crystal components, AM components with textured polycrystalline microstructures may or may not display symmetry with respect to the specimen reference frame [20]. Even considering an AM component with fixed geometry, heat source scan strategy alone is capable of causing drastic changes in the texture [19, 107, 108], and consequently the elastic anisotropy. A framework to quantify the elastic properties of textured materials must account for any symmetry between isotropic (2 independent elastic constants) and triclinic (21 independent elastic constants). This complicates analysis by RUS, as an explicit number of independent elastic constants must be specified for existing RUS inversion codes [55, 58, 59, 63, 74]. Even the robust Hamiltonian Monte Carlo (HMC) based RUS inversion method, Cmd-Stan RUS [68], requires a base (traditionally single-crystal) symmetry to exist at some rotation within the specimen. For certain axial texture symmetries, an orthorhombic (9 independent components) specimen symmetry elastic tensor can be utilized with rotations to generate a convergent solution, but this is not robust across a range of texture strengths and orientations. Therefore, the capability to account for all 21 possible elastic constants as independent parameters is necessary for characterization of arbitrary textures. However, this introduces both the risk of overfitting a higher symmetry microstructure and the requirement of informative priors for each parameter.

To further characterize arbitrarily textured polycrystalline AM components using RUS, it is necessary to determine and account for the unknown anisotropy in the elastic tensor.

3.2 Background

To account for unknown (arbitrary) anisotropy, explicit use of the triclinic (21 independent components) bulk elastic tensor is needed to calculate the resonant frequencies of the textured specimens. Most inversion frameworks use block-diagonalization to reduce computational costs [58, 109], but this approach is not possible for symmetries lower than orthorhombic. Of the approaches that are capable of parameterizing all 21 components during RUS inversions [67, 68, 110], several rely on pulse echo measurements to supplement RUS measurements and achieve satisfactory numerical results [67, 74, 110]. Pulse echo measurements require both large specimens (to approximate plane wave behavior) and individual measurements along specific planes in the specimen (scaling with the number of independent elastic constants) [60]. However, these measurements do not reduce the error in determining the off-axis (C_{14}, C_{15}...) elastic constants to the level of the shear or longitudinally dependent constants. Off-axis elastic constants are critical for determining textures that are not clearly aligned with the sample reference frame. Additionally, pulse echo methods have calculated significantly different elastic constant magnitudes compared to RUS in damped media due to the frequency dependence of attenuation [104]. These limitations preclude the use of pulse-echo in the current investigation.

Complicating the need for triclinic bulk elastic symmetry, it is both computationally inefficient and numerically difficult to achieve meaningful accuracy when sampling 21 independent elastic constants. Despite the aggregate (polycrystalline) elastic constants being induced by texture, the texture and induced anisotropy are often inferred from ratios of the aggregate elastic constants without direct consideration of the single crystal elastic anisotropy [74]. Determining the texture requires the apriori knowledge of the full elastic tensor of the aggregate, even in the robust texture convolution framework

established by Lan et al. [93]; the limiting step for texture determination through RUS is therefore the quantitative and accurate representation of the aggregate elastic constants as dependent on the texture, with the single crystal elastic anisotropy controlling both the sensitivity of the aggregate elastic constants and the aggregate elastic symmetry inside the simulation. Attempts to relate the orientation distribution function (ODF) coefficients of textured materials to the calculated elastic constants [69, 70] within the formalism of [71, 85, 86] show the potential to directly estimate the texture coefficients during an inversion. Unfortunately, the use of orthorhombic elastic specimen symmetry and the simplicity of the averaging scheme (e.g. Voigt, Reuss, Hill) reduce the applicability of these frameworks to arbitrary AM textures [69, 111]. As mentioned by Seiner et al. [110] and Ledbetter [72], only the Hershey-Kroner-Eshelby self-consistent solution [91] is capable of reproducing the elastic constants with satisfactory accuracy compared to ultrasound measures of elasticity.

Recent advances in the representation of texture and the calculation of elastic properties have enabled more precise homogenization and materials design [93, 112, 113]. Of most relevance, a tensorial representation of the ODF has enabled rapid and precise calculation of the second-order Hashin-Shtrikman bounds and linearized self-consistent solution [95, 114]. This tensorial ODF representation shows potential to characterize textured polycrystals, specifically within the context of inverse problems. The tensorial texture coefficients (4th rank tensor V^4_{pqrs}) are used to calculate the second-order Hashin-Shtrikman bounds ($C^{HS-upper}_{ijkl}$ and $C^{HS-lower}_{ijkl}$) and the linearized self-consistent solution ($C^{Self-Consistent}_{ijkl}$) of the elastic constants for a given polycrystalline microstructure, assuming the single crystal elastic constants are of cubic symmetry and known magnitude [95].

A new approach is presented for characterization of arbitrarily textured AM compo-

nents by utilizing all 9 independent coefficients of the ODF as inputs into RUS inversion, determining the texture coefficients and fully anisotropic elastic tensor through the resonant frequencies. This parameterization of the texture is incorporated as the linearization of the self-consistent solution, as specified in [95]. In addition to texture, residual stresses significantly influence the resonant frequencies of additively manufactured components. For example, a 1.7-2.1% increase of all resonant frequencies was observed after a stress-relief heat treatment (no recrystallization) of AM nickel-base alloys (Chapter 6), suggesting that the effect is driven by inelastic factors. This result is supported by an observed change in the RUS-measured elastic modulus when different scanning strategies were used to induce distinct residual stress states in AM SS316L samples [115]. Therefore, any shift in the resonant frequencies resulting from residual stresses must be explicitly and separately accounted for in order to accurately invert for either the elastic constants or the texture.

High-performance alloys are currently being investigated for processing by additive manufacturing due to their excellent high temperature mechanical properties [116], and are consequently used as a model material in this study. However, many of these high-performance alloys, such as nickel-base superalloys, contain a large volume fraction of the strengthening γ' phase, making them susceptible to cracking during printing or post-print heat treatment and severely degrading mechanical performance [117, 118, 119]. The alloy utilized in this study is a novel cobalt-nickel-based superalloy, SB-CoNi-10, that was originally designed for use in single-crystal castings [120]. SB-CoNi-10 was recently demonstrated to possess solidification properties amenable to the production of crack-free specimens using LPBF, in spite of the presence of a high volume fraction of γ' after heat treatment [121]. Additionally, this novel alloy forms an alumina scale under high temperature exposure to air, has a mass density similar to 2nd-generation Ni-base

single crystal superalloys [120], and demonstrates low sensitivity to process parameter variation by both LPBF [121] and electron beam melting (EBM) [122]. The SB-CoNi-10 powder used in this study was produced with a higher carbon content than previously used, and is denoted SB-CoNi-10C for distinction.

The purpose of this chapter is: 1. Texture and polycrystalline elastic properties are concurrently determined from the resonant frequencies in a single, unified model without assumptions of macroscropic polycrystalline symmetry. 2. A novel, additively manufactured cobalt-nickel-base superalloy, SB-CoNi-10C is characterized in both the as-built and stress-relieved state. 3. A freely determined residual stress term has been added to the forward model calculation, enabling residual stress induced frequency shifts during stress-relief heat treatment to be accounted for when supplying as-built frequencies to the calculation. 4. Parallelized sequential Monte Carlo is utilized for Bayesian inference of the simulation, reducing the prohibitive computational cost by an order of magnitude. Probability distributions are calculated for all parameters.

3.3 Materials and methods

SB-CoNi-10C specimens were printed on an Aconity3D AconityMINI system at the University of California Santa Barbara (UCSB). The powder had a size distribution of 15-53 µm and was provided by Carpenter Technology[2]. The composition of the powder is given in Table 3.1.

Rectangular AM specimens were printed with nominal dimensions of 10 x 10 x 13 mm for the x, y, and z (build direction) axes, respectively. The as-printed specimens and scan strategy are depicted in Figure 3.1. The scan strategy was bi-directional with a 90° rotation between successive build layers. The AM specimens were printed without contours. The build plate was preheated to 200° C, the beam diameter was 80 μm, and

[2]Carpenter Technology, 1735 Market Street, 15th Floor, Philadelphia, PA 19103 USA

Chemical analysis (wt.%)										
	Co	Ni	Al	W	Ta	Cr	C	B	Y	Hf
Nominal	Bal.	35.75	5.98	3.09	10.63	5.24	0.070	0.015	0.003	0.054
Measured	Bal.	35.93	5.98	3.06	10.40	5.24	0.069	0.013	0.006	0.057

Table 3.1: Chemical analysis of SB-CoNi-10C powder prior to build. Major constituents were measured by X-ray. B was measured by mass spectrometry and Y was measured by wet-chem analysis. All measurements were carried out at Carpenter Technologies. Quantities in wt.% [121].

the layer thickness was set to 30 μm. The as-built specimens were removed from the build plate using wire electrical discharge machining (EDM). Witness lines (horizontal marks on the sides of the as-built specimens) were observed; these indicated areas of small interruptions in the grain structure relative to the build direction due to small temperature fluctuations in the optics of the AM machine.

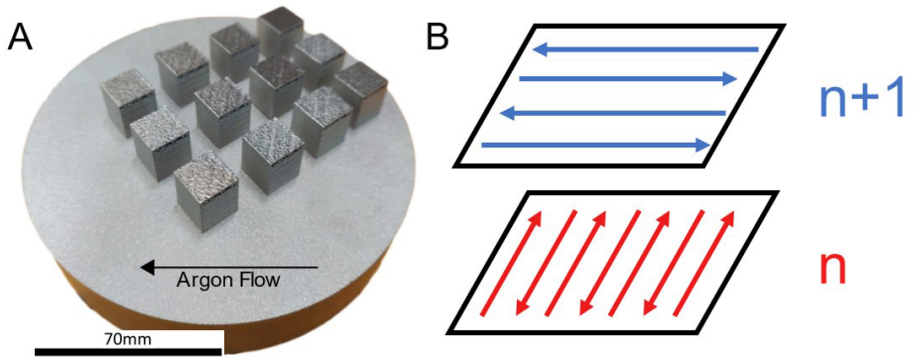

Figure 3.1: A) As-printed AM specimens with arrow indicating the direction of argon flow across the build plate during printing. B) Schematic of two consecutive layers (layer n and layer n+1) illustrating the laser scan path; a bi-directional scan pattern with 90° rotation after each layer.

Laser power and scan speed were varied for each specimen such that each specimen was printed with a distinct energy density. Two of the fully dense specimens, as determined by light microscopy, were selected for further study by RUS. These specimens were printed with similar process parameters, as shown in Table 3.2. All specimens were built with the longest dimension (13 mm) aligned with the build direction.

Electron Backscatter Diffraction (EBSD) was performed on the XZ face of each speci-

Process Parameters			
Specimen ID	Power (W)	Scan Speed (m/s)	Hatch Spacing (μm)
R2	152	1.122	80
R4	130	0.833	80

Table 3.2: Process parameters for the printed AM blocks selected for further study.

men to characterize grain structure and microstructural variability with respect to process parameters. These scans are shown in Figure 3.2. Despite the difference in process parameters, the microstructural texture was not differentiable between the pole figures of specimens R2 and R4. An FEI Versa 3D Dualbeam microscope with an EDAX OIM-Hikary XM4 detector was used for all EBSD scans. All scans were performed using an accelerating voltage of 30 kV and a beam current of 12 nA. Note that the pole figures in Figure 3.2 were generated using the MATLAB MTEX package [123], using the 'deLaValleePoussin' kernel with a halfwidth of 2.4°. The other pole figures generated from EBSD in this manuscript were generated with a Dirichlet kernel (halfwidth 4.3°) and limited to 4th order for direct comparison to the simulations.

Specimens selected for RUS were sectioned by EDM at nominal 0° and 20° inclinations from the build direction for specimens R4 and R2, respectively. EDM was additionally used to remove 1 mm of depth from each surface, removing surface-induced alterations in the microstructure. The EDM scale was removed by polishing with 600-grit sandpaper. The final rectangular parallelepiped geometries were 8.672 ± 0.007 mm x 8.215 ± 0.005 mm x 6.914 ± 0.005 mm (R2), and 10.355 ± 0.010 mm x 8.883 ± 0.0088 mm x 8.370 ± 0.014 mm (R4). The dimensional measurement uncertainty incorporates the non-planarity of the specimen faces. Specimen masses were 4.2443 ± 0.0001 g (R2) and 6.6168 ± 0.0001 g (R4), resulting in densities of 8591.4 kg/m^3 (R2) and 8593.9 kg/m^3 (R4) assuming no porosity. These densities broadly agree with the Archimedes measurement of density (8650 kg/m^3) from an arc-melted specimen of SB-CoNi-10 [120]. EBSD was also performed on specimen R2 after sectioning to determine the true inclination of the

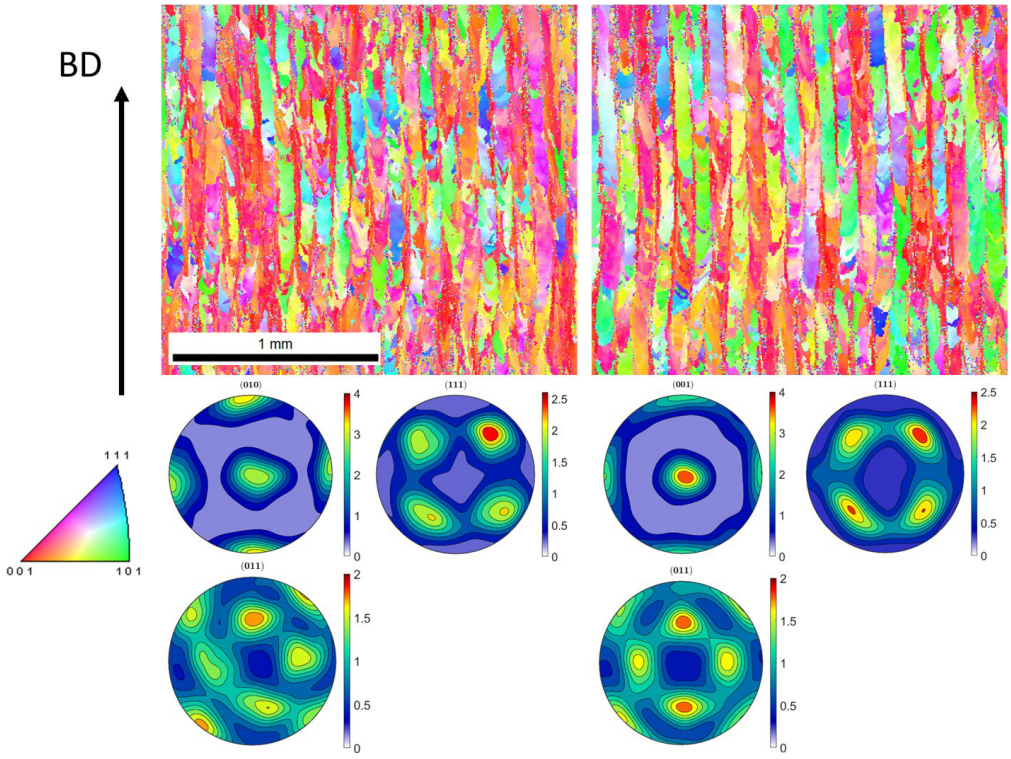

Figure 3.2: EBSD scans and corresponding pole figures for specimen R2 (left) and R4 (right). Inverse pole figure (IPF) coloring of scans corresponds to the build direction (north relative to image). Pole figures are auto-generated using MATLAB MTEX package with units in multiples of random distribution (MRD).

build direction relative to the sectioned specimen faces, as shown in Figure 3.3 (not to scale). The inclination was determined to be 22.3° to the build direction. Parallelepiped specimen preparation for RUS was completed in the as-built state.

To further study the effect of residual stresses (and the subsequent relief of residual stresses) on the resonant frequencies, a stress-relieving heat treatment of 1100°C for 2h was utilized. This heat treatment was performed in an open air furnace, and each specimen was air cooled prior to gathering RUS measurements. The stress-relief heat treatment was performed at ∼100°C below the γ'-solvus temperature. The stress-relief heat treatment did not result in any detectable recrystallization (by EBSD) of the as-printed grain structure.

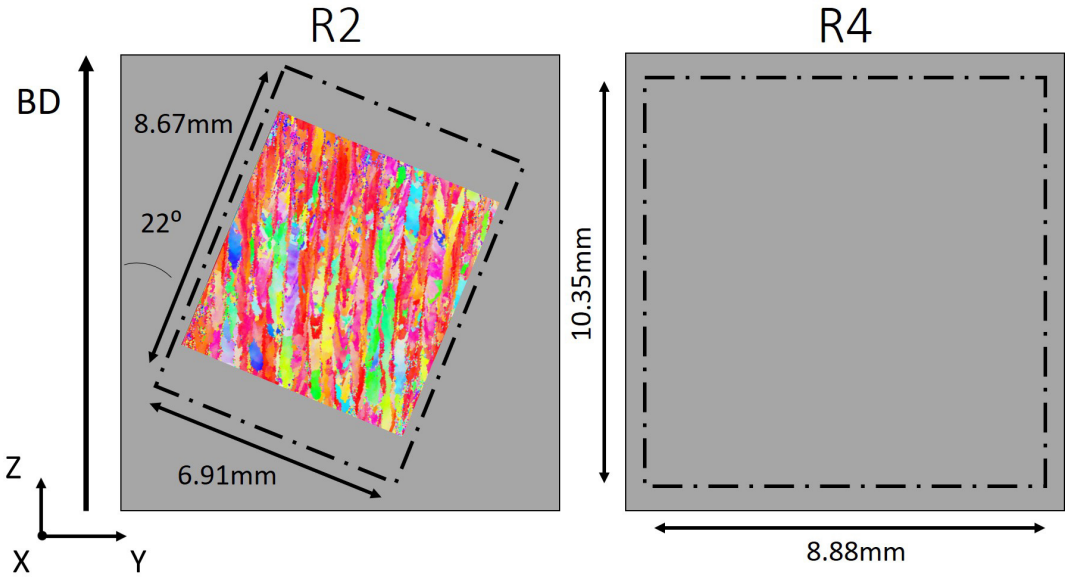

Figure 3.3: Sectioning strategy and Y/Z dimensions for the R4 and R2 specimens. Note that the removal of the outer layer of material negated any effect of heterogeneous grain structures at the surface. R2 was sectioned at a nominal 20° relative to the build direction. EBSD was completed after sectioning to validate the sectioning angle, and the measured inclination of the grain structure was 22.3° relative to the build direction. EBSD scans were taken both prior to sectioning (Figure 3.2) and after sectioning for specimen R2. Note that the EBSD taken after sectioning (shown here) is not to scale.

3.3.1 Resonant ultrasound spectroscopy: measurements

Figure 3.4 demonstrates the experimental RUS setup. The specimen rested on piezoelectric transducers under its own weight, negating the role of externally induced contact forces. The piezoelectric transducers detect an increased amplitude (i.e. resonance) response at a given driving frequency when mechanical resonance is achieved. The piezoelectric transducers both drive and detect the frequencies. A broadband kHz spectrum was swept to capture the first 75-100 modes, with sampling step sizes of 3 Hz and dwell times of 1 ms. The piezoelectric transducers and specimen holder were provided by Vibrant Corporation[3].

[3]Vibrant Corporation, 8916 Adams St NE, Albuquerque, NM 87113

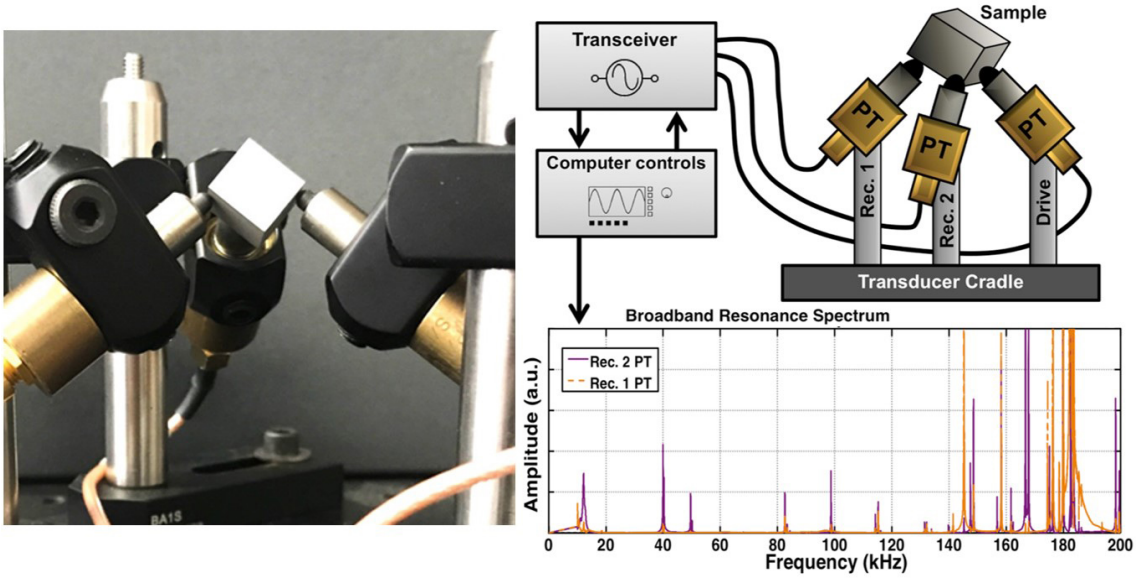

Figure 3.4: Resonant ultrasound spectroscopy experimental setup with AM parallelepiped specimen (left). The specimen rested on the piezoelectric transducers by its own weight, eliminating any contact forces. Piezoelectric transducers both excited and detected the resonant frequencies. Beginning with the lowest resonant frequency, >75 resonant frequencies were measured (right). Each specimen was scanned three to five times.

Each specimen was scanned by RUS three to five times, with each frequency averaged across all scans. The specimen position was reset in the cradle after each test, avoiding potential missed modes due to zero displacement points on the specimen surface. The first 70 modes were utilized for RUS inversions. Measurements of the specimen dimensions are used to calculate resonant frequencies during the inversion, therefore a $\pm 1\%$ dimensional tolerance is considered the maximum allowable geometric uncertainty during specimen preparation. The error in preparing and measuring the specimen with a set of vernier calipers was estimated at a maximum of ± 25 μm.

3.3.2 Forward model

The use of RUS to quantify elastic constants is an inverse problem, where the desired calculation of elastic constants from resonant frequencies is not known analytically, but the reverse calculation of resonant frequencies from elastic constants is known. Therefore, the calculation of resonant frequencies is referred to as the *forward model*. A traditional

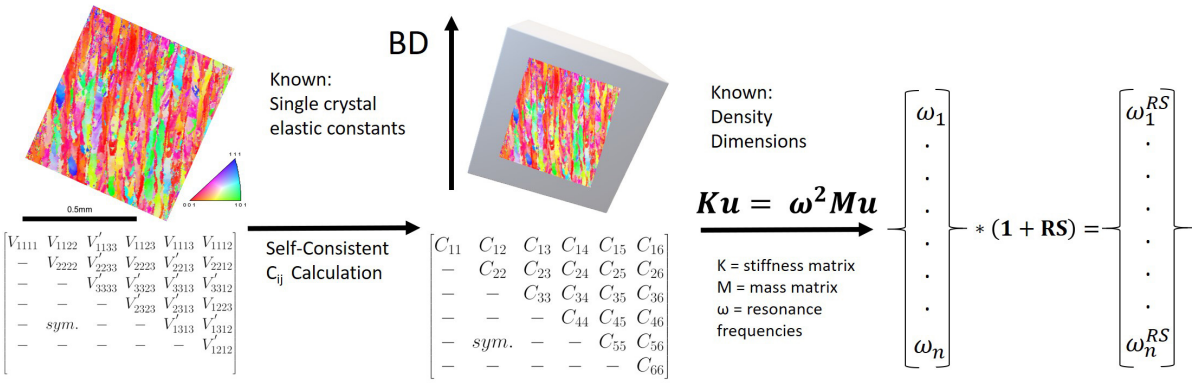

Figure 3.5: Forward model to calculate resonant frequencies from texture coefficients. Arbitrarily anisotropic textures are fully represented by the nine 4th order tensorial texture coefficients (left). These coefficients are utilized to calculate the full elastic tensor (center) and consequently calculate the resonant frequencies. The residual stress (RS) term is a degree of freedom during the inversion, used to shift calculated frequencies and account for the influence of residual stresses on experimentally measured frequencies. Note that the EBSD image (center) is not to scale relative to the parallelepiped specimen.

RUS inversion framework consists of iteratively solving the forward model to calculate the resonant frequencies from the elastic constants, and comparing the calculated and experimentally-measured frequencies.

Due to the dependence of elastic symmetry on texture morphology and orientation, characterizing AM specimens requires direct parameterization of the texture coefficients. The research presented here extends the traditional forward model to include a calculation of the bounded polycrystalline elastic constants from texture. The forward model here therefore involves the use of texture coefficients to calculate elastic constants and elastic constants to generate resonant frequencies, as represented in Figure 3.5.

Following Section 2.2.1, a tensorial representation of the ODF coefficients established by Fernandez et al. [95] is used here to produce the second-order Hashin-Shtrikman bounds of the anisotropic elastic constants. These bounds are significantly tighter than representations such as Voigt and Reuss. Though isotropic two-point statistics (spherical grain shape) are assumed in the model [95], and many AM samples do not display isotropic two-point statistics, an assumption about grain shape must be made to generate

the forward model. This work utilizes isotropic two-point grain statistics to fit texture coefficients of unknown AM microstructures, with the understanding that the inverse framework will incorporate any unparameterized quantities in the model into the parameter uncertainties associated with the final fit of the frequencies. The general form of the tensorial ODF is given by Equation 3.1, with the ODF $f(Q)$ representing the relative amount of grains with orientation Q over $Q \in SO(3)$. The ODF is given in terms of the tensorial texture coefficients $V_{\langle\alpha\rangle\beta}$, the basis tensors $F_{\langle\alpha\rangle\beta}$ fixed by the microscopic symmetry, and the tensor order α. The tensorial texture coefficients are then directly translatable to or from the coefficients C_{lmn} traditionally utilized for quantitative texture analysis [87] by using the functions T_{lmn} (Euler angle parameterization). These relations are supplied in [95], with the translation from tensorial to traditional parameterization provided for reference in Equation 3.1 below. Note that brackets $\langle\rangle$ indicate an orientation average over $SO(3)$, l indicates order, and m,n correspond to the indices at that order.

$$\begin{aligned} f(Q) &= \sum_{\alpha=0}^{4}\sum_{\beta=1}^{n_\alpha^H}(1+2\alpha)V_{\langle\alpha\rangle\beta}\cdot F_{\langle\alpha\rangle\beta}(Q) \\ C_{lmn} &= (1+2l)\langle f, T_{lmn}\rangle = (1+2l)^2\sum_{\beta=1}^{n_\alpha^H}\langle V_{\langle l\rangle\beta}\cdot F_{\langle l\rangle\beta}, T_{lmn}\rangle \end{aligned} \tag{3.1}$$

Note that $\beta = 1, ..., n_\alpha^H \leq 1+2\alpha$ with $n_\alpha^H \leq 1+2\alpha$ representing the number of existing basis tensors given a microscopic and macroscopic symmetry. For microscopically cubic symmetry materials, there is a single existing independent basis function (at 4th order), so the β term is omitted in further representations of the tensorial texture coefficient. To implement this framework into the inverse model, it is necessary to identify the minimum number of independent texture coefficients to estimate. It is well documented that the ODF coefficients up to 4th order are the only coefficients needed to fully parameterize the

elastic tensor for microscopically cubic materials [69, 71, 93, 96, 114]. Further, the 0th through 3rd order coefficients are constant for microscopically cubic materials. Therefore, the nine 4th order coefficients and the three single crystal elastic constants fully characterize the effect of texture on the aggregate elastic constants. The nine independent 4th order coefficients are shown in tensorial form (normalized Voigt notation) in Equation 3.2.

$$V_{\langle 4\rangle pqrs} = \begin{bmatrix} V_{1111} & V_{1122} & V'_{1133} & V_{1123} & V_{1113} & V_{1112} \\ - & V_{2222} & V'_{2233} & V_{2223} & V'_{2213} & V_{2212} \\ - & - & V'_{3333} & V'_{3323} & V'_{3313} & V'_{3312} \\ - & - & - & V'_{2323} & V'_{2313} & V_{1223} \\ - & sym. & - & - & V'_{1313} & V'_{1312} \\ - & - & - & - & - & V'_{1212} \end{bmatrix} \tag{3.2}$$

$$V'_{1133} = -V_{1111} - V_{1122}, V'_{2233} = -V_{1122} - V_{2222}, V'_{2213} = V_{1223}$$
$$V'_{3333} = V_{1111} + 2V_{1122} + V_{2222}, V'_{3323} = -V_{1123} - V_{2223}, V'_{3313} = -V_{1113} - V_{1223}$$
$$V'_{3312} = -V_{1112} - V_{1222}, V'_{2323} = -V_{1122} - V_{2222}, V'_{2313} = -V_{1112} - V_{1222}$$
$$V'_{1313} = -V_{1111} - V_{1122}, V'_{1312} = V_{1123}, V'_{1212} = V_{1122}$$

The parameters denoted with (') in Equation 3.2 depend on the nine independent components of the tensor. The tensorial form is used with the single crystal elastic constants to calculate the Hashin-Shtrikman bounds and self-consistent average elastic constants as detailed in [95]. Equation 3.3 details the construction of the Hashin-Shtrikman bounds C^{HS} in terms of the corresponding upper/lower zeroth-order elastic tensor C^{0+-}, the inverse of the polarization tensor $P0$ (calculated from C^{0+-}), and the inverse of the ori-

entation average $\langle f, C^{SC} \rangle$. The zeroth-order bounds are calculated from the eigenvalues $\lambda_{1,2,3}$ (1x, 2x, 3x) of the single-crystal elastic tensor C^{SC}, with the constant isotropic projectors P_1 and P_2 as detailed in [98]. The orientation average $\langle f, C^{SC} \rangle$ with cubic microsymmetry is calculated with constants h_{I1}, h_{I2}, H_4 determined by the harmonic decomposition of C^{SC}. Note that all quantities besides the 4th order texture coefficient tensor $V_{\langle 4 \rangle pqrs}$ are fully determined by the single crystal elastic constants.

$$\begin{aligned} C^{HS} &= C^{0+-} - [P_0(C^{0+-})]^{-1} + [\langle f, C^{SC} \rangle]^{-1} \\ C^{0+} &= \lambda_1 P_1 + \lambda_2 P_2, \quad C^{0-} = \lambda_1 P_1 + \lambda_3 P_2 \\ \langle f, C^{SC} \rangle &= h_{I1} P_1 + h_{I2} P_2 + H_4 V_{\langle 4 \rangle pqrs} \end{aligned} \tag{3.3}$$

An important distinction of the frequency calculation implemented here is the incorporation of a residual stress term. The presence of residual stresses in AM components has been shown to induce global shifts across all resonant frequencies [124], therefore the final calculation of frequencies includes an offset term as described in Equation 3.4. The calculated list of n resonant frequencies at the end of the model evaluation (ω_n^{RS}) are shifted by a residual stress (RS) factor compared to the frequencies calculated from the elastic constants ($\omega_n^{C_{ij}}$).

$$\omega_n^{RS} = \omega_n^{C_{ij}}(1 + RS) \tag{3.4}$$

The calculation of the resonant frequencies (from the elastic constants) was therefore separated from any potential effects of the residual stress on the frequencies. The RS factor was allowed to vary freely as an independent parameter during the inversion. There is a physical basis for this parameterization of the residual stress: A global shift in all resonant frequencies cannot be explained by the global changes in elasticity that occur

during a low temperature heat treatment (i.e. no recrystallization), as elasticity changes that induce a global change in frequencies would require a change in elastic symmetry.

The combined forward model therefore uses texture coefficients to calculate the bounded polycrystalline elastic constants (Equation 3.1), then uses those elastic constants to calculate resonant frequencies (Equation 2.32). The residual stress term is freely determined, and shifts all frequencies to a final set of calculated frequencies ω_n^{RS} (Equation 3.4). The combined forward model in Figure 3.5 is iterated for the inversion, with ω_n^{RS} compared to the experimentally-measured resonant frequencies. The computational code for calculation of elastic constants from texture was rewritten in Python 3 for efficiency. Single crystal elastic constants were characterized for SB-CoNi-10 as C_{11}^{SC}=236.4 GPa, C_{12}^{SC}=150.8 GPa, C_{44}^{SC}=134.1 GPa at 23°C [125], using a Bayesian inference framework.

3.3.3 Bayesian inference with sequential Monte Carlo

$V = [V_1 \dots V_9] = [V_{1111} \dots V_{2223}]$, the vector of the 9 independent coefficients of the tensorial crystallite ODF V_{pqrs}; i.e., V_{pqrs} in Equation 3.2 is constructed with the vector of nine random variables V. The numerator of the right hand side comprises the likelihood function $\pi(\omega_n|V)$ (which represents the likelihood of observing the measured resonant frequencies given V) and the prior $\pi(V)$ (which represents prior knowledge of the model parameters). The prior distribution can be defined by physical bounds (e.g., strictly positive) or more subjectively through domain knowledge and previously conducted experiments. The denominator is the marginal likelihood and involves integration over the entire parameter support, $\Omega = \{V \in \mathbb{R}^9\}$.

The following hyperparameters and definitions are maintained throughout all subsequently presented RUS inversions. For all model parameters, a uniform distribution for each of the priors was chosen; i.e., $V_i \sim \text{Uniform}(-\inf, +\inf)$ for $i = 1, \dots, 9$. The initial particle population was sampled from a proposal distribution defined as a multivariate

normal distribution, with each parameter having a mean of 0.0 and a standard deviation of 0.2. The initial particle population is intended to fill the entire solution space within the tensorial texture coefficient condition ($|V_{pqrs}^{norm}| \leq 1$), with those parameters violating the condition being discarded. Independent and identically distributed, zero-mean Gaussian errors were assumed for the measured ω_n values such that Equation 2.41 applies. This assumption is supported by repeated measurements of the resonant frequencies. For SMC, 5500 particles were used with $30 - 45$ target distributions (including prior and posterior). Each pass through the MCMC kernel (a standard Metropolis algorithm implemented in `SMCPy`) involved construction of Markov chains with length 5. The final sample in the chain was taken to be the mutated particle. Hyperparameter tuning was not in the scope of this work. These tuning parameters were selected to ensure samples were generated from the full posterior (i.e. all modes represented) while balancing sample size with computation time.

3.3.4 Generation of pole figures from texture coefficient distributions

An ODF is typically fitted to experimental orientation or pole figure data. Here, each tensorial texture coefficient was solely constrained by the condition that the fourth order tensorial representation obeys the condition ($|V_{pqrs}^{norm}| \leq 1$) [96, 114]. The tensorial texture components were translated back to the traditional generalized spherical harmonic Fourier coefficients (C_{lmn}) for convenience and plotting [87, 95, 126]. The pole figures were then generated from these coefficients using the MATLAB toolbox, MTEX [123, 127].

Estimating the ODF coefficients by Bayesian inference results in a full probability distribution for each of the Fourier coefficients (C_{lmn}) of the ODF. As a result, it is necessary to propagate the probability distribution of each coefficient through to the ODF, resulting in a valuable measure of the uncertainty in the ODF and corresponding

pole figures. Uncertainty in the ODF has been previously studied by fitting error metrics to discrete points in the pole figure [128, 129], using experimental variation to calculate the error. To measure the pole figure uncertainty here, the calculated texture coefficients V for every forward evaluation (particle) from the final (convergent) timestep of SMC is converted to its own set of nine C_{lmn} parameters. The value of each particle's C_{lmn} parameters are translated to individual ODFs in MTEX [123]. The value of each ODF in MTEX is then discretized at 3° intervals of the Euler angles (ZYZ convention) and utilized to calculate the standard deviation of the value at each 3° resolution of the pole figures. The result is a pole figure of the pointwise standard deviation (units of multiples of random). This is used in conjunction with the pole figure of the mean values to visualize the uncertainty at each orientation. The MATLAB codes used to construct these pole figures from the output of the Python codes are provided in Appendix A.

3.4 Results

3.4.1 Residual stress

After a stress-relief heat treatment at 1100°C for 2h, a global increase in the resonant frequencies was observed for both specimens R2 and R4. For specimen R2, this increase was normally distributed across the frequencies, with a mean of 1.66% and standard deviation of 0.08%. The shift was observed across all 75 measured modes. The first 30 resonant frequencies are given in both the as-built and stress-relieved states in Table 3.3.

For specimen R4, the increase across all frequencies was normally distributed with a mean of 1.38% and standard deviation of 0.11% across the 75 measured frequencies. The increased standard deviation of specimen R4 relative to specimen R2 is a result of a single outlier mode with a shift of 0.84% (mode 33). This mode was identified through mode-type resonant frequency modeling in ABAQUS as a dilation/compression-type mode. None of these mode-types were observed when modeling specimen R2. The

Specimen R2 frequencies in as-built and stress-relieved states			
Res. Freq.	As-built (kHz)	SR (1100°C 2h) (kHz)	% Change
f_r^1	165.681 ± 0.008	168.556 ± 0.007	1.71
f_r^2	195.949 ± 0.016	199.339 ± 0.012	1.70
f_r^3	206.810 ± 0.007	210.539 ± 0.006	1.77
f_r^4	222.811 ± 0.012	226.639 ± 0.008	1.69
f_r^5	228.217 ± 0.011	232.021 ± 0.005	1.64
f_r^6	233.106 ± 0.019	237.250 ± 0.018	1.75
f_r^7	234.223 ± 0.014	238.002 ± 0.017	1.59
f_r^8	246.221 ± 0.023	250.114 ± 0.003	1.56
f_r^9	250.092 ± 0.006	254.277 ± 0.002	1.65
f_r^{10}	250.937 ± 0.016	255.022 ± 0.014	1.60
f_r^{11}	267.258 ± 0.020	271.813 ± 0.008	1.68
f_r^{12}	267.465 ± 0.009	272.477 ± 0.009	1.84
f_r^{13}	289.417 ± 0.007	294.100 ± 0.011	1.59
f_r^{14}	294.841 ± 0.017	299.395 ± 0.006	1.52
f_r^{15}	303.570 ± 0.010	308.670 ± 0.007	1.65
f_r^{16}	309.586 ± 0.006	314.662 ± 0.010	1.61
f_r^{17}	311.800 ± 0.007	317.023 ± 0.020	1.65
f_r^{18}	314.172 ± 0.016	319.530 ± 0.006	1.68
f_r^{19}	328.498 ± 0.012	334.296 ± 0.006	1.73
f_r^{20}	334.716 ± 0.006	340.207 ± 0.012	1.61
f_r^{21}	339.306 ± 0.010	345.405 ± 0.014	1.77
f_r^{22}	340.657 ± 0.007	346.561 ± 0.013	1.70
f_r^{23}	342.806 ± 0.018	348.982 ± 0.017	1.77
f_r^{24}	359.425 ± 0.012	365.973 ± 0.009	1.79
f_r^{25}	364.406 ± 0.016	370.156 ± 0.012	1.55
f_r^{26}	369.208 ± 0.009	375.072 ± 0.008	1.56
f_r^{27}	372.671 ± 0.023	379.531 ± 0.013	1.81
f_r^{28}	379.375 ± 0.019	385.389 ± 0.018	1.56
f_r^{29}	382.324 ± 0.020	388.440 ± 0.005	1.57
f_r^{30}	399.913 ± 0.010	406.224 ± 0.013	1.55

Table 3.3: Experimentally measured resonant frequencies for specimen R2 in the as-built and stress-relieved (1100°C 2h) states. RUS measurements are in kHz, with ± indicating the standard deviation across four measurements of the frequency. All stress-relieved frequencies exhibit a positive percent change with a mean and standard deviation of 1.66% ± 0.08%. Trend persists across all 75 measured modes.

first 30 resonant frequencies of specimen R4 are given in Table 3.4

The magnitude of the difference between the stress-relief heat treatment frequency

Specimen R4 as-built and stress-relieved frequencies			
Res. Freq.	As-built (kHz)	SR (1100°C 2h) (kHz)	% Change
f_r^1	150.342 ± 0.019	152.558 ± 0.007	1.45
f_r^2	168.671 ± 0.013	171.193 ± 0.020	1.47
f_r^3	173.096 ± 0.042	175.575 ± 0.009	1.41
f_r^4	192.030 ± 0.008	195.185 ± 0.009	1.62
f_r^5	196.953 ± 0.017	199.554 ± 0.007	1.30
f_r^6	197.908 ± 0.028	200.676 ± 0.009	1.38
f_r^7	207.327 ± 0.016	210.151 ± 0.009	1.34
f_r^8	213.036 ± 0.003	215.523 ± 0.011	1.15
f_r^9	219.402 ± 0.009	222.325 ± 0.009	1.31
f_r^{10}	222.423 ± 0.010	225.583 ± 0.008	1.40
f_r^{11}	223.732 ± 0.012	226.793 ± 0.011	1.35
f_r^{12}	230.922 ± 0.016	234.800 ± 0.007	1.65
f_r^{13}	238.283 ± 0.009	241.527 ± 0.012	1.34
f_r^{14}	249.543 ± 0.004	252.683 ± 0.010	1.24
f_r^{15}	256.561 ± 0.005	259.860 ± 0.012	1.27
f_r^{16}	257.191 ± 0.004	260.725 ± 0.012	1.36
f_r^{17}	259.585 ± 0.003	263.502 ± 0.011	1.49
f_r^{18}	264.193 ± 0.010	267.999 ± 0.028	1.42
f_r^{19}	268.195 ± 0.011	272.153 ± 0.005	1.45
f_r^{20}	278.371 ± 0.016	282.271 ± 0.016	1.38
f_r^{21}	286.089 ± 0.011	290.364 ± 0.008	1.47
f_r^{22}	287.727 ± 0.008	292.054 ± 0.032	1.48
f_r^{23}	288.006 ± 0.023	292.220 ± 0.004	1.44
f_r^{24}	315.538 ± 0.004	319.586 ± 0.011	1.27
f_r^{25}	317.632 ± 0.009	322.604 ± 0.017	1.54
f_r^{26}	319.279 ± 0.014	323.464 ± 0.019	1.29
f_r^{27}	319.524 ± 0.028	324.432 ± 0.009	1.51
f_r^{28}	327.624 ± 0.005	332.003 ± 0.010	1.32
f_r^{29}	331.013 ± 0.019	335.171 ± 0.012	1.24
f_r^{30}	339.924 ± 0.008	344.187 ± 0.012	1.24

Table 3.4: Experimentally measured resonant frequencies for specimen R4 in the as-built and stress-relieved (1100°C 2h) states. ± indicates the standard deviation across four measurements of the frequency. All stress-relieved frequencies exhibit a positive percent change with a mean and standard deviation of 1.38% ± 0.11%.

shifts on specimen R2 (1.66%) and R4 (1.38%) is 0.28%. The difference likely stems from different processing parameters in each specimen, with correspondingly different residual stress states. Given identical hatch spacing was used for each specimen, the change in

power and scan speed given in Table 3.2 are considered. Following [115], increases in the ratio of laser power/ scan speed (analogous to energy density) results in reduced residual stresses. Given that specimen R4 has a value of laser power/ scan speed that is 15% greater than that of specimen R2, the observation of a lower calculated residual stress term in specimen R4 agrees with the residual stress trend observed in [115]. Mass and dimensional changes of the specimens were negligible after heat treatment, with a measured mass change of 0.0010 g and 0.0005 g for specimens R2 and R4 respectively. Any dimensional change was within the measurement error of ±25 um, as dimensions were measured identically before and after heat treatment.

3.4.2 Build direction aligned specimen - R4

All inversions used a polynomial order of 14 and 70 modes for the frequency forward model. The build direction aligned specimen (R4) was scanned via RUS, and the mea-

Specimen R4 final parameter estimates from SMC											
	V_{1111}	V_{1112}	V_{1113}	V_{1122}	V_{1123}	V_{1222}	V_{1223}	V_{2222}	V_{2223}	RS (%)	$\sigma(kHz)$
Mean	0.182	0.001	0.001	-0.106	0.000	0.000	0.001	0.182	-0.001	-0.97	1.26
Std. Dev	0.003	0.015	0.015	0.002	0.011	0.011	0.012	0.003	0.014	0.06	0.14

↓

	C_{400}	C_{410}	C_{420}	C_{430}	C_{440}
Mean	2.165	0.019 - 0.007 i	-0.002 - 0.033 i	0.003 - 0.005 i	1.720 + 0.007 i

Table 3.5: SMC texture inversion parameters for specimen R4. As-built specimen state used to generate resonant frequencies. Mean and standard deviation (normal distribution) for each parameter are calculated at the final timestep of the simulation. The simulation does not constrain the parameters to any specific distribution, though the results displayed normal distributions for all parameters. Parameter means are converted to conventional C_{lmn} coefficients for plotting.

sured resonant frequencies were inputs to the SMC inversion framework. The mean and standard deviation of the posterior distribution for each normally distributed parameter are given in Table 3.5. The simulation does not constrain each parameter to be normally distributed, but the results reveal each parameter to be normally distributed. Note that the σ term can be considered as a measure of the fit between the calculated and mea-

sured resonant frequencies. The σ parameter is represented in Equation 2.41 and is an independently determined parameter.

Specimen R4 elastic constants calculated by SMC (GPa)						
	Voigt	C^{HS}_{upper}	$C^{self-consistent}$	C^{HS}_{lower}	Hill	Reuss
C_{11}	269.4	260.0	258.3 ± 1.0	255.7	259.4	249.4
C_{12}	138.5	141.9	142.6 ± 0.7	143.7	142.4	146.3
C_{13}	130.1	136.1	137.1 ± 1.0	138.7	136.2	142.3
C_{22}	266.6	259.1	257.5 ± 1.0	255.0	257.3	248.1
C_{23}	133.0	136.9	137.9 ± 0.9	139.4	138.3	143.7
C_{33}	274.9	265.0	263.0 ± 1.0	260.0	263.5	252.1
C_{44}	116.3	109.1	107.4 ± 1.5	104.5	105.5	94.7
C_{55}	113.4	107.6	105.8 ± 1.7	102.8	101.9	90.4
C_{66}	121.8	116.9	115.6 ± 1.1	113.3	112.9	104.1
C_{14}	0.0	-0.1	-0.1 ± 4.5	-0.1	0.0	0.0
C_{15}	0.0	0.3	0.3 ± 3.5	0.2	0.0	0.0
C_{16}	-1.4	-0.5	-0.5 ± 3.9	-0.5	-1.4	-1.3
C_{24}	0.0	0.8	0.8 ± 5.8	0.7	0.0	0.0
C_{25}	0.0	-1.0	-1.0 ± 4.7	-1.0	0.0	0.0
C_{26}	1.8	-0.3	-0.3 ± 2.3	-0.3	1.7	1.6
C_{34}	0.0	-0.7	-0.7 ± 5.1	-0.7	0.0	0.0
C_{35}	0.0	0.7	0.7 ± 4.8	0.7	0.0	0.0
C_{36}	-0.4	0.8	0.8 ± 3.8	0.8	-0.3	-0.3
C_{45}	-0.4	0.9	0.9 ± 4.5	0.9	-0.4	-0.5
C_{46}	0.0	-1.3	-1.4 ± 6.4	-1.5	0.0	0.0
C_{56}	0.0	-0.1	-0.1 ± 6.1	-0.1	0.0	0.0

Table 3.6: Bulk elastic constant values calculated from the posterior distribution of the SMC calculated texture coefficients (Table 3.5). Inversion carried out with resonant frequencies in the as-built state (RS term included).

The inversion result displays orthorhombic elastic symmetry in the sample reference frame as shown in Figure 3.6, despite not constraining the simulation to any symmetry. The inversion framework developed here can recreate the results of build direction oriented AM specimen inversions without constraining the specimen symmetry inside the model.

The agreement between the SMC-calculated texture coefficients and EBSD data from specimen R4 is demonstrated in Figure 3.6 by plotting pole figures for each set of coeffi-

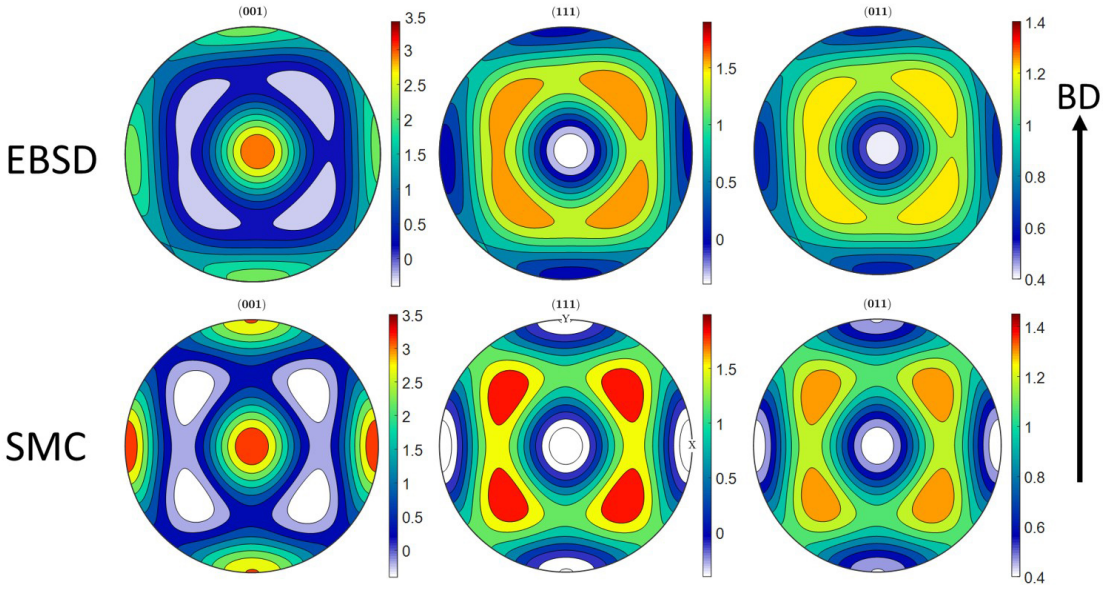

Figure 3.6: Pole figures generated from EBSD scan on specimen R4 (upper) and pole figures generated by SMC inversion result (lower). Plotted in the MATLAB MTEX toolbox with units of multiples of random distribution (MRD). Fourier coefficients of EBSD-generated pole figures were limited to 4th order. Quantitative agreement exists between EBSD results and SMC results. Resonant frequencies collected in the as-built state were used as inputs to SMC.

cients. The SMC generated pole figures agree quantitatively with EBSD-generated pole figures across all orientations. As mentioned in Section 3.3, the EBSD-generated ODF is limited to 4th order for the pole figures in Figure 3.6. This enables direct comparison to the SMC results, which are also limited to 4th order Fourier coefficients. The high magnitude MRD locations for the (011) pole figure are spread across a larger area compared to the pole figures in Figure 3.2, which are not limited to 4th order. Note that the convergent mean values of the texture coefficients were used to generate the SMC pole figure. Looking at the calculated standard deviation (described in Section 3.3.4) at each point within the SMC-calculated pole figure in Figure 3.7, agreement between all points with a single standard deviation is clearly seen between the EBSD measured and calculated pole figure.

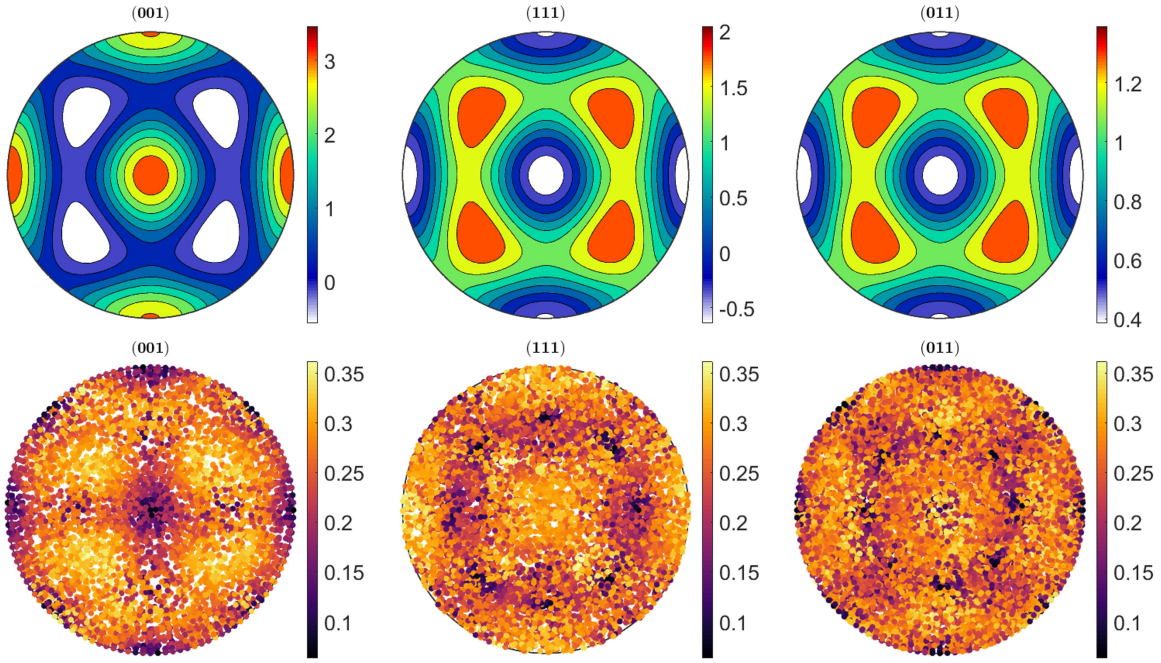

Figure 3.7: SMC texture results (upper) and pointwise standard deviation (lower) generated from posterior distribution of specimen R4 stress relieved state inversion. Upper pole figure was generated with the mean values of each texture parameter (Table 3.5). Full probability distributions from all nine texture parameters were combined to generate the the standard deviations of the pole figure values at 3° intervals of the orientations (lower). All units are in multiples of random distribution (MRD).

3.4.3 22.3° inclined to build direction specimen - R2

Specimen R2 (sectioned 22.3° from the build direction) demonstrates the ability of the RUS texture inversion framework to quantify the position and magnitude of an arbitrary AM microstructure relative to the specimen reference frame. The frequency data from the as-built specimen was fed into the framework, with the posterior distribution of each of the parameters given in Table 3.7. EBSD data was obtained after sectioning and used to validate the SMC inversion results relative to the sectioned specimen axes. This EBSD was used to generate the upper pole figure in Figure 3.8. Quantitative agreement between the pole figure values is observed in Figure 3.8, as well as positional accuracy of the high magnitude MRD locations.

Specimen R2 final parameter estimates from SMC											
	V_{1111}	V_{1112}	V_{1113}	V_{1122}	V_{1123}	V_{1222}	V_{1223}	V_{2222}	V_{2223}	RS (%)	$\sigma(kHz)$
Mean	0.077	-0.001	0.099	-0.082	0.000	0.001	-0.017	0.157	0.000	-1.63	1.26
Std. Dev	0.003	0.011	0.003	0.002	0.006	0.009	0.003	0.002	0.011	0.05	0.12

↓

	C_{400}	C_{410}	C_{420}	C_{430}	C_{440}
Mean	1.002	1.054 + 0.007 i	0.730 - 0.017 i	-0.725 - 0.006 i	1.250 - 0.014 i

Table 3.7: SMC inversion of texture from RUS data for specimen R2 (sectioned at 22.3° measured to the build direction). Resonant frequencies were measured in the as-built state to input into the SMC inversion. Mean and standard deviation for each tensorial texture parameter was normally distributed, though the simulation does not constrain the parameters to any distribution. Parameter means were converted to conventional C_{lmn} Fourier coefficients for plotting.

The posterior distribution of all 21 independent elastic constants was generated from the posterior distribution of the texture coefficients. Though the self-consistent average elastic constants were utilized during the inversion, the Reuss, Voigt, Hill, upper Hashin-Shtrikman, and lower Hashin-Shtrikman bounds can also be generated within the code. These alternative sets of elastic constants are given in Table 3.8 for specimen R2, demonstrating the accuracy of the elastic constants compared to wider bounds such as Voigt and Reuss. Note that the ± for the self-consistent elastic constants indicates the standard deviation of the posterior distribution at the end of SMC sampling. This error does not include the spread between the HS bounds or assumed uncertainty in the grain average model used. The indicated error reflects the standard deviation of the posterior distribution for each propagated parameter, arising solely from the fit between experimental and calculated frequencies. Each elastic constant average (C^{HS}_{upper}, C^{HS}_{lower}) was propagated using the full posterior distribution (5500 forward model evaluations at the final SMC timestep) of the texture coefficients, as represented in Table 3.7. The error of each Hashin-Shtrikman bound mimics that of the self-consistent solution, and is therefore not shown.

Parameter plots are generated for each sampled parameter in SMC, demonstrating

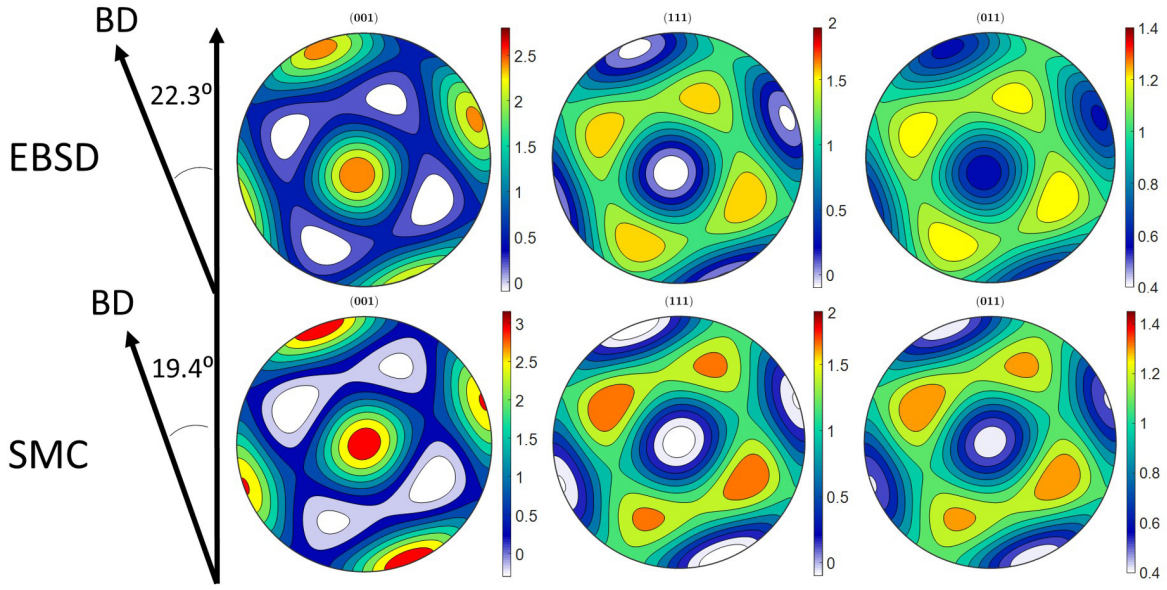

Figure 3.8: Experimental pole figure generated from EBSD scan on 22.3° sectioned specimen R2 (upper) and pole figure generated from SMC inversion result (lower). Plotted in the MATLAB MTEX toolbox with units of multiples of random distribution (MRD). Quantitative agreement exists between EBSD results and simulated SMC results, with small positional discrepancies for the high magnitude locations. Agreement between the 22.3° inclination in the EBSD and 19.4° inclination of the SMC results is observed. Note that the EBSD generated pole figure utilized a Dirichlet kernel here and was limited to coefficients at 4th order for direct comparison with the model.

the robust convergence of each parameter to a normal distribution relative to the every other sampled parameter. Figure 3.9 demonstrates the convergence of the simulation for specimen R2 with representative parameter plots. Each point in the parameter plots represents a forward model evaluation, with a given set of the parameters, during the final convergent timestep. 55 parameter plots are generated for the interdependence between each of the 11 independent parameters (9 components of V_{pqrs}, RS, and σ), as well as additional plots for the propagated 21 elastic constants.

Standard deviations are propagated from the weighted parameter distribution to the pole figure using the technique described in Section 3.3.4. As shown in Figure 3.10, the pointwise standard deviation magnitude is ≤ 0.35 MRD throughout the pole figure, supporting the calculated texture as the convergent solution. The magnitude of each

Polycrystalline elastic constants calculated by SMC (GPa)						
	Voigt	C^{HS}_{upper}	$C^{self-consistent}$	C^{HS}_{lower}	Hill	Reuss
C_{11}	294.1	283.9	281.6 ± 0.6	277.9	281.0	267.9
C_{12}	130.7	135.6	136.6 ± 0.4	138.2	136.4	142.1
C_{13}	113.2	118.5	119.7 ± 0.5	121.8	120.6	128.0
C_{22}	278.0	267.5	265.4 ± 0.4	262.0	265.9	253.8
C_{23}	129.3	134.8	136.0 ± 0.3	137.7	135.7	142.1
C_{33}	295.5	284.7	282.3 ± 0.6	278.4	281.7	267.9
C_{44}	112.6	105.1	103.3 ± 0.5	100.0	101.0	89.5
C_{55}	96.5	88.7	86.9 ± 0.6	83.9	85.8	75.0
C_{66}	114.0	106.9	105.1 ± 0.5	101.9	102.8	91.5
C_{14}	-0.1	-0.1	-0.1 ± 1.3	-0.1	-0.1	-0.1
C_{15}	-19.7	-19.8	-19.6 ± 0.6	-19.2	-18.3	-16.9
C_{16}	0.1	0.1	0.1 ± 2.5	0.1	0.1	0.1
C_{24}	0.0	0.0	0.0 ± 2.2	0.0	0.0	0.0
C_{25}	3.4	3.1	3.0 ± 0.6	2.9	2.9	2.3
C_{26}	-0.3	-0.3	-0.3 ± 1.9	-0.3	-0.3	-0.3
C_{34}	0.1	0.1	0.2 ± 2.1	0.2	0.1	0.2
C_{35}	16.4	16.7	16.6 ± 0.5	16.3	15.5	14.6
C_{36}	0.2	0.2	0.2 ± 2.6	0.2	0.2	0.2
C_{45}	0.2	0.2	0.2 ± 2.7	0.2	0.2	0.2
C_{46}	3.4	4.1	4.2 ± 0.8	4.5	4.1	4.8
C_{56}	-0.1	-0.1	-0.1 ± 1.5	-0.1	-0.1	-0.1

Table 3.8: Elastic constant averages propagated from the posterior distribution of the SMC calculated texture coefficients (Table 3.7). Inversion carried out with resonant frequencies from specimen R2 in the as-built state (RS term included).

point in the lower pole figure represents the standard deviation (in 3° intervals of each euler angle) of the corresponding location in the mean pole figure (upper). For example, the center of the (001) mean pole figure has a value of approximately 3.0 MRD with a standard deviation of ±0.1 MRD.

3.5 Discussion

The computation time of a SMC inversion (with uninformed priors) is on the order of 24-48 hours for a 8-core parallel computation (5500 particles, 30 timesteps, 6 MCMC iterations, polynomial order of 14, and 70 modes). This is a significant computational cost reduction compared to the other existing Bayesian inference RUS framework [68],

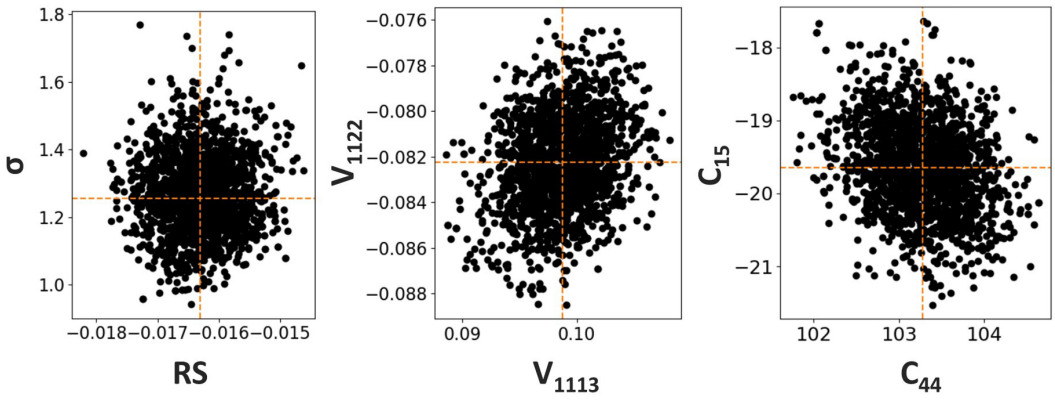

Figure 3.9: SMC parameter plots for R2 specimen in as-built state. Overall inversion error σ is shown versus the residual stress term (left). Tensorial texture coefficients V_{1122} and V_{1113} are plotted (middle). Propagated elastic constants C_{15} vs. C_{44} demonstrate the convergence of the elastic tensor (right). Each point represents a forward model evaluation during the final (convergent) timestep. 2000 of the final 5500 forward evaluations are shown here for visualization. Note that each variable is demonstrated as normally distributed around its mean, though the simulation does not constrain it as normally distributed.

where this computation takes approximately 14-20 days. Further, this time can be dramatically reduced by increasing the number of cores used for the computation. The simulation is parallelizable up to the number of particles (5500 in this case), theoretically yielding a computation time of 480 seconds (30 timesteps, 6 MCMC iterations). If an informed estimate of the texture is known prior to the start of the inversion, the timestep number can be reduced to ≤ 10, reducing the computation time to $\frac{1}{3}$. While there are cases in which convergence of the posterior is not fully achieved after the 30 timestep computation, the usual cause is low-quality input frequencies (such as a missed frequency experimentally). Additionally, the user can easily re-inform the simulation from its endpoint if the parameters were too restrictive for convergence.

There is evidence that RUS inherently measures the (aggregate) elastic constants dependent on longitudinal displacements (C_{11}, C_{22}, C_{12}) with less accuracy than the constants dependent on transverse displacements [64, 74, 110, 130]. Additional constraints such as pulse-echo measurements are often used to overcome this limitation, but these

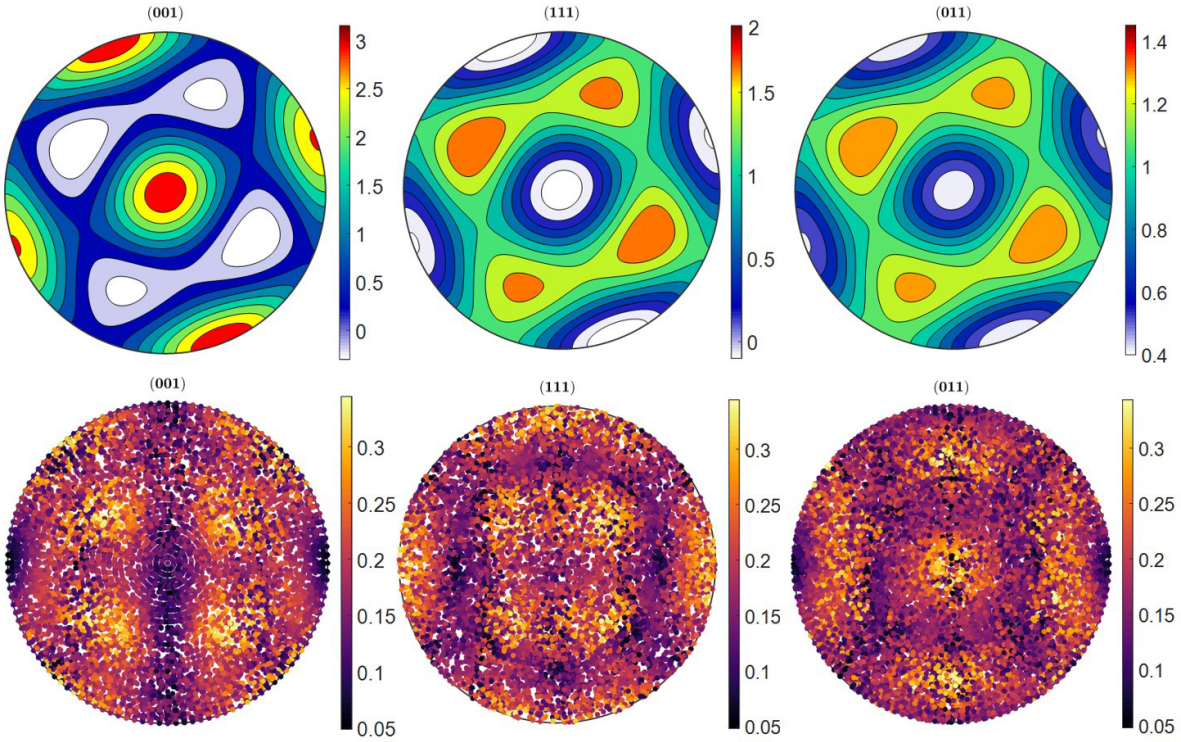

Figure 3.10: SMC texture results (upper) and pointwise standard deviation (lower) generated from posterior distribution. Specimen R2 resonant frequencies in the as-built state (with RS term) utilized for inversion. Upper pole figure was generated with the mean values of each texture parameter (Table 3.7). Full probability distributions from all nine texture parameters were combined to generate the the standard deviations of the pole figure values at 3° intervals of the orientations (lower). All units are in multiples of random distribution (MRD).

measurements have not yet been observed as necessary when utilizing Bayesian Inference by HMC [125] or SMC on AM specimens. The error functions utilized for RUS inversion by optimization [64, 74] are likely responsible, as these error functions are not capable of exploring the solution space as Bayesian inference does. Individually sampling each of the 21 independent elastic constants generally results in numerical convergence difficulties, but the elastic constants calculated in Table 3.8 demonstrate that parameterizing the elastic constants through the texture coefficients enables robust convergence. Further, parameterizing the texture (with built-in single crystal anisotropy) automatically constrains and controls the sensitivity of each component of the aggregate elastic tensor

during the simulation. The standard deviation of each off-axis elastic constant (C_{14}, C_{15}...) is tighter than those in studies using pulse-echo [67, 110], proving that parameterizing the texture results in reduced uncertainty on all the elastic constants. Therefore, directly parameterizing the texture for this inversion (rather than estimating it from the elastic constants) is highly advantageous. Despite this, the capability to directly invert for any number of independent elastic constants is maintained in the SMC framework.

The pole figures demonstrate agreement between the SMC calculation and the EBSD for both specimens, with the value of σ (overall inversion error between calculated and measured frequencies) indicating that the fit between the calculated list of frequencies and the experimentally measured frequencies still incorporates a significant difference. The mean value of σ is 1.26 kHz for both specimen R4 and R2 (as-built frequencies solved with RS term). This is significantly reduced compared to the mean values of 2.69 kHz and 3.97 kHz calculated for the as-built states (without RS term) of specimen R4 and R2 respectively. With the RS term included, there is agreement between the SMC calculated value of -1.63% $\pm$ 0.05% and the measured difference of -1.66% $\pm$ 0.08% after stress-relief heat treatment for specimen R2. For specimen R4, the calculated value of -0.97% $\pm$ 0.06% does not agree within a standard deviation of the experimentally measured value of -1.38% $\pm$ 0.11%. The existence of a single outlier mode for specimen R4 (as described in Section 3.4.1), relative to the shift of the other modes, may indicate a fitting error during the inversion. Otherwise, the origin of this difference could be attributed to unknown experimental mechanisms causing a larger shift, a lack of fidelity in the model in accounting for those unknown mechanisms, or a combination of both. Regardless, the addition of the RS term effectively reduces the magnitude of the σ term by the magnitude of the RS term for specimen R4. For specimen R2, the change in the magnitude of σ when including the RS term is more significant than for specimen R4.

SMC calculated self-consistent elastic constants of R2 specimen (GPa)				
	As-built	As-built (RS Term)	Stress-relieved	Hill Avg.
C_{11}	272.3 ± 2.6	281.6 ± 0.6	281.8 ± 0.5	284.1
C_{12}	133.9 ± 3.8	136.6 ± 0.4	136.7 ± 0.3	133.4
C_{13}	131.8 ± 4.2	119.7 ± 0.5	119.5 ± 0.5	120.5
C_{22}	267.7 ± 4.3	265.4 ± 0.4	265.6 ± 0.3	270.1
C_{23}	136.4 ± 1.8	136.0 ± 0.3	135.7 ± 0.3	134.5
C_{33}	269.9 ± 3.8	282.3 ± 0.6	282.8 ± 0.5	283
C_{44}	108.0 ± 2.0	103.3 ± 0.5	102.9 ± 0.4	100.9
C_{55}	104.2 ± 4.1	86.9 ± 0.6	86.4 ± 0.5	84.9
C_{66}	107.4 ± 4.2	105.1 ± 0.5	105.0 ± 0.5	98.8
C_{14}	-13.8 ± 4.3	-0.1 ± 1.3	0.0 ± 1.1	5
C_{15}	-21.6 ± 4.3	-19.6 ± 0.6	-18.9 ± 0.5	-13.6
C_{16}	1.9 ± 8.6	0.1 ± 2.5	-0.4 ± 2.4	5.7
C_{24}	10.3 ± 6.3	0.0 ± 2.2	0.0 ± 2.1	-11.5
C_{25}	11.5 ± 6.3	3.0 ± 0.6	2.5 ± 0.6	-2
C_{26}	-11.9 ± 9.0	-0.3 ± 1.9	0.0 ± 2.2	-5.9
C_{34}	3.5 ± 6.8	0.2 ± 2.1	0.0 ± 2.0	6.5
C_{35}	10.1 ± 7.8	16.6 ± 0.5	16.5 ± 0.5	15.5
C_{36}	10.0 ± 6.1	0.2 ± 2.6	0.4 ± 2.3	0.2
C_{45}	13.5 ± 7.3	0.2 ± 2.7	0.4 ± 2.3	0.2
C_{46}	11.4 ± 7.1	4.2 ± 0.8	3.5 ± 0.7	-2.1
C_{56}	-14.5 ± 5.4	-0.1 ± 1.5	0.1 ± 1.3	5.4
RS	-	-1.63% ± 0.05%	-	-
$Sigma$	3.02 ± 0.43	1.26 ± 0.12	1.22 ± 0.11	-

Table 3.9: SMC calculated elastic constants for specimen R2 (inclined 22.3° to the build-direction) using as-built frequencies, as-built frequencies with a freely varying residual stress (RS) term, and stress-relieved (1100°C 2hrs) frequencies. Hill average (generated from EBSD data) is shown for reference. Agreement is observed between calculated elastic constants for the stress-relieved state and the as-built state with the RS term. Agreement is observed between the calculated RS term (-1.63% ± 0.05%) and the experimentally observed change (-1.66% ± 0.08%) across all frequencies after stress-relief heat treatment in Table 3.3. Note that the as-built calculation (no RS term) only converged to the solution here by rotating each of the 4 non-unique elastic tensor solutions observed in the results to a single solution (described in Section 3.3). The other calculations were not constrained, converging to a single mode of the triclinic tensor.

This distinction is clear in Table 3.9, with the elastic constants for the as-built inversion (no RS term) displaying different means as well as significantly increased uncertainties.

Therefore, incorrect determination of the elastic constants is not the sole concern when

examining the role of residual stresses in the inversion. When conducting inversions on resonant frequencies for AM specimens in the as-built state (without the RS term), the σ term is unable to distinguish between the sources of discrepancies (residual stresses vs. experimental noise) in the measured and calculated frequencies. Also, σ incorporates the entire difference due to residual stress and experimental error correspondingly, leading to a poorer overall fit of the measured frequencies. As a result of the lower quality fit, all of the elastic constants and texture coefficients have increased uncertainty with their mean as shown in Figure 3.11. The parameters correspondingly cover a larger portion of the solution space, often resulting in multiple modes (variants of the non-unique solution) being concurrently sampled.

The multi-modal solution must then be corrected in post-processing, as described in Section 3.3.2. Correspondingly, the aggregate elastic constants given in Table 3.9 are numerically correct, but have 3 other representations. An example of these rotations for the as-built state (no RS term) is displayed in Figure 3.12

As a result, the given variant of the solution is not known to be the correctly oriented solution relative to the specimen faces. To determine the correct permutation of the non-unique solution, approaches such as mode shape imaging would be required as described in [67]. Note that the particles displayed in Figures 3.11 and 3.12 have equal weights; this is due to resampling within SMC prior to application of the final MCMC kernel.

Consequently, inversions with σ values above 2.5 kHz are not considered numerically convergent. This value is based on the convergence of simulations with and without the RS term, as well as evidence that supplying a set of resonant frequencies with an experimentally missing mode results in an increased σ magnitude of 1.5-2.0 kHz. Experimental noise has been shown to result in up to 1.5 kHz of error for AM specimens (Chapter 6), supporting this criterion. Further, limiting acceptable σ values to $\leq$2.5 kHz constrains

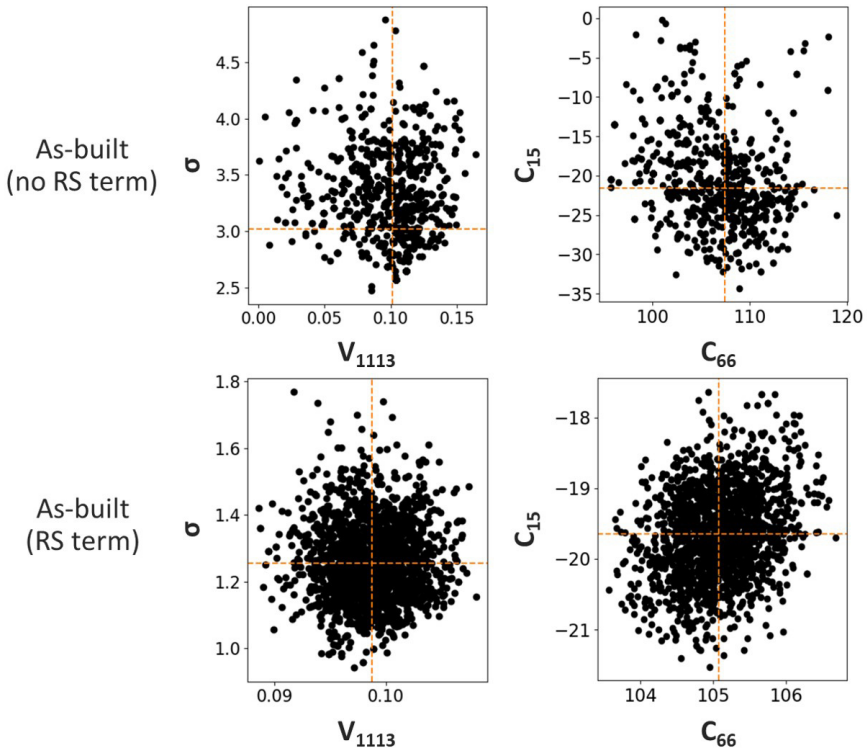

Figure 3.11: Specimen R2 SMC parameter plots demonstrating a higher uncertainty (σ) when the inversion does not include the residual stress (RS) term (upper). Note that for the as-built frequencies (upper), the simulation was unable to converge to either the positive or negative symmetric value of C_{15} (non-unique solution, as mentioned in Section 3.3.2) and required post processing to display single mode behavior as shown here. When including the RS term (lower), the simulation is able to fit the frequencies more precisely, not requiring the rotational post-processing correction to converge to a single mode. Note that the number of particles for each simulation was 5500, but that many particles were discarded as solutions when the RS term was not included (due to violating the texture condition $|V_{pqrs}^{norm}| \leq 1$).

the standard deviation on the elastic constants to $\leq \pm 7.0$ GPa, including the spread of the HS bounds. Regarding missed modes, low amplitude frequency peaks (high damping materials) can be missed during RUS measurement. Though the chances of a missed mode are negligible in this study, other approaches employing laser-based RUS [64] and machine learning (ML) approaches [131] could further reduce the uncertainty of missing a mode in a given RUS spectra. Specifically, ML could be integrated with the current approach in the future to robustly incorporate mode-type into the analysis. This could be

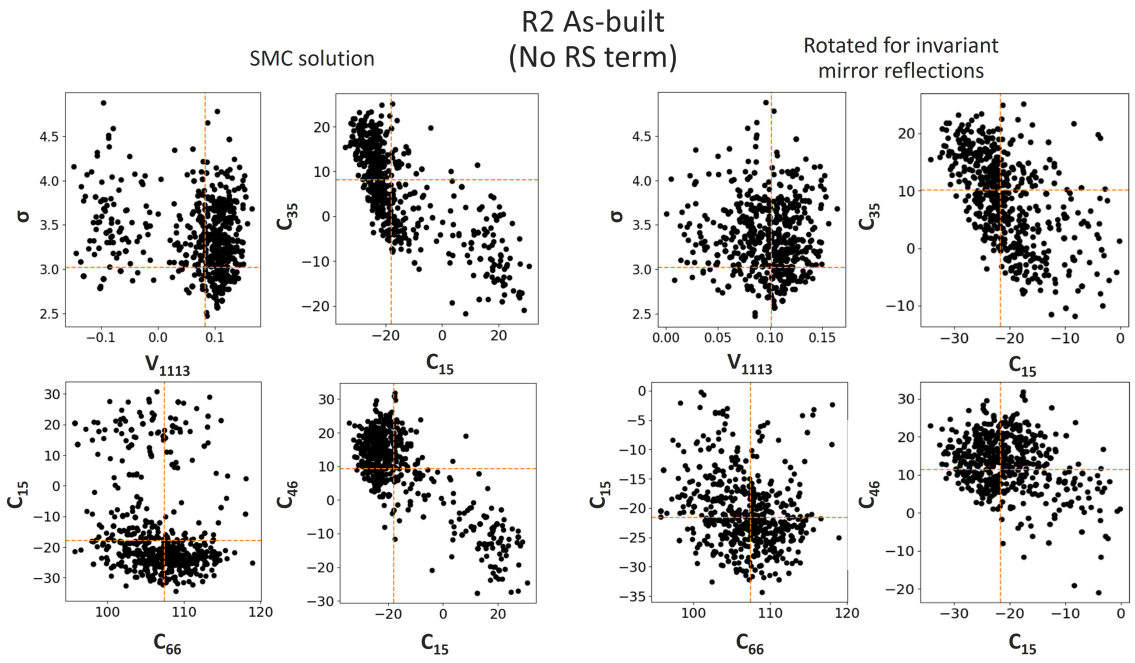

Figure 3.12: Specimen R2 as-built inversion displayed before (left) and after rotations (right) for various texture coefficients, σ, and bulk elastic constants. After correcting for the invariant solutions (Section 3.3.2), the correctly convergent single-mode is observed for each parameter.

particularly important if residual stress-induced shifts on the frequencies are discovered to be mode-type dependent in certain materials.

Homogeneity is a given assumption for RUS analysis, as any quantity being calculated from the resonant frequencies depends on bulk elastic waves. Given the inherent potential for AM microstructural heterogeneity resulting from geometric and process parameter differences [16, 24], there could be a gradient in the bulk elastic constants across macroscopic regions of the component. However, mode type order is significantly affected only if gradients in the elastic constants across the specimen exceed 15-20% [132]. This elastic gradient would represent extreme texture heterogeneity (which would be evident from the AM process conditions and component geometry) and exclude the specimen from the type of homogeneous bulk-texture analysis described here. If such a gradient affected the frequencies, it could be analyzed by gathering mode shape information with

laser vibrometry. In summary, any texture or elastic constants calculated using frequency data will be a homogenization, but this is unlikely to be a source of error in this study; surfaces were polished off during specimen preparation and the studied components were printed as simple rectangular parallelepipeds. EBSD confirms that the microstructure does not significantly deviate throughout the specimen (Figure 3.2). Regardless, heterogeneity could be an important consideration for future studies such as testing different regions of geometrically complex components.

Unparameterized sources of error within the model include uncertainty in the provided single crystal elastic constants, measurement uncertainty of the specimen dimensions (including imperfectly parallel parallelepiped specimen faces), inelastic effects on the resonance spectrum (i.e. porosity), and assumptions in the texture forward model such as isotropic two-point statistics [95]. For example, grain morphology was recently quantified as significantly affecting estimates of the elastic constants [133], meriting a more detailed treatment in future forward models. Tane et al. demonstrated a $\sim$2% increase in C_{11} and corresponding $\sim$2% decrease in C_{12} and C_{44} for single-crystal copper if a grain shape aspect ratio $\geq$5 was neglected in the model [66]. The isotropic two-point statistics used in the model do not reduce the impact of this study, as the ability of the model to predict unknown textures (with unknown two-point grain statistics) is shown. Inelastic inclusions such as porosity and pore geometry have been proven to have a negligible effect on the ultrasonic velocity compared to the texture, so long as large amounts of interconnected porosity (>90% dense) are avoided by suitable choice of hatch spacing [134]. Overall error is accounted for by the lumped σ (kHz) term of the `SMCPy` RUS inversion, effectively representing a goodness of fit between the measured and calculated resonant frequencies. Regardless, any of these errors affect the magnitude of the σ term without indication of their origin, reinforcing the importance of parameterizing significant

effects on the frequencies whenever possible. For example, if residual stresses causing a global shift in frequencies were not accounted for in the model, a significantly increased σ magnitude would be observed (as demonstrated in Table 3.9). Similarly, if each resonant frequency was not equally shifted by the residual stresses (as assumed in the model), the calculated RS term in the model would not be sufficient to eliminate the effects of residual stresses on the fit of the frequencies, increasing the magnitude of the σ term. Given a single mode of specimen R4 deviated from the global residual stress-induced-shift, further testing of other residual stress and texture combinations will be necessary to isolate the effect and confirm the use of a global shift for the model.

The quantification of texture in the inversion framework relies on the dependence of the elastic constants of the specimen (and therefore the resonant frequencies) to changes in the texture. Consequently, if the constituent material's single crystal elastic constants are less anisotropic, the overall sensitivity of the aggregate (polycrystal) elastic constants to changes in the texture will be reduced. This is a common problem for inferring texture from the aggregate elastic constants [74]. The inversion method here captures the sensitivity of the resonant frequencies to the texture through the single-crystal elastic constants of the given material, but the sensitivity of each aggregate elastic constant to changes in the single crystal elastic constants is not explicitly quantified here. The effect of texture on the elastic properties is primarily of interest for materials with large changes in properties for small changes in texture, precluding the issue in practice. Regardless, materials with less significant single crystal anisotropies may result in a reduced sensitivity (increased uncertainty during the inversion calculation) to the detection of texture components. The error metrics generated according to Section 3.3.4 would reflect the increased errors. The SB-CoNi-10C alloy used here is very anisotropic, described by a Zener anisotropy ratio of $\frac{2*C_{44}^{SC}}{C_{11}^{SC}-C_{12}^{SC}} = 3.13$ [125, 135]. This study therefore has not devel-

oped quantitative metrics for determining the sensitivity of resonant frequencies to each individual texture coefficient. Further work will be needed to quantify the sensitivity of the resonant frequencies to each texture coefficient, perhaps by implementing a HMC (rather than MCMC) kernel and its associated derivatives [68] into the `SMCPy` package.

Regarding the origin of the residual stress shifts, variations in the single crystal during stress-relief are of interest. Given that there was no recrystallization, precipitation of second phases, or appreciable shape change in the SB-CoNi-10C specimens studied here, second phase fractions and aggregate elastic changes can be ignored. Holding the calculated texture of specimen R2 constant at the values in Table 3.7, simulations indicate the single crystal elastic constants must concurrently increase by C_{11}^{SC} - 5.4 GPa, C_{12}^{SC} - 2.4 GPa, and C_{44}^{SC} - 5.0 GPa to account for the observed increase in the resonant frequencies after stress-relief heat treatment. This validates the use of the RS term, though the interdependence of the single crystal constants with the texture coefficients could be further studied with `SMCPy` in future work.

3.6 Conclusions

- Interrogating arbitrarily textured microstructures is critical to characterize additively manufactured components. A novel resonant ultrasound spectroscopy (RUS) inversion framework is developed to quantify the texture coefficients, and convergently determine the bulk elastic constants, through the resonant frequencies of arbitrarily textured parallelepipeds with cubic microsymmetry. The single crystal elastic constants must be known to calculate the texture from polycrystalline resonant frequencies.

- The sequential Monte Carlo in Python (`SMCPy`) package enables Bayesian inference of both the texture (ODF) coefficients and the full elastic tensor by parallelizing

the intensive forward model. The computation time has been reduced from 14-20 days to 24-48 hours for a 8-core machine.

- SB-CoNi-10C specimens, printed by laser powder bed fusion, are scanned by RUS and analyzed within the RUS inversion framework. The calculated texture results for both the 0°-inclined to the build direction (specimen R4) and 22.3°-inclined to the build direction (specimen R2) specimens show quantitative agreement with the textures determined by EBSD. Further, the texture coefficients are used to quantify all 21 self-consistent elastic constants to a bounded accuracy of at most ± 1% between the Hashin-Shtrikman bounds. This bound is tighter than the computational error resulting from the Monte Carlo simulation itself. Direct parameterization of the texture enables robust convergence and high fidelity calculations of each elastic constant compared to existing techniques that directly calculate the elastic constants.

- Residual stresses are demonstrated to cause global decreases of 1.66% and 1.38% across all the resonant frequencies for specimen R2 and R4, respectively. A stress-relief heat treatment of 1100° C for 2 h was utilized to determine the resonant frequencies without the presence of residual stresses. Incorporation of a residual stress term as an independent model parameter in the Bayesian inference enables the determination of the residual stress-induced frequency shifts directly from the as-built specimen frequencies. Determining residual stress-induced frequency shifts without a stress-relief heat treatment is a novel implementation of RUS inversion.

Chapter 4
Single Crystal Elastic Constants Determined from Polycrystalline AM Components with RUS

Bayesian inference with Sequential Monte Carlo was used to determine the single crystal elastic constants of additively manufactured (AM) cobalt-nickel-based superalloy specimens from only the resonant frequencies and texture data. This novel framework enables the quantification of the single crystal elastic constants for AM and polycrystalline specimens using only electron backscatter diffraction (EBSD) and Resonant Ultrasound Spectroscopy (RUS), avoiding the expense of bulk single crystal fabrication or synchrotron experiments. A parallelizable and open-source Python package (SMCPy) was used to perform Bayesian inference of the single crystal elastic constants from resonant frequencies of AM specimens. The single crystal elastic constants determined from AM cobalt-nickel-base superalloy specimens were validated with measurements of the single crystal elastic constants on a bulk single crystal specimen. EBSD texture data was used to determine the single crystal elastic constants from the resonant frequencies of AM specimens, and validated with neutron diffraction data by considering the experimental uncertainty in both the EBSD and neutron diffraction data. The robustness of this framework for varied texture orientations relative to the build direction (BD) was demonstrated for AM specimens printed at 0° and 20° BD-inclinations.

4.1 Motivation

Single crystal elastic constants govern the fundamental mechanical response of single crystalline and polycrystalline materials, and are necessary to inform crystal-scale property calculations. Considering the microstructural variability within additively manufac-

tured (AM) components due to variations in process parameters, component geometry, and build conditions [17, 24]; accurate knowledge of the single crystal elastic constants is critical for building inspection protocols and constitutive models.

Traditional measurements of single crystal elastic properties involve the fabrication of a bulk single crystal and subsequent mechanical [136, 137] or ultrasonic [40, 103, 138] testing. However, single crystal growth is extremely difficult. Given the high thermal gradients and large solidification interface velocities [30, 139] involved in AM, designing an alloy to control the columnar to equiaxed transition further increases the difficulty to grow a single crystal. Even for alloys amenable to single crystal fabrication, the production of single crystals requires specialized equipment and is expensive/ time-consuming. Consequently, methods such as time-of-flight neutron diffraction [140, 141, 142] and mechanical loading with in-situ high energy x-ray measurements [65, 143, 144] have been proposed to evaluate single crystal elastic constants from polycrystalline specimens. However, these approaches involve high cost synchrotron-based methods and access to these facilities.

It is critical to develop methods capable of quantifying the single crystalline elastic properties from polycrystalline components using rapid and cost-effective measurement techniques available in the laboratory. Of particular interest is the determination of single crystal properties from polycrystalline elastic properties [66, 145]. The determination of single crystal properties from the polycrystal elastic properties involves an inverse problem, where homogenizations (e.g. Voigt/ Reuss averaging [145]) are iteratively calculated for a known microstructure. The single crystal elastic constants are varied until the calculated polycrystalline elastic constants fit the measured polycrystalline elastic constants. The precision of the calculated single crystal constants can be increased through utilizing self-consistent estimates [65, 66], supplementing the elasticity with indentation

data [146], and using Bayesian inference/ machine learning techniques [65, 131].

Looking toward non-destructive evaluation techniques, recent developments on surface acoustic wave (SAW) measurements [147] demonstrate that the single crystal elastic constants can be accurately resolved from ultrasound measurements of polycrystals. However, SAW measurements primarily probe the near-surface region of a volume, and therefore are subject to AM factors such as heterogeneous residual stresses and grain orientations that would alter the calculated result. Additionally, the inverse determination of the single crystal elastic constants from SAW measurements lacks the robust convergence and uncertainties provided by Bayesian inference. Measurements of bulk elasticity from techniques such as Resonant Ultrasound Spectroscopy (RUS) have shown promise for characterization of the single crystal constants when combined with texture data from electron backscatter diffraction (EBSD) and X-ray diffraction (XRD) [66]. Existing RUS approaches lack the uncertainty quantification yielded by Bayesian inference approaches [65, 68] and contain symmetry assumptions on the bulk elastic constants within the model. Additionally, RUS-determined aggregate elastic constants are often utilized without incorporating resonant frequency measurement error [66]. Therefore, Bayesian approaches to quantify the single crystal elastic constants need to be tied to the resonant frequencies within a larger forward model, without incorporating symmetry assumptions.

This work proposes a Bayesian inference model to determine the single crystal elastic constants of arbitrarily printed AM components, utilizing only the resonant frequencies and texture data. A novel cobalt-nickel-based superalloy, SB-CoNi-10, is selected as a model material to develop the proposed framework. High-performance alloys such as SB-CoNi-10 are currently being investigated for processing by additive manufacturing due to their excellent high temperature mechanical properties [116]. SB-CoNi-10 possesses solidification properties amenable to the production of crack-free specimens using laser powder

bed fusion (LPBF), in spite of a high volume fraction of γ' after heat treatment [121]. Additionally, this novel alloy forms an alumina scale under high temperature exposure to air, has a mass density similar to 2nd-generation Ni-base single crystal superalloys [120], and demonstrates low sensitivity to AM process parameter variation [121, 122]. The SB-CoNi-10 powder used in this study was produced with a higher carbon content than previous iterations [121], and is denoted SB-CoNi-10C for distinction.

The purpose of this chapter is: 1. The creation of a model to determine the single crystal elastic constants of an additively manufactured, or any textured polycrystalline, parallelepiped specimen from only the resonant frequencies. 2. Determination of the single crystal elastic constants of a novel cobalt-nickel-based superalloy (SB-CoNi-10C) from an AM specimen, validated against bulk single crystal measurements. Single crystal elastic constants were validated for AM specimens printed at both 0° and 20° inclinations to the build direction. 3. The single crystal elastic constants were determined with EBSD texture data and validated against neutron diffraction texture measurements by considering measurement error in each technique. 4. Robust uncertainty estimates and reductions in computational cost by an order of magnitude were achieved through the use of parallelized Sequential Monte Carlo (SMC) to solve the inverse problem.

4.2 Materials and methods

SB-CoNi-10C specimens were printed on an Aconity3D AconityMINI[1] system at the University of California Santa Barbara. The powder had a size distribution of 15-53 µm and was provided by Carpenter Technology[2]. The composition of the powder is given in Table 3.1.

[1]Specific vendor and manufacturer names are explicitly mentioned only to accurately describe the test hardware. The use of vendor and manufacturer names does not imply an endorsement by the U.S. Government nor does it imply that the specified equipment is the best available.

[2]Carpenter Technology, 1735 Market Street, 15th Floor, Philadelphia, PA 19103 USA

Rectangular AM specimens were printed with nominal dimensions of 10 mm x 10 mm x 13 mm for the x, y, and z (build direction) axes, respectively. The scan strategy was bi-directional with a 90° rotation between build layers. The build plate was preheated to 200°C, the beam diameter was 80 μm, and the layer thickness was set to 30 μm. Specimens selected for RUS were sectioned by electrical discharge machining (EDM) at nominal 0° and 20° inclinations from the build direction for specimens R4 and R2, respectively. EDM was used to remove 1 mm of depth from each surface, removing surface-induced alterations in the microstructure. The final rectangular parallelepiped geometries were 8.672 ± 0.007 mm x 8.215 ± 0.005 mm x 6.914 ± 0.005 mm (R2), and 10.355 ± 0.010 mm x 8.883 ± 0.0088 mm x 8.370 ± 0.014 mm (R4). The dimensional measurement uncertainty incorporates the non-planarity of the specimen faces. Specimen densities were 8591.4 kg/m^3 (R2) and 8593.9 kg/m^3 (R4) assuming no porosity, in agreement with the Archimedes measurement of density (8650 kg/m^3) from an arc-melted specimen of SB-CoNi-10 [120]. Parallelepiped specimen preparation for RUS was completed in the as-built state, with stress relief heat treatments performed after removal from the build plate.

A stress-relieving heat treatment of 1100°C for 2h was performed in an open air furnace, and each specimen was air cooled prior to gathering RUS measurements. The stress-relief heat treatment was performed at 100°C ± 5°C below the solvus temperature of the γ' precipitates. The stress-relief heat treatment did not result in any detectable recrystallization (by EBSD) of the as-printed grain structure. SB-CoNi-10 has been grown via the Bridgman technique as a bulk single crystal in [125], with single crystal elastic constants quantified as $C_{11}^{SC} = 236.4 \pm 1.0$ GPa, $C_{12}^{SC} = 150.8 \pm 0.8$ GPa, $C_{44}^{SC} = 134.1 \pm 0.1$ GPa at 23°C. These constants were determined using RUS in a Bayesian inference framework [68], and will be used as ground-truth data throughout this work.

4.2.1 Electron Backscatter Diffraction

EBSD data was gathered across a nominal 4 mm x 8 mm area of each of the specimen faces. To reduce distortion, individual 2 mm x 3 mm scans were performed and then aggregated using the MATLAB toolbox, MTEX [123, 127]. A FEI Versa 3D Dualbeam microscope with an EDAX OIM-Hikary XM4 detector was used for all EBSD scans. All EBSD data was gathered using an accelerating voltage of 30 kV and current of 6.4 nA. Raw EBSD pattern images were collected for indexing with the EMSphInxEBSD package developed by Lenthe et al. [148]. Points below a confidence index of 0.18 (<10% of the datapoints) were removed prior to orientation distribution function (ODF) generation in MTEX. The EMSphInxEBSD-indexed scans are shown in Figure 4.1.

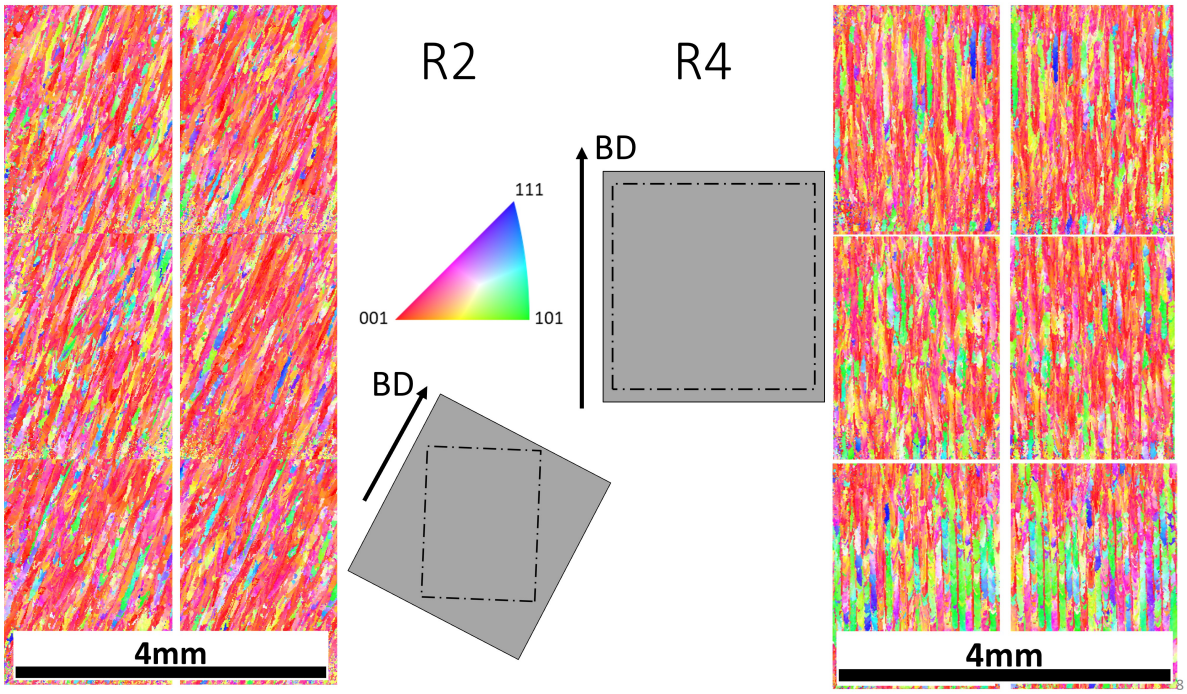

Figure 4.1: Electron backscatter diffraction data from the SB-CoNi-10C specimens. Inverse pole figure coloration is referenced relative to the build direction for each set of images. EBSD pattern indexing was completed using the EMSphInxEBSD package [148]. The build direction aligned specimen (right) contained an increased density of (101) oriented grains (green) in the first 1.5 mm of the build height due to epitaxial growth off the build plate. Orientation data was aggregated to generate each ODF, minimizing the impact of the observed heterogeneity as a source of error.

4.2.2 Neutron diffraction

Neutron diffraction measurements were carried out at Los Alamos National Laboratory with the High-Pressure Preferred Orientation (HIPPO) diffractometer [149]. A diagram of the neutron diffractometer is shown in Figure 4.2.

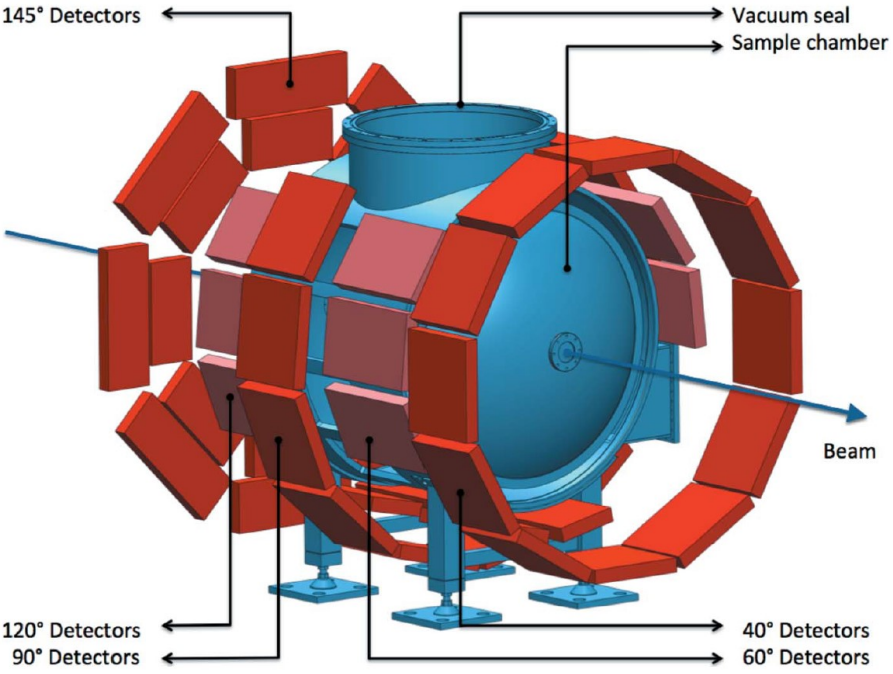

Figure 4.2: Schematic of the HIPPO diffractometer at Los Alamos National Laboratory. Sample chamber (blue) surrounded by detector rings (red). Reprinted from [149] with permission of author.

The Rietveld refinement software, Material Analysis using Diffraction (MAUD) [150], was used to analyze the neutron diffraction data following the procedure of Saville et al [151]. In brief, the software fits a diffraction spectra to the measured spectra via iterative minimization of least squared error. Each SB-CoNi-10C specimen had neutron diffraction measurements carried out on the bulk scale. Consistent with [151], the "R"-values intrinsic to the refinement process were examined after each successive refinement to determine the data fit. In general, lower R-values indicate better peak fits. There is a distinction between the calculation of the weighted (R_{wp}) and expected (R_{exp}) R-values

within the software, with R_{wp} given as the reference R-values here. The calculation of $R = R_{wp}$ is given in Equation 4.1 [151]. $y_{obs,i}$ represents the intensity of a given datapoint i as measured by the detector, while $y_{calc,i}$ represents the calculated intesity of that datapoint. The err term represents the measurement uncertainty for the associated intensity value $y_{obs,i}$, and w_i encapsulates the weight.

$$\begin{aligned} R = R_{wp} &= \sqrt{\frac{\sum_i w_i (y_{calc,i} - y_{obs,i})^2}{\sum_i w_i (y_{obs,i})^2}} \\ w_i &= \frac{1}{err^2(y_{obs,i})} \end{aligned} \tag{4.1}$$

After four refinements, specimen R2 had an R-value of 9.0% and specimen R4 had an R-value of 6.8%. A lattice spacing of 3.54 Å was determined from these refinements. Further refinements with altered lattice constants, background parameters, and fitting parameters did not result in better convergence, and resulted in artificially sharpened textures. An alternate refinement (referred to as non-convergent) of specimen R4 with artificially sharpened texture, resulting in $R = 13.2\%$, was utilized to demonstrate the effect of neutron data processing on the results.

4.2.3 Orientation distribution functions

For the EBSD data, both a Dirichlet kernel and an 'optimally-calculated' kernel were tested to generate the ODF in MTEX. A single ODF was generated from the aggregated EBSD data of each specimen. The 4th order texture coefficients generated with each kernel were not distinct to one another, in contrast with prior use of the Dirichlet kernel (on smaller datasets) in Chapter 3. As a result, the 'optimally-calculated' kernel was calculated by MTEX as the 'deLaValleePoussin' kernel (halfwidth 2.4°), and used for ODF generation.

For the neutron diffraction data, the ODF was derived from the calculated texture of

the final Rietveld refinement using the vector-based extended-Williams, Imhof, Matthies, and Vinel algorithm [151]. The data was exported in beartex format with 5° resolution. The pole figures were imported into MTEX for plotting.

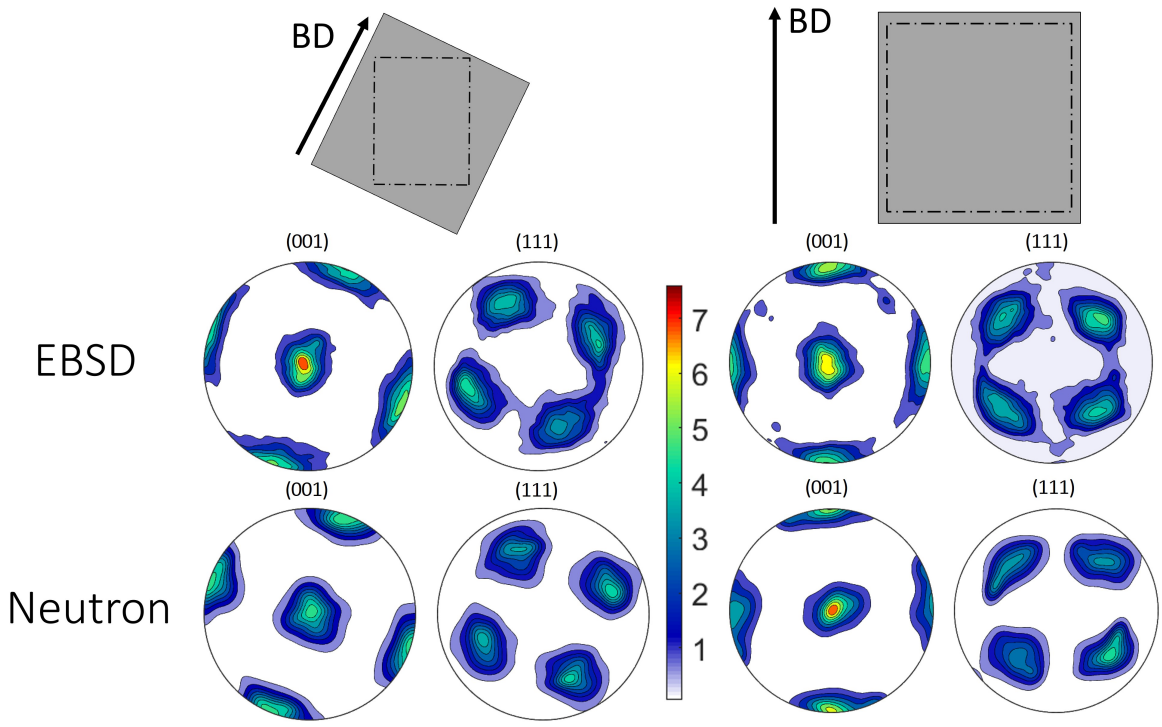

Figure 4.3: (001) and (111) pole figures plotted in MTEX from calculated ODFs. Pole figures calculated from both EBSD and neutron diffraction data agreed across all orientations for both specimens. (101) pole figures also showed agreement, but are not shown given a maximum value of 1.5 multiples of random distribution (MRD). For specimen R2 (left), the neutron data had a lower MRD at the centerpoint of the (001) pole figure relative to the EBSD, though all other intensities are similar. All pole figures are scaled to the same colorbar.

The ODF calculated pole figures for both the EBSD and neutron diffraction data are given in Figure 4.3. The orientation distribution function coefficients from each set of pole figures were generated in MTEX and truncated at 4th order. These texture coefficients were used to inform calculations of the single crystal constants for each texture measurement technique.

4.2.4 Resonant ultrasound spectroscopy measurements

The experimental RUS measurements of SB-CoNi-10C specimens R2 and R4 are described in Chapter 3. Resonant frequencies in the stress relieved specimen state were used. The specimen rested on piezoelectric transducers without externally induced forces. Sampling step sizes of 3 Hz and dwell times of 1 ms were used. The piezoelectric transducers, transceiver, and computer control were provided by Vibrant Corporation[3].

Each specimen was scanned by RUS three to five times, with each frequency averaged across all scans. The specimen position was reset in the cradle after each test, avoiding potential missed modes due to zero displacement points on the specimen surface. The first 45 modes were utilized for RUS inversions.

4.3 Computation

4.3.1 Forward model

The forward model is demonstrated in Figure 4.4.

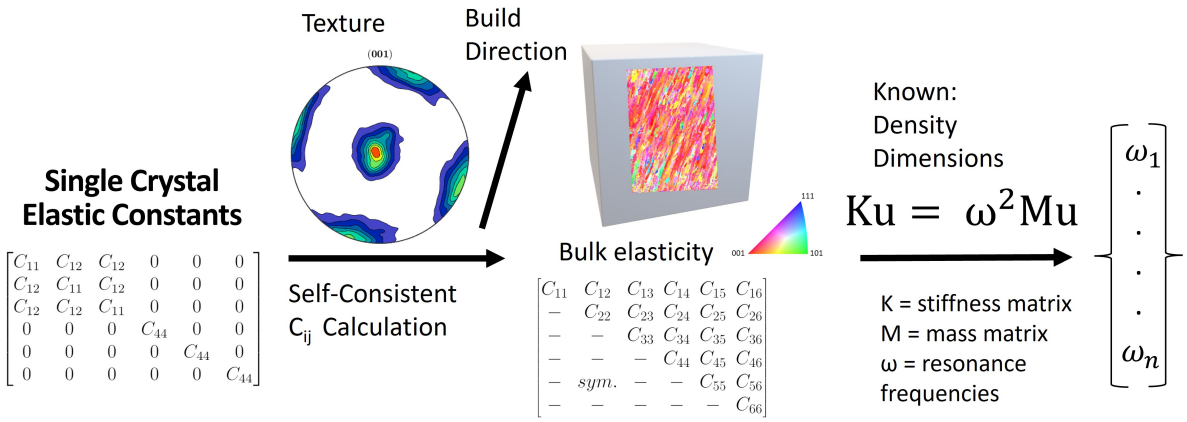

Figure 4.4: Forward model depicting the single crystal elastic constants to be determined (left), the self-consistent calculation (with texture of the AM test block known) of the aggregate elastic constants, and the final calculation of the resonant frequencies (right). The EBSD data overlaid on the block is not to scale.

[3]Vibrant Corporation, 8916 Adams St NE, Albuquerque, NM 87113

Following Section 2.1.3, the effect of texture on the aggregate elastic constants was represented by the ODF $f(Q)$ is defined to represent the relative amount of grains with orientation Q over $Q \in SO(3)$. $SO(3)$ denotes the standard special orthogonal group of $\mathbb{R}^3$. The ODF is given in terms of the tensorial texture coefficients $V_{\langle\alpha\rangle\beta}$, the basis tensors $F_{\langle\alpha\rangle\beta}$ fixed by the microscopic symmetry, and the tensor order α (as given in [95]).

$$f(Q) = \sum_{\alpha=0}^{4} \sum_{\beta=1}^{n_\alpha^H} (1+2\alpha) V_{\langle\alpha\rangle\beta} \cdot F_{\langle\alpha\rangle\beta}(Q) \tag{4.2}$$

β is the index of each independent basis tensor, omitted in further representations given n_α^H=1 for materials with cubic single crystal symmetry. The 4th-order ODF coefficients (α=4) fully define the effect of preferential grain orientations on the aggregate elastic tensor for cubic materials. The self-consistent elastic constants (specimen reference frame) [91], assuming isotropic grain shapes, are generated at each iteration of the forward model using the single crystal elastic constants and a tensorial representation of the 4th order ODF coefficients [95]. The self-consistent elastic constant calculation considers arbitrary (triclinic) anisotropy on the macroscopic scale with nine independent 4th-order texture components of $V_{\langle 4\rangle pqrs}$. Equation 4.3 details the construction of the self-consistent elastic constants with isotropic grain-shapes ($C^{self,iso}$) in terms of the zeroth-order reference elastic tensor $C_0^{self,iso}$, the inverse of the isotropic polarization tensor P_0 (calculated with $C_0^{self,iso}$), and the inverse of the orientation average $\langle f, L\rangle$. The reference tensor L is defined in place of the traditional single crystal elastic constants C^{SC} in the orientation average, as the self-consistent solution here is defined consistent with the Hashin-Shtrikman-type bounds in [95]. L inherits the cubic symmetry of C^{SC}, as it is calculated as the linear combination of the single crystal elastic constants C^{SC}, the zeroth-order reference stiffness $C_0^{self,iso}$, and the polarization tensor P_0. As a result of the assumption of isotropic grain shape statistics in [95], the self-consistent solution

is fully defined by the same texture coefficients used to generate the Hashin-Shtrikman upper/lower bounds and the Voigt/Reuss bounds. The polarization tensor also assumes isotropic grain statistics, allowing the polarization to be analytically determined with the calculated reference stiffness $C_0^{self,iso}$. The constants h_{I1}, h_{I2} , and $H_{\langle 4\rangle 1}$ are determined by the harmonic decomposition (hd) of L, with P_1 and P_2 as isotropic projectors, consistent with [95].

$$\begin{aligned} C^{self,iso} &= C_0^{self,iso} - [P_0(C_0^{self,iso})]^{-1} + [\langle f, L\rangle]^{-1} \\ L &= [C^{SC} - C_0^{self,iso} + [P_0(C_0^{self,iso})]^{-1}]^{-1} \\ hd(L) &\rightarrow h_{I1}, h_{I2}, H_4 \\ \langle f, L\rangle &= h_{I1}P_1 + h_{I2}P_2 + H_4 V_{\langle 4\rangle pqrs} \end{aligned} \tag{4.3}$$

Under the assumption of spherical grain shapes (semi-axes parameters $a_1 = a_2 = a_3 = 1$), the polarization tensor for ellipsoidal inclusions is determined analytically [95]. The inclusion of a non-isotropic polarization tensor ($a_1 \neq a_2 \neq a_3$) is technically admissible within this framework by numerical integration of P_0 for ellipsoidal inclusions [152], but invalidates the derivation of the texture coefficients [95] where the first and second order bounds are described by the same set of texture coefficients. Additionally, the non-isotropic calculation of P_0 still requires the reference stiffness ($C_0^{self,iso}$/ C_0) to be defined, meaning an assumption of the stiffness of the medium would still be necessary to determine the polycrystalline stiffness and the resonant frequencies. Because the reference stiffness is calculated from the independently determined single crystal constants, there is a relationship between these parameters that is not well studied relevantly to inverse solving with this model [97]. Consequently, the analytical determination of isotropic P_0 is used, as given in Equation 4.4. P_1 and P_2 are same isotropic projectors as in Equation 4.3, c_1 and c_2 are constants, and λ_1 and λ_2 are the eigenvalues of the isotropic stiffness

tensor C_0.

$$\begin{aligned} P_0 &= c_1 * P_1 + c_2 * P_2 \\ c_1 &= \frac{1}{\lambda_1 + 2\lambda_2}, c_2 = \frac{2}{5\lambda_2} * \frac{\lambda_1 + 3\lambda_2}{\lambda_1 + 2\lambda_2} \end{aligned} \tag{4.4}$$

The zeroth-order elastic tensor ($C_0^{self,iso}$) is determined analytically by generating the self-consistent elastic solution (Equation 4.3) where the reference stiffness of the medium C_0 is identical to its self consistent solution, i.e. an untextured aggregate of spherical (isotropic) grains with single crystal elasticity C^{SC}. Isotropic projectors (P_1 and P_2) are again utilized to generate the isotropic reference stiffness of the medium ($C_0^{self,iso}$) by supplying the single-crystal elastic tensor C^{SC} as detailed in Equation 4.5 [95, 98]. The zero-order bounds therefore do not contain grain shape or orientation information, and are used in Equation 4.3.

$$\begin{aligned} C_0^{self,iso} &= C_0 - [P_0(C_0)]^{-1} + \langle f^{iso}, L \rangle^{-1} \\ L &= [C^{SC} - C_0 + [P_0(C_0)]^{-1}]^{-1} \\ C_0 &= C_0^{self,iso} \end{aligned} \tag{4.5}$$

The calculation of resonant frequencies from elastic constants as a generalized eigenvalue problem (calculated with the elastic constants $C_{ij} = C^{self,iso}$), is identical to its representation in Chapters 2 and 3. All inversions used a polynomial order of 12 and 45 resonant modes for the frequency forward model. All of the resonant frequencies were measured on specimens in the stress-relieved state, so the calculation of the resonant frequencies (from the elastic constants) was not subject to effects of the residual stress state on the frequencies [124].

4.3.2 Bayesian inference with sequential Monte Carlo

Bayes' Theorem provides a mechanism to update prior knowledge of the RUS model parameters with new resonant frequency observations. The updated knowledge is the solution of the inverse problem and is represented by the posterior probability density function,

$$\pi(\Theta|\omega_n) = \frac{\pi(\omega_n|\Theta)\pi(\Theta)}{\int_\Omega \pi(\omega_n|\Theta)\pi(\Theta)d\Theta} \tag{4.6}$$

where $\Theta = [C_{11}^{SC}, C_{44}^{SC}, A]$ is the vector of the three independent parameters: two single crystal elastic constants (C_{11}^{SC}, C_{44}^{SC}) and the Zener anisotropy ratio ($A = 2C_{44}^{SC}/(C_{11}^{SC} - C_{12}^{SC})$) [135]. Note that sampling the Zener anisotropy ratio A is equivalent to sampling the single crystal elastic constant C_{12}^{SC}, with advantageous numerical sampling dependencies between parameters [68, 69]. Therefore, all three independent elastic constants for cubic materials are sampled.

Following Chapter 3, the numerator of the right hand side of Equation 4.6 comprises the likelihood function $\pi(\omega_n|\Theta)$ (which represents the likelihood of observing the measured resonant frequencies given Θ) and the prior $\pi(\Theta)$ (which represents prior knowledge of the single crystal elastic constants). The denominator is the marginal likelihood and involves integration over the entire parameter support, $\Omega = \{\Theta \in \mathbb{R}^3\}$. By assuming that the measurement errors are independently and identically distributed as zero-mean Gaussian distributions with variance σ^2, a closed form expression is obtained for the likelihood as given in Chapter 3. An open-source Python implementation of sequential Monte Carlo, `SMCPy`[4], was used to estimate the posterior distribution of single crystal constants. `SMCPy` is based on the algorithm presented in [100]. The parallel particle evaluations in `SMCPy` are vectorized using `numpy` to achieve single-core speedup, but `SMCPy` is also Message Passing Interface (MPI)-enabled to allow parallel computation on distributed

[4]SMCPy Python package available open-source at https://github.com/nasa/SMCPy.

memory systems.

The following hyperparameters and definitions are maintained throughout all subsequently presented RUS inversions. Hyperparameter tuning was not in the scope of this work. The tuning parameters were selected to ensure samples were generated from the full posterior (i.e. all modes represented) while balancing sample size with computation time. For all model parameters (Θ), improper uniform priors were chosen; i.e., $\Theta_i \sim \text{Uniform}(0, +\text{inf})$ for $i = 1, \ldots, 3$. The initial values of the model parameters for the particles, referred to as the initial particle population, were sampled from a multivariate normal distribution with each parameter mean informed from independent normal distributions. The informed parameter means $\pm$ standard deviation were $C_{11}^{SC} = 236.4 \pm 30.0$ GPa, $C_{44}^{SC} = 134.1 \pm 15.0$ GPa, and $A = 3.3 \pm 0.3$ (i.e $C_{12}^{SC} = 150.8 \pm 20.0$ GPa) corresponding to the means determined in [125] for a grown (bulk) single crystal of SB-Co-Ni-10. Uniform distributions with means $\pm$ 100 GPa were also tested, and resulted in identical final parameter estimates at higher computational cost.

Independent and identically distributed, zero-mean Gaussian errors were assumed for the measured ω_n values such that Equation 2.41 applies. In all SMC simulations, 1500 particles were migrated through a series of target distributions that started at the prior and ended at the posterior distribution. An adaptive algorithm was used that controlled the step size between target distributions using an effective sample size (ESS) threshold of 85%. To avoid particle degeneracy, an MCMC kernel was used at each step to move particles toward the new target distribution. Each step size was chosen such that the ESS of the updated particle population was equal to this value until the final target distribution (i.e. the posterior) was reached. These parameters typically resulted in $20 - 35$ target distributions (including prior and posterior) for each simulation. Each pass through the kernel involved the construction of Markov chains of length 14, retaining

the 14th for the next iteration. These choices resulted in computation times of 14-24 hrs utilizing 10 CPU cores. This is a vast improvement over previous Bayesian inference work with RUS [68], where serial computations resulted in 14-20 day computation times.

4.4 Results

SMC-calculated single crystal elastic constants					
	Ref. Crystal [68]	R4 Neutron	R2 Neutron	R4 EBSD	R2 EBSD
C_{11} (GPa)	236.4 ± 2.0	235.7 ± 4.8	236.3 ± 8.0	238.7 ± 6.2	239.4 ± 7.4
A	3.13 ± 0.01	3.76 ± 0.12	3.33 ± 0.10	3.24 ± 0.14	2.63 ± 0.10
C_{12}^{calc} (GPa)	150.8 ± 1.6	159 ± 5.2	153.8 ± 8.2	154.2 ± 6.8	143.4 ± 8.34
C_{44} (GPa)	134.1 ± 0.2	144.2 ± 2.0	137.3 ± 2.6	137.1 ± 2.5	126.3 ± 2.0
σ (kHz)	0.08 ± 0.02	1.09 ± 0.26	1.44 ± 0.32	1.59 ± 0.38	1.59 ± 0.36

Table 4.1: Single crystal elastic constants of 20°-inclined-to-BD (R2) and 0°-to-BD (R4) specimens, varying the input texture method. ± represents 2 standard deviations on each parameter, determined from the fit of the measured frequencies. In addition to the single crystal elastic constants C_{11}, C_{12}^{calc}, and C_{44}, the measurement error (σ) was sampled independently in SMC. C_{12}^{calc} is calculated through the Zener anisotropy ratio (A) as an independent parameter, C_{11}, and C_{44}. The first 45 resonant frequencies of each specimen (stress-relieved specimen state) were supplied to each calculation.

SMC simulations were run for both the 0°-inclined (R4) and 20°-inclined (R2) specimens to the build direction. Simulations were completed for each specimen with textures informed by either EBSD or neutron diffraction data, as given in Table 4.1. The same 45 resonant frequencies were used for each altered-texture simulation. The single crystal elastic constants obtained from the AM specimens agree with the bulk single crystal values within 2 standard deviations for both C_{11} and C_{12}, for both the EBSD and neutron diffraction informed simulations. The C_{44} values determined by both EBSD and neutron diffraction informed simulations deviated from the bulk single crystal C_{44} by $\leq$7.5%, and therefore were not within 2 standard deviations. Relative to the bulk single crystal values, the AM specimen derived constants have uncertainties on each parameter $\sim$3 times larger for C_{11} and C_{12}, and $\sim$10 times larger for C_{44}. Given the resonant frequencies of each AM specimen contain unparametrized errors such as grain heterogeneity effects

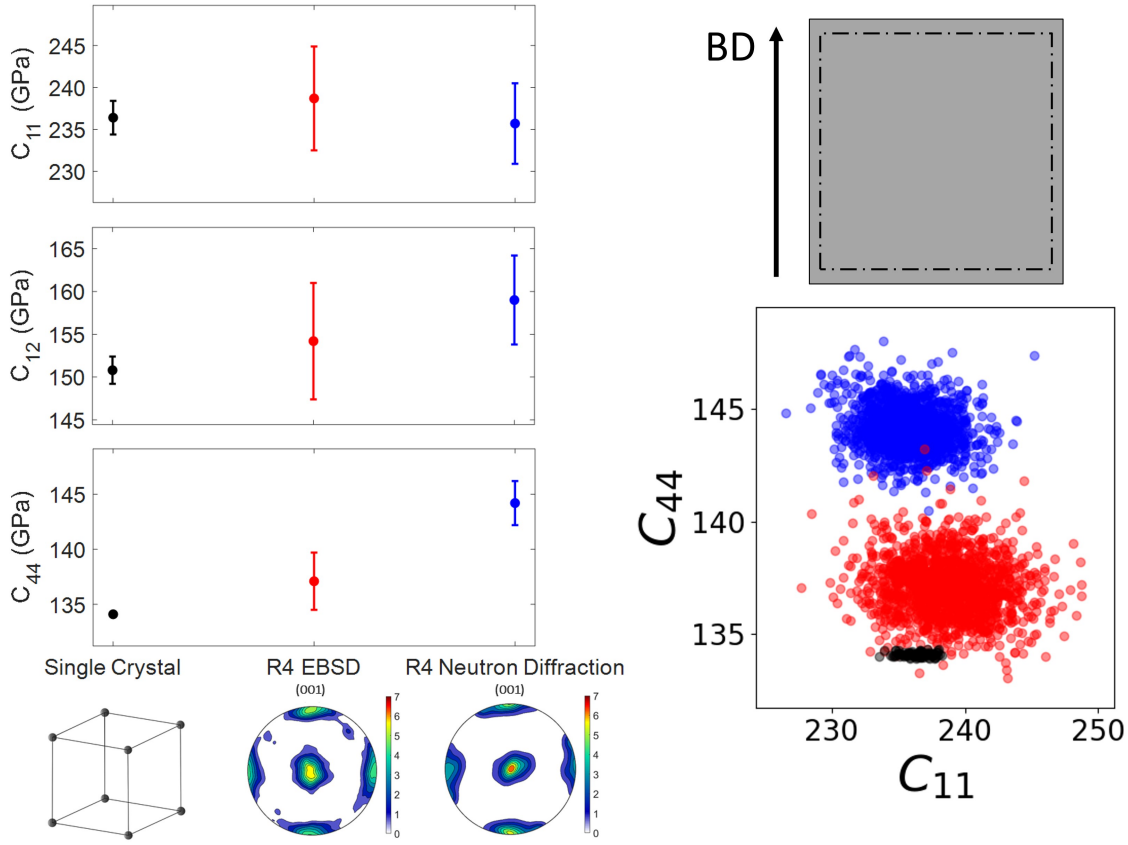

Figure 4.5: Single crystal elastic constants of SB-CoNi-10C specimen R4 (BD-aligned). Identical specimen frequencies informed the EBSD and neutron diffraction simulations, therefore the difference in the mean single crystal elastic constants determined by EBSD or neutron diffraction is a result of numerical differences in the texture inputs. Considering experimental error within each technique, both EBSD data or neutron diffraction data are suitable for use in these simulations. Parameter plots (right) between C_{44} and C_{11} are generated using the posterior distributions of each simulation.

[124] that are not accounted for in the model, increased uncertainty is expected.

Comparing EBSD-informed and neutron diffraction-informed simulations, the calculated values (for both specimens) lie within 2 standard deviations of one another for both the C_{11} and C_{12}, but not for C_{44}. The agreement between EBSD, neutron diffraction, and bulk single crystal data is compared in the parameter plots of Figure 4.5 for specimen R4 (build-direction aligned). The EBSD data fits the bulk single crystal elastic constants more closely than the neutron diffraction data, but a similar uncertainty on each param-

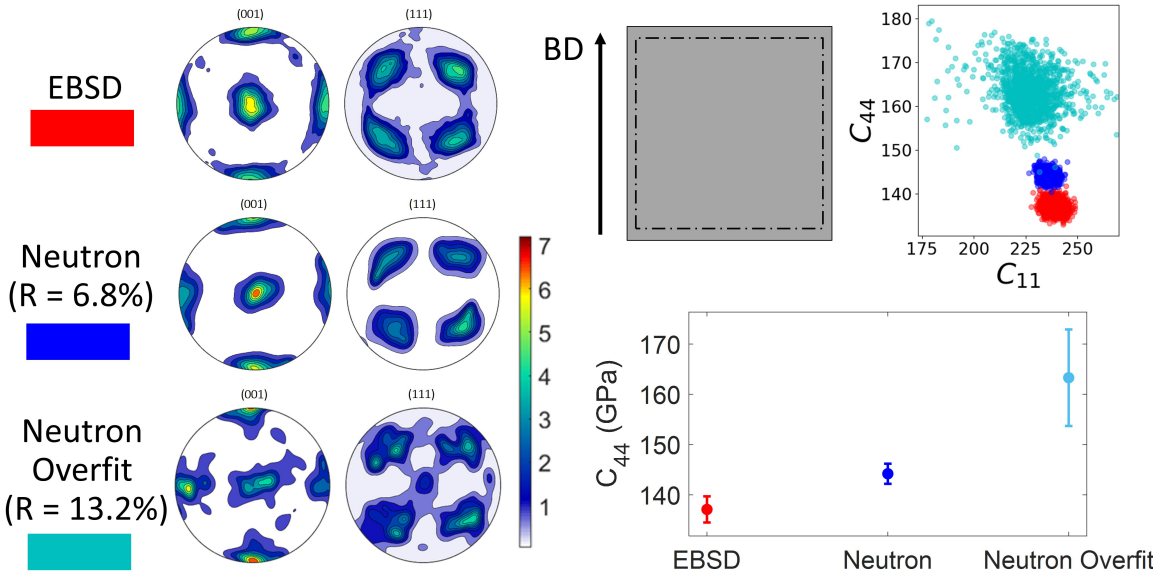

Figure 4.6: The difference in means between EBSD-informed or neutron data-informed simulations stem from numerical differences in the input texture. Small changes in the numerics of the texture, such as for a fit of the neutron data with $R = 13.2\%$, results in altered values of the single crystal constants. Therefore, either EBSD or neutron data is suitable for determination of the single crystal elastic constants. Identical neutron diffraction data was used when performing the 'overfitted' Rietveld refinement (light blue, $R = 13.2\%$) and convergent refinement (blue, $R = 6.8\%$).

eter for the simulations indicates that both simulations fit the data adequately. Identical specimen frequencies informed the EBSD and neutron diffraction simulations, therefore the difference in each mean value results solely from the numerical difference in texture inputs. The results of specimen R2 support this conclusion, as the neutron-informed simulations agree with the bulk single crystal values more closely than the EBSD-informed simulations, in contrast to the trend observed for specimen R4. Therefore, the texture data analysis and associated error (unaccounted for in the SMC model) affect the resultant mean single crystal elastic constants calculated, but do not preclude either technique as more accurate than the other. The quantity of texture data is not significant unless reduced to the point that the local texture heterogeneity results in the mean texture coefficients deviating from the bulk texture. An instructive example to demonstrate the effect of texture input can be observed by utilizing an alternate (higher data fit error)

Rietveld refinement of the same neutron diffraction dataset for specimen R4. The altered texture coefficients in the simulation result in biased predictions of the single crystal elastic constants. The bias for C_{44} is observed as a 13% increased mean value and a 5-fold increased uncertainty in Table 4.2 and Figure 4.6.

Single crystal elastic constants of BD-aligned specimen			
	EBSD	Neutron (R=6.8%)	Neutron (R=13.2%)
C_{11} (GPa)	238.7 ± 6.2	235.7 ± 4.8	241.0 ± 70.4
A	3.24 ± 0.14	3.76 ± 0.12	5.44 ± 0.88
C_{12}^{calc} (GPa)	154.2 ± 6.8	159.0 ± 5.2	180.7 ± 74.4
C_{44} (GPa)	137.1 ± 2.5	144.2 ± 2.0	163.3 ± 9.6
σ (kHz)	1.59 ± 0.38	1.09 ± 0.26	3.58 ± 0.82

Table 4.2: EBSD and neutron diffraction data produce comparable estimates of the single crystal elastic constants, considering that using 'overfitted' neutron data (Rietveld refinement $R = 13.2\%$) results in altered mean values and a factor of 5 increase in the uncertainty. The first 45 resonant frequencies of specimen R4 were identically supplied to each calculation, proving that the numerics of the texture fed to the model are controlling the differences in the single crystal means.

Compared to the ($R = 6.8\%$) refinement used to generate the results in Figure 4.5, this alternate refinement utilized additional polynomial background parameters [151] that result in an increased $R = 13.2\%$. This R value and refinement is within acceptable limits, but results in artificial sharpening of the pole figure and corresponding texture coefficients. The choice of EBSD kernel and indexing technique (Hough or EMSphInxEBSD) did not display nearly as strong of an effect on the texture coefficients generated with identical EBSD data, compared to the effect of the neutron diffraction refinement parameters. The resolution of the EBSD data did not display a strong effect on the final texture coefficients, given that the data is aggregated to generate the ODF. Note that the particles displayed in Figure 4.6 have equal weight.

With the effect of texture data in context, it is critical that the single crystal elastic constants are determinable regardless of the orientation of the build-direction-dependent microstructure. The single crystal elastic constants are determined for specimen R2

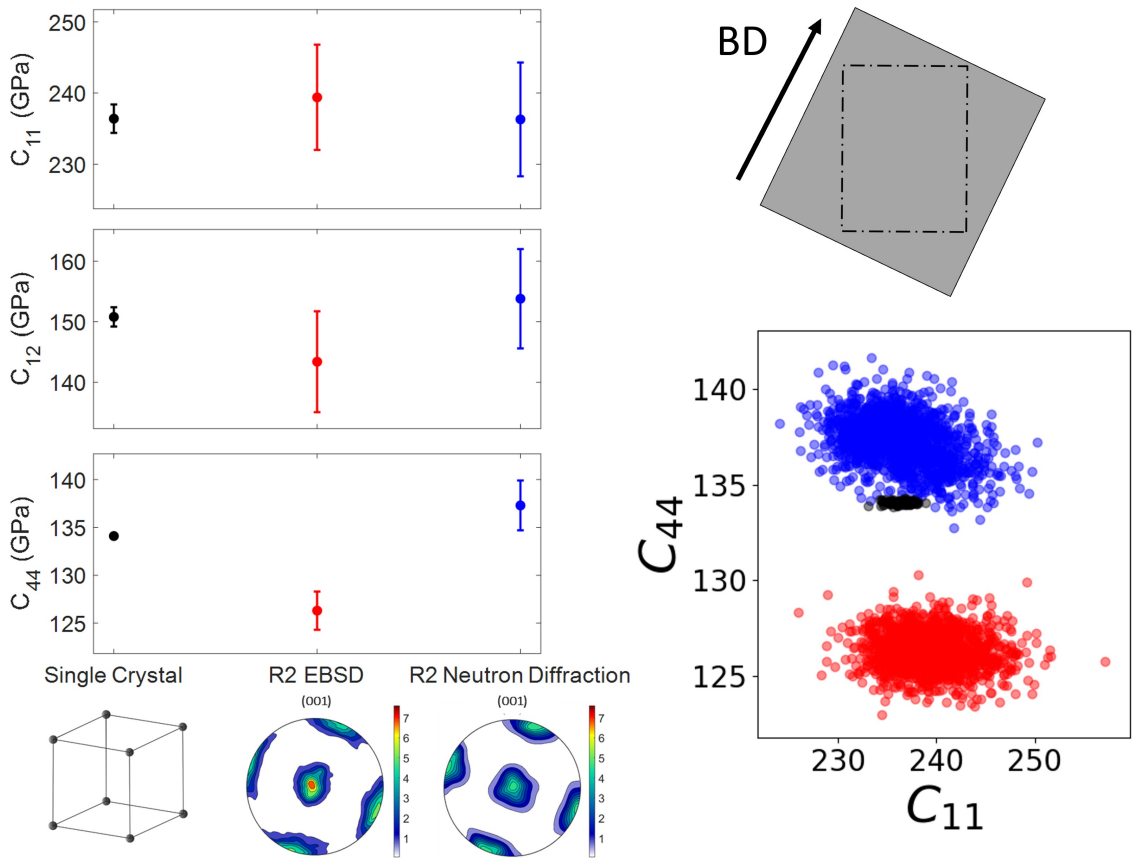

Figure 4.7: Single crystal elastic constants of specimen R2 (inclined 20° to build-direction) are determined to the same accuracy and precision as those of the build-direction aligned specimen (R4), proving the use of this framework for textures misaligned from the specimen. Bulk single crystal values (black) are provided from [125].

(20° inclined to build direction) to comparable precision as specimen R4, as shown in Figure 4.7. The simulations of specimen R2, using both neutron diffraction data and EBSD data, produce similar behavior as specimen R4 across all parameters; C_{11} and C_{12} are within 2 standard deviations of the bulk single crystal crystal values, while the C_{44} estimates deviate by $\leq$7.5%. The framework is therefore validated for use with misaligned specimens. Again, the specimen frequencies supplied to the EBSD and neutron diffraction simulations were identical, indicating that the difference in mean values were induced by the numerics of the supplied texture coefficients.

4.5 Discussion

This work demonstrates that the single crystal elastic constants can be directly quantified through NDE techniques on polycrystals, rather than growing a bulk single crystal. This work enables rapid and non-destructive screening of novel alloy systems for their single crystal elastic properties, though some care must be taken in interpreting the results. As shown in Figures 4.5 and 4.7, the distribution of parameters such as C_{44} do not lie within 2 standard deviations of one another. The difference in C_{44} values is primarily a result of the increased sensitivity of C_{44} (relative to C_{11}) to alterations in the resonant frequencies, which has been well documented [65, 69]. This effect can be observed in the pairwise parameter plots between C_{11}, C_{12}, and C_{44}, as the off-axis constant C_{12} and shear constant C_{44} are dependent on the same mode-types and correspondingly display a linear correlation, under a tighter range of C_{11}. The linear relation between C_{44} and C_{12} is displayed in the parameter plots of Figure 4.8 for both specimen R2 and R4, demonstrating that the sampling and distributions of the single crystal elasticity of each specimen do not change under a change in bulk elastic symmetry.

The standard deviation given for each parameter is directly calculated within SMC from the fit of the resonant frequencies and therefore does not parameterize potential error in generating the texture coefficients from EBSD or neutron diffraction data. The texture coefficients are provided to the model as known constants that are multiplied with the independent single crystal elastic constants, and therefore directly alter the mean values of the single crystal elastic constants. The factors affecting the numerics of the texture coefficients are errors in data analysis, thresholding of experimental noise in the neutron/ EBSD data, specimen preparation, the quantity of data utilized, and whether the measured texture reflects the texture throughout the specimen volume. The volume of EBSD data to accurately represent the bulk texture is dependent on specimen

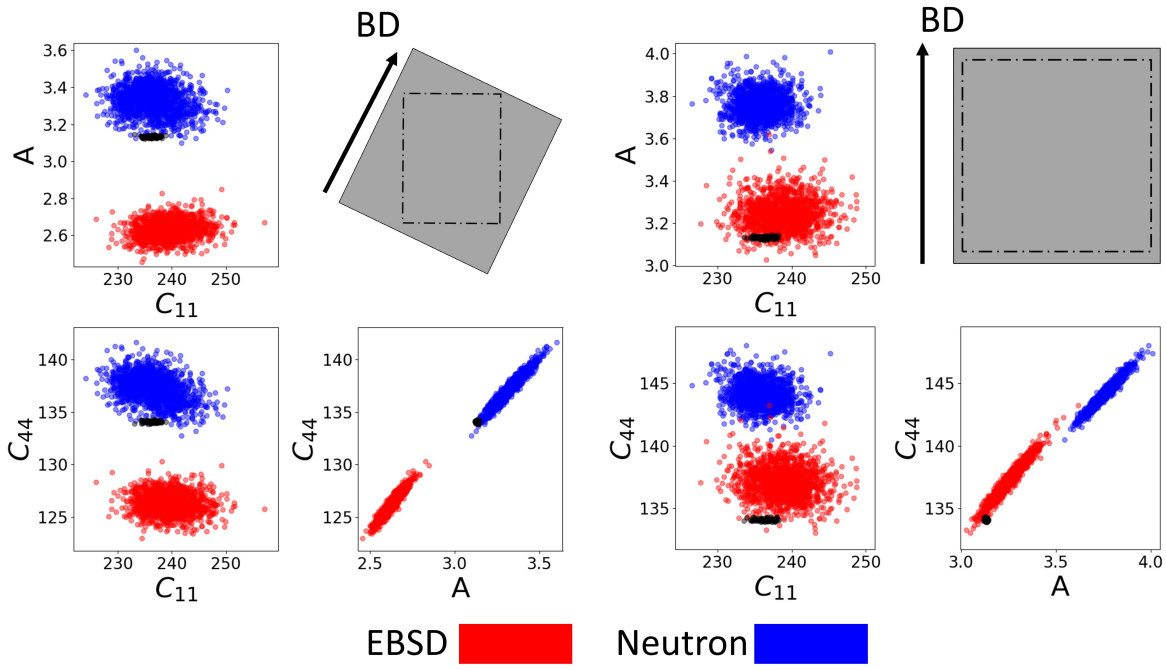

Figure 4.8: Parameter plots of the single crystal elastic constants of both specimens under study display similar behavior between each studied parameter. The bulk elastic symmetry has no effect on sampling, as it is captured by the texture supplied to each simulation. Datapoints in black are sourced from the literature [125].

texture heterogeneity and grain size, making it difficult to recommend best practices. The combined effect of these errors is difficult to estimate, therefore texture variability could not be directly incorporated into the model as a quantified error. Setting all of the texture coefficients independent (as in Chapter 3) with independent single crystal elastic constants results in unrealistic parameter correlations, solution identifiability/ uniqueness issues with altered bulk elastic symmetries, and convergence issues with uninformative priors.

To elaborate, the SMC calculated standard deviations on each parameter incorporate all factors affecting the experimental frequencies through the fit (or lack thereof) of the calculated frequencies. The SMC-calculated measurement error term, σ is a lumped term for the fit of frequencies, with increasing σ reflecting increasingly inadequate fits

of the frequencies given a set of independent parameters. The texture coefficients are therefore capable of affecting the overall fit of the frequencies as well as directly altering the convergent mean values of the single crystal elastic constants. Sources of error specific to polycrystals such as residual stress [124], grain boundary dispersion, and grain structure heterogeneity result in the greater uncertainties compared to those calculated from a bulk single crystal. Additional errors include measurement uncertainty of the specimen dimensions, such as improperly parallel specimen faces, and inelastic effects on the resonant spectrum, such as cracks and porosity. Small alterations of the specimen dimensions could be artificially applied to quantify the effect of error, but results in prohibitive computation expense to rerun the SMC model for each alteration of geometry. The effect of geometric change on the estimated elasticity of a single crystalline cylinder has been observed [153] to scale with the amount of geometric deviation in % (i.e. a 2.5% change in radius causes at most a 2.5% change in measured elasticity), indicating that the EDM-machined specimens here are unlikely to cause significant deviations in the elasticity. All of these factors alter the experimental frequencies, such that alterations of the single crystal constants cannot generate frequencies that fit the altered experimental frequencies, and can result in apparent increases in fitted (σ) measurement noise levels. Further, this analysis assumes unambiguous knowledge of the resonant frequencies supplied to the specimen (i.e. no missed resonant modes). High damping materials typically contain low amplitude frequency peaks, emphasizing the need for unambiguous knowledge of the frequencies. Given that SB-CoNi-10C did not display significant damping of the frequencies, the chances of a missed mode are negligible here. For high damping materials, this work could be supplemented with RUS mode-shape measurement via lasers [64] or machine learning frequency analysis with mode shape modeling [131]. Alternatively, this work enables the determination of the single crystal elastic properties from arbitrarily shaped specimens that require finite element modeling to determine the

resonant frequencies [63], given mode shape information is not necessary for Bayesian implementations of RUS [68].

Given that the EBSD data reveals elongated grains in both of the specimens under study, the grain aspect ratio could be considered as an independent parameter. While this appears to be intuitive, the reference stiffness ($C_0^{self,iso}$) of the medium is not known prior to analysis, meaning that without assuming isotropic grain statistics the analytical determination of $C_0^{self,iso}$ from the single crystal elastic constants cannot be performed. An arbitrary choice of the reference stiffness would then need to be selected, so isotropic grain statistics were assumed.

Despite these limitations, testing was carried out with a fixed reference stiffness informed by the final aggregate elastic constants of specimen R2 and R4 (informed from Chapter 3) to separate the dependencies within the model. Including the grain aspect ratio (ellipsoid semi axis a_3 aligned with BD corresponding to [154]) as a free parameter with $a_1 = a_2 = 1$ resulted in a negligible effect on the values of the single crystal elastic constants. The lack of sensitivity to the aspect ratio parameter is demonstrated in the parameter plots of Figure 4.9 for both the misaligned and aligned specimen.

The convergence to $\frac{a_3}{a_1} \sim 1$ technically implies that the grain shape is spherical, which given the EBSD is not physically true. However, given the reference stiffness is calculated as an isotropic tensor from the single crystal elastic constants, it is likely that the single crystal elastic constants are changing to affect the reference stiffness (in place of the aspect ratio) and make up for any aggregate effect of the aspect ratio on the resonant frequencies. For reference, other studies report changes of 2 GPa to 5 GPa (C_{11}) in the single crystal elastic constants of copper for values of $\frac{a_3}{a_1} > 10$ [66], while Bayesian estimates of the single crystal constants of Ti–10V–2Fe–3Al (Ti1023) displayed $\frac{a_3}{a_1} = 3$ - 5 for a specimen with EBSD-measured $\frac{a_3}{a_1} = 8$ - 10 [65]. Though these studies seem to indicate that the

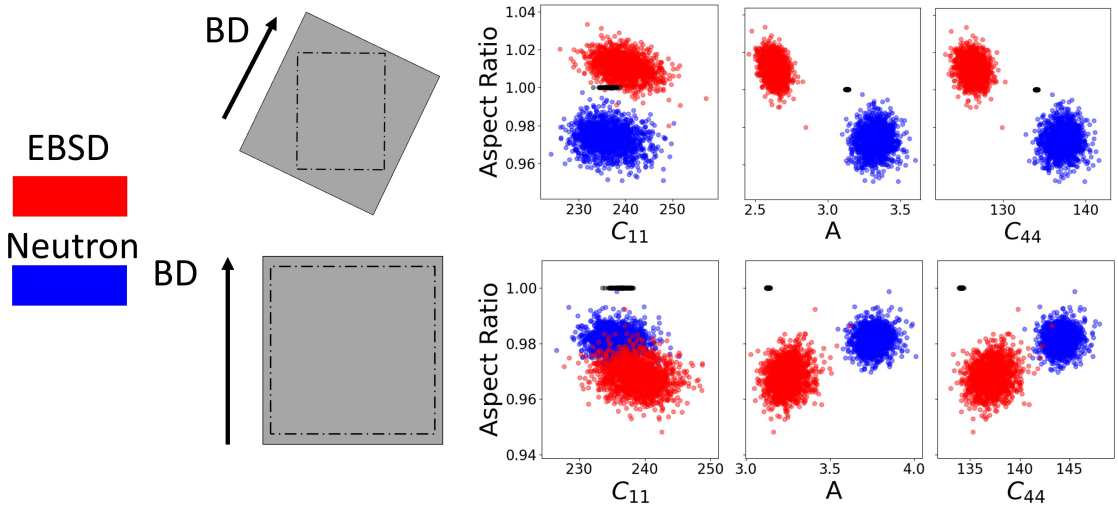

Figure 4.9: The inclusion of aspect ratio in the single crystal inversions of specimen R2 and R4 results in a convergent aspect ratio (a_3/a_1) equal to 1, meaning it had no effect on the determined parameters. As observed, the EBSD and neutron results for each specimen are identical to those calculation in Section 4.4 above. Considering the calculation of reference stiffness (Section 4.3) is dependent on the single crystal elastic constants, the effect of aspect ratio is likely negated. Datapoints in black are sourced from the literature [125].

aspect ratio is important to determine the single crystal elastic constants, the inclusion of $\frac{a_3}{a_1}$ in [65] altered the means of the single crystal elastic constants C_{11} and C_{12} by 41.7 GPa (31%) and 19 GPa (19%) respectively, and increased the standard deviation of C_{44} from 1 GPa to 7 GPa. Given the referenced studies used fixed bulk elastic constants determined from tensile tests [65] or RUS measurements [66], it is difficult to compare them to the direct use of resonant frequencies for determining the single crystal values. Further study is needed to assess the impact of grain aspect ratio when inversely solving for the single crystal elastic constants with different experimental measurement techniques.

The anisotropy of the bulk elastic constants in concert with the texture is critical for determination of the single crystal elastic constants. Though the forward model calculation here incorporates all the necessary texture coefficients to account for arbitrary (triclinic) symmetry, the numerics of these coefficients may display a lower macroscopic elastic symmetry depending on the measured texture orientations. The texture that

is utilized to inform a calculation of the single crystal elastic constants must induce a state of distinctly defined, anisotropic bulk elasticity relative to the x,y,z directions of the parallelepiped specimen faces. Though rotations of the texture are easily accounted for, the texture must induce anisotropy in the bulk elastic constants that is distinct from an isotropic sample state. For example, extremely weak textures are isotropic on the bulk scale and have fewer independent terms than a cubic single crystal. The single crystal elastic constants are therefore indeterminable, with no sensitivity of the resonant frequencies to changes in each single crystal elastic constant. Similarly, a material with a single crystalline Zener anisotropy ratio [135] of 1 induces no anisotropy on the bulk elastic constants (regardless of texture strength/ symmetry), and neither the texture coefficients or single crystal elastic constants are therefore determinable from the resonant frequencies. Ultimately, if the combination of texture (MRD strength) and single crystal anisotropy is sufficient to enable the bulk elastic constant values to be differentiated from one another during inverse solving (i.e. $C_{55}^{bulk} \pm$ std. dev. $\neq C_{66}^{bulk} \pm$ std. dev. for an orthotropic polycrystal), the polycrystal has sufficient texture to determine the single crystal elastic constants. These anisotropy limitations have historically hampered ultrasonic characterization techniques [155], but are not an issue for the textured AM microstructures here.

Given that a well-defined (anisotropic) microstructure is necessary to determine single crystal elastic constants, there must be homogeneity across the microstructure as well. All of the microstructure information is obtained from bulk elastic waves and the resultant resonant mode-shapes, so elastic gradients across the sample would cause deviations in resonant frequencies that are not accounted for in a single aggregate elastic tensor relative to the specimen axes. Homogeneity does not imply that only simple textures may be used, as discussed at length in Chapter 3. Rather, the combined effect of the

texture should not originate from local regions of differently oriented textures within the component, such that its crystallographic orientations "cancel" one another. The thin walled specimens shown in [28] are an excellent example of this effect, where the grains grow symmetrically inward from the outer specimen surfaces and effectively mirror the effect of the other on aggregate elasticity. This limitation is of utmost importance for microstructures where the primary phase transforms from a parent phase (such as Ti-6Al-4V), resulting in multiple orientation variants from a single parent phase orientation [156]. As a result, efforts to apply this technique to Ti-6Al-4V have been unsuccessful.

4.6 Conclusions

- A Bayesian inference framework with Sequential Monte Carlo was developed to determine the single crystal elastic constants of additively manufactured components, utilizing only the measured resonant frequencies and texture. Parallelized simulations enabled computations in 12-24hr, an order of magnitude reduction to serial computation time.

- The C_{11} and C_{12} single crystal elastic constants calculated from AM specimens, both aligned and misaligned from the build direction, were in agreement with a grown single crystal specimen within the calculated Bayesian uncertainty. The calculated C_{44} values diverged from the bulk single crystal values by $\leq$7.5%.

- Texture data gathered across 5 mm x 8 mm areas with EBSD produced single crystal elastic constants that displayed comparable uncertainties to those calculated with neutron diffraction data, validating its use to inform the texture of these simulations. The values of C_{11} and C_{12} between neutron-informed and EBSD-informed calculations agreed within their uncertainties, while differences in C_{44} were shown as dependent on texture data analysis. Future work could incorporate ODF

coefficient uncertainty within the calculation of the single crystal elastic constants in order to directly quantify this effect.

- The technique developed here provides a novel method to estimate the single crystal elastic constants of AM and engineering alloys by providing the resonant frequencies and EBSD information from a single specimen face. Successful determination of the single crystal elastic constants depends upon the existence of homogeneous and directionally defined crystallographic texture within the specimen.

Chapter 5
Practical Determination of Single Crystal Elastic Constants: RUS of AM Specimens with Minimal Texture Data

Resonant Ultrasound Spectroscopy is capable of determining the single crystal elastic constants from polycrystalline specimens with known crystallographic texture. However, the calculated single crystal elastic constants vary with the numerics of the measured texture as dependent on an orientation distribution function (ODF) calculation, resulting in inconsistency for additively manufactured (AM) specimens with heterogenous texture regions. In this Chapter, the single crystal elastic constants are robustly determined by incorporating the uncertainty of the texture in the determination of single crystal elastic constants, using small quantities of electron backscatter diffraction data (EBSD) to do so. The single crystal elastic constants are determined by Bayesian inference with sequential Monte Carlo for AM specimens of a cobalt-nickel-base superalloy (SB-CoNi-10C), nickel-base-superalloy Inconel 625 (IN625), and Ti-6Al-4V (Ti64). The Bayesian calculated single crystal elastic constants from AM specimens of each alloy agree with literature values, with the calculated Bayesian uncertainties capturing the variation in reported values. Sequential Monte Carlo is parallelized, resulting in an order of magnitude reduction in computational cost.

5.1 Motivation

Single crystal elastic constants describe the fundamental mechanical response of crystalline materials. Knowledge of the single crystal elastic constants is critical for property prediction of materials with variable microstructures, such as additively manufactured

(AM) components. Despite the importance of precise knowledge of the single crystal elastic constants, historical measurements required the growth of a single crystal specimen and mechanical [136, 137] or ultrasonic [40, 103, 138] testing. Because single crystal growth requires high cost equipment and expertise, there is a driving force for the determination of the single crystal elastic properties from polycrystalline specimens [65, 141, 142]. Unfortunately, the majority of the polycrystal-based approaches still require access to synchrotron facilities.

Consequently, techniques to quantify the single crystalline elastic properties from polycrystals on the laboratory scale are of interest. Recently, ultrasound has been used to determine the single crystal elastic constants from bulk elastic properties of polycrystalline materials [66, 147]. These efforts involve the use of localized surface acoustic wave measurements [147] or bulk ultrasound measurements [66] to infer the single crystal properties. Given the low expense of these ultrasonic approaches, a framework has been developed to inversely determine the single crystal elastic constants from resonant ultrasound spectroscopy (RUS) measurements of (textured) additively manufactured specimens (Chapter 4). Chapter 4 incorporated Bayesian inference into the inverse determination of the single crystal elastic constants, generating probability distributions and uncertainties on each independently determined parameter from the measured resonant frequencies. However, Chapter 4 required the specimen's crystallographic texture as a fixed input to the calculation, resulting in the single crystal elastic constants depending on both the method and quantity of texture data collected.

This research serves to increase both the accuracy and robustness of the single crystal elastic constants as determined from polycrystalline-specimen RUS measurements, by incorporating uncertainty in the supplied texture as determined by Electron Backscatter Diffraction (EBSD). This work further develops the Bayesian inference framework created

in Chapter 4, and is demonstrated on the cobalt-nickel-based superalloy (SB-CoNi-10C) specimens described there. The novel framework is then demonstrated to quantify the single crystal elastic constants of AM Inconel 625 (IN625) and AM Ti-6Al-4V (Ti64) using resonant frequencies and EBSD data.

The results of the work presented in this chapter are: 1. To develop a framework to determine the single crystal elastic constants from RUS measurements, incorporating texture uncertainty for both cubic and hexagonal materials. 2. To rigorously account for uncertainty in the EBSD and RUS data and increase the accuracy of the resultant single crystal elastic constants. 3. To report the single-crystal elastic constants of SB-CoNi-10C (cobalt-nickel-base superalloy), Inconel 625, and Ti64 from AM specimens, and compare with previously reported literature values.

5.2 Materials and methods

5.2.1 SB-CoNi-10C: Laser powder bed fusion

An Aconity3D AconityMINI system at the University of California, Santa Barbara was used to print rectangular SB-CoNi-10C[1] specimens with nominal dimensions of 10 mm x 10 mm x 13 mm (build direction). The powder was provided by Carpenter Technologies[2], with composition given in Table 5.1.

SB-CoNi-10C Chemical analysis (wt.%)										
	Co	Ni	Al	W	Ta	Cr	C	B	Y	Hf
Nominal	Bal.	35.75	5.98	3.09	10.63	5.24	0.070	0.015	0.003	0.054
Measured	Bal.	35.93	5.98	3.06	10.40	5.24	0.069	0.013	0.006	0.057

Table 5.1: Chemical analysis of SB-CoNi-10C powder prior to build as measured by Carpenter Technologies. Major constituents were measured by x-ray. B was measured by mass spectrometry and Y was measured by wet-chem analysis. Quantities in wt.%.

As described in Chapter 4, a printed specimen of SB-CoNi-10C was sectioned by

[1]Commercially available at Carpenter Technologies[2] as Gamma Print 700™

[2]Carpenter Technology, 1735 Market Street, 15th Floor, Philadelphia, PA 19103 USA

electrical discharge machining (EDM) with alignment along the build direction. A bi-directional scan strategy with a 90° rotation between build layers was utilized with the build plate preheated to 200°C. The beam diameter was 80 μm and the layer thickness was 30 μm. The sectioned and polished specimen geometry was 10.355 mm x 8.883 mm x 8.370 mm. A stress relief heat treatment at 1100°C for 2h was performed after EDM sectioning to the final parallelepiped shape. EBSD data was gathered across a nominal 4 mm x 8 mm area of the specimen face. To reduce distortion, individual 2 mm x 3 mm scans were performed and then aggregated using the MATLAB toolbox, MTEX [123, 127]. A FEI Versa 3D Dualbeam microscope with an EDAX OIM-Hikary XM4 detector was used for all EBSD scans. All EBSD data was gathered using a scanning electron microscope (SEM) accelerating voltage of 30 kV and current of 6.4 nA. Raw EBSD pattern images were collected for indexing with the EMSphInxEBSD package developed by Lenthe et al. [148]. Points below a confidence index of 0.18 (<10% of the datapoints) were removed prior to orientation distribution function (ODF) generation in MTEX. The EMSphInxEBSD-indexed scans are shown in Figure 5.1.

5.2.2 Inconel 625: Laser powder bed fusion

IN625 Chemical analysis (wt.%)																
	Ni	Cr	Fe	Mo	Nb	Co	Ti	Al	Si	Mn	P	Ta	C	S	O	N
Powder	Bal.	20.86	0.62	9.03	3.95	0.17	0.35	0.31	0.07	0.04	<0.010	<0.01	0.01	<0.005	0.022	0.008
Solid	Bal.	20.00	0.80	8.80	3.80	-	0.37	0.32	0.10	0.05	0.006	-	0.01	<0.001	-	0.0001

Table 5.2: IN625 composition of powder and solid measured by inductively-coupled plasma atomic emission spectroscopy for all elements (ASTM E1479) except C/S measured by combustion (ASTM E1019) and O/N measured by fusion (ASTM 1019) [157]. All measurements are in wt.%.

Inconel 625 (IN625) specimens were provided by the National Institute of Standards and Technology (NIST) corresponding to the AM Bench 2022-04 modeling challenge[3] [157]. Specimens were printed by LPBF with an EOS M270 in two different raster conditions, 'X' corresponding to a 180° scanning direction rotation between build layers

[3]Additive Manufacturing Benchmark Test Series: https://www.nist.gov/ambench

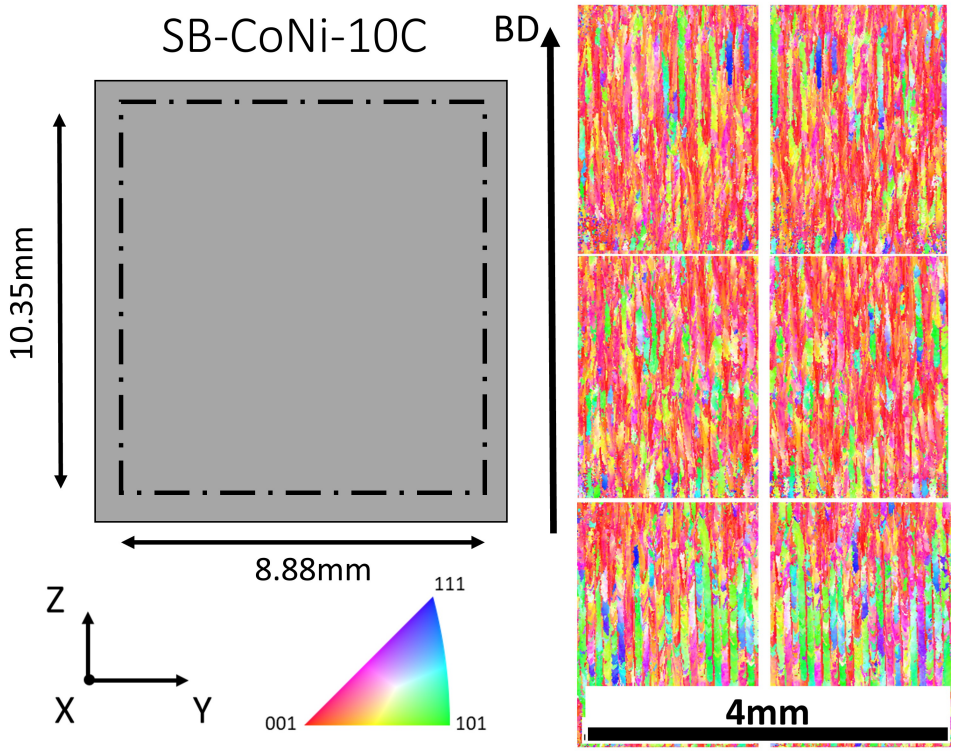

Figure 5.1: Electron backscatter diffraction data and sectioning strategy of the SB-CoNi-10C specimen. Inverse pole figure coloration is referenced relative to the build direction. EBSD pattern indexing was completed using the EMSphInxEBSD package [148].

and 'XY' corresponding to a 90° rotation between build layers. The laser power was 195 W, scan speed 800 mm/s, hatch spacing 100 μm, and layer thickness 20 μm. As-received powder was used for the build. Rectangular specimens were printed with nominal dimensions of 15 mm (x, raster direction) x 10 mm (y) x 20 mm (z, build direction). One printed specimen of each raster condition (X, XY) was chosen for further study, with two parallelepiped specimens sectioned with EDM from each selected specimen to nominal dimensions 6.50 mm (x-raster direction) x 8.50 mm (y) x 11.00 mm (z-build direction). The sectioning strategy is shown in Figure 5.2. Each specimen was sectioned 3mm from the build plate to avoid epitaxially affected grain growth, with 0.5 mm 'skimming' cuts along each specimen surface to remove near-surface grain regions. The 4 total specimens are denoted X_S1, X_S2, XY_S1, XY_S2 with measured densities 8.415 $\frac{g}{cm^3}$, 8.410 $\frac{g}{cm^3}$,

8.429 $\frac{g}{cm^3}$, and 8.412 $\frac{g}{cm^3}$ respectively.

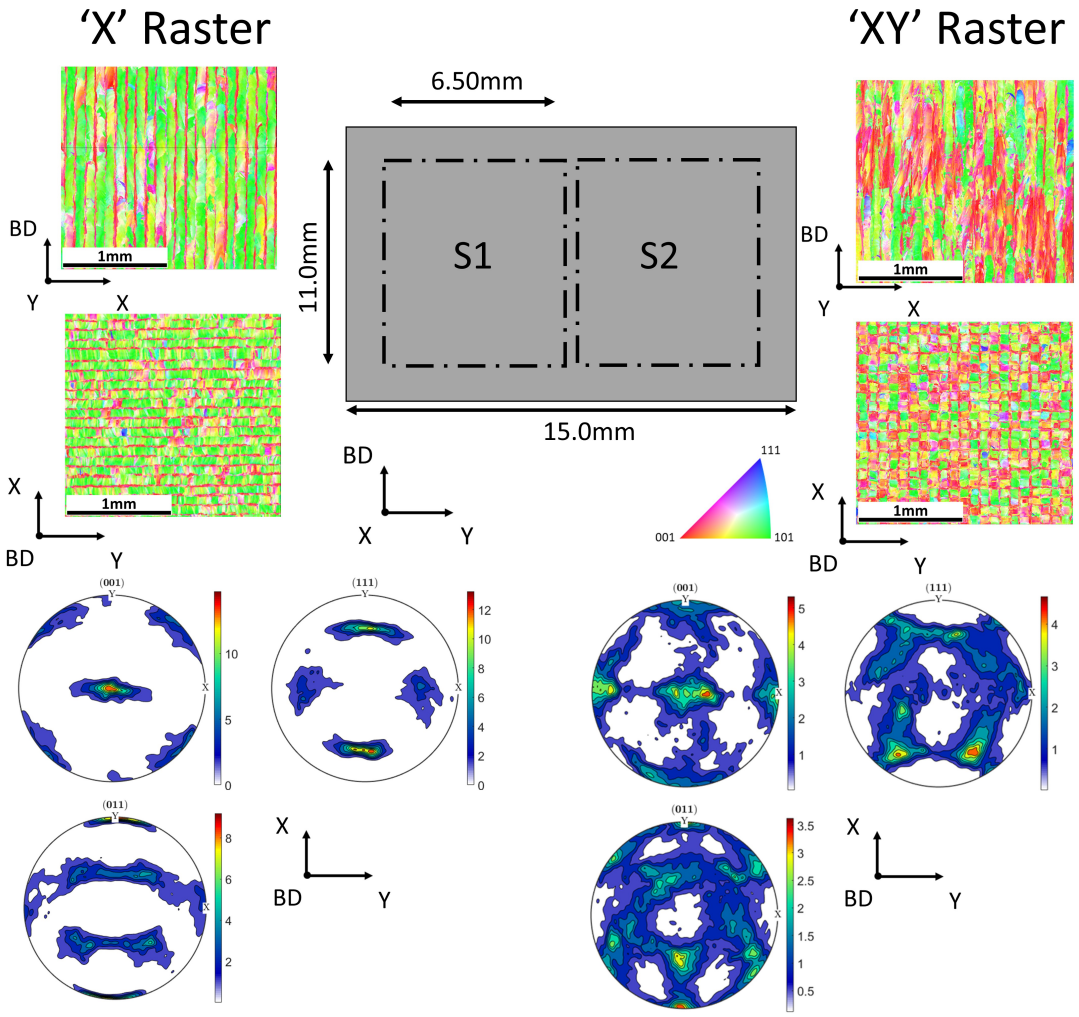

Figure 5.2: EBSD and sectioning strategy for the rectangular IN625 blocks printed with each raster condition. Specimens and EBSD data was provided by NIST AM Bench Test Series[3]. Pole figures were generated from the EBSD scans with BD out of the page (lower).

EBSD was provided for each raster condition in 2 mm x 2 mm total nominal areas of two different faces relative to the build direction. The EBSD scans were gathered by NIST on duplicate specimens in the build, with the same geometry as those studied by RUS here. The EBSD measurements were performed on three orthogonal planes using a field emission scanning electron microscope operated with the following parameters: 20 kV accelerating voltage, 120 μm aperture, 19 mm working distance, 500x magnification

and dynamic focus. The multi-tile EBSD acquisition parameters were: 4x4 binning, 200 frames per second, tiles of approximately 440 μm x 430 μm with 5% overlap, 0.5 μm step size and the nickel phase indexed.

5.2.3 Ti-6Al-4V: Electron beam melting

Ti-6Al-4V specimens were provided by NASA JPL[4]. The cylindrical specimens were printed by CalRAM [5] on an ARCAM A2X with nominal dimensions 90 mm (height) x 16 mm (diameter) by electron beam melting (EBM). Standard EBM Ti64 powder was used for the build, as supplied by CALRAM. A standard printing strategy for Ti64 was used, consisting of a hatch, outer and inner contour regions. Three sets of AM settings were used to print the cylinders, denoted Standard Energy (SE), Low Energy (LE), and High Energy (HE) corresponding to decreased and increased beam power. The three power settings were selected within a range of beam currents (12-18 mA) to replicate a range of common AM process parameters.

The SE printing parameters were used for both the initial ∼15 mm and final ∼15 mm of the build height across all the printing conditions, with the LE and HE sets of printing parameters applied for the central ∼60 mm of the build height. Parallelepiped specimens were each extracted with EDM from each cylinder, as shown in Figure 5.3. The specimens selected for further study were sectioned with at least 5 mm between the specimen edge and the transition region (between processing parameters), ensuring that each sectioned specimen contained identical processing parameters throughout. The SE and HE parallelepipeds were extracted ∼50 mm from the build plate of the cylinders, while the LE specimen was ∼62 mm from the build plate.

Similar to SB-CoNi-10C in Section 5.2.1, EBSD tiles were gathered across nominal

[4]NASA Jet Propulsion Laboratory, California Institute of Technology, Pasadena CA
[5]California Manufacturing Technology Consulting® (CMTC), a Carpenter Company

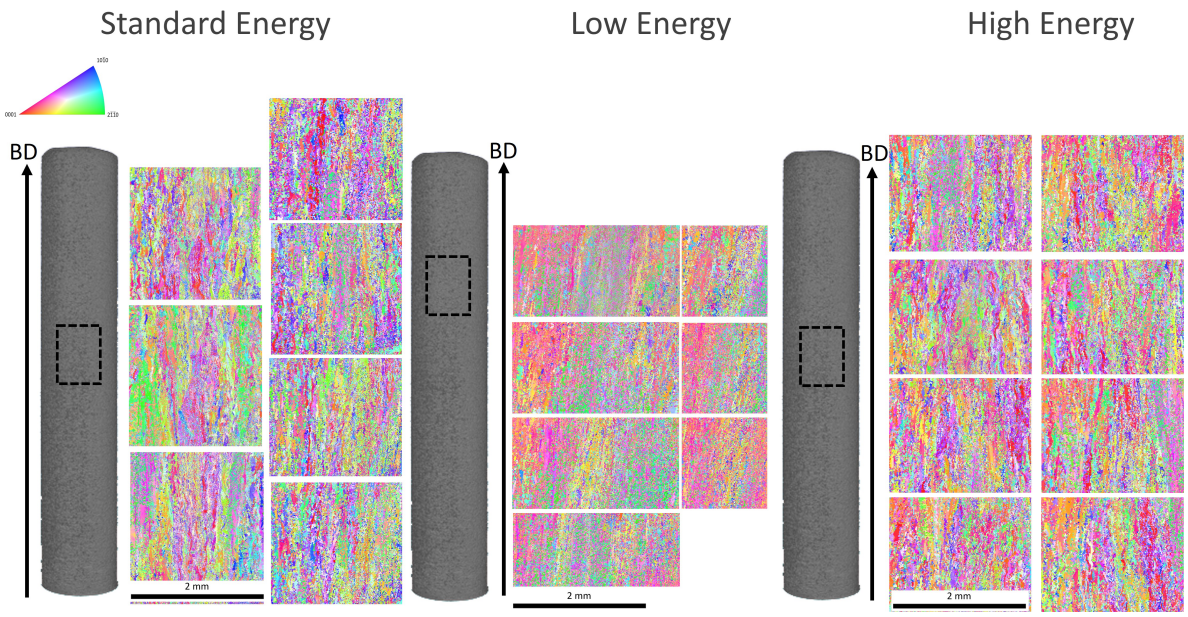

Figure 5.3: AM Ti64 specimens were sectioned from as-printed cylinders. Specimens were extracted 50-70 mm up the build height of the 90 mm build height cylinder. EBSD scans were gathered as smaller subscans across the surface of each extracted parallelepiped specimen and aggregated to generate texture coefficients distributions.

4 mm x 7 mm total areas of a selected specimen face of each parallelepiped. All EBSD data was gathered using an accelerating voltage of 20 kV and current of 1.6 nA. Indexing was completed on raw pattern images with the EMSphInxEBSD package [148] prior to analysis in MTEX.

The nominal dimensions of each parallelepiped after EDM was 7.97 mm x 10.07 mm x 10.97 mm (build direction). Specimen densities were measured as 4.409 $\frac{g}{cm^3}$, 4.422 $\frac{g}{cm^3}$, and 4.401 $\frac{g}{cm^3}$ for the standard, low, and high energy parallelepipeds respectively. Computed tomography (CT) was performed on the as-printed cylinders at NASA JPL[6]. The CT data revealed a greater quantity of small-scale defects for the LE cylinder than in the SE cylinder, and a lower quantity of small-scale defects for the HE cylinder. A coarse representation of the CT data is given in Figure 5.4, where each individually identified defect volume is plotted relative to the specimen's build height.

[6]CT performed by John Bescup

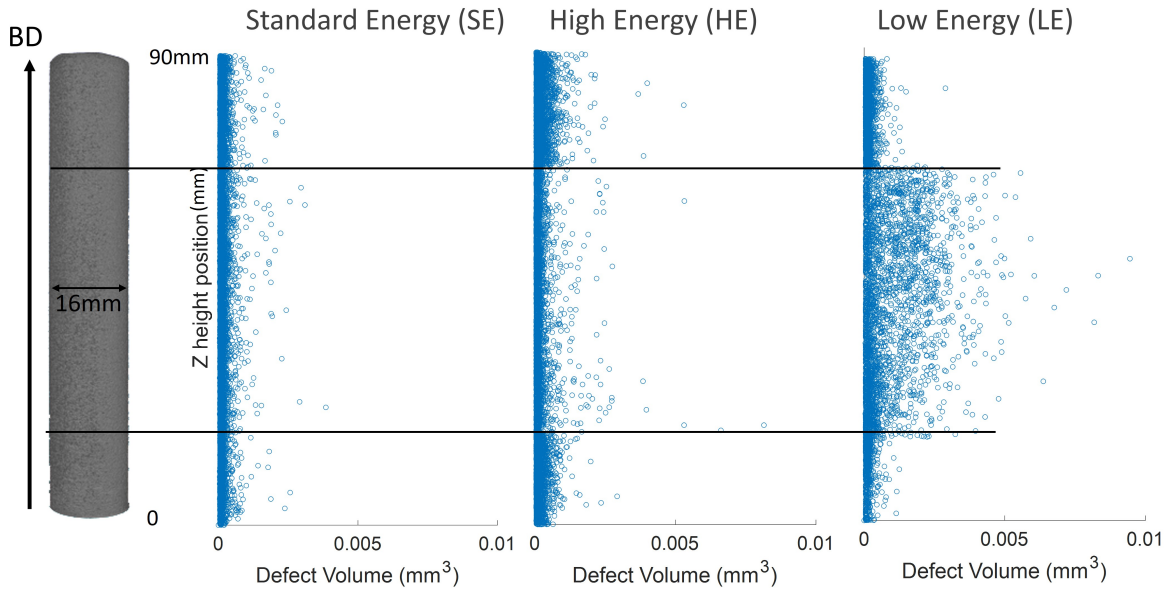

Figure 5.4: Defects detected by computed tomography (CT) of Ti64 as-built cylinders. The initial 15mm and final 15 mm of the build height were printed with standard processing parameters, while the high and low energy processing parameters were induced in the 'gauge' section, from which the RUS specimens were sectioned.

The defects that did exist in the HE cylinder existed at the boundary of the contour scan, and were larger than the average defects observed in the SE condition. The total calculated volume of the porosity was 0.008% for SE, 0.02% for LE, and 0.01% for HE.

5.2.4 Resonant ultrasound spectroscopy measurements

Consistent with Chapters 3 and 4, RUS was performed with each AM parallelepiped specimen freely resting on piezoelectric transducers to prevent any external contact forces. Figure 5.5 demonstrates this setup, with two receiving transducers and 1 driving transducer. All of the specimens in this study were parallelepipeds, and were measured with the same RUS parameters. The first 50-75 modes were measured for each specimen with sampling step sizes of 5 Hz and a dwell time of 1 ms. The piezoelectric transducers, transceiver, and computer control were provided by Vibrant Corporation[7]. Broadband scans were repeated three to five times for each specimen, altering the position of the

[7]Vibrant Corporation, 8916 Adams St NE, Albuquerque, NM 87113

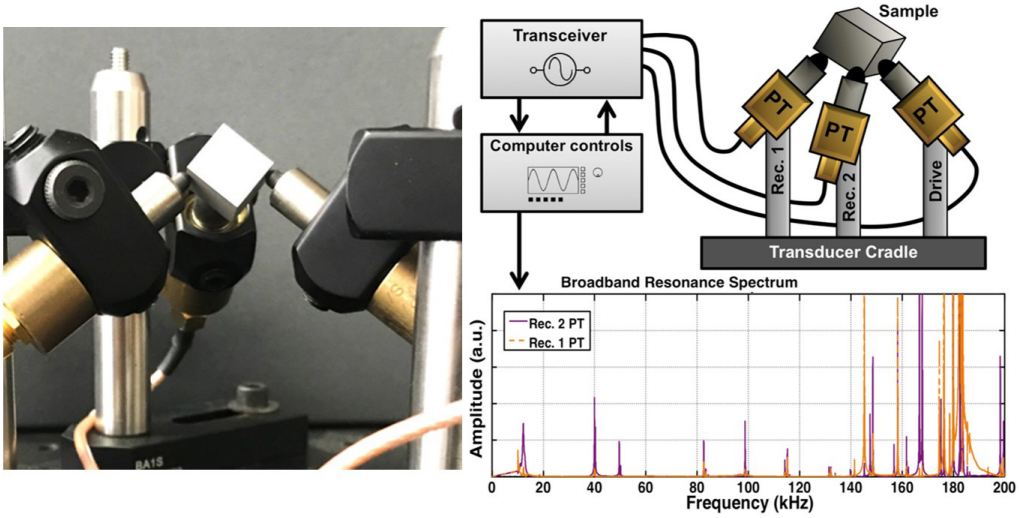

Figure 5.5: Resonant ultrasound spectroscopy testing setup with AM specimen. Each specimen freely rested under its own weight.

specimen/ transducer between each scan. Measured frequencies were averaged across all the measured scans. A $\pm 1\%$ dimensional tolerance was considered the maximum allowable uncertainty during specimen preparation. This $\pm 1\%$ maximum allowable uncertainty correlates to $\leq \pm 25$ μm for specimen dimension preparation and measurement with a set of vernier calipers.

5.3 Theory/ computation

5.3.1 Developing texture prior probability distributions with EBSD

As demonstrated in Chapter 4, variability in the input texture values directly affects the values of the single crystal elastic constants when determined from polycrystalline specimens. To increase the robustness of the accuracy of the determined single crystal elastic constants, texture coefficient uncertainty needs to be quantitatively incorporated into the calculation by incorporating texture coefficients as random variables.

However, the independent parameter determination of arbitrary texture coefficients (e.g. bulk elastic constants with arbitrary symmetry elasticity) results in an invariant solution of the resonant frequencies. To account for the invariant 3-fold mirror reflections

without resonant mode shape imaging, each invariant solution can be rotated to a single solution with post-processing (Chapter 3). As a result of parameter interdependencies between the texture coefficients and single crystal elastic constants, sampling multiple modes (invariant solutions) of the texture during inverse solving results in inconsistent estimates of the single crystal elastic constants. Therefore, the texture coefficients must be incorporated as random variables without falling victim to this invariant solution during sampling.

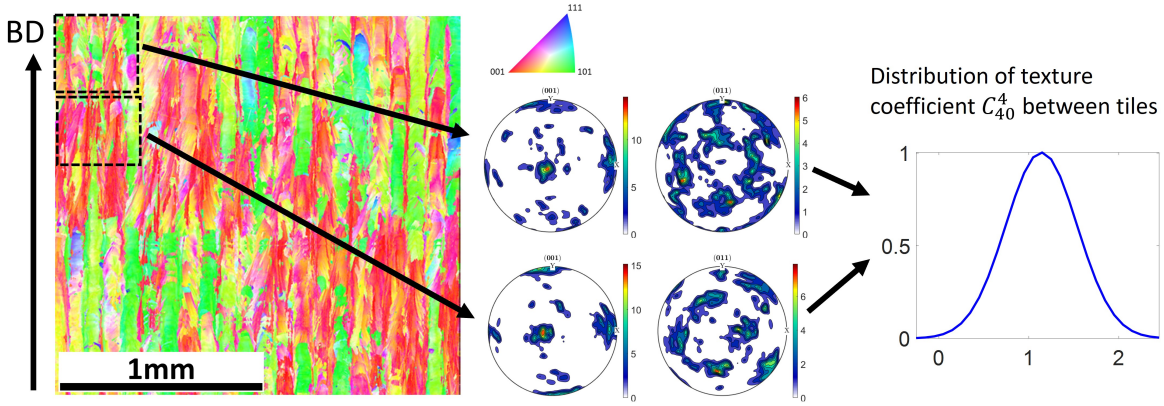

Figure 5.6: Distributions of each ODF coefficient are generated by dividing EBSD measurements into smaller datasets and generating the ODF coefficients at each EBSD 'tile'. This method is demonstrated for an IN625 EBSD dataset provided by the NIST AM Bench Test series[3]. The distributions of each texture parameter are used to inform the Bayesian prior of each simulation, enabling increased accuracy for the determined single crystal elastic constants.

In order to treat the texture coefficients as random variables alongside the single crystal elastic constants, information about these texture coefficients for a given specimen is used to restrict the variables and avoid the identifiability issues when searching parameter space. This information is encoded as prior distributions during Bayesian inference. As shown in Figure 5.6, EBSD data was sub-divided into smaller 'tiles', with the ODF and corresponding texture coefficients generated at each tile with the MATLAB toolbox, MTEX [123, 127]. The texture coefficients across all the tiles were aggregated and used to generate distributions of each texture coefficient, which were observed to be normally

distributed. The normal distribution of each coefficient represents the possible range of the coefficient on the bulk scale, and therefore were used to inform the prior distribution. Generating a distribution of each coefficient and enabling the inference to fit each value enables the use of significantly smaller EBSD datasets for the determination of the single crystal elastic constants.

5.3.2 Forward model calculation of resonant frequencies

The calculation of resonant frequencies is referred to as the forward model. The forward model combines the calculation of resonant frequencies from the bulk elastic constants with a self-consistent calculation of those bulk elastic constants from the texture and single crystal elastic constants [95]. The forward model is shown in Figure 5.7.

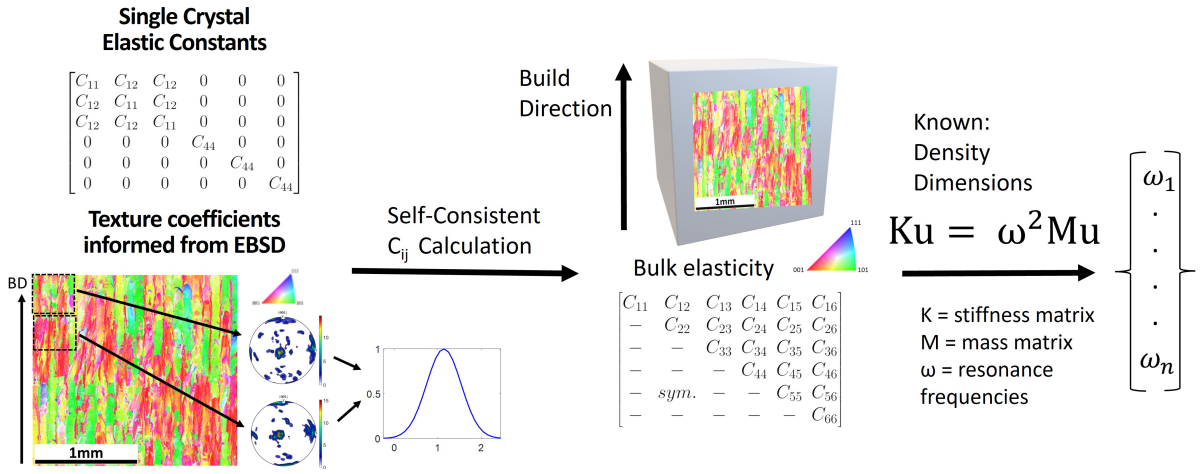

Figure 5.7: Forward model depicting the single crystal elastic constants to be determined (left), the texture coefficients initialized from EBSD to complete the self-consistent calculation of the aggregate elastic constants (middle), and the final calculation of the resonant frequencies (right). The EBSD data overlaid on the block is not to scale.

The calculation of resonant frequencies for a parallelepiped specimen involves solving a generalized eigenvalue equation as given in Equation 5.1. Following [58, 68], the resonant frequencies ω are determined given a mass matrix M (constructed from the specimen dimensions and density), a stiffness matrix K (constructed from the specimen

self-consistent stiffness C^{self}), and u as the 3-dimensional displacement vector. $\phi(x, y, z)$ represents the basis, with N representing the polynomial order.

$$\begin{aligned} Ku &= \omega^2 Mu \\ \phi(x, y, z) &= x^n y^m z^l \\ n + m + l &\leq N \end{aligned} \tag{5.1}$$

The computation of the stiffness matrix K requires the bulk elastic constants, which are calculated as the self-consistent solution $C^{self,iso}$ given in Equation 5.2, as developed for tensorial texture coefficients in [95]. The reference tensor L is defined in place of the traditional single crystal elastic constants C^{SC} in the orientation average, as the self-consistent solution here is defined consistent with the Hashin-Shtrikman-type bounds and assumed isotropic grain-shapes ($C^{self,iso}$) in [95]. L inherits the symmetry of C^{SC}, as it is calculated as the linear combination of the single crystal elastic constants C^{SC}, the zeroth-order reference stiffness $C_0^{self,iso}$, and the isotropic polarization tensor P_0. $C_0^{self,iso}$ is calculated by assuming an isotropic texture, and solving for the condition that the self-consistent solution is equal to its reference stiffness $C_0^{self,iso} = C_0$ for a given C^{SC}. f represents the ODF defined over $SO(3)$, and $\langle\rangle$ denotes an orientation average.

$$\begin{aligned} C^{self,iso} &= C_0^{self,iso} - [P_0(C_0^{self,iso})]^{-1} + [\langle f, L\rangle]^{-1} \\ L &= [C^{SC} - C_0^{self,iso} + [P_0(C_0^{self,iso})]^{-1}]^{-1} \\ hd(L) &\rightarrow h_{I1}, h_{I2}, H_{2,1}, H_{2,2}, H_4 \\ \langle f, L\rangle &= h_{I1}P_1 + h_{I2}P_2 + H_{2,1} * V_{\langle 2\rangle ij} + H_{2,2} * V_{\langle 2\rangle ij} + H_{4,1} * V_{\langle 4\rangle pqrs} \end{aligned} \tag{5.2}$$

The constants $h_{I1}, h_{I2}, H_{2,1}, H_{2,2}, H_{4,1}$ are determined by the harmonic decomposition (hd) of L, as dependent on the single crystal elastic constants C^{SC}. $V_{\langle g\rangle}$ indicates a tensorial texture tensor, with g as the tensor order. The number of texture tensors

that affect the specimen elasticity is dependent on the number of harmonic basis tensors for the given single crystal elastic constant symmetry, as given in [95]. The number of independent texture coefficients within each texture tensor is then dependent on the specimen symmetry, taken to be arbitrarily anisotropic (triclinic). For microscopically cubic materials, $H_{2,1} = 0$ and $H_{2,2} = 0$, meaning only the fourth order texture tensor $V_{\langle 4 \rangle pqrs}$ with nine independent terms is needed (Equation 5.3) to define an arbitrary macroscopic symmetry.

$$V_{\langle 4 \rangle pqrs} = \begin{bmatrix} V_{1111} & V_{1122} & V'_{1133} & V_{1123} & V_{1113} & V_{1112} \\ - & V_{2222} & V'_{2233} & V_{2223} & V'_{2213} & V_{2212} \\ - & - & V'_{3333} & V'_{3323} & V'_{3313} & V'_{3312} \\ - & - & - & V'_{2323} & V'_{2313} & V_{1223} \\ - & sym. & - & - & V'_{1313} & V'_{1312} \\ - & - & - & - & - & V'_{1212} \end{bmatrix} \tag{5.3}$$

Note that the parameters denoted with $'$ in Equation 5.3 are determined through linear combinations of the other parameters. For hexagonal materials, the second order texture tensor with five independent terms is also considered (Equation 5.4), given a single second order basis tensor exists.

$$V_{\langle 2 \rangle ij} = \begin{bmatrix} V_{11} & V_{12} & V_{13} \\ - & V_{22} & V_{23} \\ sym. & - & V_{11} - V_{22} \end{bmatrix} \tag{5.4}$$

Again, an arbitrarily anisotropic polycrystal is fully defined by the triclinic macrosymmetry here, with the second and fourth order texture tensors containing five and nine independent terms, respectively.

5.3.3 Single crystal elastic constants determined with sequential Monte Carlo

Bayesian inference is used to solve RUS inverse problem. Following Chapter 4, Bayes' Theorem involves the addition of new resonant frequency observations to update prior knowledge of the independent model parameters. The independent model parameters are both the texture coefficients and single crystal elastic constants here. The posterior probability density function represents this updated knowledge as the solution to the inverse problem,

$$\pi(\Theta|\omega_n) = \frac{\pi(\omega_n|\Theta)\pi(\Theta)}{\int_\Omega \pi(\omega_n|\Theta)\pi(\Theta)d\Theta} \tag{5.5}$$

where Θ is the vector of the independent parameters. These independent parameters differ for each material under study here, depending on the single crystal symmetry and residual stress presence.

For SB-CoNi-10C: $\Theta^{CoNi} = [C_{11}^{SC}, C_{44}^{SC}, A, V_{\langle 4\rangle 1111}, V_{\langle 4\rangle 1122}, V_{\langle 4\rangle 2222}, V_{\langle 4\rangle 1112}, V_{\langle 4\rangle 1113}, V_{\langle 4\rangle 1123}, V_{\langle 4\rangle 2212}, V_{\langle 4\rangle 2223}, V_{\langle 4\rangle 1223}]$: two single crystal elastic constants (C_{11}^{SC}, C_{44}^{SC}) and the Zener anisotropy ratio ($A = 2C_{44}^{SC}/(C_{11}^{SC} - C_{12}^{SC})$) [135] constituting the single crystal elastic behavior, and nine 4th-order texture coefficients constituting the effect of grain orientations on elasticity for cubic materials [95]. Note that sampling the Zener anisotropy ratio A is equivalent to sampling the single crystal elastic constant C_{12}^{SC}, such that all three independent elastic constants for cubic materials are sampled.

For IN625: $\Theta^{IN625} = [\Theta^{CoNi}, RS]$, represents the same independent parameters as SB-CoNi-10C with an additional residual stress term (RS) to account for residual stress induced frequency shifts (Chapter 3, [124]) given the IN625 specimens were measured in the as-built state. The resonant frequencies of SB-CoNi-10C were measured on specimens in the stress-relieved state, and did not require the residual stress term.

For Ti64: Θ^{Ti64} is constituted by five single crystal elastic constants: $[C_{11}^{SC}, C_{33}^{SC},$

C_{13}^{SC}, C_{44}^{SC}, C_{66}^{SC}], five 2nd order texture coefficients: $[V_{\langle 2\rangle 11}, V_{\langle 2\rangle 12}, V_{\langle 2\rangle 13}, V_{\langle 2\rangle 22}, V_{\langle 2\rangle 23}]$, and nine 4th order texture coefficients: [$V_{\langle 4\rangle 1111}$, $V_{\langle 4\rangle 1122}$, $V_{\langle 4\rangle 2222}$, $V_{\langle 4\rangle 1112}$, $V_{\langle 4\rangle 1113}$, $V_{\langle 4\rangle 1123}$, $V_{\langle 4\rangle 2212}$, $V_{\langle 4\rangle 2223}$, $V_{\langle 4\rangle 1223}$] [95, 158]. The Ti64 specimens were manufactured by electron beam melting, with the powder bed preheat negating the role of residual stresses on the frequencies.

Following Chapter 3, the numerator of the right hand side of Equation 5.5 comprises the likelihood function $\pi(\omega_n|\Theta)$ (which represents the likelihood of observing the measured resonant frequencies given Θ) and the prior $\pi(\Theta)$ (which represents prior knowledge of the independent parameters Θ). The denominator is the marginal likelihood and involves integration over the entire parameter support, $\Omega = \{\Theta \in \mathbb{R}^3\}$. By assuming that the measurement errors are independently and identically distributed as zero-mean Gaussian distributions with variance σ^2, a closed form expression is obtained for the likelihood as given in Chapter 3.

An open-source, parallelized Python implementation of Sequential Monte Carlo, `SMCPy`[8], was used to estimate the posterior distribution of single crystal constants. Hyperparameters were selected to ensure samples were generated from the full posterior (i.e. all modes represented) while balancing sample size with computation time. Following Section 5.3.1, the selection of texture coefficient priors was carried out by calculation from experimental EBSD data. For the single crystal elastic constants, improper uniform priors were chosen; i.e., $\Theta_j^{CoNi} \sim$ Uniform(0, 500 GPa) for $j = 1, \ldots, 3$. For the texture coefficients $j = 4, \ldots, 12$, normal distributions $\Theta_j^{CoNi} \sim \text{norm}(mean, std)$ were generated for each coefficient from representative EBSD data as described in Section 5.3.1.

The initial particle populations for all parameters were sampled from independent normal distributions, and referred to as the *proposal*. The proposal of each texture

[8]SMCPy Python package available open-source at https://github.com/nasa/SMCPy.

coefficient was set to the same mean value as their prior, with the standard deviation as 50% of the standard deviation of the prior. For the single crystal elastic constants, the proposal mean values were informed from the literature, ± one standard deviation to cover the reported range of values in the literature. Uniform distributions with means ± 100 GPa were separately tested, and resulted in identical final parameter estimates at higher computational cost.

Proposal Normal distributions - Single crystal elastic constants (GPa)					
	C_{11}	C_{12}	C_{44}	C_{13}	C_{33}
SB-CoNi-10C	236.4 ± 30.0	150.8 ± 20.0	134.1 ± 15.0	-	-
IN625	243.0 ± 25.0	152.0 ± 20.0	117.8 ± 8.0	-	-
Ti64	169.0 ± 35.0	79.0 ± 35.0	40.0 ± 10.0	62.0 ± 35.0	200.0 ± 35.0

Table 5.3: Proposal distribution (normally distributed) of each single crystal elastic constant for each material. ± indicates one standard deviation on the mean. Ranges were chosen to cover the reported literature values.

The proposal normal distributions for each material's single crystal elastic constants are given in Table 5.3. For SB-CoNi-10C, the means correspond to the means determined in [125] for a grown (bulk) single crystal. For IN625, the mean and standard deviation are set to cover the range of values reported in [140, 159]. For Ti64, the mean single crystal elastic constants were set as those determined in [144], with the standard deviation set to capture all the reported literature values. Note that when the Zener anisotropy ratio (for cubic materials) or C_{66} is sampled in place of another single crystal elastic constant, its proposal is calculated using the multivariate normal distibutions listed in Table 5.3.

In all SMC simulations, $1,800$ particles were migrated through a series of target distributions that started at the prior and ended at the posterior distribution. An adaptive algorithm was used [160] that controlled the step size between target distributions using an effective sample size (ESS) threshold of 85%. Each step size was chosen such that the ESS of the updated particle population was equal to this value until the final target distribution (i.e. the posterior) was reached. To avoid particle degeneracy, an MCMC

kernel was used at each step to move particles toward the new target distribution. Each pass through the kernel involved the construction of Markov chains of length 14, retaining the 14th for the next iteration. These choices resulted in $20-35$ target distributions (including prior and posterior) and corresponding computation times of 18-36 hrs when utilizing 10 CPU cores. All inversions used a polynomial order of 12 with 45 resonant modes.

5.4 Results and discussion

5.4.1 SB-CoNi-10C

To demonstrate the advantage of allowing variability in the texture coefficients, a BD-aligned SB-CoNi-10C specimen is studied. The single crystal elastic constants of this specimen were studied in Chapter 4, as determined for 'fixed' texture coefficients informed by EBSD and neutron diffraction. Here, the single crystal elastic constants are calculated from the resonant frequencies with 'freely' determined texture coefficients corresponding to calculations of the priors from EBSD in Section 5.3.1. Then, the single crystal elastic constants are compared to those calculated under the 'fixed' texture condition. These comparative calculations are carried out for each set of initialized (mean) texture coefficients in Chapter 4, corresponding to tiled EBSD data, neutron diffraction data, and overfitted neutron diffraction data. Note that for the 'free' texture conditions, the mean texture coefficients are initialized from the tiled EBSD, neutron diffraction, or overfitted neutron, while the distribution of coefficients is informed by the calculation of texture uncertainty from EBSD.

As observed in Figure 5.8, the final values of the single crystal elastic constants show less dependence on their initialization conditions due to the added degrees of freedom in the texture. The same resonant frequencies, specimen dimensions, density, and polynomial order are used for each varied texture/ calculation.

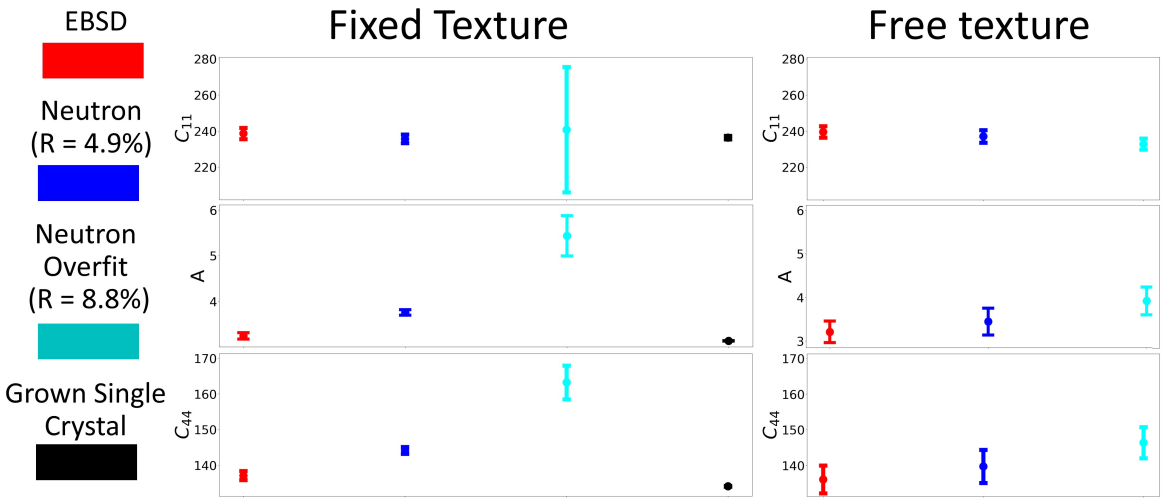

Figure 5.8: The single crystal elastic constants from the AM SB-CoNi-10C specimen from Chapter 4 (left), where numerical differences in the fixed texture inputs generated differences in the calculated single crystal elastic constants, despite identical resonant frequencies being used for each calculation. In contrast, the single crystal elastic constants are calculated within one standard deviation of one another when the texture is freely determined with EBSD-informed priors in the calculation (right), regardless of the initialization value of the mean texture values.

The incorporation of the texture variability from EBSD (Figures 5.1, 5.6) shifts the mean values of the calculated single crystal constants to within one standard deviation of the reference values (black), regardless of whether the mean values are initialized with EBSD or neutron diffraction. For the overfitted neutron diffraction, some dependence on the initial mean is observed for C_{44}, but the solution is significantly closer to the reference values. Therefore, this framework provides a more robust method than using fixed texture coefficients to determine the single crystal elastic constants from the resonant frequencies of AM specimens.

Comparing the calculated single crystal constants to literature reference values [125] in Table 5.4, a lower reported standard deviation is observed on the reference values. The lower standard deviation is a result of [125] being calculated from the resonance frequencies of a grown single crystalline specimen. True single crystal specimens on the bulk scale have fewer independent parameters than the free-texture condition here, as

SB-CoNi-10C Single Crystal Elastic Constants with Fixed Texture (Ch. 4)				
	EBSD	Neutron (R=4.9%)	Neutron (R=8.8%)	Ref. Crystal [125]
C_{11} (GPa)	238.7 ± 3.1	235.7 ± 2.4	241.0 ± 35.2	236.4 ± 1.0
A	3.24 ± 0.07	3.76 ± 0.06	5.44 ± 0.44	3.13 ± 0.004
C_{12}^{calc} (GPa)	154.2 ± 3.4	159.0 ± 2.6	180.7 ± 37.2	150.8 ± 0.8
C_{44} (GPa)	137.1 ± 1.27	144.2 ± 1.0	163.3 ± 4.8	134.1 ± 0.1
σ (kHz)	1.59 ± 0.19	1.09 ± 0.13	3.58 ± 0.41	0.08 ± 0.01
SB-CoNi-10C Single Crystal Elastic Constants with Free Texture (Present)				
C_{11} (GPa)	239.6 ± 3.2	237.1 ± 3.5	232.9 ± 3.1	236.4 ± 1.0
A	3.21 ± 0.25	3.45 ± 0.31	3.92 ± 0.32	3.13 ± 0.004
C_{12}^{calc} (GPa)	154.4 ± 2.2	155.6 ± 2.2	157.8 ± 2.1	150.8 ± 0.8
C_{44} (GPa)	136.1 ± 3.9	139.8 ± 4.6	146.4 ± 4.4	134.1 ± 0.1
σ (kHz)	0.76 ± 0.10	0.77 ± 0.11	0.76 ± 0.10	0.08 ± 0.01

Table 5.4: Single crystal elastic constants of SB-CoNi-10C specimen when initialized with different fixed-texture data (upper, as given in Chapter 4) or freely determined texture with priors determined by EBSD (lower). There is agreement within 1 standard deviation (±) of each single crystal elastic constant mean when the texture is allowed to vary, regardless of the initialized mean texture. These results agree with measurements on a grown single crystal as reported in [125].

well as significantly less noise in the actual measurement of resonant frequencies.

The simulations with texture variability were also applied to a specimen sectioned at 20°-to-BD, previously studied in Chapter 4. The 20°-to-BD specimen demonstrated equally robust agreement between EBSD and neutron-diffraction informed simulations.

5.4.2 Inconel 625

In625 Single Crystal Elastic Constants						
	X_S1	X_S2	XY_S1	XY_S2	Ref. [140]	Ref. [159]
C_{11} (GPa)	243.2 ± 9.0	240.0 ± 7.3	233.0 ± 9.5	231.7 ± 8.0	243.3	234.6
A	3.13 ± 0.51	3.66 ± 0.54	3.05 ± 0.51	2.95 ± 0.36	2.72	2.83
C_{12}^{calc} (GPa)	164.5 ± 6.7	168.7 ± 6.2	152.9 ± 7.7	150.7 ± 6.6	156.7	145.4
C_{44} (GPa)	121.2 ± 7.8	128.6 ± 7.7	120.0 ± 7.9	118.3 ± 6.3	117.8	126.2
RS(%)	-0.5 ± 0.9	-0.6 ± 1.0	-0.1 ± 1.1	0.1 ± 1.2	-	
σ (kHz)	1.09 ± 0.14	0.83 ± 0.10	0.98 ± 0.13	0.85 ± 0.11	-	-

Table 5.5: IN625 single crystal elastic constants of AM specimens agree within 1 standard deviation (±) across raster conditions ('X','XY') and specimen-specimen variability (S1,S2). 'X' represents a bidirectional (180° rotation between build layers) scanning strategy while 'XY' represents a scan strategy with 90° rotations between build layers.

Each IN625 specimen (X_S1, X_S2, XY_S1, and XY_S2) was interrogated for their

single crystal elastic constants, with texture coefficient variability informed by the EBSD scans oriented with the BD facing upward in Figure 5.2. These EBSD scans were each nominally 2 mm x 2 mm, demonstrating that small quantities of EBSD data are sufficient to inform the texture. Following the observed effects of residual stresses on RUS in Chapter 3, a freely-determined residual stress (RS) term was included in each calculation.

As shown in Table 5.5, the single crystal elastic constants are within one standard deviation of one another across all parameters, with some specimen to specimen variation observed in the individual means. The specimen to specimen variability is isolated by studying the specimens S1 and S2 of each raster condition, which is observed to be less than the difference between raster conditions. The value of the RS term was 0 within its uncertainty, indicating a negligible effect of residual stresses on the frequencies. While other IN625 parts were discovered to have significant residual stresses affecting RUS data in Chapter 6, the builds studied here were printed with the goal of minimizing residual stresses. The parameter means $\pm$ standard deviation are shown along with pairwise parameter plots in Figure 5.9.

Comparing the two raster conditions 'X' and 'XY', agreement is again observed within 1 standard deviation across all the parameters. This agreement demonstrates that the determination of single crystal elastic constants is robust to variation in the dominant texture components (EBSD in Section 5.2.2). The convergence of the parameters validates the use of this framework for a wide variety of AM printing conditions. Relative to the range of single crystal values in the literature [140, 159], all of the specimens in this study agree within 1 standard deviation except for A of X_S2. Considering the reference values in [140, 159] do not include uncertainties, the agreement with literature is excellent.

Following Chapter 3, the distributions of texture coefficients resulting from each set

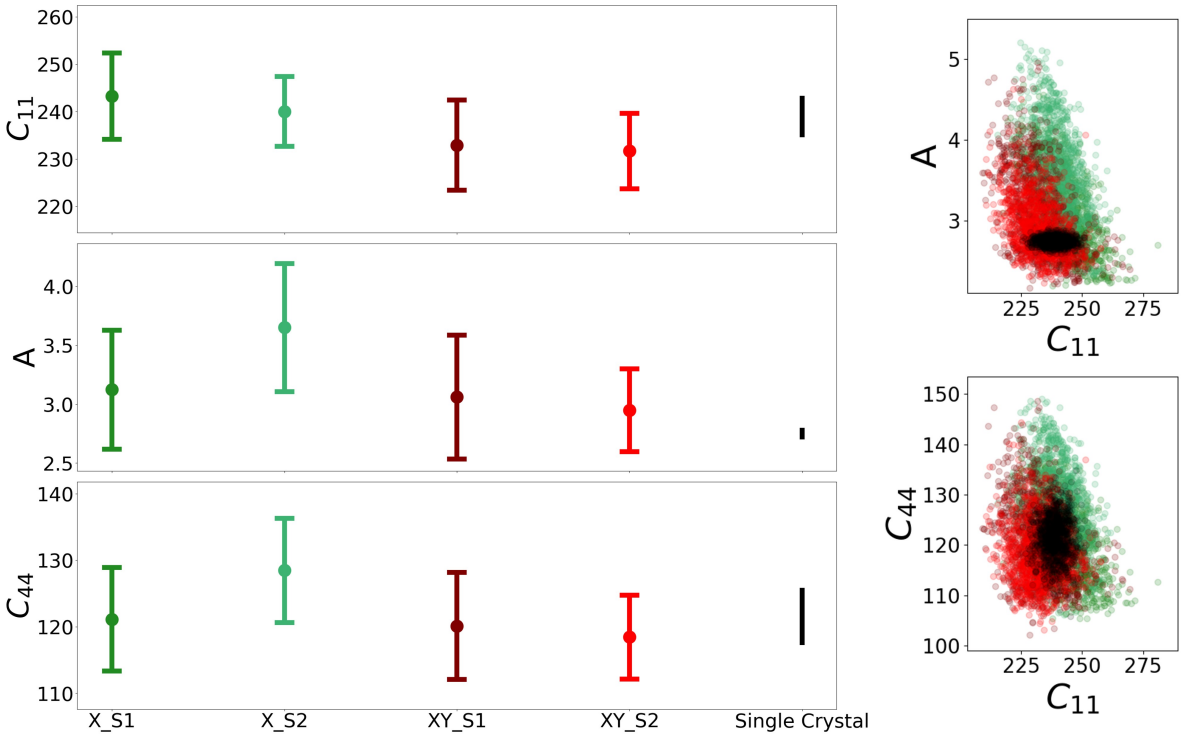

Figure 5.9: Single crystal elastic constants of AM IN625 comparing specimen to specimen (S1 vs S2) and raster condition (X vs XY). All the single crystal elastic constants agree within 1 standard deviation (error bars). The literature single crystal elastic constant values are represented by the range (black), with endpoints from [140] and [159] (no uncertainties provided). All of the specimens interrogated in this study showed agreement with the literature range within 1 standard deviation, except for the anisotropy ratio (A) of X_S2.

of specimen resonant frequencies can be used to plot both the polefigures representing the texture in the specimen (mean values) and the standard deviation at each point in the polefigure. By doing so, the polefigures can be compared to experimentally determined polefigures and analyzed for accuracy. Correspondingly, the mean values of the texture coefficients for specimen XY_S2 were used to plot the effective texture in Figure 5.10, along with the standard deviation generated with 3° resolution (intervals) in the polefigure. The texture coefficients across all 1800 particles were used to determine the standard deviation polefigure.

Figure 5.11 displays a low standard deviation throughout the pole figure, indicating a strongly convergent determined texture. Considering the texture is estimated together

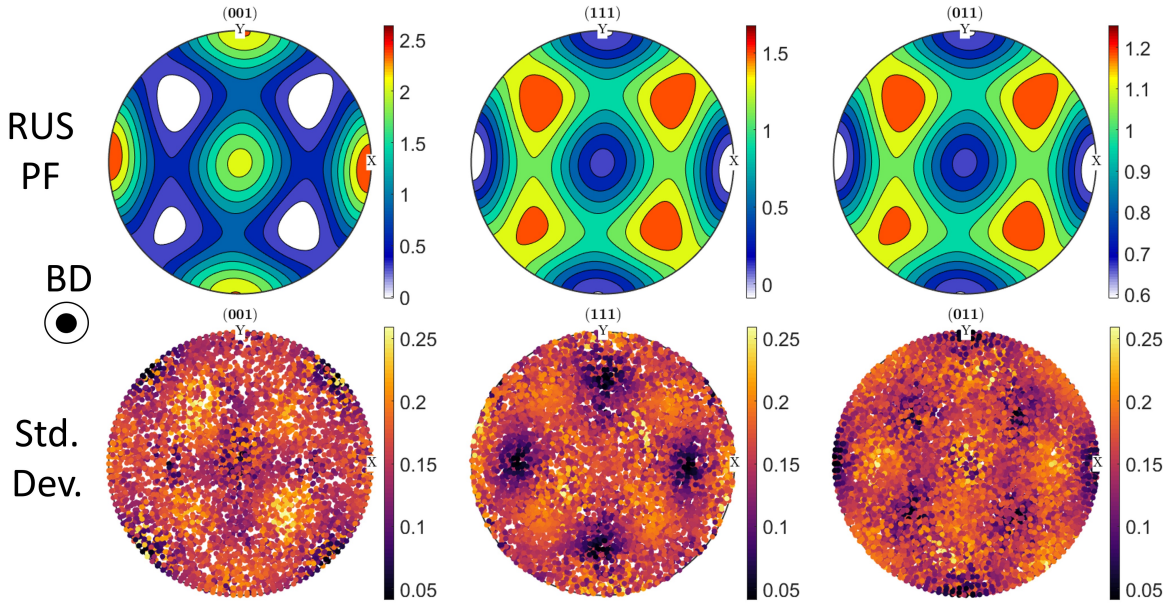

Figure 5.10: Convergent mean polefigures (upper) and pointwise standard deviation (lower) as determined from the RUS data for AM IN625 specimen XY_S2.

with the single crystal elasticity, this result is a powerful example of the capabilities of this technique. Comparing the texture (polefigures) determined from the resonant frequencies with those determined from EBSD measurements (Figure 5.2), agreement is observed in Figure 5.11.

The (001) and (111) polefigures display strong agreement in the positions of their high-MRD points, while the non-dominance of (011) orientations in the XY specimen makes the MRD points of the (011) polefigures appear to be less similar than the (001)/(111). Following Chapter 3, the agreement between the polefigures is even greater than it appears, as the RUS polefigures are effectively homogenizations from the elastic behavior (limited to 4th order coefficients), while the EBSD is discretely sampled from pointwise orientation measurements.

5.4.3 Ti-6Al-4V

The single crystal elastic constants were determined for AM Ti64 specimens printed with high, low, and standard electron beam energies. As described in Section 5.2.3, each

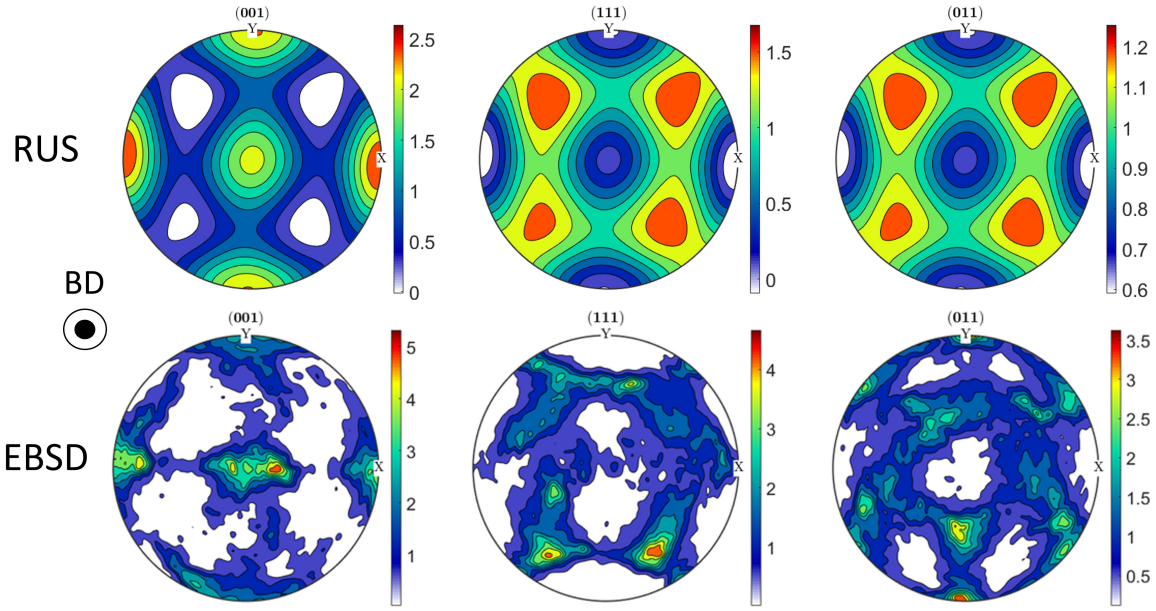

Figure 5.11: Convergent polefigures (upper) determined from the resonant frequencies and EBSD measured polefigures (lower) for AM IN625 specimen XY_S2. The RUS-derived polefigure is effectively a homogenization, resulting in the appearance of lower multiple of random distribution (MRD) values at the peaks of the polefigure compared to the EBSD polefigure.

parallelepiped specimen was sectioned coincident with the build direction.

As shown in Figure 5.12, there is agreement across all processing conditions with the range of values reported in the literature, besides C_{11}/ C_{13}, which agree within 2 standard deviations. However, there are small differences between the single crystal elastic constants of each printing condition, as the standard deviations do not predictably overlap between each mean value. Additionally, the range of reported values for the single crystal constants of Ti64 is broad as shown in Table 5.6, with the precise estimates of [144] (C_{11}=169.0 GPa, C_{33}=196.0 GPa, C_{12}=62.0 GPa, C_{13}=89.0 GPa, C_{44}=43.0 GPa, C_{66}^{calc}=40.0 GPa) closest in value to the reported single crystal constants here. The values in [144] are pointwise estimates, and therefore do not have an associated standard deviation ($\pm$) or measurement error (σ).

The difference in single crystal constants between each EBM power is likely a result

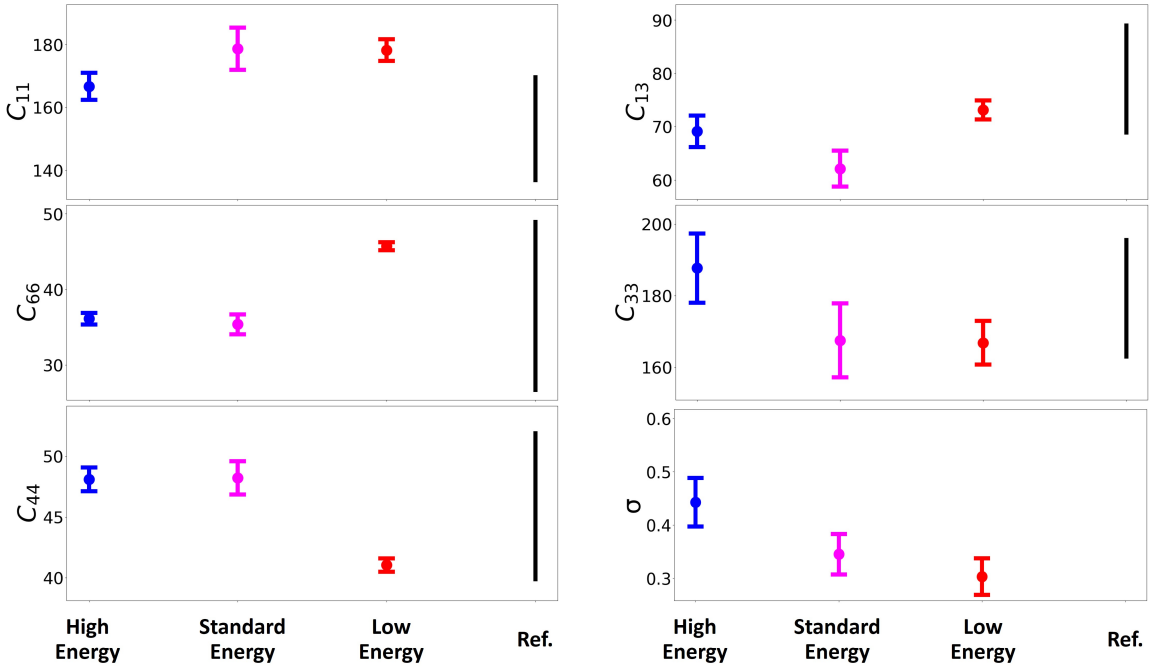

Figure 5.12: Ti64 single crystal elastic constants calculated from specimens produced with different EBM power settings. Ti64 elastic constant range of values from literature [144, 155, 161, 162] agree well with calculated elastic constants (black).

Ti64 Single Crystal Elastic Constants				
	High Energy	Standard Energy	Low Energy	Lit. Range [144, 155, 161, 162]
C_{11} (GPa)	166.8 ± 4.4	178.5 ± 6.8	178.2 ± 3.5	136.0 - 170.0
C_{33} (GPa)	187.4 ± 9.9	167.7 ± 10.4	167.0 ± 6.2	163.0 - 196.0
C_{12}^{calc} (GPa)	94.6 ± 4.8	107.8 ± 8.0	86.7 ± 3.5	62.0 - 92.0
C_{13} (GPa)	69.0 ± 3.0	62.1 ± 3.4	73.2 ± 1.8	68.0 - 89.0
C_{44} (GPa)	48.1 ± 1.0	48.2 ± 1.4	41.0 ± 0.5	40.0 - 52.0
C_{66} (GPa)	36.1 ± 0.8	35.4 ± 1.3	45.7 ± 0.5	26.0 - 48.0
σ (kHz)	0.44 ± 0.05	0.35 ± 0.04	0.30 ± 0.03	-

Table 5.6: Single crystal elastic constants calculated from AM Ti64 specimens printed with different electron beam melting powers. Observed range of elastic constants for Ti64 from literature [144, 155, 161, 162] in agreement with measured values across all processing conditions.

of specimen to specimen variability related to residual stresses, porosity, phase fraction of retained β-phase, prior β-grain size, and interstitial content. Following [65], the values of the α-phase single crystal elastic constants are extremely sensitive to changes in the independently fitted parameters, as the inclusion of grain shape altered the constants C_{11} and C_{12} by 41.7 GPa (31%) and 19 GPa (19%), respectively. These shifts support the

high sensitivity of the solution here to small changes in specimen processing. Specimen to specimen variability is compounded by factors such as α-phase-variant selection during the solidification of Ti64 from its parent cubic-β phase [156]. While this phenomenon is fairly well understood relative to solidification, the effect of variant selection on texture heterogeneity and its effect on an RUS inversion through resonant mode sensitivity is completely unexplored.

The observed difference in the single crystal elastic constants of the low energy condition could stem from increased scattering with the higher volume fraction of voids (as noted in Section 5.2.3). Despite the quantification of voids here, altering the density of the component does not rigorously account for the effects of inelastic scattering on the resonant frequencies in an anisotropic medium. In fact, the effect of inelastic scattering in an anisotropic medium are not well quantified via current models and therefore could not be incorporated here.

5.5 Conclusions

- The single crystal elastic constants of cobalt-nickel-base superalloy SB-CoNi10C, nickel-base Inconel 625, and Ti-6Al-4V are quantified using additively manufactured, polycrystalline specimens. Agreement with literature values is observed within the calculated uncertainty of each single crystal elastic constant.

- The accuracy of the single crystal constants is significantly increased by incorporating texture coefficient uncertainty within the model, with priors determined from EBSD measurements. 2 mm x 2 mm areas of EBSD data are shown to be sufficient to inform the texture priors of the single crystal elastic constant calculations.

- The variability of the calculated single crystal constants of Ti64 between different processing conditions is shown to be significant, likely resulting from secondary

effects on the resonant frequencies such as scattering from voids, inclusions, and secondary phase effects.

Chapter 6
RUS and FEM Quantification of Grain Structure Evolution: Arbitrary Geometry AM Parts with Residual Stress

Despite the advantages of metal additive manufacturing (AM), ensuring integrity and reproducibility for built components is a barrier to the implementation of AM components in critical applications. Component qualification necessitates Non-Destructive Evaluation (NDE), but existing NDE frameworks are insufficient for the rapid and cost effective screening of variable AM components. In this work, alterations in laser powder bed fusion (LPBF) AM process parameters were characterized using Resonant Ultrasound Spectroscopy (RUS). Samples that were subjected to a Hot Isostatic Press (HIP) and Heat Treatment (HT) post-processing step exhibited changes in resonance frequencies that varied in magnitude and direction with the type of resonance mode. The initial build direction prior to HIP and HT had a negligible effect on resonant frequency changes after recrystallization. The change in resonant frequencies at each process condition was predicted using Finite Element Modeling (FEM) informed with Electron Backscatter Diffraction (EBSD) data. FEM identified that the experimentally measured change in resonant response between the initially textured state and the recrystallized state was dominated by grain orientation dependent changes in elasticity. The EBSD-estimated elastic constants and FEM results were validated using experimental laser vibrometry and RUS inversion of elastic constants. RUS Inversion by Bayesian inference and Hamiltonian Monte Carlo has not been used to characterize an AM nickel-base alloy prior to this work. These results demonstrate that RUS is capable of detecting part to part microstructure variability between built AM components.

The nickel-based alloy IN625 served as the model material in this work, demonstrating the potential to use RUS integrity prediction for other AM alloys. Characterization of a single phase, solid-solution strengthened nickel alloy with RUS additionally establishes a proof of concept to study more complex alloy systems with RUS. IN625 is additively manufacturable with either laser or electron beams as the heat source. There has been a significant amount of research on the solidification of IN625 by AM, but problems such as non-equilibrium precipitate formation and build repeatability remain [163, 164, 165, 166]. Different microstructures, texture strengths, and levels of residual stress result in varying kinetics and behavior for these components. RUS has been used to quantify microstructure evolution in Ni-based alloys undergoing recrystallization [167], motivating its usage to detect variability in these AM components.

6.1 Materials and methods

IN625 AM samples were provided by The Air Force Research Laboratory (AFRL)[1] as part of the MID^{3}AS (Materials inform data-driven design for additive structures) initiative [168, 169]. This AFRL AM Modeling Challenge Series involved predicting macroscopic properties from varied AM specimens and microstructures under the MID^{3}AS effort. The composition of the powder used in printing is given in Table 6.1.

IN625 specimens were printed in an EOS M280 LPBF system. Process parameters were within the EOS standards for IN625. Each milli-tensile dogbone sample (Figure 6.1) was printed as a rectangular block of dimensions 60mm x 12mm with varied thicknesses of 1mm, 3mm, or 5mm. These dimensions correspond to the Z, Y, and X dimensions in Figure 6.1, respectively. The specimens were machined to the milli-tensile geometry from the as-printed plates. The remaining as-printed surfaces (YZ faces) of the milli-

[1] Air Force Research Laboratory, Materials and Manufacturing Directorate, Wright-Patterson AFB, OH, 45433

Chemical Analysis (wt.%)						
C	Si	Mn	P	S	Cr	Ni
0.03	<0.01	<0.01	<0.004	0.002	21.20	Bal.
0.01	0.05	<0.01	<0.001	<0.01	21.69	Bal.
Mo	Nb	Ti	Al	B	Co	Cu
8.91	3.56	0.01	0.05	0.001	<0.01	0.01
9.06	3.75	0.02	0.04	0.001	<0.01	0.01
Fe	N	O	Ta	Mg		
3.09	0.008	0.015	<0.01	<0.001		
2.12	0.005	0.035	<0.02	<0.001		

Table 6.1: Chemical Analysis of IN625 Powder (Prior to build). Two measurements are shown below each element. Quantities in wt.% [169].

tensile specimens were either surface ground with 600 grit silicon carbide sandpaper or left as as-built surfaces to examine the effect of surface roughness during tensile testing. All RUS results shown here were gathered from 5mm thick samples, though the same trends were present across all sample thicknesses. In this work only specimens with as-built surfaces were studied, incorporating surface roughness variability into the sample to sample variability. The experimentally observed frequency shift from surface grinding was consistent with predicted resonance frequency changes as part dimensions are reduced. Therefore, changes in surface condition were not investigated further. Studying 5mm thick samples enabled a minimization of uncertainty originating from dimensional tolerances as a percentage of the specimen thickness. The samples were varied in inclination from the build plate, at either 50° or 90° from the build plate as depicted in Figure 6.1. All milli-tensile samples underwent a standard stress-relief heat treatment while still attached to the build plate, and subsequently half of these 60 samples were hot isostatic pressed (HIP) and heat treated (HT). A total of 3-5 samples were tested with each combination of parameters. Parameter combinations under study were therefore build inclination, surface condition, and samples that did or did not undergo HIP and HT.

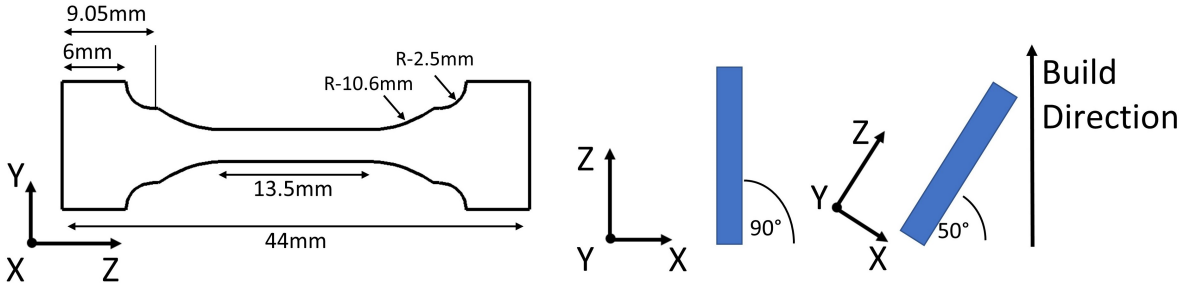

Figure 6.1: Milli-tensile dogbone specimen dimensions (left). Build orientations under study (right). Build direction is parallel to long axis of 90° specimen (z-axis in local coordinates). Thickness changes for the specimens occur along the x direction.

Samples were analyzed in either the stress-relieved (SR) state or the SR + HIP + HT state. These states will be referred to as the textured state and the recrystallized state, respectively. In AM, microstructures are often columnar grain structures aligned with the direction of the highest thermal gradient during solidification. The build direction corresponds to the highest thermal gradient as the part conducts to the build plate, resulting in preferred crystal growth along the <001> preferred growth directions for cubic crystals [16, 20, 170, 171].

6.1.1 Experimental resonant ultrasound spectroscopy and laser vibrometry

The experimental resonant ultrasound spectroscopy setup used to test the milli-tensile dogbones is shown in Figure 6.2. RUS operates by contacting piezoelectric transducers to the sample and exciting elastic waves. Characteristic mechanical resonance is measured when the sample has an increased amplitude (i.e. resonance) response at a given driving frequency. The piezoelectric transducers are used for both excitation and detection. These resonant modes are observed as amplitude peaks in a broadband kHz spectrum. The piezoelectric transducers and specimen holder were provided by Vibrant Corporation.[2] No bonding or loading was used to affix the specimen to the transducers. By allowing the specimens to freely deflect away from the transducers, contact forces

[2]Vibrant Corporation, 8916 Adams St NE, Albuquerque, NM 87113

that would alter the conditions for free resonance are avoided. Laser vibrometry was conducted by Vibrant Corporation on a Polytec PSV-400 Scanning Laser Vibrometer to a resolution of 0.1 nm.

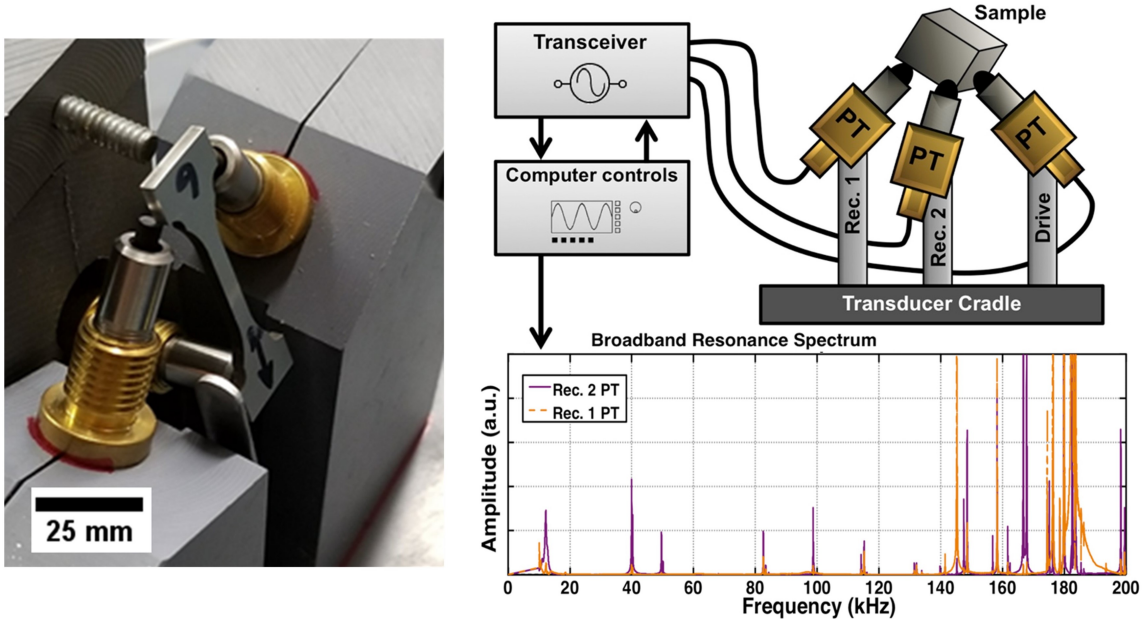

Figure 6.2: Experimental setup for measuring resonant frequencies of AM tensile specimens (left). Sample freely rests on piezoelectric transducers to eliminate contact forces. Piezoelectric transducers are used for both excitation and detection of resonance frequencies. Size of broadband frequency spectrum (right) is set prior to scan to ensure >75 resonance modes are measured. Each sample is scanned 3 times, with the sample being adjusted in the cradle between each run to ensure no modes are missed based on sample configuration in the cradle.

6.1.2 EBSD

Electron Backscatter Diffraction (EBSD) was carried out on an FEI[3] Teneo scanning electron microscope with an EDAX[4] detector and EDAX TSL OIM software. The backscatter data was taken with the build direction at the top of the image as indicated in Figure 6.4. EBSD was conducted with a beam current of 6.4 nA, voltage of 30 keV, and step size of 1.5 μm . EBSD Crystal orientation data are colored using inverse pole figure coloration relative to the <100> direction (build direction).

[3]Thermo Fisher Scientific, 5350 NE Dawson Creek Drive, Hillsboro, Oregon 97124
[4]EDAX Inc, 392 East 12300 South, Suite H, Draper, UT 84020

6.1.3 Finite element modeling

Modeling was completed in ABAQUS. Milli-tensile dogbone specimens were modeled according to nominal dimensions in Figure 6.1 as provided by AFRL. Mesh densities were progressively refined until results converged for the Lanczos-Eigensolver frequency analysis with 80 modes calculated. Homogenized elastic tensors were derived from EBSD data in both the textured and recrystallized state (Figure 6.4), and used to assign the material an effective elastic tensor relative to the build direction. The MTEX package in MATLAB was used to calculate the effective aggregate elastic tensor of each sample state [127]. The required single crystal elastic constants (C_{11}^{SC}=243.3 GPa, C_{12}^{SC}=156.7 GPa, C_{44}^{SC}=117.8 GPa) for IN625 were taken from Wang et al. [172]. The average of the Voigt and Reuss bounds, known as the Hill average, was used for elastic tensor estimation [20]. The Hill averaging scheme has been validated [173] to estimate the elasticity of textured polycrystals with the <001> direction aligned with the longitudinal wave propagation direction.

6.1.4 Quantification of effective elastic constants by RUS inversion

The experimental determination of the resonant frequencies allows for the measurement of the elastic constants through an inverse calculation [51, 58]. RUS inversion involves iteratively varying the effective elastic constants and calculating the theoretical resonance frequencies of the specimen to match experimentally gathered frequencies [51, 60, 61]. Simple shapes such as parallelepipeds or spheres are preferred for computational efficiency and reduced geometrical measurement error, though more complex shapes are possible [63]. Because accurate measurements of the sample dimensions are directly used to calculate resonance frequencies during the inversion, a dimensional tolerance of $\pm$ 1% is considered the maximum allowable geometric uncertainty. The AM sample used for RUS inversion was fabricated using the same AM process parameters

as the milli-tensile specimens, then machined to a rectangular parallelepiped geometry (4.85 x 6.82 x 18.24 mm) using electrical discharge machining. The open source inversion codes used here (Cmd-Stan-RUS) [68] are capable of calculating both the elastic tensor of the specimen and the rotations of the effective elastic constants in a Bayesian inference framework with Hamiltonian Monte Carlo (HMC). Bayesian inference frameworks are significantly more robust toward avoiding local minima solutions than optimizations used by traditional inversion frameworks [58]. AM components have not been examined using Bayesian inference prior to this work. All RUS inversion results presented here utilized the Bayesian inference framework. Each inversion utilized 6 independent Markov Chain calculations, a warmup of 300 Markov Chain sampling steps for each chain, and 1000 sampling steps to calculate the steady-state behavior of the chain. A polynomial order of 12-14 was used to calculate the theoretical resonance frequencies and compared to the first 45-65 experimentally measured resonance frequencies. The standard deviation between the calculated resonant frequencies and experimentally measured resonant frequencies was calculated to be 1.2 - 1.4 kHz.

RUS inversion of a sample's effective elastic constants does not depend on the single crystal elastic constants or choice of averaging scheme (i.e. Voigt, Reuss), providing a measurement of the effective elastic tensor of the specimen. The RUS inversion calculation was used to validate the Hill elastic tensor estimated from EBSD data.

6.2 Results

6.2.1 Experimental resonant ultrasound spectroscopy

Analysis of RUS data from samples with different combinations of build direction, surface condition, and thermal history indicated that recrystallization during HIP + HT resulted in the largest shifts in resonance response. Analysis of the raw RUS spectra from representative samples is shown in Figure 6.3. The frequency shift at each sample

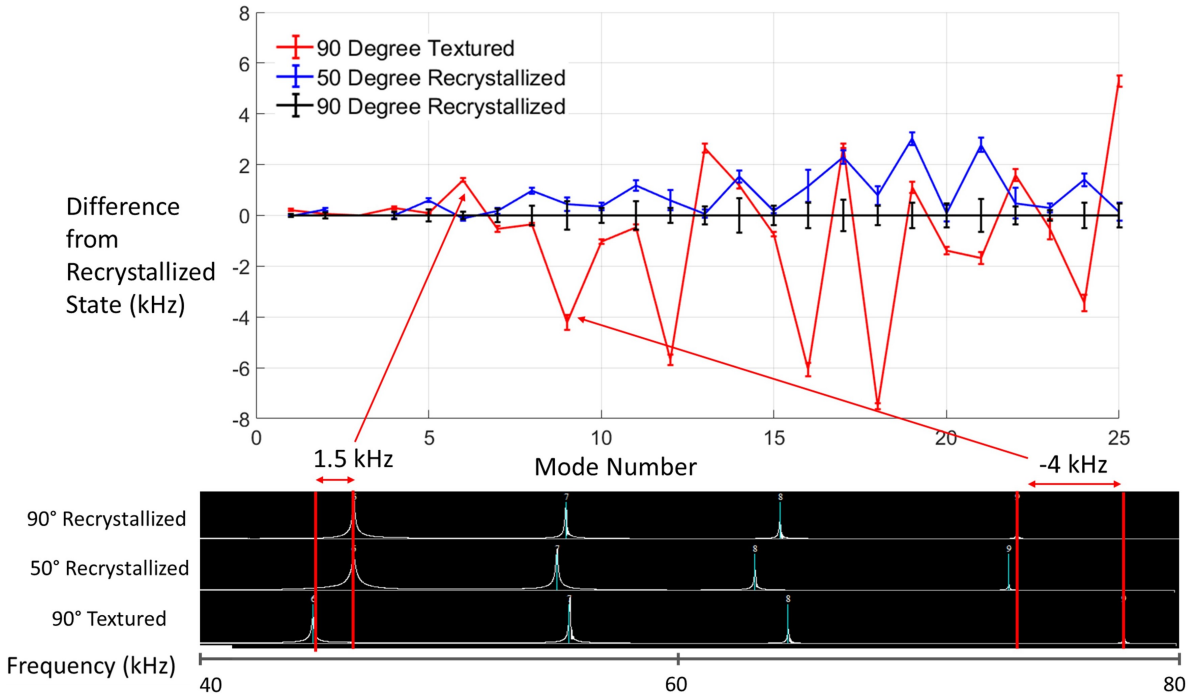

Figure 6.3: Experimental results from AM milli-tensile specimens of different states. Each state contains 3-5 samples with error bars representing standard deviation. The 90° recrystallized state (top spectra) was chosen as the reference state for comparison and is set as zero at each mode. Shifts from the recrystallized state to the 90° textured state (bottom spectra) are more significant than those to the 50° recrystallized state (middle spectra).

condition was an average of 3-5 samples, with standard deviations shown. Shifts between the textured and recrystallized state were larger than those between the 90° and 50° recrystallized states. The shift in frequency was larger and displayed a more varied trend across the spectrum for the shift between the 90° recrystallized and 90° textured samples. The as-received samples did not contain any 50° samples in the textured state, but the effect on the RUS response is understood as a rotation of the sample relative to the build direction dependent grain structure.

6.2.2 Finite element modeling and laser vibrometry

Finite element models were conducted for both the recrystallized and textured states. The model inputs were the homogenized elastic tensor, density, and sample geometry. The elastic tensor for each state was generated using the EBSD data in Figure 6.4. This

EBSD data was used to simulate the grain orientation dependent Hill effective elastic tensor in MTEX with single crystal elastic constants of IN625. The homogenized elastic tensors displayed orthorhombic symmetry.

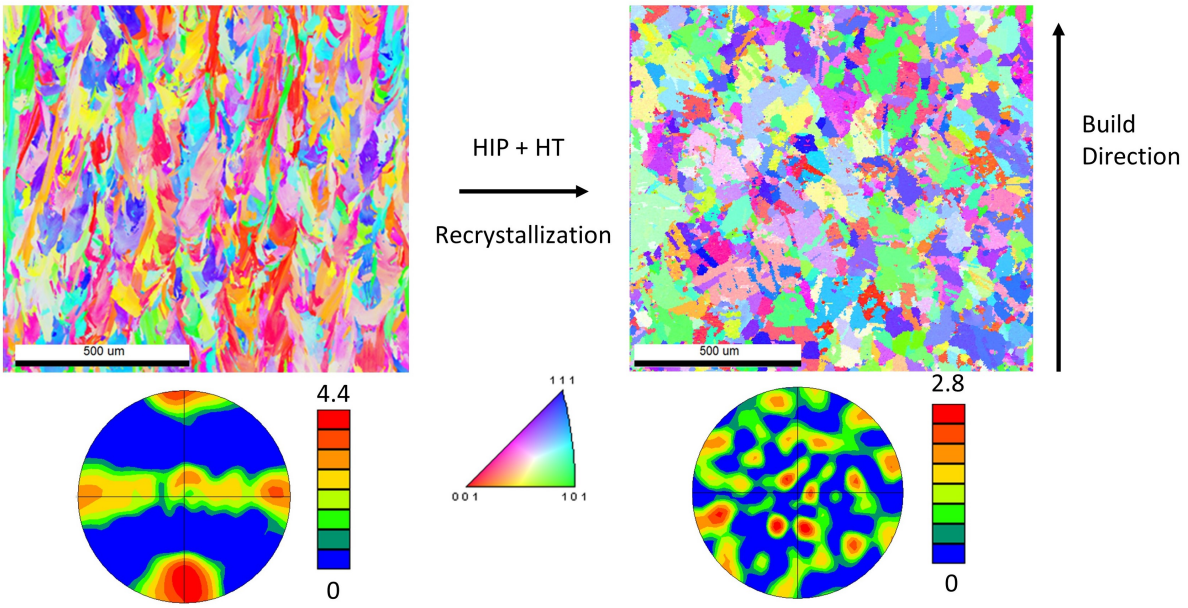

Figure 6.4: Electron Backscatter Diffraction of textured specimen (left) and recrystallized specimen (right). Corresponding pole figures below each EBSD map indicate that the dominant <001> texture in the textured state was reduced during recrystallization. The scale bars correspond to multiples of random and are unitless. Both EBSD maps are taken from milli-tensile specimens with the loading axis of the tensile sample aligned with the build direction (90° built samples).

Resonant frequencies were calculated in FEM and compared to the experiment. ABAQUS enables visualization of mode-type at each resonance frequency, therefore the modes identified in FEM could be quantitatively compared to resonance frequencies measured by experiment. Figure 6.5 shows the change in resonance frequency for each mode between the recrystallized and textured states. The difference in resonance frequency plotted in Figure 6.5 is defined for the modeled case in Equation 6.1 below.

$$Shift(\%kHz) = \frac{f_r^{Model}(Recrystallized) - f_r^{Model}(Textured)}{f_r^{Model}(Textured)} * 100 \qquad (6.1)$$

Note that the difference (y-axis) in Figure 6.5 is defined at each mode on the x-axis and

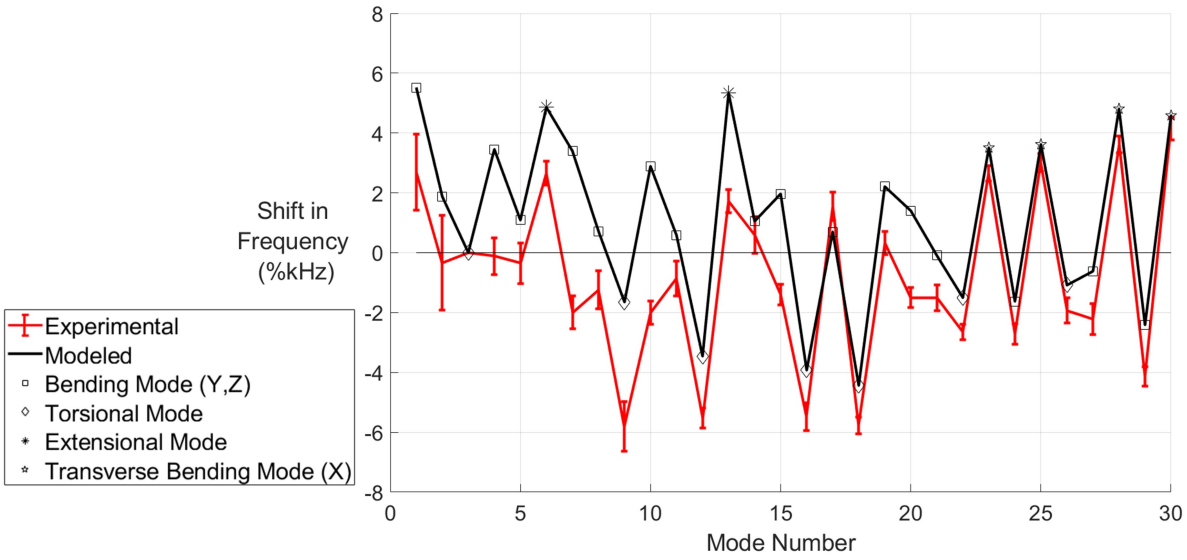

Figure 6.5: Difference in Frequency (% kHz) for 90° built samples between the recrystallized and textured states. Difference between recrystallized and textured states from experiments (red) and models (black) agree quantitatively. A difference of zero at any mode number indicates no change between the recrystallized and texture state at that mode. Mode shape information is overlaid on modeled results. Agreement is observed across the first 30 modes, indicating that the FE modeled changes in texture intensity during recrystallization replicate the dominant trends observed by RUS experimentally.

linked to its mode-type. The difference between the two models closely matches both the magnitude and the mode-type position (e.g. first torsional mode is sixth mode in resonant spectrum) of the experimental data. Figure 6.6 shows the modeled mode shapes, previously labeled in Figure 6.5, visualized in ABAQUS. Upon recrystallization, torsional modes decrease in frequency while bending and transverse bending modes increase in frequency. The sensitivity of certain mode-types to recrystallization is dependent on the prior elastic symmetry and microstructure. Mode sensitivity is understood with solid mechanics arguments, as certain components of the elastic tensor are affected more than others during recrystallization and change the overall anisotropy of the grain structure.

The model therefore captures the dominant factor affecting resonance differences between the textured and recrystallized state, namely elastic changes due to changes in

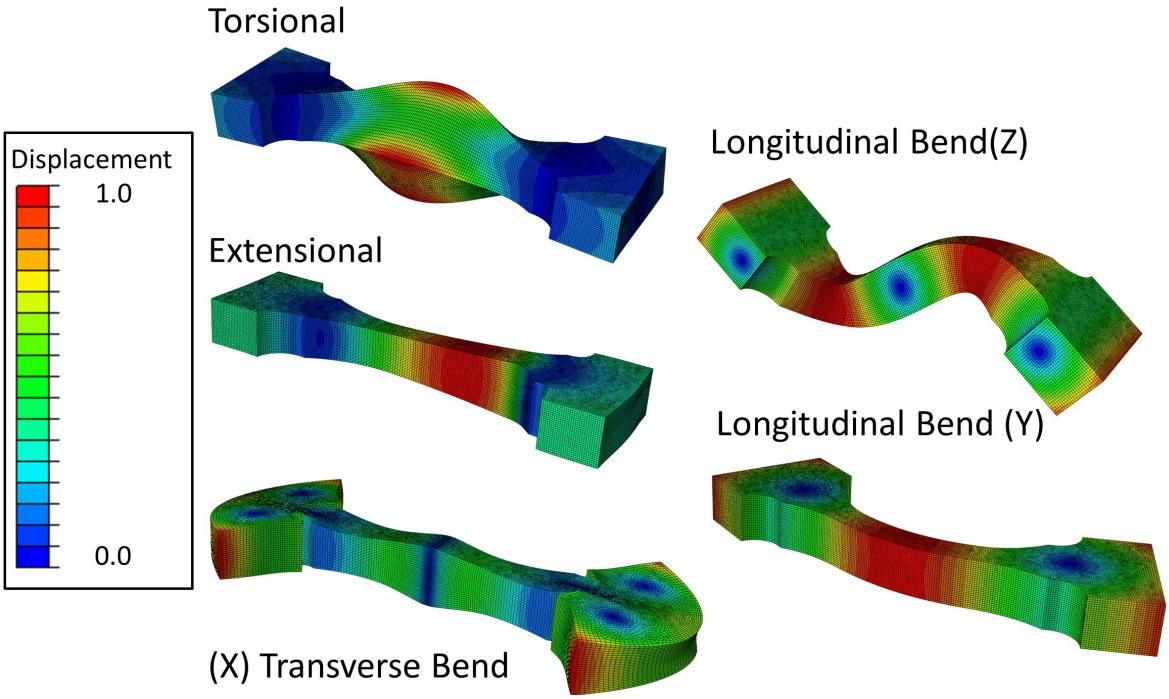

Figure 6.6: Mode shapes of AM milli-tensile specimens corresponding to those labeled in Figure 6.5. Red indicates maximum positive displacement and blue represents no displacement. Displacements are exaggerated for visualization and magnitudes are normalized as 0.0 and 1.0 for the minimum and maximum displacements, respectively. All displacements are purely elastic. Note that Z and Y bending modes behave similarly for the 90° build direction components and are therefore grouped together as longitudinal bending modes for analysis in Figure 6.5.

the aggregate texture intensity relative to the specimen reference frame. Further, mode-types identified in ABAQUS are proven to be consistent with experimentally measured frequencies in the direction and magnitude of their shift.

Experimental validation for the mode-type trend was acquired by Vibrant Corporation using laser vibrometry. Laser vibrometry confirmed the frequency and mode shape of each modeled frequency in ABAQUS. The 3rd order torsional mode in Figure 6.7 for both the textured and recrystallized states exemplifies the quantitative agreement between ABAQUS FEM results and laser vibrometry across all resonant frequencies.

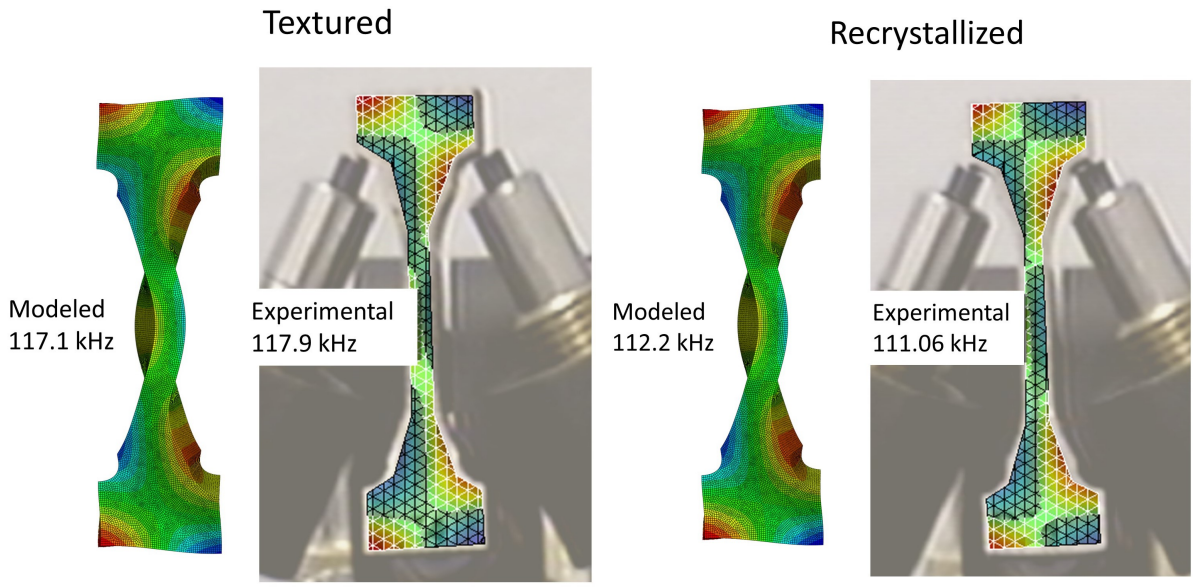

Figure 6.7: Validation of a single mode shape (3rd order torsional mode, 12th overall mode) using laser vibrometry (experimental) and ABAQUS (modeled). The difference in the 3rd order torsional resonance mode between the model and the experiment for the textured state (0.7% kHz) and the recrystallized state (1.0% kHz) indicates quantitative agreement. Laser vibrometry measures in and out of plane displacements to a maximum 1.5 nm out of plane (red) and 1.5 nm into plane (blue) at a resolution of 0.1 nm. Displacements shown in ABAQUS are also shown as in plane/ out of plane, with maximum out of plane and maximum into plane colored red and blue respectively. Laser vibrometry and modeling correlated at every resonance frequency.

6.2.3 AM aggregate elastic constants from RUS inversion

An IN625 AM specimen in the textured state was prepared in a parallelepiped geometry to validate the effective elastic tensor estimated from EBSD data. The orthotropic (9 independent component) effective elastic tensor was determined from experimentally measured RUS data using RUS inversion, as described in Section 6.1.4. The simplified parallelepiped geometry enables computationally tractable RUS inversions that can be translated to the dogbone geometry specimens in FEM. The full elastic tensor (Voigt notation) calculated using RUS inversion is given in Figure 6.8. These elastic moduli were measured in the stress-relieved state. The difference between the elastic tensor calculated by experimental RUS inversion and estimated from EBSD data was 1-2% for

each independent component of the elastic tensor. This difference was a uniform increase for each independent effective modulus value calculated from the EBSD data.

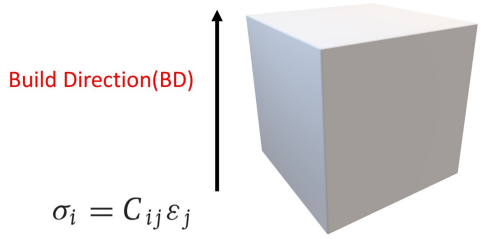

$$\sigma_i = C_{ij}\varepsilon_j$$

$$\begin{bmatrix} C_{11} & C_{12} & C_{13} & 0 & 0 & 0 \\ C_{12} & C_{22} & C_{23} & 0 & 0 & 0 \\ C_{13} & C_{23} & C_{33} & 0 & 0 & 0 \\ 0 & 0 & 0 & C_{44} & 0 & 0 \\ 0 & 0 & 0 & 0 & C_{55} & 0 \\ 0 & 0 & 0 & 0 & 0 & C_{66} \end{bmatrix}$$

289.3 ± 11.0	135.5 ± 8.7	136.5 ± 8.8			
135.5 ± 8.7	293.5 ± 6.8	137.7 ± 8.8			
136.5 ± 8.8	137.7 ± 8.8	281.5 ± 7.1			
			88.6 ± 0.3		
				89.3 ± 0.2	
					78.5 ± 0.5

Figure 6.8: RUS inversion of textured sample state (GPa). RUS inversion was carried out with Cmd-Stan-RUS open source codes using Bayesian inference [68]. ± indicates a single standard deviation calculated during convergent Markov Chain Monte Carlo behavior. Calculated in the textured (stress-relieved) state.

In addition to calculating the elastic constants with respect to the sample reference frame in Figure 6.8, a rotated elastic tensor was calculated. The Euler angles of the rotation calculation were designed to calculate the rotation of a single crystal and its intrinsic elastic constants in the case that a sample was sectioned off-axis from the principal single crystal directions [68]. In the case of a polycrystal, the rotation calculation does not have the uniform symmetry of a single crystal to calculate relative to the specimen reference frame. The rotations are instead utilized here to search for alternate representations of the 9 independent component elastic tensor relative to the specimen reference frame. The Euler angles of the rotation and the rotated elastic tensor are given in the textured (as-built) state in Figure 6.9.

The orientation calculated by the rotation component of the inversion coincided with the position of the {111} family of orientations as shown in Figure 6.10. The maxi-

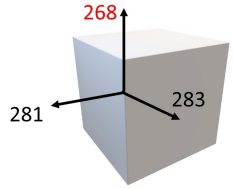

Rotations (degrees)

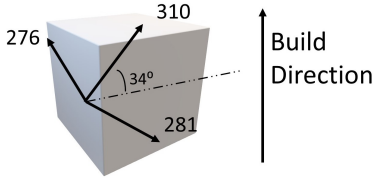

281.1 ± 7.9	131.3 ± 10.7	127.4 ± 8.1			
131.3 ± 10.7	283.4 ± 10.2	129.2 ± 8.6			
127.4 ± 8.1	129.2 ± 8.6	268.0 ± 8.4			
			84.7 ± 0.8		
				87.2 ± 0.7	
					76.9 ± 0.6

*

172.0
34.2
72.5

=

280.8 ± 11.1	137.1 ± 12.2	124.4 ± 9.3			
137.1 ± 12.2	309.5 ± 9.9	109.3 ± 8.3			
124.4 ± 9.3	109.3 ± 8.3	275.5 ± 10.7			
			69.4 ± 1.0		
				88.1 ± 2.1	
					74.4 ± 1.1

Figure 6.9: Inversion results in GPa for textured sample state. Sample specific effective elastic constants (left) are given in the as-built state, and are of reduced magnitude compared to the stress-relieved state shown in Figure 6.8. Residual stresses result in reduced resonant frequencies, and consequently reduced elastic constants compared to Figure 6.8. Calculated rotations (Bunge Euler angles) and independent elastic tensor for {111} orientations (right). The Euler angles correspond to a 34° inclination from the build plate.

mum texture strength of the {111} orientations calculated from EBSD (39° from the build plate) agreed with the values calculated through inversion to within 5°. Further, 6 independent calculations of the rotations resulted in 6 distinct, but equivalent, representations of the 34° orientation relative to the build plate. The corresponding rotated tensor aligned to each unique rotation.

6.3 Discussion

Laser vibrometry results demonstrate that mode-type identification is critical during analysis, as adjacent modes can display shifts of opposite sign. The modes then deviate from their original mode-type order, requiring mode-type information in both the original and final state to identify the shifts of each mode. A shift in certain mode-types could be completely misinterpreted without mode-type information. Similarly, defects such as porosity could close up during the HIP and HT process, altering the resonance response

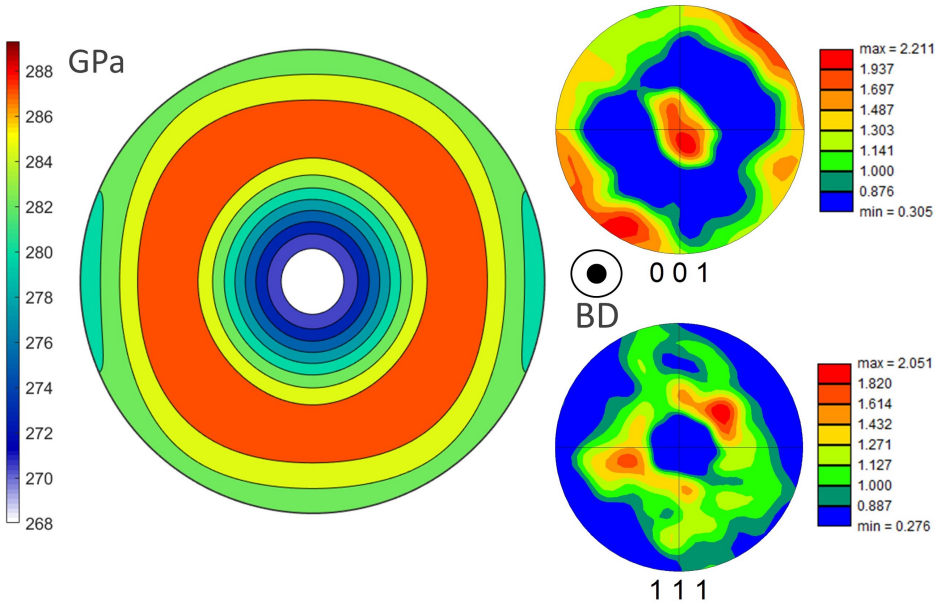

Figure 6.10: EBSD results(right) for {111} orientations in the textured AM sample state closely match maximum modulus direction (left) calculated by inversion. Build direction is out of the page for both EBSD and modulus spherical representation. Effective elastic modulus given in GPa. EBSD data given in multiples of random (MRD).

concurrently with the texture. The change in resonance frequencies due to the defects is easily modeled with the forward modeling framework presented here, but typically results in a small change in the resonance frequencies due to the low overall volume occupied by the defects. The porosity was measured by optical microscopy as 0.018% prior to HIP and 0.016% after HIP [169], and therefore neglected in this analysis. In situations where the defect content is significant, techniques such as x-ray computed tomography (CT) could complement the capabilities of RUS presented here by quantifying the defect content before and after HIP and HT.

Discrepancies greater than 2% exist between model and experiment for resonance frequencies in the textured state but not the recrystallized state, indicating that residual stresses and microstructure heterogeneity are likely the primary sources of error in the model. This is supported by the sensitivities of certain mode-types to recrystallization as reported by Rettberg et al. [167]. Despite AM recrystallization occurring throughout the

bulk rather than solely at the surface as in [167], mode-type correlation demonstrates that the dominant trend is elasticity changes due to changes in grain structure. Quantities such as residual stress are observed to cause global changes to the resonance frequencies, not mode-dependent trends, supporting this intuition. However, the observation of residual stress relief does not fully explain the changes as measured by RUS inversion.

Changes in the elastic tensor due to residual stresses were quantified by RUS inversion before and after stress-relief HT; residual stress relief results in a global 1.7-2.1% increase in each resonant frequency for this AM inversion sample. This global 1.7-2.1% change in each resonant frequency corresponds to a difference between the as-built elastic tensor shown in Figure 6.9 and the stress-relieved tensor in Figure 6.8 (left). The % change of each mode (up to mode 50) is shown in Figure 6.11.

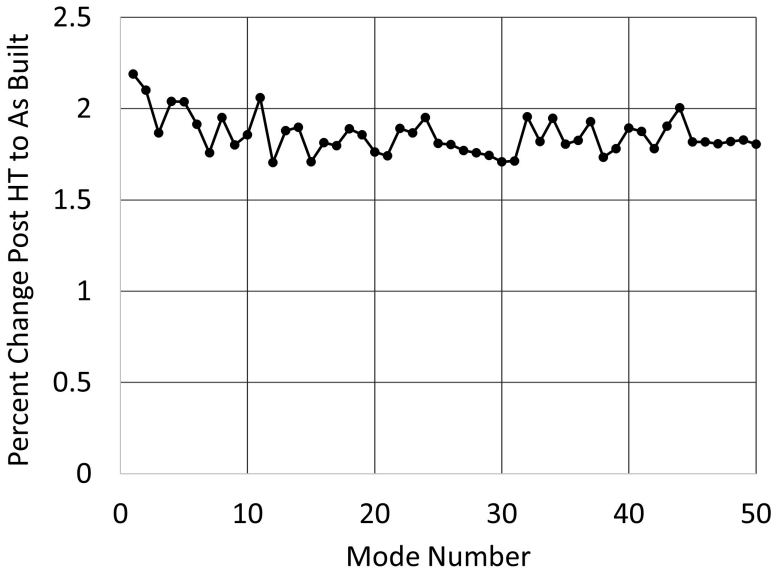

Figure 6.11: Percent change of each resonant frequency after IN625 stress relief. Despite observation of uniform shift across all frequencies, build direction dependent elastic constants show larger shifts in their values after stress-relief, indicating that residual stresses are strongest along the build direction.

The changes in the effective elastic constants are $<C_{11}>$ (3.2 GPa), $<C_{22}>$ (6.2 GPa), $<C_{33}>$ (8.6 GPa), $<C_{12}>$ (-1.1 GPa), $<C_{13}>$ (-0.1 GPa), $<C_{23}>$ (1.1 GPa), $<C_{44}>$ (2.2

GPa), $<C_{55}>$ (2.2 GPa) and $<C_{66}>$ (2.6 GPa) after stress-relief. The changes in the $<C_{33}>$ and $<C_{66}>$ indicate that residual stress relief causes larger changes in the build direction dependent components of the elastic tensor (low modulus directions that align with the <001> texture in Figure 6.10). The moduli changes are given in % in Figure 6.12.

1.4%	**0.7%**	**0.4%**			
0.7%	**2.2%**	**1.3%**			
0.4%	**1.3%**	**2.9%**			
			2.6%		
				2.5%	
					3.2%

Figure 6.12: Percent change of each elastic moduli value after IN625 stress relief.

The larger changes in $<C_{33}>$ and $<C_{66}>$ agree with literature observations of residual stresses, shown to be higher in magnitude along the build direction for printed AM IN625 components [174]. Additional AM specimens with varying texture strengths and residual stresses will need to be studied to further elucidate the relation between residual stress relief and calculated elastic constants by RUS inversion. The 1.7-2.1% increase in all frequencies after stress-relief appears to be the most reliable indicator. This is supported by the effective orientation of the {111} calculated by the inversion codes; the calculated 34° inclination of the {111} orientations from the build plate is identical before and after stress-relief HT.

The inversion rotation calculation quantifies the orientation of the {111} orientations

in these AM IN625 parts, but has not been extended to more complex cases. Using RUS to non-destructively quantify texture strengths, texture symmetries relative to the sample, or texture distributions would further develop RUS as a valuable tool for metal AM. For example, layer by layer AM grain growth is often slightly inclined toward the heat source scanning direction. This results in the <001> growth direction of each scan track being inclined away from the build direction as in [21]. The rotation component of the RUS inversion framework should be capable of calculating the angle and effective stiffness of the resolved <001> component, despite each <001> columnar grain being misaligned relative to each other and the build direction. However, the robustness of the rotation calculation is yet to be proven when multiple texture components are present with their own symmetries. Determination of this capability will require additional AM samples with controlled textures.

Comparing the calculated elastic moduli of AM IN625 to the literature, the aggregate elastic constants of the LPBF IN625 specimen deviated from literature values for both conventionally produced IN625 (annealed) and AM IN625 produced by directed energy deposition (DED) [172]. The directional modulus of the LPBF IN625 here was calculated to be 198 GPa along the build direction, slightly lower than the isotropic macroscopic Young's modulus of the annealed IN625 (207 GPa) material and higher than the DED IN625 (152.0 GPa) as measured by neutron diffraction in [172]. The <001> texture strength is generally higher for DED components, supporting the accuracy of the RUS measurement for the LPBF material here [2, 16].

A limitation on the usage of RUS to compare AM components is the separation of effects on the RUS spectra for each independent phenomenon changing in the specimen. Though any effect (i.e. recrystallization, closure of porosity) can be accounted for within the FE framework, accounting for each individually would be computationally costly as

the number of AM factors taken into account grows. Machine learning approaches present future possibilities for automating the separation of RUS shifts due to concurrent factors.

The sensitivity of RUS to recrystallization is also material specific. The single crystal elastic anisotropy of the base material controls the magnitude of the changes in elasticity between a textured and isotropic component. For materials with very low anisotropy at the single crystalline level, the difference between a single crystal and an isotropic polycrystal would be difficult to detect, limiting the applicability of RUS for detecting recrystallization.

RUS could be further optimized to assess the variability of Ni-base AM components intended for service. For example, the sensitivity of torsional modes to recrystallization could be used to determine whether a part has been subjected to higher temperatures than intended during build or post-processing. The change in resonance frequencies based on residual stress could be used to screen parts against one another and determine if any experienced variable thermal conditions and resultant variable residual stresses.

6.4 Conclusion

- AM IN625 samples with a variety of build orientations and heat treatment conditions were measured by RUS. Larger differences in resonant response were observed after HIP and HT compared to changes in build orientation.

- The aggregate effective elastic constants of both the recrystallized and textured states were estimated from EBSD scans. EBSD elastic tensor estimates were used as inputs to the finite element modeling framework to simulate grain orientation effects. The elastic tensor estimates were validated by experimental RUS inversions.

- The experimentally measured resonance frequency shifts between the textured and recrystallized state matched the FEM calculated shifts. Changes in grain orienta-

tion were therefore identified as the dominant effect on resonance frequencies during recrystallization.

- Identification and tracking of resonance mode-types through FEM enables experimental identification of mode-types and quantitative tracking of recrystallization in AM components. Mode-type trends enable differentiation of recrystallization from other mechanisms such as geometric change. Mode-types calculated by FEM were experimentally validated using laser vibrometry.

- Stress relief heat treatments are observed to cause uniform increases of 1.7 - 2.1 % across the measured resonance frequencies.

- Experimental RUS inversion of the elastic constants by Bayesian inference calculated the orientation of the {111} texture component.

- This work provides evidence that RUS is capable of detecting differences in thermal history and microstructure between built AM components.

Chapter 7
Interpretation of RUS Results: Insights from Complex Specimens

Given that Chapters 3 - 6 addressed specific developments of RUS as an analysis technique for polycrystalline/ AM materials, the purpose of this chapter is to provide context for the application of this technique under varied specimen conditions. These conditions comprise different microstructural texture symmetries and strengths relative to exemplary material geometries, existence of secondary phases, and the application to non-AM textured/ non-textured materials. This chapter will also discuss wave propagation effects, such as attenuation (damping) and residual stresses, on ultrasound analysis with the goal of demonstrating potential errors. The analysis of each effect is couched in the context of numerical results.

7.1 Single crystal elastic constants of MPEA specimens with minimal texture

To demonstrate the effect of conducting single-crystal-elastic-constant-RUS inversions on polycrystals with unknown texture, a study of several multiprincipal element alloy (MPEA) and refractory specimens is introduced. MPEAs are of significant interest to the aerospace and space community as there is a push to extend the operational temperature of high-temperature components [175].

7.1.1 Materials and methods

The refractory/ MPEAs of interest in this study were C103, MoNbTi, HfNbTaTi, HfNbTaTiZr, and NbTiZr. C103, MoNbTi, HfNbTaTi, and HfNbTaTiZr were provided

by ATI[1]. The NbTiZr was provided by Professor Mitra Taheri[2]. and produced by double arc-melting in a partial argon environment, with the specimen flipped and melted 5 times. MoNbTi and HfNbTaTi were produced by arc-melting at ATI1. The arc-melted 'buttons' were flipped several times with a non-consumable electrode, and x-ray radiography was used to confirm homogeneous mixing. The specimens cooled in the argon environment of the arc-melter prior to removal. C103 was provided as a commercially available wrought bar (vacuum arc remelt and extruded), while HfNbTaTiZr was cast in a plasma arc furnace and HIP'ed at 1200°C for 4 h at 30 ksi in argon atmosphere. The 3.5 in diameter HfNbTaTiZr was then forged at 1149°C, 1 in/s, and 3.23 in/pass. The HfNbTaTiZr ingot cracked during the first forging pass. The specimen used for RUS analysis was removed from a region away from the cracked portion of the ingot. Measured compositions of each alloy are provided in Table 7.1

Regardless of the composition of each specimen, the difference in production (arc-melt vs cast) and post-process treatments (HIP, anneal) should induce variability in texture. Following the discussion given in Chapter 4, an isotropic microstructure will result in indeterminate measurements of the single crystal elastic constants from the resonant frequencies, as the degrees of freedom on the specimen scale (2 independent elastic constants) are lower than the degrees of freedom to be determined (3 independent cubic single crystal elastic constants). However, both the bulk elastic properties and the single crystal elastic properties are of interest in these alloys, so even a 'failed' determination of the single crystal elastic constants due to lack of texture will yield useful values of the bulk elastic constants. Further, few single crystal elastic constant values have been reported for MPEAs in general, particularly experimentally [176].

RUS parallelepiped specimens were prepared using wire-electrical discharge machining

[1]Alleghany Technologies Incorporated, Dallas TX
[2]Johns Hopkins University, Baltimore MD

Elemental compositions of Multi-principal element alloys					
	Hf (at.%)	Mo (at.%)	Nb (at.%)	Ta (at.%)	Ti (at.%)
C-103	5.4	–	92.6	–	2.02
MoNbTi	–	33.7	32.9	–	33.5
HfNbTaTi	9.8	–	34.4	31.8	24.1
HfNbTaTiZr	29.7	–	20.2	30.7	20.2
$NbTiZr^{nominal}$	–	–	33.3	-	33.33
	Zr (at.%)	C (ppmw)	O (ppmw)	N (ppmw)	
C-103	–	< 20	140	38	
MoNbTi	–	20	80	< 20	
HfNbTaTi	–	70	930	< 20	
HfNbTaTiZr	20.2	52	450	41	
$NbTiZr^{nominal}$	33.33	–	-	–	

Table 7.1: Multi-principal element alloy compositions. Major elements (Hf, Mo, Nb, Ta, Ti, Zr) given in at.%, interstitials (C, O, N) given in parts per million weight (ppmw). NbTiZr did not have compositional measurements, and thus is given in its nominal equimolar composition. All other specimens have major elements measured by inductively coupled plasma - optical emission spectrometry (ICP-OES) and interstitials measured by LECO analysis, as provided by ATI[1].

(EDM) from each larger specimen volume, as constrained by the quantity of supplied material for each chemistry. Nominal dimensions were chosen as 6 mm x 7 mm x 8 mm, except for NbTiZr which was constrained by a smaller volume of material, and chosen to be nominally 4 mm x 4.5 mm x 6 mm. Aspect ratios between the side lengths of the parallelepipeds were designed to be similar between the specimens, near 1. Maintaining an aspect ratio near 1 limited the possible resonant mode types and reduced the error in specimen preparation. The specimen dimensions, calculated density (by measured mass, not accounting for porosity), and proposal distribution of each estimated single crystal elastic constant are given in Table 7.2.

Following Chapters 4 and 5, 45 or more resonant frequencies were gathered for each specimen in order to carry out RUS inversions. The standard procedure of measuring the frequencies 3-5 times, and replacing the specimen in the cradle after each measurement, were followed. Hyperparameters of each RUS inversion of the single crystal elastic con-

MPEA Specimen Dimensions and Densities for RUS Inversion					
	HfNbTaTi	HfNbTaTiZr	C103	MoNbTi	NbTiZr
d_1 (mm)	5.96	6.00	6.00	6.01	4.20
d_2 (mm)	6.96	7.01	6.98	6.99	4.41
d_3 (mm)	7.98	7.96	7.97	7.96	5.94
ρ (g/cm^3)	10.61	9.83	8.75	7.67	6.64
Proposal Distribution of Single crystal elastic constants					
	HfNbTaTi	HfNbTaTiZr	C103	MoNbTi	NbTiZr
C_{11} (GPa)	200.0 ± 150.0	200.0 ± 150.0	200.0 ± 150.0	200.0 ± 150.0	175.0 ± 30.0
A	3.0 ± 1.5	3.0 ± 1.5	3.0 ± 1.5	3.0 ± 1.5	3.2 ± 0.4
C_{12}^{calc} (GPa)	159.0	159.0	159.0	159.0	142.0
C_{44} (GPa)	80.0 ± 30.0	80.0 ± 30.0	80.0 ± 30.0	80.0 ± 30.0	51.0 ± 10.0
σ (kHz)	1.2 ± 0.8	1.2 ± 0.8	1.2 ± 0.8	1.2 ± 0.8	1.5 ± 0.5

Table 7.2: MPEA specimen dimensions and proposal distribution of single crystal elastic constants. Prior knowledge of each single crystal elastic constant was set as a uniform distribution ($0 \rightarrow$ inf), resulting in a completely unconstrained parameter space.

stants were 1800 particles, ESS threshold of 85%, and 12 MCMC steps. A polynomial order of 12 with 45 resonant modes were used for each specimen.

7.1.2 NbTiZr fixed texture single crystal elastic constants

To assess the feasibility of 'free texture' inversions (presented in Chapter 5) given an arc-melted and annealed specimen, EBSD data was gathered on one of the NbTiZr specimen faces, and a 'fixed texture' inversion (Chapter 4) of the single crystal elastic constants was carried out. The determination of the single crystal elastic constants with 'fixed' texture from EBSD was carried out to set a baseline for the textures of these non-AM specimens and their potential textural limitations. The single crystal elastic constants of equiatomic NbTiZr have been theoretically calculated as $C_{11}^{DFT,MS} = 143.0, 149.6$ GPa, $C_{12}^{DFT,MS} = 111.0, 111.5$ GPa, and $C_{44}^{DFT,MS} = 64.0, 61.5$ GPa by molecular statics (MS) and density functional theory (DFT), respectively [177, 178]. These values correspond to $A^{DFT} = 4.0$ and $A^{MS} = 3.2$, a wide range of anisotropy that is differentiated from an isotropic state of A = 1. The proposal distribution of the single crystal constants was therefore chosen to contain the entire range of single crystal elastic constants of NbTiZr

in the literature [176, 177], as shown in Table 7.2.

Following Chapter 4, an EBSD scan of the specimen was used to inform the crystallographic texture of the single crystal elastic constant inversion. The EBSD scan was measured using 30 kV accelerating voltage, 6.4 nA beam current, EBSD step size 2 μm, and indexed as cubic niobium. As in Chapter 4, the EMSphinxEBSD package was used to index raw EBSD pattern images. Black points in the EBSD data represent points with a confidence index below 0.18, which were removed as noise after indexing. The EBSD (Figure 7.1) indicated a state of minimal texture strength by observing the generated pole figures in MTEX, but could not be quantitatively concluded until RUS inversion of the single crystal elastic constants was completed. The single crystal elastic constants, bulk elastic constants, and EBSD scan used to inform the calculation are given in Figure 7.1.

The single crystal elastic constants were convergently determined as identical to the bulk elastic constants in Figure 7.1, i.e. $C_{44}^{SC} = C_{44}^{bulk} \sim 29$ GPa. Given the literature range $C_{44}^{SC,lit} = 61.5$ - 64.0, this is clearly not a possible single crystal state for this material. This example demonstrates the single crystal elastic constants as indeterminable from an isotropic sample state, despite a convergently determined solution from the resonant frequencies. The texture must induce enough anisotropy in the bulk elastic constants that each value is differentiable from the same materials bulk isotropic specimen state. This is critical when considering specimens that are either slightly textured or exhibit a low anisotropy ratio on the single crystalline level.

7.1.3 MPEA single crystal elastic constants

Following the investigation of NbTiZr with 'fixed texture', an investigation of the single crystal elastic constants given arbitrary texture (Chapter 5) was carried out. Alongside the investigation of single crystal constants for these MPEAs, the possibility of

Calculated Single Crystal Elastic Constants

C_{11}	154.4 ± 8.4
C_{12}	101.1 ± 8.4
C_{44}	29.2 ± 0.97

Bulk Elastic Constants

156.2 ± 8.2	100.2 ± 8.4	100.0 ± 8.4	-0.03 ± 0.03	0.04 ± 0.03	-0.06 ± 0.05
	156.3 ± 8.3	100.0 ± 8.4	0.01 ± 0.01	0.03 ± 0.02	0.03 ± 0.03
		156.4 ± 8.2	0.02 ± 0.02	-0.06 ± 0.06	0.02 ± 0.02
			28.11 ± 0.08	0.02 ± 0.02	0.03 ± 0.02
	Symm.			28.15 ± 0.07	-0.03 ± 0.03
GPa					28.27 ± 0.14

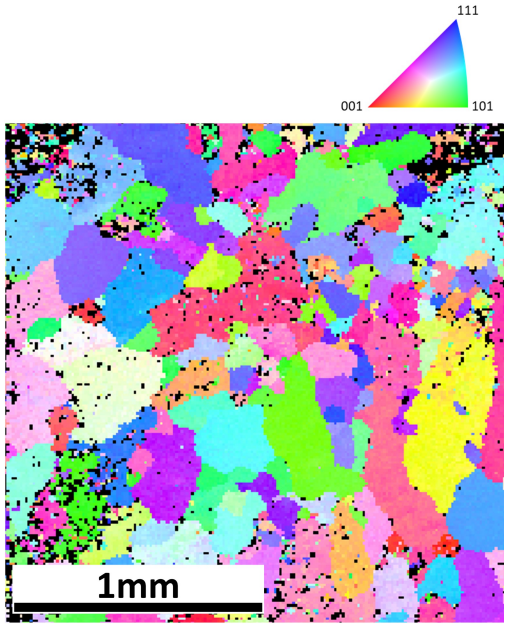

Figure 7.1: Use of RUS on untextured MPEA specimen (NbTiZr) displays RUS's inability to determine the cubic single crystal elastic constants under an isotropic texture. Both a constant texture (Chapter 4) and a freely determined texture (Chapter 5) displayed identical single crystal elastic constants, equivalent to the convergent bulk elastic constants, indicating isotropy at the specimen level. EBSD scan is inverse pole figure (IPF) colored relative to the normal direction (out of page).

initializing the freely determined texture coefficients without carrying out EBSD on each specimen was investigated.

NbTiZr, as well as the other MPEA specimens (C103, MoNbTi, HfNbTaTi, HfNbTaTiZr) were inverted for their single crystal elastic constants, using assumed texture coefficients. The texture of each specimen was initialized corresponding to the texture coefficient distribution calculation from EBSD data in Chapter 5 (SB-CoNi-10C specimen aligned with the build direction). While this approach may seem naive given the resonant frequencies are the only known quantity of each MPEA specimen, the approach tests the robustness of SMCPy to sample the combined single crystal/ texture parameter space without falling into local minima. Additionally, while the proposal of each texture was informed by the EBSD, the prior distribution was allowed to vary anywhere in space

(including a state of isotropic texture). In this manner, an assumption of relatively strong texture (SB-CoNi-10C specimen R4 aligned with the build direction from Chapter 5) was employed to initialize the calculations, but the specimen texture was allowed to diverge to a state of isotropy if induced by the fit of the frequencies.

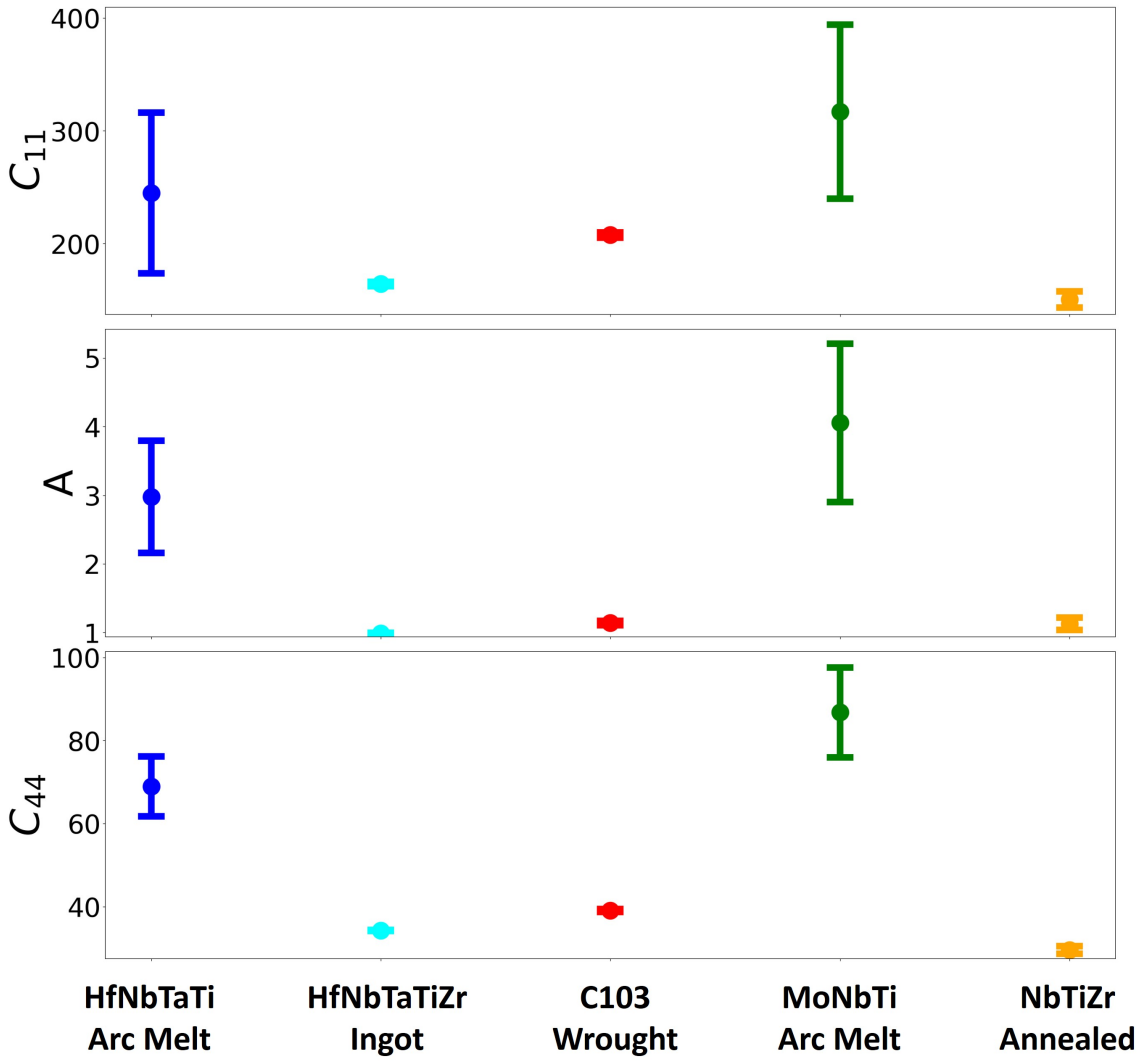

Figure 7.2: MPEA single crystal elastic constants calculated from resonant frequencies of polycrystalline specimens. Inversions were informed from assumed texture data on other specimens, but allowed to freely vary with the single crystal elastic constants as independent parameters.

As shown in Figure 7.2, for 3 of the 5 MPEA alloy specimens under study, the single crystal Zener anisotropy ratio (A) converged to ∼1, considering the standard deviation.

Comparing the result of NbTiZr in Figure 7.2 to the fixed texture NbTiZr single crystal values in Figure 7.1, the ability of the single crystal elastic constants to converge to A∼1, despite being informed with strong texture proposal distributions, is confirmed.

The convergent solution of HfNbTaTiZr and C103 display very similar behavior to NbTiZr, with tight error bars on each calculated single crystal elastic constant value. Therefore, the simulation is simply fitting a case of isotropy in the texture, making the single crystal indeterminable. This result corresponds to A∼1 on both the specimen and single crystal level, even though the bulk elastic symmetry is capable of capturing triclinic (arbitrary) symmetry. Considering the literature references for single crystal anisotropy are $A^{HfNbTaTiZr}$=2.6 [179] and A^{Nb}=1.82 (no single crystal estimate available for C103) [180], a determined anisotropy of A=1 cannot be the fundamental single crystal behavior.

The convergence to isotropy is further evidenced by the difference between the single crystal elastic constants of HfNbTaTiZr produced as a ingot with heat treatment, and HfNbTaTi which was arc-melted. Despite compositional similarities, the lack of isotropy of the as-arc-melted HfNbTaTi was indicated by A $\neq$ 1. Correspondingly, the single crystal elastic constants of MoNbTi and HfNbTaTi are supplied here with their associated errors stemming from the measured resonant frequencies. The single crystal constants are given in Table 7.3.

Single crystal elastic constants of MPEAs		
	HfNbTaTi	MoNbTi
C_{11}	245.0 ± 71.3	316.3 ± 77.1
A	3.0 ± 0.8	4.0 ± 1.2
C_{44}	68.9 ± 7.1	86.7 ± 10.8
C_{12}^{calc}	196.5 ± 71.4	270.5 ± 75.3

Table 7.3: Single crystal elastic constants of MPEA specimens with requisite texture to induce macroscopic anisotropy and thus enable the determination from resonant frequencies. ± indicates a single standard deviation, calculated at the final timestep of sequential Monte Carlo (SMC) given both independent texture coefficients and single crystal elastic constants.

The single crystal elastic constants for both HfNbTaTi and MoNbTi display substantial standard deviations on each value relative to their mean, with the fit of the single crystal constants from the resonant frequencies containing enough error to affect the practical use of the determined values. However, the precision of the shear dependent terms (C_{44}, A) is higher than the longitudinally dependent terms, and is thus useful to compare to computational estimates. The directional Young's modulus of HfNbTaTi (117 GPa, C_{33}^{bulk} direction) compares well with the reported tensile test determined literature value of 111 GPa (homogenized specimen state) [181]. The single crystal elastic constants of MoNbTi are only available as computational estimates in the literature [182] (C_{11} = 279.1, C_{12} = 126.3, C_{44} = 69.7), and require 2 standard deviations ($\pm$) to overlap the estimates here (C_{11} = 316.3 $\pm$ 77.1, C_{12} = 270.5 $\pm$ 75.3, C_{44} = 86.7 $\pm$ 10.8). However, the computational estimates are carried out at 0°K, reducing the significance of this disparity.

Following the observation of larger standard deviations on the longitudinal-wave dependent single crystal elastic constants for the non-isotropic MPEA specimens HfNbTaTi and MoNbTi in Table 7.3, a mode number study was carried out to determine if the longitudinally dependent resonant modes (extensional modes) were left out of the original 45 mode analysis. Given MoNbTi displayed significant damping and could not be used to reliably measure additional modes, the HfNbTaTi inversion was rerun with 60 resonant modes. A polynomial order of 12 was maintained between the SMC runs, with the results in Table 7.4 demonstrating that the single crystal elastic constants do not change with the increase in mode number. Each single crystal elastic constant displays a similar uncertainty between the altered 45/ 60 mode number runs, overlapping within its standard deviation. This indicates that each calculated mean is not differentiable from one another, as rerunning the analysis produces a distribution of means within the

standard deviation.

Single crystal elastic constants of MPEAs		
	HfNbTaTi (N=45)	HfNbTaTi (N=60)
C_{11}	245.0 ± 71.3	303.8 ± 83.9
A	3.0 ± 0.8	3.1 ± 0.8
C_{44}	68.9 ± 7.1	69.0 ± 6.1
C_{12}^{calc}	196.5 ± 71.4	257.6 ± 86.1
σ	2.962 ± 0.389	3.064 ± 0.329

Table 7.4: Single crystal elastic constants of HfNbTaTi determined with 45 and 60 resonant modes display no dependence of the determined single crystal elastic constant values on the mode number.

As previously mentioned, experimental measurements of the bulk elastic moduli are a significant achievement for MPEAs, given the lack of literature on the elastic constants. The bulk elastic constants of each alloy are provided in Table 7.5 with their associated uncertainties, along with the fitted Young's modulus (E) and Poisson's ratio (ν).

Following Chapter 5, non-zero values of the off-axis bulk elastic constants, as well as differences between the axially dependent constants that are equal under isotropic conditions (i.e. C_{44} and C_{55}), indicate that both HfNbTaTi and MoNbTi are textured. These differences induce differences in the resonant frequencies, from which the single crystal elastic constants are determinable.

Comparing the bulk elastic constants to the literature, non-computational estimates exist for C103 by ATI, NbTiZr through compression testing [183], and HfNbTaTiZr via ultrasound [184]. The modulus of C103 exceeds the ATI value of 90.0 GPa by 12 GPa, though the given value does not provide an uncertainty and there appears to be some inconsistency in the reported values across the literature. NbTiZr has a reported E = 80.4 GPa [183], agreeing with the measured value of 78.7 GPa here. The HfNbTaTiZr measurement via ultrasound is the most detailed [184] ($C_{11}^{Ref,bulk}$ = 172.0 ± 6.0 GPa, $C_{44}^{Ref,bulk}$ = 28.0 ± 1.5 GPa), and despite being determined on an equimolar composition unlike the alloy studied here, the bulk moduli are determined without an inherent

SMC calculated bulk elastic constants (GPa)					
	HfNbTaTi	HfNbTaTiZr	C103	MoNbTi	NbTiZr
C_{11}	265.0 ± 70.5	164.0 ± 2.0	210.5 ± 2.4	343.0 ± 75.2	153.1 ± 6.9
C_{12}	187.6 ± 71.6	95.1 ± 2.1	138.1 ± 2.4	257.4 ± 75.8	96.8 ± 7.0
C_{13}	185.4 ± 71.7	95.1 ± 2.0	137.0 ± 2.4	257.0 ± 76.2	96.5 ± 7.1
C_{22}	266.8 ± 70.3	164.0 ± 2.0	209.5 ± 2.4	359.4 ± 74.8	152.9 ± 6.9
C_{23}	183.6 ± 71.8	95.1 ± 2.0	138.0 ± 2.4	240.6 ± 76.7	96.6 ± 7.0
C_{33}	269.0 ± 70.3	163.9 ± 2.0	210.6 ± 2.4	359.8 ± 74.5	153.3 ± 6.9
C_{44}	49.2 ± 1.7	34.4 ± 0.0	38.0 ± 0.1	44.6 ± 3.0	28.1 ± 0.1
C_{55}	52.0 ± 1.9	34.3 ± 0.0	37.0 ± 0.1	65.8 ± 5.5	27.9 ± 0.1
C_{66}	53.0 ± 2.3	34.3 ± 0.0	38.1 ± 0.1	60.5 ± 4.5	28.3 ± 0.1
C_{14}	0.4 ± 1.0	0.0 ± 0.0	0.1 ± 0.1	0.5 ± 1.4	0.0 ± 0.0
C_{15}	5.4 ± 4.6	0.0 ± 0.1	0.2 ± 0.3	14.4 ± 5.2	0.2 ± 0.1
C_{16}	-2.0 ± 5.6	0.0 ± 0.0	0.0 ± 0.2	-0.3 ± 7.0	-0.1 ± 0.0
C_{24}	1.5 ± 3.9	0.0 ± 0.0	0.1 ± 0.3	-0.2 ± 3.5	0.0 ± 0.0
C_{25}	-0.8 ± 2.8	0.0 ± 0.0	0.0 ± 0.2	1.1 ± 3.5	0.0 ± 0.0
C_{26}	0.6 ± 4.1	0.0 ± 0.0	0.0 ± 0.1	1.9 ± 6.6	0.1 ± 0.1
C_{34}	-1.9 ± 4.3	0.0 ± 0.0	-0.2 ± 0.4	-0.3 ± 4.1	0.0 ± 0.0
C_{35}	-4.7 ± 4.8	0.0 ± 0.1	-0.2 ± 0.4	-15.5 ± 6.1	-0.2 ± 0.1
C_{36}	1.4 ± 9.0	0.0 ± 0.0	0.0 ± 0.2	-1.6 ± 12.7	-0.1 ± 0.0
C_{45}	1.3 ± 9.2	0.0 ± 0.0	0.0 ± 0.2	-1.4 ± 11.8	-0.1 ± 0.0
C_{46}	-1.2 ± 3.4	0.0 ± 0.0	0.0 ± 0.2	-0.7 ± 3.2	0.0 ± 0.0
C_{56}	0.0 ± 2.2	0.0 ± 0.0	0.1 ± 0.1	1.1 ± 3.0	0.0 ± 0.0
E^{calc}	117.8	94.2	102.0	145.0	78.7
ν^{calc}	0.38	0.37	0.40	0.28	0.39

Table 7.5: Determined single crystal and bulk elastic constants (self consistent estimate) of MPEA specimens. ± indicates a single standard deviation of each propagated value from the convergent single crystal elastic constants and texture coefficients determined from the resonant frequencies. Isotropic Young's modulus (E^{calc}) and poisson's ratio (ν^{calc}) is provided for isotropic specimens, while 'z' (33 axis) directional Young's modulus and 'yz' (22/ 33 axis) poisson's ratio is given for anisotropic specimens

isotropic assumption. The reported elastic constants [184] agree well with the constants measured here (C_{11}^{Ref} = 164.0 ± 2.0 GPa, C_{44}^{Ref} = 34.4 ± 0.1 GPa), within 6.4 GPa of C_{44} and 8.0 GPa of C_{11}.

Interestingly, an EBSD study of HfNbTaTiZr [184] displays significant lattice distortion, indicating substantial storage of dislocations [184]. The ultrasonic elastic measurements of HfNbTaTiZr [184] on material with significant dislocation content, alongside

the comparison to computational estimates that calculate the Young's modulus as more than 20% different to other literature values [185], indicate that experimental ultrasonic measurements of elasticity are critical to accurately determine the elastic behavior of these materials. Further, the observation of complex dislocation storage behavior supports the observation of significant damping (likely due to dislocation damping [186]) in the textured MPEA specimens here, where the isotropic specimens (e.g. C103) had easily identifiable modes. Moving forward, RUS could prove critical to rapidly quantify the elasticity of the rapidly changing MPEA design space.

7.2 Texture complexity insights from BD mis-aligned AM Ti64 specimens

To demonstrate the intricacies of inverting the single crystal elastic constants from high-complexity specimens, the Ti64 cylinders used in Chapter 5 were further explored. Rather than sectioning additional specimens aligned with the BD as in Figure 5.3, specimens were extracted at 20° to BD using EDM.

7.2.1 Specimen preparation

Following Chapter 5, EBSD tiles were gathered across $\sim$ 4 mm x 6 mm total areas of a selected specimen face of each parallelepiped. All EBSD data was gathered using an accelerating voltage of 20 kV and current of 1.6 nA. Indexing was completed on raw pattern images with the EMSphInxEBSD package [148] prior to analysis in MTEX. The sectioning strategy and EBSD of each sectioned specimen is shown in Figure 7.3, with the EBSD indexed to the α-phase of titanium. The grains are IPF colored relative to the build direction.

The nominal dimensions of each parallelepiped after EDM were 8 mm x 10 mm x 11 mm, with small variations for each specimen after polishing. Specimen densities

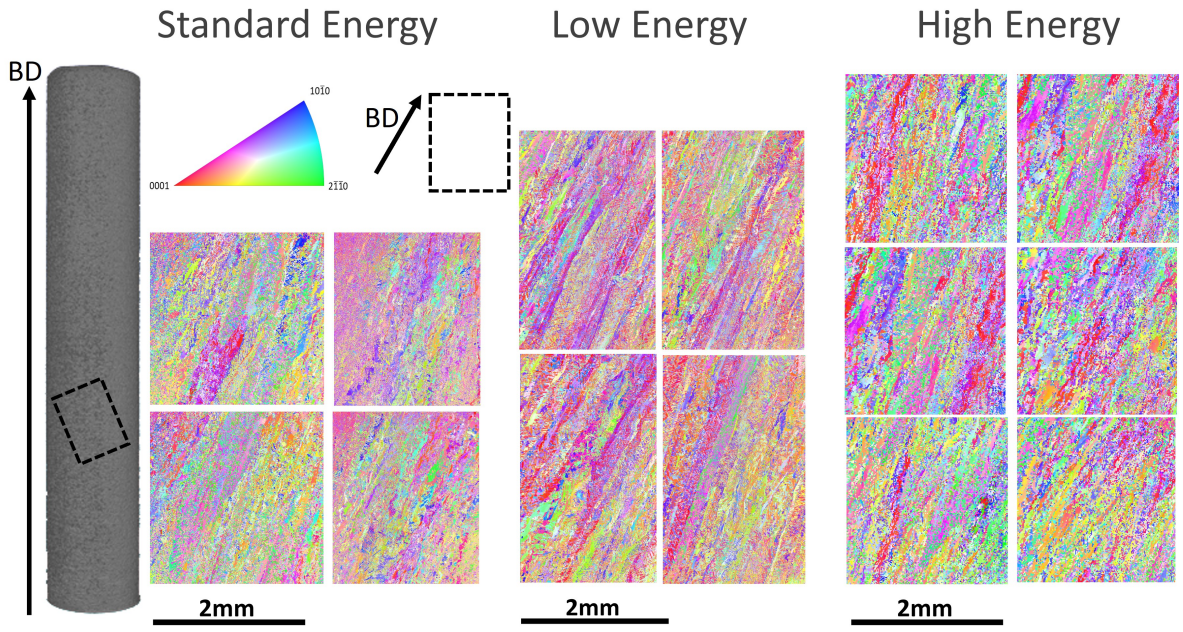

Figure 7.3: AM Ti64 specimens were sectioned from as-printed cylinders at 20° to BD. Specimens were extracted ∼20 mm from the build plate. EBSD scans were gathered as smaller subscans and aggregated to generate distributions of possible texture coefficients as shown in Figure 5.6.

were measured as 4.4176 $\frac{g}{cm^3}$, 4.4122 $\frac{g}{cm^3}$, and 4.4205 $\frac{g}{cm^3}$ for the standard, low, and high energy parallelepipeds respectively. Each specimen was sectioned by EDM with the 'lowest' point of the sectioned specimen at least ∼20mm from the build plate. This sectioning strategy ensured that the entire specimen contained texture induced by the relevant processing parameters (high, low, or standard energy), given that the standard energy printing parameters were used for the initial and final ∼15mm of the build height. The change in defect character corresponding to the change in processing parameters is given in Chapter 5, Figure 5.4.

Following Chapter 5, resonance frequencies were gathered on each AM parallelepiped, and used to initialize RUS inversions of the single crystal elastic constants. The standard methodology of measuring the resonant modes 3-5 times and averaging the measured modes was employed, removing and replacing the parallelepipeds within the RUS trans-

ducer cradle between runs. Because of problematic mode identification above mode 50, a polynomial order of 12 and mode number of 45 were used for all inversions.

7.2.2 Inverse determination of single crystal constants

To study the effect of arbitrary texture for these complex specimens, both fixed texture calculations (Chapter 4) of the single crystal elastic constants and 'free texture' calculations of the single crystal elastic constants (Chapter 5) were carried out, each informed by the identical EBSD and RUS data from each specimen condition. Following Chapter 5, the 19 independent parameters $\Theta^{Ti64,free}$ of the 'free texture' sequential Monte Carlo model were constituted by five single crystal elastic constants: [C_{11}^{SC}, C_{33}^{SC}, C_{13}^{SC}, C_{44}^{SC}, C_{66}^{SC}], five 2nd order texture coefficients: [$V_{\langle 2\rangle 11}, V_{\langle 2\rangle 12}, V_{\langle 2\rangle 13}, V_{\langle 2\rangle 22}, V_{\langle 2\rangle 23}$], and nine 4th order texture coefficients: [$V_{\langle 4\rangle 1111}$, $V_{\langle 4\rangle 1122}$, $V_{\langle 4\rangle 2222}$, $V_{\langle 4\rangle 1112}$, $V_{\langle 4\rangle 1113}$, $V_{\langle 4\rangle 1123}$, $V_{\langle 4\rangle 2212}$, $V_{\langle 4\rangle 2223}$, $V_{\langle 4\rangle 1223}$].

The fixed texture calculations of the single crystal elastic constants (Chapter 4) were used to study the complex interdependencies between model parameters in the 'free texture' model, with only the single crystal elastic constants as independent model parameters. Correspondingly, $\Theta^{Ti64,fixed} = [C_{11}^{SC}, C_{33}^{SC}, C_{13}^{SC}, C_{44}^{SC}, C_{66}^{SC}]$. The prior and proposal distribution of the single crystal elastic constants were identical between the free and fixed texture conditions, as given in Table 7.6.

Prior/Proposal distributions - Single crystal elastic constants (GPa)					
	C_{11}	C_{12}	C_{44}	C_{13}	C_{33}
Prior Uniform (min→ max)	(0→300)	(0→250)	(0→100)	(0→250)	(0→300)
Proposal Normal (mean,std dev)	(169.0,35.0)	(79.0,35.0)	(40.0,10.0)	(62.0,35.0)	(200.0,35.0)

Table 7.6: Prior and proposal distributions used for the SMC determination of single crystal elastic constants for Ti64. The prior was initialized as a uniform distribution while the proposal was normally distributed. Ranges of the proposal were chosen to cover the reported literature values [144, 155, 161, 162].

For the fixed texture calculation, only the mean values of the texture coefficients were supplied to the model, while for the free texture condition, the normally distributed prior

and proposal of texture coefficients are informed by the EBSD data (Chapter 5). The framework developed in Chapter 5 is implemented to concurrently estimate the misoriented texture and single crystal elastic constants while solving, but the combination of specimen configuration and microsymmetry represents a combination of multiple analysis considerations that may cause concurrent errors in the inverse solver. The potential complications are the conditions of 19 independent parameters (14 texture parameters and 5 single crystal elastic constants), a phase that has transformed from a parent phase with variant selection, the invariant solution across the 3 mirror reflections given a misaligned texture, and a limitation to experimental identification of 45 modes.

Hyperparameters of all inversions were 1800 particles, an ESS threshold of 85%, and 15 MCMC steps at each iteration. Each SMC run was parallelized across 10-18 CPU cores, requiring 24-48 h to complete.

7.2.3 Results

The fixed texture (calculated from EBSD as described in Chapter 4) and free texture results are shown in Figure 7.4, with significantly increased precision and convergence of the elastic constants for the free condition. Note that for the fixed texture case, only the 5 single crystal elastic constants were independent parameters (no free texture), with the invariant solution therefore not an issue.

Comparing the fixed and free texture conditions, both the accuracy of the determined single crystal constants between the low, high, and standard energy conditions, as well as the standard deviation, are of higher accuracy under the free texture condition. Looking more closely at the standard deviations on the single crystal elastic constants of the standard energy (SE) condition, it appears the invariant solution (multiple equivalent modes being sampled) causes improper convergence. This is indicated by a representative parameter plot of C_{33} and C_{66}, where the SE solution (purple) appears to contain several

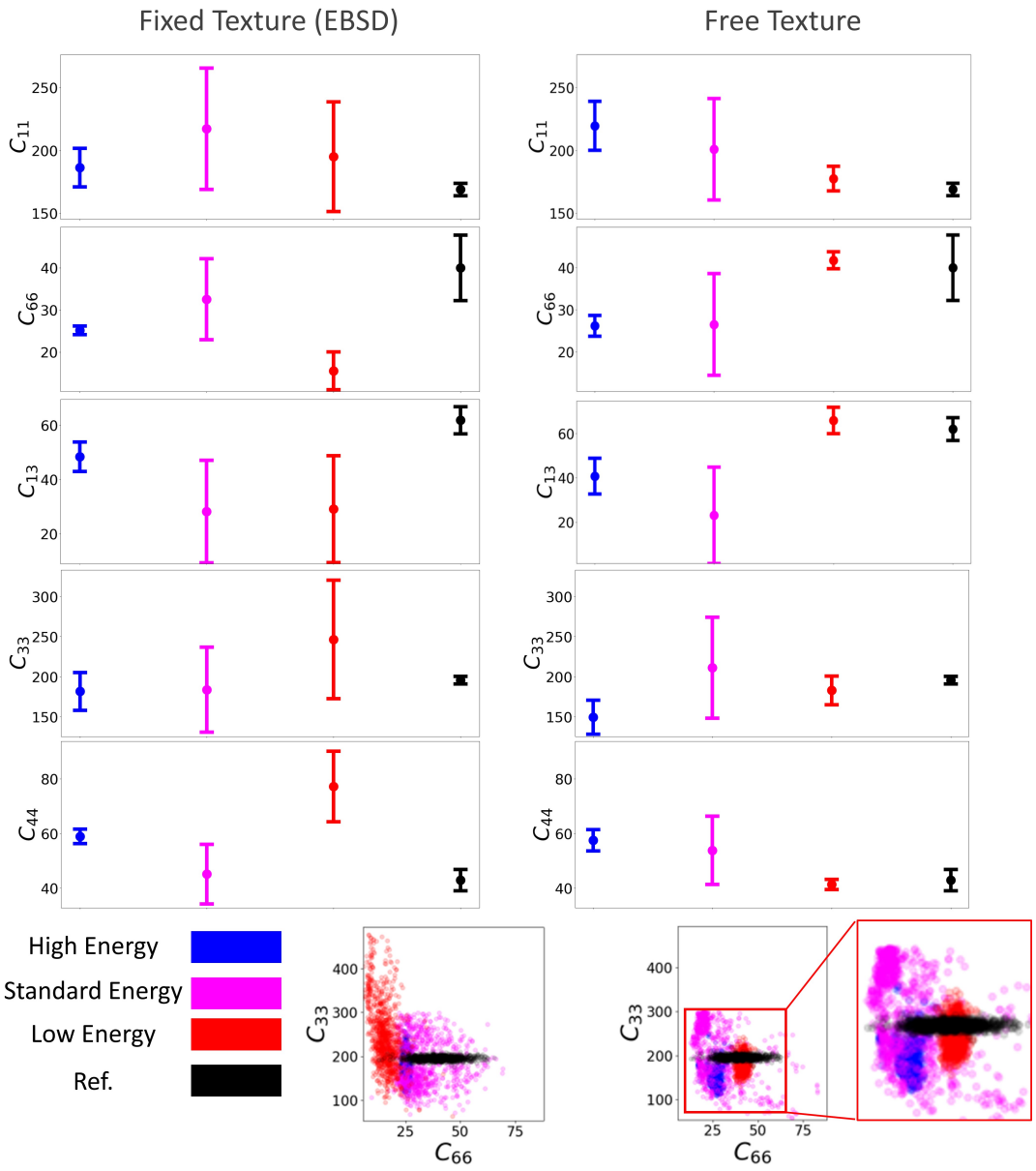

Figure 7.4: Ti64 single crystal elastic constants from EBM as-printed specimens sectioned 20° to the BD. Ti64 single crystal elastic constants from [144, 155, 161, 162] are included as literature range of reported values (described in Chapter 5).

clustered groups of datapoints, representing multiple (invariant) modes.

As explained in Chapter 3, these modes represent the mirror reflections across the specimen axes, which are apparently in close enough proximity for the SE texture state of Ti64 that the bounded Bayesian prior from experimental EBSD data (Section 5.3.1)

does not negate the effect. The range of each single crystal elastic constant in the free-texture SE specimen state are overestimated and potentially misidentified, as shown in Table 7.7.

Ti64 Single Crystal Elastic Constants - EBSD Texture				
	High Energy	Standard Energy	Low Energy	Lit. Range [144, 155, 161, 162]
C_{11} (GPa)	186.6 ± 15.3	215.9 ± 48.8	195.8 ± 44.3	136.0 - 170.0
C_{33} (GPa)	181.2 ± 23.3	184.5 ± 53.6	245.5 ± 74.5	163.0 - 196.0
C_{12}^{calc} (GPa)	136.3 ± 15.6	150.7 ± 54.1	164.6 ± 43.5	62.0 - 92.0
C_{13} (GPa)	48.5 ± 5.5	29.0 ± 19.4	29.1 ± 19.6	68.0 - 89.0
C_{44} (GPa)	59.0 ± 2.7	45.3 ± 11.0	77.2 ± 13.0	40.0 - 52.0
C_{66} (GPa)	25.2 ± 1.0	32.6 ± 9.8	15.6 ± 4.6	26.0 - 48.0
σ (kHz)	0.28 ± 0.03	1.83 ± 0.19	2.47 ± 0.23	-
Ti64 Single Crystal Elastic Constants with Free Texture				
	High Energy	Standard Energy	Low Energy	Lit. Range [144, 155, 161, 162]
C_{11} (GPa)	219.5 ± 19.5	180.8 ± 47.0	177.6 ± 9.8	136.0 - 170.0
C_{33} (GPa)	149.6 ± 20.7	201.5 ± 56.1	183.0 ± 17.8	163.0 - 196.0
C_{12}^{calc} (GPa)	167.1 ± 21.6	125.1 ± 44.7	94.2 ± 10.7	62.0 - 92.0
C_{13} (GPa)	40.8 ± 8.0	44.7 ± 27.1	65.7 ± 5.9	68.0 - 89.0
C_{44} (GPa)	57.4 ± 3.7	59.4 ± 17.4	41.3 ± 1.9	40.0 - 52.0
C_{66} (GPa)	26.2 ± 2.4	27.9 ± 13.3	41.7 ± 2.0	26.0 - 48.0
σ (kHz)	0.40 ± 0.04	1.73 ± 0.19	0.53 ± 0.07	-

Table 7.7: Single crystal elastic constants calculated from AM Ti64 specimens printed with different electron beam melting powers. Observed range of elastic constants for Ti64 from literature [144, 155, 161, 162]

This multi-modal behavior during solving demonstrates a limitation of the framework developed in Chapter 5, as misaligned textures may lie in close enough proximity to the principal x, y, z axes of the parallelepiped that the multi-modal solution is explored, even with the restrictions placed by the EBSD gathered. This phenomena would in turn need to be identified and corrected using the rotation code provided in Chapter 3. This analysis reveals that the arbitrary texture framework developed in Chapter 5 is suitable for use with specimens with this level of complexity, and that when a convergence issue occurs, it does so obviously. The sensitivity of the determined α-Ti single crystal elastic constants to the more nebulous effects of secondary phases and the potential for ultrasound interactions with those secondary phases is of interest moving forward.

7.3 Existence of secondary and transformed phases in Ti64

Following the complexity of Ti64 microstructures and the observation of substantial uncertainties on the single crystal constants for both aligned-to-BD specimens in Chapter 5 and misaligned-to-BD specimens in Section 7.2, there is a need to understand the dependence of the final estimated quantities on the existence of second phases. In the case of Ti64, this involves the well-studied transformation of primary (hexagonal) α-phase from cubic β-phase, and any retained β that does not transform. Given the Ti64 in Section 7.2 was intentionally printed with small variations in process parameters, alternate specimens with different phase fractions of non-α phases are needed to serve as a suitable model material for the study of second phases.

Specimens that were previously characterized in [187] were provided by Alec Saville[3], and a study of the effect of β phase on the determination of the single crystal elastic constants of α-Ti was undertaken. Briefly, the hexagonal α-phase transforms from a cubic single crystalline 'parent' phase, β, after the β phase solidifies from the molten liquid [156]. The solidification of the β-phase occurs analogously to the other cubic materials studied here (IN625 and SB-CoNi-10C), with primarily columnar grains growing along an <001> direction. Ti64 is an extremely well-studied material, with the choice of different equivalent orientations of the α-grains termed 'variant selection' [156]. That is to say, many different orientations may form from the same 'parent' β-grain orientation, all of which are related crystallographically. After the transformation of α-phase, some β is generally still present in the microstructure, referred to as 'retained' β. More importantly, because the parent β-grain orientations control the α-grain orientations, the properties of the component are dependent on the solidification and size of the parent β grains.

[3]Colorado School of Mines, Golden CO

7.3.1 Specimen preparation

Three specimen scanning strategies were employed to print nominally 15 mm x 15 mm x 25 mm (BD) test blocks. These scanning strategies were denoted random (R), Dehoff (D), and raster (L) following the conventions and scan parameters set out in [187]. A portion of the top of each block was sectioned using EDM for RUS analysis, then polished with silicon carbide sandpaper to final dimensions (x,y,BD) of 4.23 mm x 4.82 mm x 4.13 mm (BD), 2.60 mm x 5.46 mm x 3.46 mm (BD), and 3.38 mm x 6.09 mm x 3.48 mm (BD) for the Dehoff, random, and raster condition specimens respectively. This sectioning strategy, with a representative pole figure of the α-phase texture relative to the build direction, is shown for the random raster condition specimen in Figure 7.5.

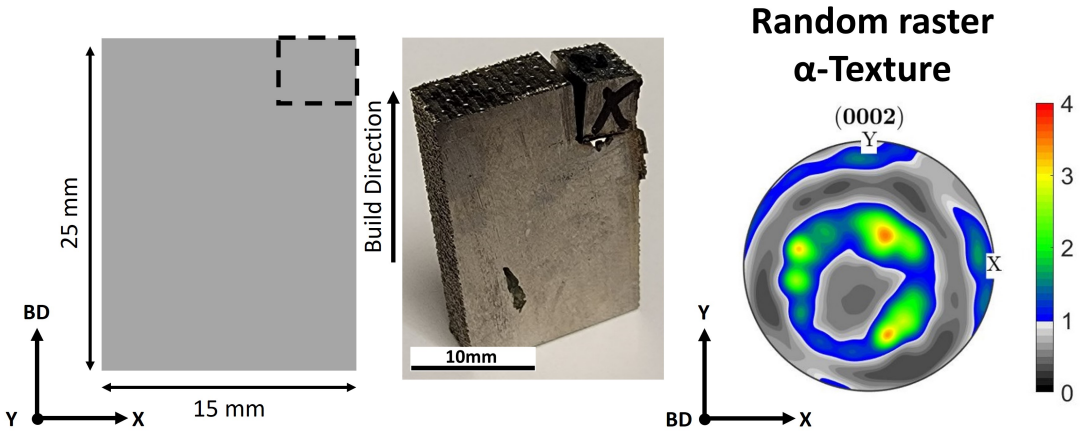

Figure 7.5: Ti64 sectioning strategy for RUS specimen extraction from as-printed blocks. Specimens were polished after sectioning. Figures were supplied by and reprinted with permission of Alec Saville[4].

7.3.2 Texture quantification

The right half (7.5-15 mm of x direction) of each specimen was interrogated by neutron diffraction at the High-Pressure-Preferred-Orientation (HIPPO) neutron diffraction beamline at the Los Alamos Neutron Science Center (LANSCE) at Los Alamos National Laboratory (LANL). The details of the neutron diffraction experiment are given

in [151, 187], with a nominal 10 mm beam diameter. The MAUD [151] software was used to calculate orientation distribution functions (ODF) and export recalculated pole figures with 5° resolution. This methodology was nearly identical to the neutron diffraction data analysis of SB-CoNi-10C data in Chapter 4. The MAUD-recalculated pole figures were imported into the MATLAB MTEX toolbox [123] for plotting, as displayed for each condition in Figure 7.6.

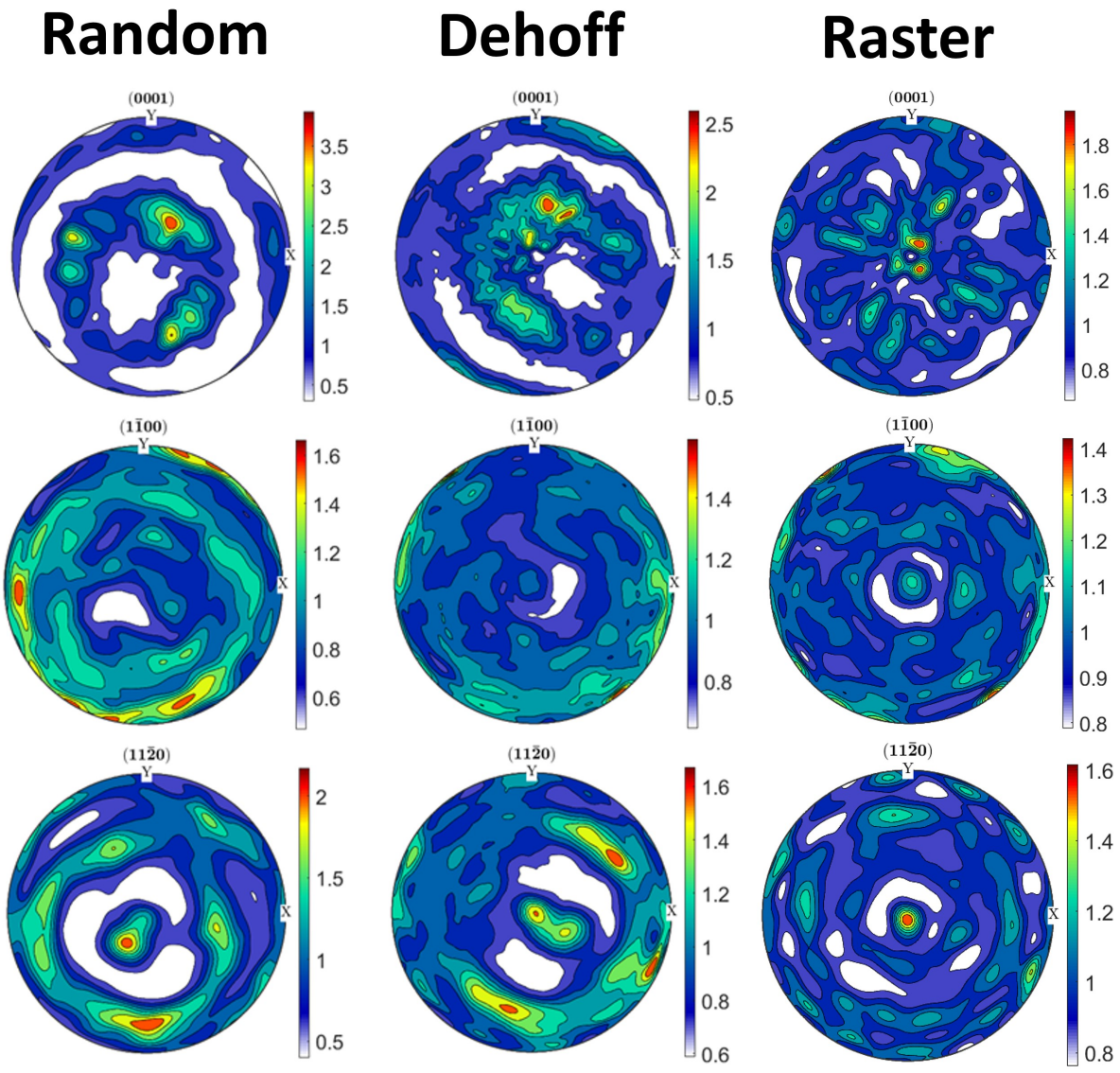

Figure 7.6: Ti64 α-phase pole figures from neutron diffraction of each specimen printing condition. Figures are reproduced from [187] with permission of authors.

The neutron diffraction pole figures indicate strong α-texture throughout each specimen, avoiding the possibility of an indeterminate single crystal solution due to elastic isotropy on the bulk scale (Section 7.1). By using neutron diffraction texture data, the danger of using unrepresentative EBSD data for the RUS inversions of α-Ti single crystal elastic constants is negated, and the impact of β-phase effects can be isolated. Following the neutron diffraction analysis of these specimens in [151], estimates of the β-phase fraction are determined to be 4-5%, 3-4%, and <1% for the random, Dehoff, and raster conditions.

Large-scale EBSD of the α-phase was conducted on each specimen [187] prior to sectioning to quantify texture and reconstruct the prior parent β phase grains. Reconstructions of the parent β grains were completed using MTEX 5.4 and TIBOR code [188]. Both the measured α-indexed EBSD and reconstructed β are shown for each raster condition in Figure 7.7, with IPF coloration relative to the build direction.

Note that the prior β-grain size is large (up to 2 mm long) relative to the specimen dimensions for the raster printing strategy, whereas for the Dehoff or random condition the β-grain size is much smaller. For the raster condition, the width (3.38 mm) and height (3.48 mm) of the RUS specimen correspond to the width of the EBSD map, demonstrating that very few prior beta grains (<2 for large grains) are captured within the build height of the RUS specimen. Consequently, the resonant frequencies are prone to containing heterogeneous regions of α grains, that may deviate from the bulk texture measured by neutron diffraction.

7.3.3 Inverse determination of single crystal elastic constants

To demonstrate the effect of the prior and retained β-phase presence on α-Ti single crystal elastic constant inversions, RUS inversions were carried out on each specimen following the method of Chapter 4. The texture variability calculations described in

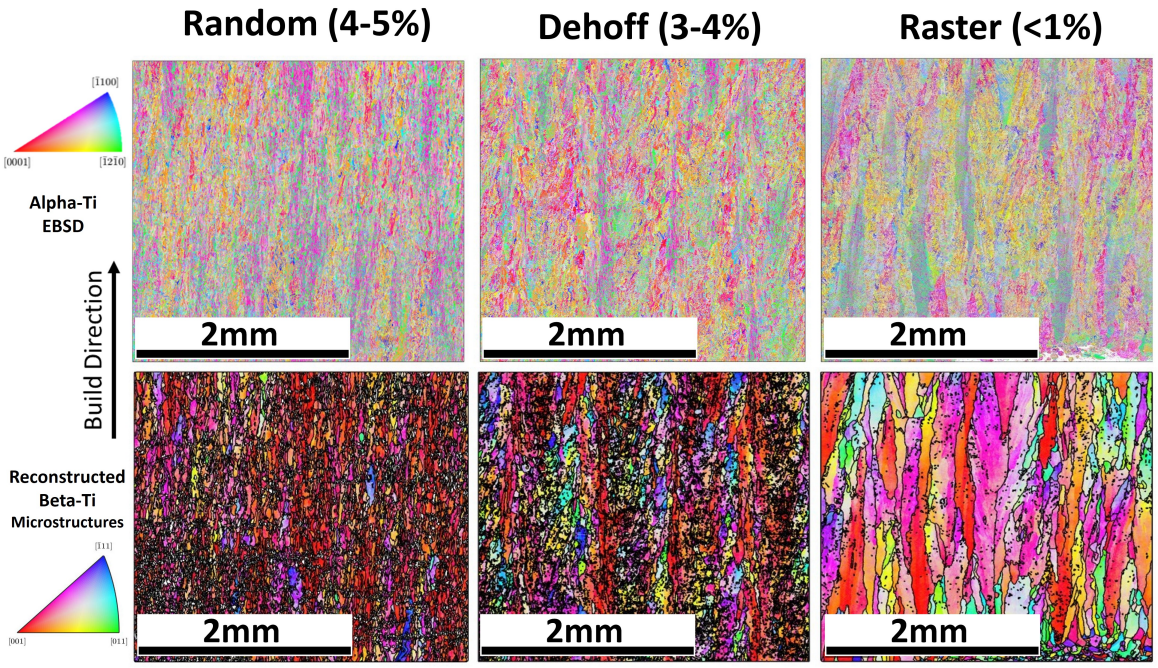

Figure 7.7: Ti64 α-phase EBSD and reconstructed β-phase for each raster condition. The approximate retained β phase fraction remaining in each microstructure is indicated in each title (calculated from neutron diffraction measurements). EBSD scans are IPF-colored relative to the build direction, respective to each IPF key (left). Figures are reproduced from [187] with permission of authors.

Chapter 5 were not performed to calculate these estimates, as the effect of the supplied α texture (from neutron diffraction) relative to the properties probed by each set of experimental frequencies was the goal. Following Chapter 4, the neutron diffraction data of each specimen condition was used to inform the texture.

Prior/Proposal distributions - Single crystal elastic constants (GPa)					
	C_{11}	C_{12}	C_{44}	C_{13}	C_{33}
Prior Uniform (min→ max)	(0→300)	(0→250)	(0→100)	(0→250)	(0→300)
Proposal Normal (mean,std dev)	(169.0,50.0)	(79.0,20.0)	(43.0,15.0)	(62.0,20.0)	(196.0,50.0)

Table 7.8: Prior/ proposal distributions of α-Ti to study the effect of β-Ti on the frequencies. The prior was initialized as a uniform distribution while the proposal was normally distributed.

Because the self consistent estimate only accounts for a textured aggregate of a single phase [95] here, the independent parameters of each inversion were the hexagonal single crystal elastic constants: $\Theta^{Ti64} = [C_{11}^{SC}, C_{33}^{SC}, C_{13}^{SC}, C_{44}^{SC}, C_{66}^{SC}]$ and the estimated

measurement error σ. A polynomial order of 12 and 45 resonant modes were used for each inversion. Hyperparameters of 1500 particles, MCMC chains of length 12, and 30 SMC time-steps were used, following Chapter 3. The prior and proposal distribution of each single crystal elastic constants are given in Table 7.8. The mean of the proposal distribution was informed by α-Ti values calculated in [144], with the standard deviation selected to capture the range of values observed in the literature.

7.3.4 Results

The results of each calculation of the single crystal elastic constants are provided in Table 7.9.

α-Ti Single Crystal Elastic Constants (GPa)			
	Raster	Dehoff	Random
C_{11}	197.15 ± 89.1	219.35 ± 38.2	274.6 ± 60.5
C_{12}	97.5 ± 95.5	164.7 ± 38.5	218.8 ± 59.3
C_{13}	75.7 ± 52.5	50.7 ± 11.3	12.8 ± 10.2
C_{33}	249.3 ± 148.9	131.5 ± 41.0	211.4 ± 60.2
C_{44}	65.0 ± 38.6	60.3 ± 6.3	42.1 ± 5.8
σ	22.47 ± 2.51	1.58 ± 0.19	3.49 ± 0.40

Table 7.9: Single crystal elastic constants of Ti64 (α-phase) display significant variability due to the presence of retained β-phase and prior β-grain size relative to specimen dimensions.

Looking at each set of single crystal elastic constants, it is observed that the fit of frequencies, represented by the measurement noise term σ, is quite poor even for the 'best' fitting inversion (Dehoff condition). For reference, the measurement noise term σ is measured in kHz, numerically indicating the difference between the (final) calculated frequencies to the measured frequencies. The poor fits of the frequencies exist across all the conditions, with standard deviations close in magnitude to many of the mean values. These results indicate very little certainty in the single crystal values, therefore the numerical significance of each mean value is reduced.

However, the correlation between prior β-phase grain size, presence of retained β,

and determined α-Ti single crystal elastic constants is of great interest. Most importantly, the raster specimen condition was by far the worst fitted inversion (σ=22.5 kHz), corresponding to the largest prior β-grains. Given that the retained β was the lowest volume fraction in the raster condition ($< 1\%$, Figure 7.7), the poor fit is attributed to the difference in prior β-phase structure. Following the EBSD data, it is likely that the RUS specimen contained as few as 2 prior β-grains through its thickness.

Looking at the Dehoff and random printing conditions, the retained β-phase fraction was similar between the two microstructures following Figure 7.7, but the fit of frequencies is substantially worse (σ=3.49 kHz) for the random printing condition than the Dehoff (σ=1.58 kHz). The prior β grain structure of the Dehoff condition appears to contain a greater variety of grain orientations, with the final α pole figures correspondingly containing a lower MRD at every point in Figure 7.6. It is likely that the printing conditions of the Dehoff condition, intended to control the columnar-to-equiaxed transition [187], contribute to the uniformity of multi-variant α and reduce stresses due to inhomogeneities at the melt-pool interfaces. The sharply elongated α grains and fine prior β grains of the raster condition are likely responsible for the poorly determined single crystal elastic constants in the raster printing condition.

In conclusion, it appears that the resonant frequencies of these alternate-scan-strategy Ti64 builds are strongly affected by alterations of prior β-phase grain size and structure, with the resultant transformed α single crystal elastic constants becoming difficult to reliably determine. The poorly determined single crystal elastic constants indicate unparameterized error in the experimental resonant frequencies, supported by the observation of lower resonant peak amplitudes in for the poorly fit specimen conditions. The comparison of resonant mode peak/ height is provided briefly in Figure 7.8. Note that the yellow/ white lines represent the signals coming from 2 independently receiving ultrasonic

transducers contacting the specimen.

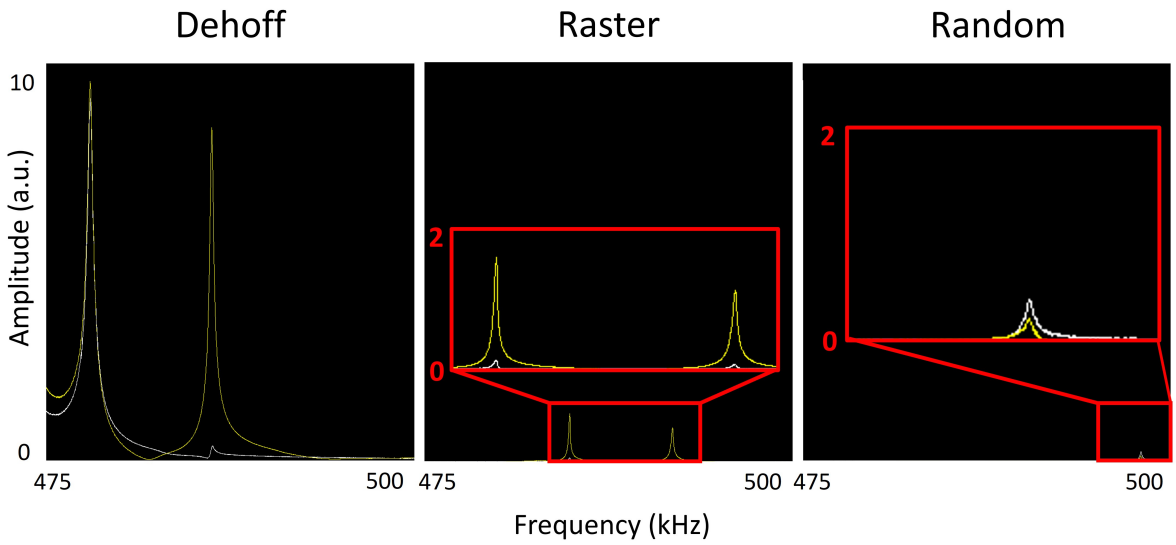

Figure 7.8: Resonant frequencies (475-500 kHz range) of Dehoff, raster, and random condition Ti64 specimens display a substantial decrease in amplitude for the random and raster conditions, which correspond to the more poorly fitted inversions. Decreased amplitude trend between these specimens persists across all 45 measured resonant frequencies. Amplitude is measured in arbitrary units (a.u.) as the freely resting RUS specimen setup only enables a qualitative comparison of amplitude. Insets display a reduced amplitude range, 0-2.

While the peak heights are non-quantitative for a 'freely' resting specimen/ transducer configuration used in this work, the resonant mode shape under a broadband frequency scan can be qualitatively observed and compared between specimen conditions. As observed in Figure 7.8, the amplitude of the raster condition is lower than that of the Dehoff condition, though the resonant modes are still identifiable. This supports the assertion that the influence of the prior β grain size effects (unrepresentative neutron diffraction data), rather than attenuation (such as damping) of the ultrasound is causing the inversion of α-Ti elastic constants to fail for the raster condition. The nearly unidentifiable resonant mode of the random printing strategy supports the conclusion that attenuation/ damping of the ultrasound from the elongated α grains and fine prior β grains are inducing the poor frequency fits. It is possible that this damping resulted

in a missed resonant mode that should have been measured in the first 45, rendering an increased error. Literature approaches to conduct RUS analyses in the presence of attenuative materials [104] could be applied in this case, though additional equipment is often required.

Overall, it appears that further study of the interplay between second phase existence, transformation, heterogeneity, and the resonant frequencies will be necessary to enable the reliable determination of elastic properties (even on the bulk scale) from AM builds with the potential for multiple phases.

7.4 Sensitivity of RUS to wave propagation effects

Motivated by the effort to account for and quantify properties in the presence of experimentally-observed residual stresses (Chapters 3 and 6) or attenuation (Section 7.3); defects, material properties (i.e. damping), and material states (residual stress/ strain) are capable of altering the ultrasonic response of a material. Though the measurement of bulk ultrasonic waves such as resonant frequencies have substantial advantages over time-of-flight measurement techniques (Section 1.2.1), the propagation of the wave (wavespeed, amplitude) is still fundamentally affected by the state of the solid material.

In Chapters 4-6, the observation of uniform resonant frequency shifts across all the resonant modes (after stress relief of AM specimens) was accounted for without direct consideration of an altered constitutive law. In fact, the observation of a uniform frequency shift after stress relief HT was previously unreported in the literature. These frequency shifts have since motivated research to develop constitutive laws for the resonance frequencies under the effects of residual stress [124, 189]. Within this work, the experimentally observed frequency shift was accounted for within the inverse model by fitting an independent term based on the observed effect, rather than by a physics based model.

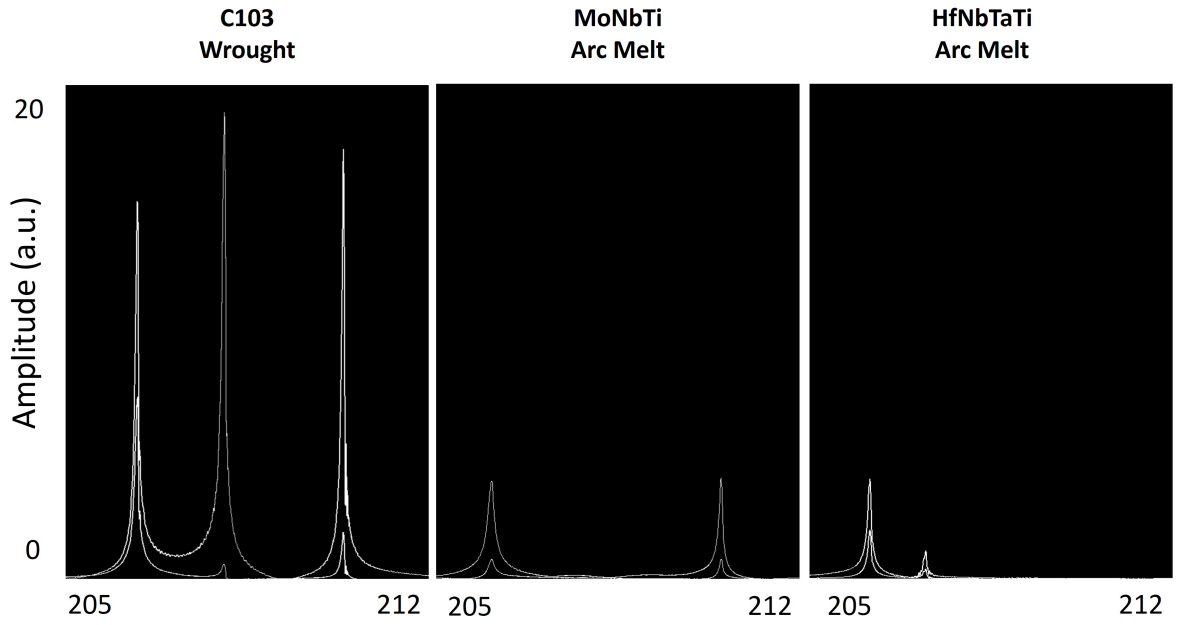

Figure 7.9: Resonant frequencies (205-212 kHz range) of MPEA specimens C103, MoNbTi, and HfNbTaTi display a decreases in amplitude for the specimens that were determined to be anisotropic (from RUS determination of single crystal constants). All 45 measured resonant frequencies display this trend across each specimen. Amplitude is measured in arbitrary units (a.u.), as the freely resting RUS experimental setup only enables a qualitative comparison of amplitude.

Moving forward, the use of RUS on complex polycrystalline specimens, such as those produced by AM, will require explicit consideration of secondary effects such as residual stresses on the frequencies. While considering each effect might complicate the use of the technique in general, it is important to note that any specimen will contain varying degrees of imperfections, as even dislocations can alter the propagation of elastic waves [186]. For the simplified treatment of elastic symmetries used historically, these effects were simply neglected.

Even for non-AM polycrystalline specimens, it has been historically difficult to differentiate between anisotropy inducing effects on the wavespeed [190]. Attenuation, such as wave scattering and absorption, can complicate the analysis of wavespeed altering effects as it reduces the intensity of the signal and can have second-order influences on wavespeed

[186]. The attenuative and residual stress effects are likely to all concurrently occur for an AM or complex polycrystalline specimen, given that thermal and mechanical processing induce them. Selecting a range of frequencies for the MPEA specimens studied in Section 7.1, Figure 7.9 shows that an isotropic wrought specimen (C103) displays significantly larger amplitudes across all the modes compared to the specimens determined to be anisotropic on the bulk scale. Again, despite the amplitude being a qualitative observation with RUS, the specimens determined to have bulk elastic anisotropy (MoNbTi and HfNbTaTi) display broader resonance peaks with lower amplitudes. Clearly, specimens displaying anisotropy are subject to much more complex wave propagation behavior.

This section serves to separate and classify the 'secondary effects', defined as anything affecting wave propagation besides the fundamental values of the elastic constants, density, and wave propagation distance. The effect of stresses (the acoustoelastic effect) and attenuation (scattering and absorption) are treated separately with regard to their effects on RUS and the results presented in this work.

7.4.1 Residual stresses

Quantitative evidence of resonant mode shifts after residual-stress-relief heat treatments are provided in Chapters 3-6, for both SB-CoNi-10C and IN625. The purpose of this section is to expand on the fundamentals of residual stresses, in order to assess their influence on wave propagation in an organized manner.

Experimental observations in AM/ cold-rolled material

The existence of residual stresses is a fundamental challenge for printing AM parts and qualifying them [191]. In this work, stress-relief heat treatments have been shown to affect the resonant frequencies, with both the magnitude and the uniformity of the frequency shifts previously unreported in the literature. While the shifts observed in Chapters 3 and 6 are observed after stress-relief heat treatments, it is yet to be determined whether

it is the change in the residual stress character of the part or a concomitant property change that induces the frequency shifts. Within the literature, residual stresses have been characterized in AM parts [174] as being on the same order as the yield stress, providing one potential source for the larger frequency shifts after stress-relief of AM parts.

For reference, representative resonant modes shifts (after stress relief HT) for the SB-CoNi-10C specimen (aligned with BD) from Chapter 3 are shown for 4 modes in Figure 7.10. The yellow and white line represent the signal coming from independently receiving ultrasonic transducers, and the y-axis represents amplitude. The amplitude is scaled identically between the two spectra, but is not a meaningful quantitative value in the free-boundary condition RUS setup here. As a result, calculations such as the Q-factor (dependent on amplitude) are not significant in this experimental setup and are not used.

Following this result, and the similar increase in resonant frequency values shown for AM IN625 specimens (after 870°C 1h) with mode shape tracking in Chapter 6, it is relevant to compare these resonant modes shifts to a conventionally processed (rolled plate) specimen. IN625 2 mm rolled plate stock was acquired given it is the only single phase material in this work with easily obtainable conventionally produced material, and the identical stress relief heat treatment from Chapter 6 (870°C for 1 h in air) was carried out. Resonant frequencies were measured on the specimen before and after the stress relief heat treatment, with the results given in Table 7.10. The magnitude of the frequency shifts after stress-relief HT are 0 - 0.5%, while the frequency shifts are substantially larger (1.7 - 2.3%) for the AM material. This demonstrates the substantial impact of AM-induced quantities on the frequencies, as the rolled plate material will contain substantial dislocation densities from the rolling process but does not display

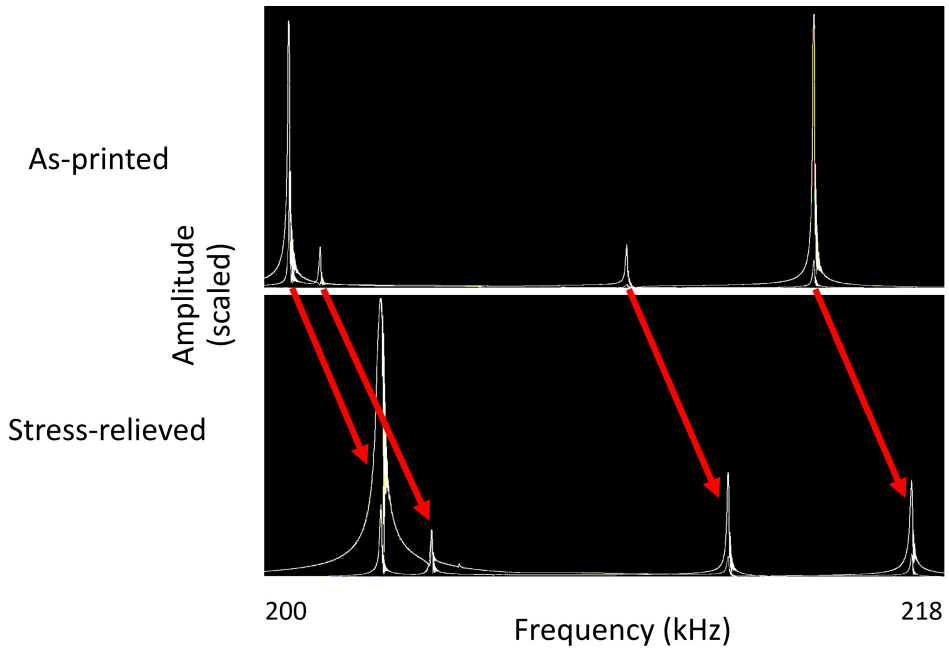

Figure 7.10: Four resonant modes of SB-CoNi-10C specimen R4 (Chapter 3) shown shifting toward higher frequency after the stress-relief heat treatment (1100°C 2h). Magnitude of resonant mode shifts is 1.38 % ± 0.28 %, representing uniformity across all resonant modes. ± represents 1 standard deviation across 75 measured resonant frequency shifts.

nearly as large of frequency shifts.

Alternative models for residual stresses with RUS inversion

Fundamentally, the effect of stress on wave propagation is well studied, and is known as acoustoelasticity [190]. Practically, this phenomenon represents the change in the second order elastic constants C_{ijkl} (from linear elastic theory in Chapter 2) with the presence of applied stress. The relationship between second order elastic constants and stress are the third order elastic constants [192], and the first-order nonlinearity between stress and strain is typically accounted for by introducing quadratic relationships between stress and strain [193]. However, in the context of a traditional RUS analysis [51], the purely linear Hooke's law is the only consideration.

As a result of these resonant mode shift observations (Chapter 3) after stress relief heat treatments in AM parts, recent modeling efforts [124] have validated that residual

Res. freq. changes of rolled and AM IN625 after stress-relief (SR) HT (870°C 1 h)						
Freq	As-rolled (kHz)	SR HT (kHz)	Shift(%)	As-built AM (kHz)	SR HT (kHz)	Shift(%)
f_r^1	5.67 ± 0.07	5.67 ± 0.01	0.07	58.65 ± 0.04	59.96 ± 0.04	2.24
f_r^2	6.89 ± 0.17	6.95 ± 0.04	0.92	73.15 ± 0.04	74.72 ± 0.07	2.15
f_r^3	12.68 ± 0.01	12.70 ± 0.00	0.14	75.92 ± 0.07	77.36 ± 0.02	1.90
f_r^4	18.04 ± 0.01	18.13 ± 0.03	0.46	127.56 ± 0.02	130.22 ± 0.05	2.08
f_r^5	26.18 ± 0.06	26.28 ± 0.00	0.40	130.77 ± 0.02	133.49 ± 0.07	2.08
f_r^6	36.13 ± 0.05	36.21 ± 0.02	0.22	147.44 ± 0.01	150.31 ± 0.02	1.95
f_r^7	43.22 ± 0.06	43.33 ± 0.02	0.26	150.09 ± 0.04	152.78 ± 0.01	1.79
f_r^8	43.66 ± 0.05	43.81 ± 0.03	0.32	210.09 ± 0.02	214.28 ± 0.05	1.99
f_r^9	48.04 ± 0.02	48.14 ± 0.01	0.21	220.01 ± 0.02	224.05 ± 0.02	1.83
f_r^{10}	60.28 ± 0.06	60.43 ± 0.02	0.24	224.14 ± 0.02	228.38 ± 0.01	1.89
f_r^{11}	61.45 ± 0.02	61.59 ± 0.02	0.23	244.71 ± 0.02	249.86 ± 0.03	2.10
f_r^{12}	70.45 ± 0.01	70.60 ± 0.01	0.22	250.08 ± 0.02	254.42 ± 0.01	1.74
f_r^{13}	71.83 ± 0.03	72.01 ± 0.02	0.26	272.16 ± 0.02	277.38 ± 0.02	1.92
f_r^{14}	75.46 ± 0.02	75.62 ± 0.00	0.20	273.69 ± 0.02	278.99 ± 0.02	1.94
f_r^{15}	76.38 ± 0.01	76.56 ± 0.00	0.24	275.66 ± 0.02	280.45 ± 0.01	1.74
f_r^{16}	89.81 ± 0.01	89.97 ± 0.00	0.18	296.35 ± 0.03	301.82 ± 0.01	1.85
f_r^{17}	102.03 ± 0.01	102.23 ± 0.01	0.20	297.14 ± 0.03	302.58 ± 0.03	1.83
f_r^{18}	107.13 ± 0.01	107.30 ± 0.00	0.16	304.95 ± 0.02	310.83 ± 0.05	1.93
f_r^{19}	109.93 ± 0.01	110.17 ± 0.00	0.22	306.93 ± 0.03	312.74 ± 0.03	1.89
f_r^{20}	112.24 ± 0.01	112.44 ± 0.00	0.18	312.64 ± 0.02	318.25 ± 0.02	1.79

Table 7.10: Stress-relief (SR) HT (870°C for 1h) typically used for AM specimens (as in Chapter 6 was applied to a conventionally produced (cold-rolled) 2 mm IN625 plate specimen. The resonant frequencies display minimal shifts compared to the uniform shift of 1.7 - 2.3%, across the first 20 modes, observed on AM IN625 in Chapter 6.

stresses are capable of generating larger shifts in the resonant frequencies than previously expected. Unlike the previous literature studying the effect of imposed stresses on RUS [194], the residual stresses in AM components are spatially inhomogeneous, but exist in equilibrium. Recent work by Kube et al. [189] has addressed these specific constraints, and developed a simple representation of an alternative constitutive relationship that incorporates the effect of prestrains. This alternative formulation directly alters the numerics of the resonant mode (elastic) deformations and their fundamental resonant frequencies, though it needs to be further studied with experimentally-measured residual stresses on an AM specimen before and after heat treatment to validate the larger magnitude shifts seen in AM specimens. The constitutive law with prestrains [189] should be incorporated into future RUS models developed for AM/ polycrystalline materials, par-

ticularly those intended to be used to quantitatively determine the single crystal elastic constants from polycrystals.

7.4.2 Attenuation

Alongside the residual stresses is the possibility for attenuation of ultrasound during RUS measurement. Attenuation of an ultrasonic wave involves both absorption and scattering, particularly when polycrystalline media (with internal boundaries/ interfaces such as grains) are considered [195]. Attenuation can be defined as a loss in wave energy of an elastic wave as the wave propagates between two points.

Attenuation is typically frequency dependent, with increasing attenuation as the frequency of the wave increases. The frequency dependence of the attenuation is defined in two regimes, the Rayleigh region where the wavelength is much larger than the size of the inclusion or feature, and the geometric region where the wavelength is significantly smaller than the scattering feature [45]. Because RUS operates at low frequencies (below 900 kHz for all the measurements described in this work), all the bulk ultrasound measurements involve wavelengths that are significantly larger than the attenuating features.

Attenuation can be induced from a variety of sources such as from grain boundaries [45], dislocations [186, 196], chemical segregation, inclusions, second phases, and elastic gradients [132]. The dislocation [186], grain boundary, grain size, and grain elongation orientation considerations are relevant for AM microstructures given that even well behaved polycrystalline specimens can display substantially different attenuation under different grain size distributions [197].

The effect of attenuation on RUS in this work is only considered in the context of 'missed' modes. That is to say, regardless of the source of the attenuation (dislocations, pores, etc), the reduction in amplitude of the resonant peaks is only considered when it approaches a level that a resonant mode signal may be reduced below the noise thresh-

old of the background. The incorporation of more robust experimental techniques such as contactless laser-RUS [64], computational mode-fitting [104], phase-locked signal processing to amplify the resonant signal [131], and inverse solvers that are more robust to missed modes [198] will be critical to the future of the technique with AM materials.

7.4.3 Specimen heterogeneity and elastic gradients

As introduced in Chapter 3, heterogeneity across the microstructure such as distinct regions of differently oriented columnar grains [21], would result in different sets of bulk elastic constants at different regions within the overall specimen microstructure. Given that properties such as the natural resonant frequencies are dependent on the bulk elastic constants of the entire microstructure, the use of any one region of well-oriented grains would not be representative of the overall bulk elastic constants and resonant frequencies. Though an ODF can be constructed from representative microstructural texture data (Section 2.1.3) of the entire specimen to calculate the true resonant frequencies, the overall statistics of the texture would not capture any of the alternate-oriented regions alone. An artificial representation of this effect is displayed in Figure 7.11, where the elasticity of each region is shown, with the combination of the two displaying a different behavior. Therefore, despite the presence of strongly preferential grain orientations, the alterations in growth direction across the microstructure result in variability that violates any textural homogeneity assumptions.

As discussed in Chapter 5, the self-consistent calculation of the effective texture and single crystal elastic constants from the resonant frequencies is reduced in impact by the presence of multiple (heterogeneous) textures within the bulk. Though any texture can be compactly represented by a single set of texture coefficients, the self-consistent calculation loses its significance. However, unlike the convergence to an isotropic single crystalline state (Figure 7.1) for isotropic bulk elasticity, the combination of distinctly

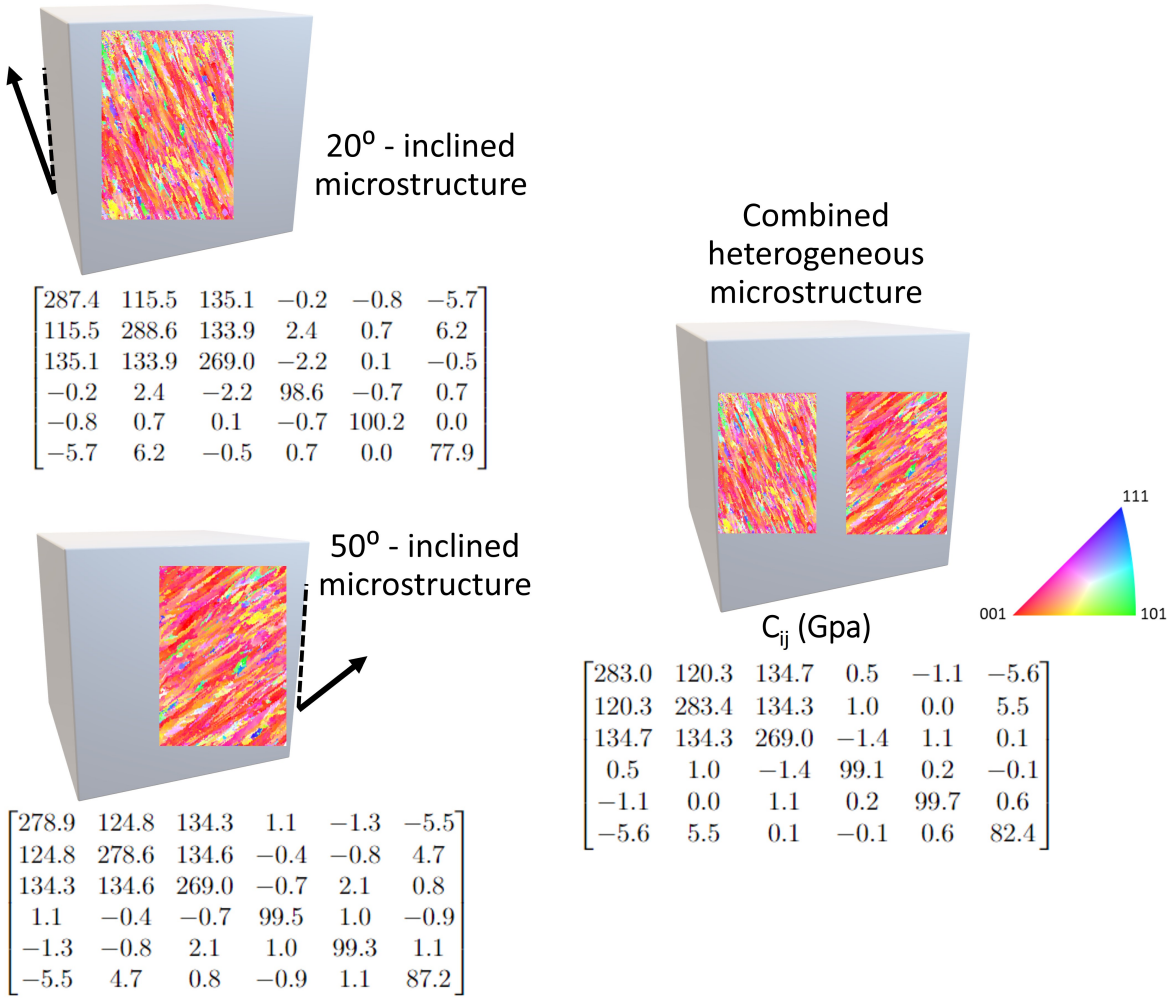

$$\begin{bmatrix} 287.4 & 115.5 & 135.1 & -0.2 & -0.8 & -5.7 \\ 115.5 & 288.6 & 133.9 & 2.4 & 0.7 & 6.2 \\ 135.1 & 133.9 & 269.0 & -2.2 & 0.1 & -0.5 \\ -0.2 & 2.4 & -2.2 & 98.6 & -0.7 & 0.7 \\ -0.8 & 0.7 & 0.1 & -0.7 & 100.2 & 0.0 \\ -5.7 & 6.2 & -0.5 & 0.7 & 0.0 & 77.9 \end{bmatrix}$$

$$\begin{bmatrix} 278.9 & 124.8 & 134.3 & 1.1 & -1.3 & -5.5 \\ 124.8 & 278.6 & 134.6 & -0.4 & -0.8 & 4.7 \\ 134.3 & 134.6 & 269.0 & -0.7 & 2.1 & 0.8 \\ 1.1 & -0.4 & -0.7 & 99.5 & 1.0 & -0.9 \\ -1.3 & -0.8 & 2.1 & 1.0 & 99.3 & 1.1 \\ -5.5 & 4.7 & 0.8 & -0.9 & 1.1 & 87.2 \end{bmatrix}$$

$$\begin{bmatrix} 283.0 & 120.3 & 134.7 & 0.5 & -1.1 & -5.6 \\ 120.3 & 283.4 & 134.3 & 1.0 & 0.0 & 5.5 \\ 134.7 & 134.3 & 269.0 & -1.4 & 1.1 & 0.1 \\ 0.5 & 1.0 & -1.4 & 99.1 & 0.2 & -0.1 \\ -1.1 & 0.0 & 1.1 & 0.2 & 99.7 & 0.6 \\ -5.6 & 5.5 & 0.1 & -0.1 & 0.6 & 82.4 \end{bmatrix}$$

Figure 7.11: Demonstration of alternate bulk elastic tensors by artificially rotating the texture of a SB-CoNi-10C specimen (Chapter 3). While each individual texture orientation (upper left, lower left) results in a set of bulk elastic constants for which the single crystal constants are determinable, the combination of these two datasets (right) violates the necessary homogeneity assumptions. Dashed lines represent the z-axis of each parallelepiped while arrows represent the grain growth direction (build direction for AM here). EBSD overlaid on each RUS parallelepiped is not to scale.

oriented regions may result in arbitrarily anisotropic bulk elastic constants that will not predictably converge to the 'correct' single crystal constants.

To demonstrate, Figure 7.11 shows the bulk elastic tensor generated from EBSD of SB-CoNi-10C specimen R4 (Chapter 3) with a counterclockwise 20° rotation (left) and

a clockwise 50° rotation (right). The figure shows the bulk elastic tensor of each microstructure, calculated using a basic Hill average in the Matlab MTEX package [123]. Then, the rotated microstructures are aggregated with an equal amount of orientation data in each. The combined bulk elastic tensor is given for the combined microstructure, which accurately represents the aggregate bulk elastic behavior of the combined microstructure, but does not represent a bulk elastic tensor from which the texture and single crystal elastic constants are necessarily determinable. The resonant frequencies of the heterogeneous microstructure violate the assumptions made in the self-consistent model to calculate texture values, with the combined effect of the texture on elasticity negating the ability to calculate the effect of each oriented region independently.

In addition to the violation of model assumptions for the self-consistent solution, wave propagation across an arbitrary number of elastic gradients at unknown locations and orientations produces unknown behavior in the resonant frequencies. While there has been a significant amount of study of wave propagation losses across the interfaces between multiple materials given the elastic constants of thin films are of interest [111, 199], the study of an elastic gradient within a single material is effectively dependent on attenuation and dispersion (Section 7.4.2). The attenuation resulting from an elastic gradient can result in significant shifts in the resonant mode order [132] due to differences in the elastic properties at each point in the specimen, meriting more detailed determination of the resonant modes across a specimen surface such as laser-based RUS. Further study of this behavior using bi-crystalline or directionally solidified specimens could elucidate these effects with regard to AM/ arbitrary microstructures.

7.5 Conclusions

The determination of the single crystal elastic constants from resonant frequencies, as measured by RUS, has been studied under the conditions of weak textures, complex/

misoriented textures, and second phase existence in order to elucidate the practical effect of these physical phenomena on the resultant single crystal elastic constants.

- Isotropic macroscopic textures in multi-principal element alloy (MPEA) specimens cause the determined single crystal elastic constants to convergence to isotropy, meaning they are indeterminable. For the weakly textured MPEA specimens, the single crystal constants are determinable using assumed texture coefficients from EBSD data on an unrelated specimen (same single crystal elastic symmetry). The minimum state of texture strength and (single crystal) anisotropy, in order to determine the single crystal elastic constants from a polycrystal, is the bulk elastic state where the non-isotropic bulk elastic constants are differentiable from one another (e.g. $C_{11}^{bulk} \pm$ std. dev. $\neq C_{33}^{bulk} \pm$ std. dev.).

- Using misoriented-to-build-direction specimens of Ti64, convergence of the single crystal constants is significantly improved by incorporating freely determined texture coefficients in the RUS inversion. For the standard energy processing condition, allowing the texture and single crystal elastic constants to both vary results in susceptibility of the solution to the invariant RUS solution (mirror reflections) of the triclinic bulk elastic tensor. This occurs despite a restriction of the Bayesian priors by the EBSD data. Rotation correction of the solution is required to obtain a convergent set of single crystal elastic constants.

- The prior β-Ti grain size is shown to significantly affect the quality of RUS inversions of Ti64, when assuming a single phase transformed α-Ti microstructure in the inversion. Given there were 3-10 β-Ti grains through the bulk of the specimen with β-Ti grain size dependence, a minimum of 25 β-Ti grains through the thickness is recommended. The retained β-Ti phase fraction appears to have a less substantial impact on the inversion, though further study on the residual stress and

attenuation induced by the size/ phase fractions of β-Ti as well as resultant α-Ti microstructure is necessary.

- The attenuation, texture, and residual stresses contained within AM components concurrently affect the ultrasonic wave propagation and resultant resonant frequencies. Physics-based models of the wave behavior considering experimental measurements of these properties in AM components need to be implemented to advance the quantitative capabilities of RUS with AM components.

Chapter 8
Conclusions and Future Outlook

This dissertation has focused on the application of resonant ultrasound spectroscopy to interrogate the properties of additively manufactured components. This section will serve to summarize the general advancements and approaches of this work, with regard to their future outlook, limitations, and potential opportunities.

8.1 Inversely determined properties from AM/ polycrystals

The depth of quantitative information that is gleaned from the resonant frequencies, particularly when compared to the traditional single crystalline or isotropic polycrystalline specimens used with RUS analysis, has been significantly extended by the consideration of arbitrary textures in this dissertation. The traditional RUS inversion of elastic properties from resonant frequencies has been extended to determine the texture coefficients and single crystal elastic constants of additively manufactured components in Chapters 3-4. Further, the limitations of how to bound these determinations of single crystal/ texture coefficients has been systematically and practically explored (Chapters 5) across a range of relevant materials (cobalt-nickel-base superalloy, nickel-base-superalloy, and titanium alloys).

Though this dissertation has shown that a breadth of information can be obtained from the resonant frequencies of a specimen given the physical properties (i.e. dimensions/ density), a substantial amount of attention was given to ensure that external errors (affecting the experimental resonant frequencies) or modeling errors (affecting the calculation of theoretical resonant frequencies) were not biasing the numerics of the solutions.

As a result, substantial microstructural/ texture information (neutron diffraction, EBSD), a traditionally produced single crystal specimen, precise control of specimen ge-

ometry, residual stress relief heat treatments, and inverse solver parameter tuning were all necessary to validate the values of the properties obtained from the AM specimens. While the single crystal elastic constants and texture measurements were precisely the information that were determined by the RUS inversions, the other quantities that substantially affect the frequencies cannot be neglected. Fundamentally, any inverse computational analysis is susceptible to this traditional misrepresentation of independent parameters. For example, a change in determined elastic constants could result from an error in measuring specimen dimensions, or on the other end of the spectrum, overfitting by incorporating every possible independent parameter.

The following sections are dedicated to potential opportunities to make the RUS analysis more reliable.

8.1.1 Reliable mode measurements

One of the largest issues with applying any inversion of properties from resonant frequency data is the knowledge that the measured resonant frequencies are complete, i.e. no resonant modes were hidden by background noise during the measurement. A single missed mode generally renders all the calculations unreliable, as even when the calculation detects a less convergent fit of the frequencies (as in Chapter 3), the mean of each value of interest is unpredictably altered.

Experimentally, the use of phase-locked measurements of the resonant modes offer the capability to increase the signal-to-noise ratio [131], while the use of contact-less excitation/detection through laser-RUS generally increases the repeatability of the measurements [200]. While solutions to the RUS inverse problem such as sequential Monte Carlo have proven extremely robust, computational advances still have the potential to increase the depth of knowledge obtained from resonant frequency data. Combined with more robust peak fitting and genetic algorithm inversion [104], the use of laser-RUS pro-

vides a path forward for difficult to measure materials such as highly damped media. Particle swarm techniques have also proven robust to unmeasured modes, given their capability to operate with incomplete data [198]. The use of machine learning (ML) to increase the robustness of the resonant frequency solution to missed modes [131] appears promising, though the time expense of generating training data for this approach appears to scale exponentially with the number of parameters. ML provides the capability to optimize a solution space given independent variables, and the potential for ML to capture unparameterized error or the existence of missed modes may be a suitable future direction. In the context of this work, ML could be used to identify the aggregate elastic symmetry and solve for the requisite number of independent texture parameters, enabling the simulation to converge more strongly in the final steps.

8.1.2 Secondary data sources

RUS data can be increased in value by correlating the frequency measurements to other experimental measurements. This has been displayed in the literature for in-situ straining [65], time-of-flight ultrasound measurements [67], and high temperature correlations [102, 131], serving to provide constraints on the inverse solution and produce elasticity results defined in terms of other material-state-variables. Experimentally, the use of laser-RUS [64] would enable the fitting of both the resonant frequency value and its mode type, enabling easier convergence by the inverse solver. Separately, the use of laser-RUS for mode shape modeling enables the identification of a single invariant solution [67], enabling the avoidance of convergence issues due to that invariance (Chapter 3).

8.2 NDE of arbitrary geometry AM components

Extending the analysis of AM with resonant frequencies to arbitrary geometries (Chapter 6) demonstrated that pairing finite element (FE) solvers with RUS enabled the extraction of specimen state information. Though the depth of quantitative information is not as great as a true RUS inversion of properties, completing a single iteration of the FEM forward model is substantially faster than running a model thousands of times within its inverse formulation (sequential Monte Carlo). Fabricating a traditional inverse determination of the bulk elastic constants is possible with any FE solver that can produce the resonant frequencies from arbitrary shapes [63] (such as ABAQUS, Chapter 6), where FE takes the place of the analytical eigenvalue solution in Section 2.2.1. Therefore, the extension of FEM to determine the single crystal constants or texture coefficients is possible, though the computational cost of doing so can be prohibitive.

A consideration for implementing the inversion of the single crystal or texture coefficients from complex geometry specimens is the fundamental resonant mode types. As the bulk elastic anisotropy becomes more complex and the ratio of specimen dimensions increases (i.e. longest dimension/ shortest dimension $>>$ 1), substantial numbers of complex mode shapes appear compared to those of a parallelepiped. Combined with the high density of modes, low amplitudes, and sparsity of high-importance modes such as extensional modes, techniques such as laser-RUS (LRUS) to correlate the mode shapes of a large number of modes [201] are often necessary to ensure reliable determination of the elastic constants. However, for arbitrarily shaped specimens, there is no guarantee that a flat surface will exist relative to the reference directions of interest to conduct LRUS for mode shape imaging. Luckily, Bayesian approaches to the inverse problem [68, 199] have proven robust without mode shape, providing the opportunity for a combined Bayesian inference/ FEM inverse model to analyze the elastic constants of arbitrary specimens

from RUS data.

Outside the applicability of FEM for directly quantifying properties, FEM could provide the opportunity for the analysis of manufactured parts through the susceptibility of the signal (resonant frequencies) to different manufacturing defects. However, the defect must be identified (such as porosity or grain recrystallization) and the boundary conditions/ constitutive models implemented within the FE solver understood, to predict the effect of that defect on the resonant frequencies of the given shape. If these conditions are met, parametric studies of the effect of the defect across a range of shapes, sizes, and values can be carried out to quantify and connect the changes in resonant frequencies to the actual tested part. RUS could then be used to quantitatively compare manufactured specimens to one another, to a known defect-free specimen's signal, or to the part before and after processing [202].

Applying this approach to AM is more difficult than for traditional components, as some degree of difference in the surface roughness, property variation, and residual stresses are expected between AM builds or even coupons within the same build [164]. More work to quantify the unknown effects of AM microstructural variables such as grain shape, size, and dislocation content on the attenuation and resonant data is necessary.

In closing, the challenges faced in quantifying and qualifying additively manufactured components due to the variability in structure and properties are numerous, yet are outweighed by the substantial advantages of AM in application. The combination of minimal destructive analysis, deeper analysis of NDE data with advanced computational techniques, and an understanding of the material behavior affecting these measurements will enable the incorporation of AM components in fracture-critical applications moving forward.

Appendix A
Data Availability

The entire forward model, inverse solving code, and results presented in Section 3, along with install instructions with SMCPy and instructions for use, are accessible open-source at https://github.com/jrossin/texture-RUS. The `SMCPy` package is accessible at https://github.com/nasa/SMCPy. MATLAB codes for generating the pole figure plots with the MTEX package are included in the the data supplement of the corresponding publication[1].

Results from Chapter 4 are available at https://github.com/jrossin/RUS_AM_Single_Crystal[2]. Results from Chapter 6 are accessible through the corresponding publication[3].

[1]Rossin, J., Leser, P., Pusch, K., Frey, C., Murray, S. P., Torbet, C. J., ... & Pollock, T. M. (2021). Bayesian inference of elastic constants and texture coefficients in additively manufactured cobalt-nickel superalloys using resonant ultrasound spectroscopy. Acta Materialia, 220, 117287. https://doi.org/10.1016/j.actamat.2021.117287

[2]Rossin, J., Leser, P., Pusch, K., Frey, C., Vogel, S., Saville, A.I., Torbet, C., Clarke A.J., Daly, S., & Pollock, T. M. (2022). Single crystal elastic constants of additively manufactured components determined by resonant ultrasound spectroscopy. Materials Characterization, 192. 112244. https://doi.org/10.1016/j.matchar.2022.112244

[3]Rossin, J., Goodlet, B., Torbet, C., Musinski, W., Cox, M., Miller, J., ... & Pollock, T. (2020). Assessment of grain structure evolution with resonant ultrasound spectroscopy in additively manufactured nickel alloys. Materials Characterization, 167, 110501. https://doi.org/10.1016/j.matchar.2020.110501

Bibliography

[1] C. Öberg and T. Shams, "On the verge of disruption: rethinking position and role–the case of additive manufacturing," *Journal of business & industrial marketing*, 2019.

[2] J. J. Lewandowski and M. Seifi, "Metal additive manufacturing: a review of mechanical properties," *Annual Review of Materials Research*, vol. 46, pp. 151–186, 2016.

[3] W. E. Frazier, "Metal additive manufacturing: a review," *Journal of Materials Engineering and Performance*, vol. 23, no. 6, pp. 1917–1928, 2014.

[4] C. W. Hull, "Apparatus for production of three-dimensional objects by stereolithography," *United States Patent, Appl., No. 638905, Filed*, 1984.

[5] J. J. Beaman and C. R. Deckard, "Selective laser sintering with assisted powder handling," July 3 1990. US Patent 4,938,816.

[6] F. Froes and B. Dutta, *The additive manufacturing (AM) of titanium alloys*, vol. 1019. Trans Tech Publ, 2014.

[7] J. Kietzmann, L. Pitt, and P. Berthon, "Disruptions, decisions, and destinations: Enter the age of 3-d printing and additive manufacturing," *Business Horizons*, vol. 58, no. 2, pp. 209–215, 2015.

[8] E. D. Herderick, "Progress in additive manufacturing," *Jom*, vol. 67, no. 3, pp. 580–581, 2015.

[9] A. Gisario, M. Kazarian, F. Martina, and M. Mehrpouya, "Metal additive manufacturing in the commercial aviation industry: A review," *Journal of Manufacturing Systems*, vol. 53, pp. 124–149, 2019.

[10] A. Saboori, A. Aversa, G. Marchese, S. Biamino, M. Lombardi, and P. Fino, "Application of directed energy deposition-based additive manufacturing in repair," *Applied Sciences*, vol. 9, no. 16, p. 3316, 2019.

[11] A. Reichardt, A. A. Shapiro, R. Otis, R. P. Dillon, J. P. Borgonia, B. W. McEnerney, P. Hosemann, and A. M. Beese, "Advances in additive manufacturing of metal-based functionally graded materials," *International Materials Reviews*, vol. 66, no. 1, pp. 1–29, 2021.

[12] J. Hiemenz, "Electron beam melting: Electron beam melting is a unique prototyping and manufacturing process that can simultaneously reduce costs, weight, and time," *Advanced Materials & Processes*, vol. 165, no. 3, pp. 45–47, 2007.

[13] A. Ladewig, G. Schlick, M. Fisser, V. Schulze, and U. Glatzel, "Influence of the shielding gas flow on the removal of process by-products in the selective laser melting process," *Additive Manufacturing*, vol. 10, pp. 1–9, 2016.

[14] J. A. Muñiz-Lerma, A. Nommeots-Nomm, K. E. Waters, and M. Brochu, "A comprehensive approach to powder feedstock characterization for powder bed fusion additive manufacturing: a case study on alsi7mg," *Materials*, vol. 11, no. 12, p. 2386, 2018.

[15] J. Rindler, C. Slone, E. Herderick, M. Mills, and A. Ramirez, "Investigation on the potential effects of laser stitching and subsequent heat treatment on the microstructure and mechanical properties of nickel alloy 718 produced via laser powder bed fusion (l-pbf)," *Additive Manufacturing*, p. 102906, 2022.

[16] P. Collins, D. Brice, P. Samimi, I. Ghamarian, and H. Fraser, "Microstructural control of additively manufactured metallic materials," *Annual Review of Materials Research*, vol. 46, pp. 63–91, 2016.

[17] M. Seifi, A. Salem, J. Beuth, O. Harrysson, and J. J. Lewandowski, "Overview of materials qualification needs for metal additive manufacturing," *JOM*, vol. 68, no. 3, pp. 747–764, 2016.

[18] Y. Kok, X. P. Tan, P. Wang, M. Nai, N. H. Loh, E. Liu, and S. B. Tor, "Anisotropy and heterogeneity of microstructure and mechanical properties in metal additive manufacturing: A critical review," *Materials & Design*, vol. 139, pp. 565–586, 2018.

[19] R. Dehoff, M. Kirka, W. Sames, H. Bilheux, A. Tremsin, L. Lowe, and S. Babu, "Site specific control of crystallographic grain orientation through electron beam additive manufacturing," *Materials Science and Technology*, vol. 31, no. 8, pp. 931–938, 2015.

Bibliography

[20] U. F. Kocks, C. N. Tomé, and H.-R. Wenk, *Texture and anisotropy: preferred orientations in polycrystals and their effect on materials properties*. Cambridge university press, 1998.

[21] H. Helmer, A. Bauereiß, R. Singer, and C. Körner, "Grain structure evolution in inconel 718 during selective electron beam melting," *Materials Science and Engineering: A*, vol. 668, pp. 180–187, 2016.

[22] G. Dinda, A. Dasgupta, and J. Mazumder, "Texture control during laser deposition of nickel-based superalloy," *Scripta Materialia*, vol. 67, no. 5, pp. 503–506, 2012.

[23] P. Rangaswamy, M. Griffith, M. Prime, T. Holden, R. Rogge, J. Edwards, and R. Sebring, "Residual stresses in lens® components using neutron diffraction and contour method," *Materials Science and Engineering: A*, vol. 399, no. 1-2, pp. 72–83, 2005.

[24] C. L. Frederick, A. Plotkowski, M. M. Kirka, M. Haines, A. Staub, E. J. Schwalbach, D. Cullen, and S. S. Babu, "Geometry-induced spatial variation of microstructure evolution during selective electron beam melting of rene-n5," *Metallurgical and Materials Transactions A*, vol. 49, no. 10, pp. 5080–5096, 2018.

[25] J. M. Waller, B. H. Parker, K. L. Hodges, E. R. Burke, and J. L. Walker, "Nondestructive evaluation of additive manufacturing state-of-the-discipline report," *NASA*, 2014.

[26] Q. Y. Lu and C. H. Wong, "Additive manufacturing process monitoring and control by non-destructive testing techniques: challenges and in-process monitoring," *Virtual and physical prototyping*, vol. 13, no. 2, pp. 39–48, 2018.

[27] A. A. Salem, J. B. Shaffer, D. P. Satko, S. L. Semiatin, and S. R. Kalidindi, "Workflow for integrating mesoscale heterogeneities in materials structure with process simulation of titanium alloys," *Integrating Materials and Manufacturing Innovation*, vol. 3, no. 1, pp. 322–343, 2014.

[28] A. A. Antonysamy, J. Meyer, and P. Prangnell, "Effect of build geometry on the β-grain structure and texture in additive manufacture of ti6al4v by selective electron beam melting," *Materials characterization*, vol. 84, pp. 153–168, 2013.

[29] A. WK47031, "Standard guide for nondestructive testing of metal additively manufactured parts used in aerospace applications," 2015.

[30] R. R. Dehoff, M. Kirka, W. Sames, H. Bilheux, A. Tremsin, L. Lowe, and S. Babu, "Site specific control of crystallographic grain orientation through electron beam additive manufacturing," *Materials Science and Technology*, vol. 31, no. 8, pp. 931–938, 2015.

[31] S. K. Everton, M. Hirsch, P. Stravroulakis, R. K. Leach, and A. T. Clare, "Review of in-situ process monitoring and in-situ metrology for metal additive manufacturing," *Materials & Design*, vol. 95, pp. 431–445, 2016.

[32] J. Gockel and J. Beuth, "Understanding ti-6al-4v microstructure control in additive manufacturing via process maps," in *2013 International Solid Freeform Fabrication Symposium*, University of Texas at Austin, 2013.

[33] W. Li and M. Soshi, "Modeling analysis of grain morphologies in directed energy deposition (ded) coating with different laser scanning patterns," *Materials Letters*, vol. 251, pp. 8–12, 2019.

[34] W. J. Sames, F. List, S. Pannala, R. R. Dehoff, and S. S. Babu, "The metallurgy and processing science of metal additive manufacturing," *International materials reviews*, vol. 61, no. 5, pp. 315–360, 2016.

[35] A. Du Plessis, P. Sperling, A. Beerlink, L. Tshabalala, S. Hoosain, N. Mathe, and S. G. Le Roux, "Standard method for microct-based additive manufacturing quality control 1: Porosity analysis," *MethodsX*, vol. 5, pp. 1102–1110, 2018.

[36] J. Raplee, A. Plotkowski, M. M. Kirka, R. Dinwiddie, A. Okello, R. R. Dehoff, and S. S. Babu, "Thermographic microstructure monitoring in electron beam additive manufacturing," *Scientific reports*, vol. 7, no. 1, pp. 1–16, 2017.

[37] A. Lopez, R. Bacelar, I. Pires, T. G. Santos, J. P. Sousa, and L. Quintino, "Non-destructive testing application of radiography and ultrasound for wire and arc additive manufacturing," *Additive Manufacturing*, vol. 21, pp. 298–306, 2018.

[38] P. Charalampous, I. Kostavelis, and D. Tzovaras, "Non-destructive quality control methods in additive manufacturing: a survey," *Rapid Prototyping Journal*, 2020.

[39] C. Mandache, "Overview of non-destructive evaluation techniques for metal-based additive manufacturing," *Materials Science and Technology*, vol. 35, no. 9, pp. 1007–1015, 2019.

[40] R. G. Leisure and F. Willis, "Resonant ultrasound spectroscopy," *Journal of Physics: Condensed Matter*, vol. 9, no. 28, p. 6001, 1997.

[41] R. W. Balluffi, *Introduction to elasticity theory for crystal defects*. World Scientific Publishing Company, 2016.

[42] S. Sokolov, "Ultrasonic oscillations and their applications," *Tech. Phys. USSR*, vol. 2, p. 522, 1935.

[43] S. Sergey, "Means for indicating flaws in materials," June 27 1939. US Patent 2,164,125.

[44] F. A. Firestone, "The supersonic reflectoscope, an instrument for inspecting the interior of solid parts by means of sound waves," *The Journal of the Acoustical Society of America*, vol. 17, no. 3, pp. 287–299, 1946.

[45] W. P. Mason and H. McSkimin, "Attenuation and scattering of high frequency sound waves in metals and glasses," *The Journal of the Acoustical Society of America*, vol. 19, no. 3, pp. 464–473, 1947.

[46] W. Mason and H. McSkimin, "Energy losses of sound waves in metals due to scattering and diffusion," *Journal of Applied Physics*, vol. 19, no. 10, pp. 940–946, 1948.

[47] W. P. Mason, "Physical acoustics and the properties of solids," *The Journal of the Acoustical Society of America*, vol. 28, no. 6, pp. 1197–1206, 1956.

[48] H. McSkimin, "Measurement of elastic constants at low temperatures by means of high frequency ultrasonic waves," *The Journal of the Acoustical Society of America*, vol. 25, no. 4, pp. 826–826, 1953.

[49] D. Fraser and R. LeCraw, "Novel method of measuring elastic and anelastic properties of solids," *Review of Scientific Instruments*, vol. 35, no. 9, pp. 1113–1115, 1964.

[50] Y. Satô, "Basic study on the oscillation of a homogeneous elastic sphere, iv," *Geophys. Mag.*, vol. 31, pp. 237–242, 1962.

[51] A. Migliori and J. Sarrao, "Resonant ultrasound spectroscopy: Applications to physics, materials measurements, and nondestructive evaluation," *Wiley*, 1997.

[52] R. Holland, "Resonant properties of piezoelectric ceramic rectangular parallelepipeds," *The Journal of the Acoustical Society of America*, vol. 43, no. 5, pp. 988–997, 1968.

[53] H. H. Demarest Jr, "Cube-resonance method to determine the elastic constants of solids," *The Journal of the Acoustical Society of America*, vol. 49, no. 3B, pp. 768–775, 1971.

[54] O. L. Anderson, "Rectangular parallelepiped resonance—a technique of resonance ultrasound and its applications to the determination of elasticity at high temperatures," *The Journal of the Acoustical Society of America*, vol. 91, no. 4, pp. 2245–2253, 1992.

[55] I. Ohno, "Free vibration of a rectangular parallelepiped crystal and its application to determination of elastic constants of orthorhombic crystals," *Journal of Physics of the Earth*, vol. 24, no. 4, pp. 355–379, 1976.

[56] I. Ohno, S. Yamamoto, O. L. Anderson, and J. Noda, "Determination of elastic constants of trigonal crystals by the rectangular parallelepiped resonance method," *Journal of Physics and Chemistry of Solids*, vol. 47, no. 12, pp. 1103–1108, 1986.

[57] A. Migliori, J. Sarrao, W. M. Visscher, T. Bell, M. Lei, Z. Fisk, and R. G. Leisure, "Resonant ultrasound spectroscopic techniques for measurement of the elastic moduli of solids," *Physica B: Condensed Matter*, vol. 183, no. 1-2, pp. 1–24, 1993.

[58] W. Visscher and A. Migliori, "On the normal modes of free vibration of inhomogeneous and anisotropic elastic objects.," *J. Acous. Soc.*, vol. 89(4B), p. 1923, 1991.

[59] A. Migliori and T. W. Darling, "Resonant ultrasound spectroscopy for materials studies and non-destructive testing," *Ultrasonics*, vol. 34, no. 2-5, pp. 473–476, 1996.

Bibliography

[60] R. G. Leisure and F. Willis, "Resonant ultrasound spectroscopy," *Journal of Physics: Condensed Matter*, vol. 9, no. 28, p. 6001, 1997.

[61] J. Maynard, "Resonant ultrasound spectroscopy," *Physics Today*, vol. 49, no. 1, pp. 26–33, 1996.

[62] R. Schwarz and J. Vuorinen, "Resonant ultrasound spectroscopy: applications, current status and limitations," *Journal of Alloys and Compounds*, vol. 310, no. 1-2, pp. 243–250, 2000.

[63] J. Plesek, R. Kolman, and M. Landa, "Using finite element method for the determination of elastic moduli by resonant ultrasound spectroscopy," *The Journal of the Acoustical Society of America*, vol. 116, no. 1, pp. 282–287, 2004.

[64] D. H. Hurley, S. J. Reese, and F. Farzbod, "Application of laser-based resonant ultrasound spectroscopy to study texture in copper," *Journal of Applied Physics*, vol. 111, no. 5, p. 053527, 2012.

[65] R. Purohit, T. Richeton, S. Berbenni, L. Germain, N. Gey, T. Connolley, and O. Castelnau, "Estimating single-crystal elastic constants of polycrystalline β metastable titanium alloy: A bayesian inference analysis based on high energy x-ray diffraction and micromechanical modeling," *Acta Materialia*, vol. 208, p. 116762, 2021.

[66] M. Tane, K. Yamori, T. Sekino, and T. Mayama, "Impact of grain shape on the micromechanics-based extraction of single-crystalline elastic constants from polycrystalline samples with crystallographic texture," *Acta Materialia*, vol. 122, pp. 236–251, 2017.

[67] P. Sedlák, H. Seiner, J. Zídek, M. Janovská, and M. Landa, "Determination of all 21 independent elastic coefficients of generally anisotropic solids by resonant ultrasound spectroscopy: benchmark examples," *Experimental Mechanics*, vol. 54, no. 6, pp. 1073–1085, 2014.

[68] B. Bales, L. Petzold, B. R. Goodlet, W. C. Lenthe, and T. M. Pollock, "Bayesian inference of elastic properties with resonant ultrasound spectroscopy," *The Journal of the Acoustical Society of America*, vol. 143, no. 1, pp. 71–83, 2018.

[69] K. Foster, S. Fairburn, R. Leisure, S. Kim, D. Balzar, G. Alers, and H. Ledbetter, "Acoustic study of texture in polycrystalline brass," *The Journal of the Acoustical Society of America*, vol. 105, no. 5, pp. 2663–2668, 1999.

[70] C. Sayers, "Ultrasonic velocities in anisotropic polycrystalline aggregates," *Journal of Physics D: Applied Physics*, vol. 15, no. 11, p. 2157, 1982.

[71] H. Pursey and H. Cox, "Xxxiv. the correction of elasticity measurements on slightly anisotropic materials," *The London, Edinburgh, and Dublin Philosophical Magazine and Journal of Science*, vol. 45, no. 362, pp. 295–302, 1954.

[72] H. Ledbetter, "Sound velocities and elastic-constant averaging for polycrystalline copper," *Journal of Physics D: Applied Physics*, vol. 13, no. 10, p. 1879, 1980.

[73] J. Markanday, M. Carpenter, N. Jones, R. Thompson, S. Rhodes, C. Heason, and H. Stone, "Occurrence of a brass texture and elastic anisotropy in laser blown powder processed superalloy in718," *Materials Science and Engineering: A*, vol. 825, p. 141781, 2021.

[74] J. A. Evans, B. T. Sturtevant, B. Clausen, S. C. Vogel, F. F. Balakirev, J. B. Betts, L. Capolungo, R. A. Lebensohn, and B. Maiorov, "Determining elastic anisotropy of textured polycrystals using resonant ultrasound spectroscopy," *Journal of Materials Science*, pp. 1–21, 2021.

[75] L. D. Landau, E. M. Lifšic, E. M. Lifshitz, A. M. Kosevich, and L. P. Pitaevskii, *Theory of elasticity: volume 7*, vol. 7. Elsevier, 1986.

[76] W. D. Callister and D. G. Rethwisch, *Materials science and engineering: an introduction*, vol. 9. Wiley New York, 2018.

[77] B. R. Goodlet, *Forward and Inverse Modeling Frameworks for Nondestructive Evaluation of Materials with Resonant Ultrasound Spectroscopy*. PhD thesis, University of California, Santa Barbara, 2018.

[78] S. C. Cowin, "Properties of the anisotropic elasticity tensor," *The Quarterly Journal of Mechanics and Applied Mathematics*, vol. 42, no. 2, pp. 249–266, 1989.

[79] S. A. Khairallah, A. T. Anderson, A. Rubenchik, and W. E. King, "Laser powder-bed fusion additive manufacturing: Physics of complex melt flow and formation mechanisms of pores, spatter, and denudation zones," *Acta Materialia*, vol. 108, pp. 36–45, 2016.

[80] A. Prasad, L. Yuan, P. Lee, M. Patel, D. Qiu, M. Easton, and D. StJohn, "Towards understanding grain nucleation under additive manufacturing solidification conditions," *Acta Materialia*, vol. 195, pp. 392–403, 2020.

[81] E. Scheil, "Notes on layer crystal formation," *International Journal of Materials Research*, vol. 34, no. 3, pp. 70–72, 1942.

[82] W. Tiller, K. Jackson, J. Rutter, and B. Chalmers, "The redistribution of solute atoms during the solidification of metals," *Acta metallurgica*, vol. 1, no. 4, pp. 428–437, 1953.

[83] R. Trivedi, J. Sekhar, and V. Seetharaman, "Solidification microstructures near the limit of absolute stability," *Metallurgical Transactions A*, vol. 20, no. 4, pp. 769–777, 1989.

[84] M. Rappaz, S. David, J. Vitek, and L. Boatner, "Analysis of solidification microstructures in fe-ni-cr single-crystal welds," *Metallurgical transactions A*, vol. 21, no. 6, pp. 1767–1782, 1990.

[85] R.-J. Roe, "Description of crystallite orientation in polycrystalline materials. iii. general solution to pole figure inversion," *Journal of Applied Physics*, vol. 36, no. 6, pp. 2024–2031, 1965.

[86] R.-J. Roe, "Inversion of pole figures for materials having cubic crystal symmetry," *Journal of Applied Physics*, vol. 37, no. 5, pp. 2069–2072, 1966.

[87] H. Bunge, "About the elastic constants of cubic materials with any texture," *Crystal and Technology*, vol. 3, no. 3, pp. 431–438, 1968.

[88] W. Voigt, *Lehrbuch der Kristallphysik (mit Ausschluss der Kristalloptik)*, vol. 34. BG Teubner, 1910.

[89] A. Reuss, "Berechnung der fließgrenze von mischkristallen auf grund der plastizitätsbedingung für einkristalle," *ZAMM-Journal of Applied Mathematics and Mechanics*, vol. 9, no. 1, pp. 49–58, 1929.

[90] Z. Hashin and S. Shtrikman, "A variational approach to the theory of the elastic behaviour of multiphase materials," *Journal of the Mechanics and Physics of Solids*, vol. 11, no. 2, pp. 127–140, 1963.

[91] J. Eshelby, "Progress in solid mechanics," *Journal of the Mechanics and Physics of Solids*, vol. 9, no. 1, pp. 67–67, 1961.

[92] E. Kröner, "Zur plastischen verformung des vielkristalls," *Acta metallurgica*, vol. 9, no. 2, pp. 155–161, 1961.

[93] B. Lan, M. A. Carpenter, W. Gan, M. Hofmann, F. P. Dunne, and M. J. Lowe, "Rapid measurement of volumetric texture using resonant ultrasound spectroscopy," *Scripta Materialia*, vol. 157, pp. 44–48, 2018.

[94] S. Bernard, G. Marrelec, P. Laugier, and Q. Grimal, "Bayesian normal modes identification and estimation of elastic coefficients in resonant ultrasound spectroscopy," *Inverse Problems*, vol. 31, no. 6, p. 065010, 2015.

[95] M. L. Fernández and T. Böhlke, "Representation of hashin–shtrikman bounds in terms of texture coefficients for arbitrarily anisotropic polycrystalline materials," *Journal of Elasticity*, vol. 134, no. 1, pp. 1–38, 2019.

[96] T. Böhlke and M. Lobos, "Representation of hashin–shtrikman bounds of cubic crystal aggregates in terms of texture coefficients with application in materials design," *Acta materialia*, vol. 67, pp. 324–334, 2014.

[97] M. Fernández and T. Böhlke, "Hashin-shtrikman bounds with eigenfields in terms of texture coefficients for polycrystalline materials," *Acta Materialia*, vol. 165, pp. 686–697, 2019.

[98] M. Lobos and T. Bohlke, "On optimal zeroth-order bounds of linear elastic properties of multiphase materials and application in materials design," *International Journal of Solids and Structures*, vol. 84, pp. 40–48, 2016.

[99] R. C. Smith, *Uncertainty quantification: theory, implementation, and applications*, vol. 12. Siam, 2013.

[100] T. L. T. Nguyen, F. Septier, G. W. Peters, and Y. Delignon, "Efficient sequential monte-carlo samplers for bayesian inference," *IEEE Transactions on Signal Processing*, vol. 64, no. 5, pp. 1305–1319, 2015.

[101] P. Del Moral, A. Doucet, and A. Jasra, "Sequential monte carlo samplers," *Journal of the Royal Statistical Society: Series B (Statistical Methodology)*, vol. 68, no. 3, pp. 411–436, 2006.

[102] B. R. Goodlet, L. Mills, B. Bales, M.-A. Charpagne, S. P. Murray, W. C. Lenthe, L. Petzold, and T. M. Pollock, "Elastic properties of novel co-and coni-based superalloys determined through bayesian inference and resonant ultrasound spectroscopy," *Metallurgical and Materials Transactions A*, vol. 49, no. 6, pp. 2324–2339, 2018.

[103] M. Radovic, E. Lara-Curzio, and L. Riester, "Comparison of different experimental techniques for determination of elastic properties of solids," *Materials Science and Engineering: A*, vol. 368, no. 1-2, pp. 56–70, 2004.

[104] M. C. Remillieux, T. Ulrich, C. Payan, J. Rivière, C. R. Lake, and P.-Y. Le Bas, "Resonant ultrasound spectroscopy for materials with high damping and samples of arbitrary geometry," *Journal of Geophysical Research: Solid Earth*, vol. 120, no. 7, pp. 4898–4916, 2015.

[105] R. Kumaresan and D. Tufts, "Estimating the parameters of exponentially damped sinusoids and pole-zero modeling in noise," *IEEE transactions on acoustics, speech, and signal processing*, vol. 30, no. 6, pp. 833–840, 1982.

[106] A. Migliori and J. Maynard, "Implementation of a modern resonant ultrasound spectroscopy system for the measurement of the elastic moduli of small solid specimens," *Review of scientific instruments*, vol. 76, no. 12, p. 121301, 2005.

[107] M. Rolchigo, B. Stump, J. Belak, and A. Plotkowski, "Sparse thermal data for cellular automata modeling of grain structure in additive manufacturing," *Modelling and Simulation in Materials Science and Engineering*, vol. 28, no. 6, p. 065003, 2020.

[108] S.-H. Sun, K. Hagihara, and T. Nakano, "Effect of scanning strategy on texture formation in ni-25 at.% mo alloys fabricated by selective laser melting," *Materials & Design*, vol. 140, pp. 307–316, 2018.

[109] B. J. Zadler, J. H. Le Rousseau, J. A. Scales, and M. L. Smith, "Resonant ultrasound spectroscopy: theory and application," *Geophysical Journal International*, vol. 156, no. 1, pp. 154–169, 2004.

[110] H. Seiner, L. Bodnárová, P. Sedlák, M. Janeček, O. Srba, R. Král, and M. Landa, "Application of ultrasonic methods to determine elastic anisotropy of polycrystalline copper processed by equal-channel angular pressing," *Acta Materialia*, vol. 58, no. 1, pp. 235–247, 2010.

[111] H. Ogi, N. Nakamura, and M. Hirao, "Advanced resonant ultrasound spectroscopy for measuring anisotropic elastic constants of thin films," *Fatigue & Fracture of Engineering Materials & Structures*, vol. 28, no. 8, pp. 657–663, 2005.

[112] M. Huang and C.-S. Man, "Explicit bounds of effective stiffness tensors for textured aggregates of cubic crystallites," *Mathematics and mechanics of solids*, vol. 13, no. 5, pp. 408–430, 2008.

[113] M. Lobos, T. Yuzbasioglu, and T. Böhlke, "Homogenization and materials design of anisotropic multiphase linear elastic materials using central model functions," *Journal of Elasticity*, vol. 128, no. 1, pp. 17–60, 2017.

[114] T. Böhlke, "Texture simulation based on tensorial fourier coefficients," *Computers & structures*, vol. 84, no. 17-18, pp. 1086–1094, 2006.

[115] A. S. Wu, D. W. Brown, M. Kumar, G. F. Gallegos, and W. E. King, "An experimental investigation into additive manufacturing-induced residual stresses in 316l stainless steel," *Metallurgical and Materials Transactions A*, vol. 45, no. 13, pp. 6260–6270, 2014.

[116] S. S. Babu, N. Raghavan, J. Raplee, S. J. Foster, C. Frederick, M. Haines, R. Dinwiddie, M. Kirka, A. Plotkowski, Y. Lee, *et al.*, "Additive manufacturing of nickel superalloys: opportunities for innovation and challenges related to qualification," *Metallurgical and Materials Transactions A*, vol. 49, no. 9, pp. 3764–3780, 2018.

[117] L. N. Carter, C. Martin, P. J. Withers, and M. M. Attallah, "The influence of the laser scan strategy on grain structure and cracking behaviour in slm powder-bed fabricated nickel superalloy," *Journal of Alloys and Compounds*, vol. 615, pp. 338–347, 2014.

[118] S. Catchpole-Smith, N. Aboulkhair, L. Parry, C. Tuck, I. Ashcroft, and A. Clare, "Fractal scan strategies for selective laser melting of 'unweldable'nickel superalloys," *Additive Manufacturing*, vol. 15, pp. 113–122, 2017.

Bibliography

[119] R. Engeli, T. Etter, S. Hoevel, and K. Wegener, "Processability of different in738lc powder batches by selective laser melting," *Journal of Materials Processing Technology*, vol. 229, pp. 484–491, 2016.

[120] C. A. Stewart, S. P. Murray, A. Suzuki, T. M. Pollock, and C. G. Levi, "Accelerated discovery of oxidation resistant coni-base γ/γ'alloys with high l12 solvus and low density," *Materials & Design*, vol. 189, p. 108445, 2020.

[121] S. P. Murray, K. M. Pusch, A. T. Polonsky, C. J. Torbet, G. G. Seward, N. Zhou, S. A. Forsik, P. Nandwana, M. M. Kirka, R. R. Dehoff, *et al.*, "A defect-resistant co–ni superalloy for 3d printing," *Nature communications*, vol. 11, no. 4975, 2020.

[122] S. P. Murray, K. M. Pusch, A. T. Polonsky, C. J. Torbet, G. G. Seward, P. Nandwana, M. M. Kirka, R. R. Dehoff, N. Zhou, S. A. Forsik, *et al.*, "Microstructure and tensile properties of a coni-based superalloy fabricated by selective electron beam melting," in *Superalloys 2020*, pp. 880–890, Springer, 2020.

[123] F. Bachmann, R. Hielscher, and H. Schaeben, "Texture analysis with mtex–free and open source software toolbox," in *Solid State Phenomena*, vol. 160, pp. 63–68, Trans Tech Publ, 2010.

[124] C. M. Kube, J. Gillespie, and M. Cherry, "Influence of residual stress and texture on the resonances of polycrystalline metals," *The Journal of the Acoustical Society of America*, vol. 150, no. 4, pp. 2624–2634, 2021.

[125] B. R. Goodlet, S. P. Murray, B. Bales, J. Rossin, C. J. Torbet, and T. M. Pollock, "Temperature dependence of single crystal elastic constants in a coni-base alloy: A new methodology," *Materials Science and Engineering: A*, p. 140507, 2020.

[126] P. R. Morris, "Generalized spherical harmonics for cubic-triclinic symmetry," *Textures and Microstructures*, vol. 24, 1970.

[127] D. Mainprice, R. Hielscher, and H. Schaeben, "Calculating anisotropic physical properties from texture data using the mtex open-source package," *Geological Society, London, Special Publications*, vol. 360, no. 1, pp. 175–192, 2011.

[128] P. Acar and V. Sundararaghavan, "Uncertainty quantification of microstructural properties due to experimental variations," *AIAA Journal*, vol. 55, no. 8, pp. 2824–2832, 2017.

[129] A. Creuziger, K. Syed, and T. Gnäupel-Herold, "Measurement of uncertainty in orientation distribution function calculations," *Scripta Materialia*, vol. 72, pp. 55–58, 2014.

[130] M. Landa, H. Seiner, P. Sedlák, L. Bicanová, J. Zidek, and L. Heller, "Resonant ultrasound spectroscopy close to its applicability limits," *Horizons World Physics*, vol. 268, pp. 97–136, 2009.

[131] S. Ghosh, M. Matty, R. Baumbach, E. D. Bauer, K. A. Modic, A. Shekhter, J. Mydosh, E.-A. Kim, and B. Ramshaw, "One-component order parameter in uru2si2 uncovered by resonant ultrasound spectroscopy and machine learning," *Science advances*, vol. 6, no. 10, p. eaaz4074, 2020.

[132] H. Seiner, P. Sedlák, L. Bodnárová, A. Kruisová, M. Landa, A. de Pablos, and M. Belmonte, "Sensitivity of the resonant ultrasound spectroscopy to weak gradients of elastic properties," *The Journal of the Acoustical Society of America*, vol. 131, no. 5, pp. 3775–3785, 2012.

[133] T. Richeton, S. Berbenni, L. Germain, G. Nathalie, T. Connolley, O. Castelnau, *et al.*, "Estimating single-crystal elastic constants of polycrystalline β metastable titanium alloy: A bayesian inference analysis based on high energy x-ray diffraction and micromechanical modeling," *Acta Materialia*, p. 116762, 2021.

[134] C. Kim, H. Yin, A. Shmatok, B. C. Prorok, X. Lou, and K. H. Matlack, "Ultrasonic nondestructive evaluation of laser powder bed fusion 316l stainless steel," *Additive Manufacturing*, vol. 38, p. 101800, 2021.

[135] C. Zener, "Contributions to the theory of beta-phase alloys," *Physical Review*, vol. 71, no. 12, p. 846, 1947.

[136] R. Hearmon, "The elastic constants of anisotropic materials," *Reviews of modern physics*, vol. 18, no. 3, p. 409, 1946.

[137] P. W. Bridgman, "Some properties of single metal crystals," in *Collected Experimental Papers, Volume III*, pp. 1795–1800, Harvard University Press, 2013.

[138] W. C. Schneider and C. J. Burton, "Determination of the elastic constants of solids by ultrasonic methods," *Journal of Applied Physics*, vol. 20, no. 1, pp. 48–58, 1949.

[139] A. T. Polonsky, N. Raghavan, M. P. Echlin, M. M. Kirka, R. R. Dehoff, and T. M. Pollock, "3d characterization of the columnar-to-equiaxed transition in additively manufactured inconel 718," in *Superalloys 2020*, pp. 990–1002, Springer, 2020.

[140] Z. Wang, A. D. Stoica, D. Ma, and A. M. Beese, "Diffraction and single-crystal elastic constants of inconel 625 at room and elevated temperatures determined by neutron diffraction," *Materials Science and Engineering: A*, vol. 674, pp. 406–412, 2016.

[141] C. Howard and E. Kisi, "Measurement of single-crystal elastic constants by neutron diffraction from polycrystals," *Journal of applied crystallography*, vol. 32, no. 4, pp. 624–633, 1999.

[142] S. Matthies, H. Priesmeyer, and M. Daymond, "On the diffractive determination of single-crystal elastic constants using polycrystalline samples," *Journal of Applied Crystallography*, vol. 34, no. 5, pp. 585–601, 2001.

[143] V. Hauk and H. Kockelmann, "Evaluation of single crystal coefficients from mechanical and x-ray elastic constants of the polycrystal," *Zeitschrift für Metallkunde*, vol. 70, no. 8, pp. 500–502, 1979.

[144] E. Wielewski, D. E. Boyce, J.-S. Park, M. P. Miller, and P. R. Dawson, "A methodology to determine the elastic moduli of crystals by matching experimental and simulated lattice strain pole figures using discrete harmonics," *Acta Materialia*, vol. 126, pp. 469–480, 2017.

[145] S. I. Wright, "Estimation of single-crystal elastic constants from textured polycrystal measurements," *Journal of applied crystallography*, vol. 27, no. 5, pp. 794–801, 1994.

[146] A. Castillo and S. R. Kalidindi, "A bayesian framework for the estimation of the single crystal elastic parameters from spherical indentation stress-strain measurements," *Frontiers in Materials*, vol. 6, p. 136, 2019.

[147] P. Dryburgh, W. Li, D. Pieris, R. Fuentes-Domínguez, R. Patel, R. J. Smith, and M. Clark, "Measurement of the single crystal elasticity matrix of polycrystalline materials," *Acta Materialia*, vol. 225, p. 117551, 2022.

[148] W. Lenthe, S. Singh, and M. De Graef, "A spherical harmonic transform approach to the indexing of electron back-scattered diffraction patterns," *Ultramicroscopy*, vol. 207, p. 112841, 2019.

[149] A. S. Losko, S. C. Vogel, H. M. Reiche, and H. Nakotte, "A six-axis robotic sample changer for high-throughput neutron powder diffraction and texture measurements," *Journal of Applied Crystallography*, vol. 47, no. 6, pp. 2109–2112, 2014.

[150] L. Lutterotti, S. Matthies, H.-R. Wenk, A. Schultz, and J. Richardson Jr, "Combined texture and structure analysis of deformed limestone from time-of-flight neutron diffraction spectra," *Journal of Applied Physics*, vol. 81, no. 2, pp. 594–600, 1997.

[151] A. I. Saville, A. Creuziger, E. B. Mitchell, S. C. Vogel, J. T. Benzing, J. Klemm-Toole, K. D. Clarke, and A. J. Clarke, "Maud rietveld refinement software for neutron diffraction texture studies of single-and dual-phase materials," *Integrating Materials and Manufacturing Innovation*, vol. 10, no. 3, pp. 461–487, 2021.

[152] R. Masson, "New explicit expressions of the hill polarization tensor for general anisotropic elastic solids," *International Journal of Solids and Structures*, vol. 45, no. 3-4, pp. 757–769, 2008.

[153] J. C. Aldrin, A. Mayes, L. Jauriqui, E. Biedermann, J. Heffernan, R. Livings, B. Goodlet, and S. Mazdiyasni, "Uncertainty quantification of resonant ultrasound spectroscopy for material property and single crystal orientation estimation on a complex part," in *AIP Conference Proceedings*, vol. 1949, p. 140010, AIP Publishing LLC, 2018.

[154] F. Ghahremani, "Numerical evaluation of the stresses and strains in ellipsoidal inclusions in an anisotropic elastic material," *Mechanics Research Communications*, vol. 4, no. 2, pp. 89–91, 1977.

[155] J.-Y. Kim and S. I. Rokhlin, "Determination of elastic constants of generally anisotropic inclined lamellar structure using line-focus acoustic microscopy," *The Journal of the Acoustical Society of America*, vol. 126, no. 6, pp. 2998–3007, 2009.

[156] G. Sargent, K. Kinsel, A. Pilchak, A. Salem, and S. Semiatin, "Variant selection during cooling after beta annealing of ti-6al-4v ingot material," *Metallurgical and Materials Transactions A*, vol. 43, no. 10, pp. 3570–3585, 2012.

[157] J. Benzing, N. Moser, O. Kafka, J. Weaver, N. Derimow, and N. Hrabe, "Am bench 2022 challenge macroscale tensile tests at different orientations (chal-amb2022-04-matto)." National Institute of Standards and Technology, 2022. doi:10.18434/mds2-2588.

[158] M. Lobos Fernández, *Homogenization and materials design of mechanical properties of textured materials based on zeroth-, first-and second-order bounds of linear behavior*, vol. 12. KIT Scientific Publishing, 2018.

[159] T. Holden, R. Holt, and A. Clarke, "Intergranular strains in inconel-600 and the impact on interpreting stress fields in bent steam-generator tubing," *Materials Science and Engineering: A*, vol. 246, no. 1-2, pp. 180–198, 1998.

[160] A. Buchholz, N. Chopin, and P. E. Jacob, "Adaptive tuning of hamiltonian monte carlo within sequential monte carlo," *Bayesian Analysis*, vol. 16, no. 3, pp. 745–771, 2021.

[161] J. Warwick, J. Coakley, S. Raghunathan, R. Talling, and D. Dye, "Effect of texture on load partitioning in ti-6al-4v," *Acta Materialia*, vol. 60, no. 10, pp. 4117–4127, 2012.

[162] V. Hasija, S. Ghosh, M. J. Mills, and D. S. Joseph, "Deformation and creep modeling in polycrystalline ti–6al alloys," *Acta materialia*, vol. 51, no. 15, pp. 4533–4549, 2003.

[163] T. Keller, G. Lindwall, S. Ghosh, L. Ma, B. M. Lane, F. Zhang, U. R. Kattner, E. A. Lass, J. C. Heigel, Y. Idell, *et al.*, "Application of finite element, phase-field, and calphad-based methods to additive manufacturing of ni-based superalloys," *Acta Materialia*, vol. 139, pp. 244–253, 2017.

[164] C. U. Brown, G. Jacob, M. Stoudt, S. Moylan, J. Slotwinski, and A. Donmez, "Interlaboratory study for nickel alloy 625 made by laser powder bed fusion to quantify mechanical property variability," *Journal of materials engineering and performance*, vol. 25, no. 8, pp. 3390–3397, 2016.

[165] E. A. Lass, M. R. Stoudt, M. E. Williams, M. B. Katz, L. E. Levine, T. Q. Phan, T. H. Gnaeupel-Herold, and D. S. Ng, "Formation of the ni 3 nb δ-phase in stress-relieved inconel 625 produced via laser powder-bed fusion additive manufacturing," *Metallurgical and Materials Transactions A*, vol. 48, no. 11, pp. 5547–5558, 2017.

[166] S. Ghosh, L. Ma, N. Ofori-Opoku, and J. E. Guyer, "On the primary spacing and microsegregation of cellular dendrites in laser deposited ni–nb alloys," *Modelling and simulation in materials science and engineering*, vol. 25, no. 6, p. 065002, 2017.

[167] L. Rettberg, B. Goodlet, and T. Pollock, "Detecting recrystallization in a single crystal ni-base alloy using resonant ultrasound spectroscopy," *NDT & E International*, vol. 83, pp. 68–77, 2016.

[168] M. Groeber, E. Schwalbach, W. Musinski, P. Shade, S. Donegan, M. Uchic, D. Sparkman, T. Turner, and J. Miller, "A preview of the us air force research laboratory additive manufacturing modeling challenge series," *JOM*, vol. 70, no. 4, pp. 441–444, 2018.

[169] https://materials-data-facility.github.io/MID3AS-AM-Challenge.

[170] W. Kurz and D. J. Fisher, *Fundamentals of solidification*, vol. 1. trans tech publications Aedermannsdorf, Switzerland, 1986.

[171] W. Kurz, C. Bezencon, and M. Gäumann, "Columnar to equiaxed transition in solidification processing," *Science and technology of advanced materials*, vol. 2, no. 1, p. 185, 2001.

[172] Z. Wang, A. D. Stoica, D. Ma, and A. M. Beese, "Diffraction and single-crystal elastic constants of inconel 625 at room and elevated temperatures determined by neutron diffraction," *Materials Science and Engineering: A*, vol. 674, pp. 406–412, 2016.

[173] S. Ahmed and R. B. Thompson, "Propagation of elastic waves in equiaxed stainless-steel polycrystals with aligned [001] axes," *The Journal of the Acoustical Society of America*, vol. 99, no. 4, pp. 2086–2096, 1996.

[174] Z. Wang, E. Denlinger, P. Michaleris, A. D. Stoica, D. Ma, and A. M. Beese, "Residual stress mapping in inconel 625 fabricated through additive manufacturing: Method for neutron diffraction measurements to validate thermo-mechanical model predictions," *Materials & Design*, vol. 113, pp. 169–177, 2017.

[175] D. B. Miracle and O. N. Senkov, "A critical review of high entropy alloys and related concepts," *Acta Materialia*, vol. 122, pp. 448–511, 2017.

[176] S. Xu, S. Z. Chavoshi, and Y. Su, "On calculations of basic structural parameters in multi-principal element alloys using small atomistic models," *Computational Materials Science*, vol. 202, p. 110942, 2022.

[177] S. Rao, B. Akdim, E. Antillon, C. Woodward, T. Parthasarathy, and O. Senkov, "Modeling solution hardening in bcc refractory complex concentrated alloys: Nbtizr, nb1. 5tizr0. 5 and nb0. 5tizr1. 5," *Acta Materialia*, vol. 168, pp. 222–236, 2019.

[178] S. Xu, E. Hwang, W.-R. Jian, Y. Su, and I. J. Beyerlein, "Atomistic calculations of the generalized stacking fault energies in two refractory multi-principal element alloys," *Intermetallics*, vol. 124, p. 106844, 2020.

[179] H. Ge and F. Tian, "A review of ab initio calculation on lattice distortion in high-entropy alloys," *Jom*, vol. 71, no. 11, pp. 4225–4237, 2019.

[180] K. J. Carroll, *Elastic constants and thermal expansion of niobium as a function of temperature*. PhD thesis, Rice University, 1962.

[181] Q. He, S. Yoshida, H. Yasuda, and N. Tsuji, "Effect of elemental combination on microstructure and mechanical properties of quaternary refractory medium entropy alloys," *Materials Transactions*, pp. MT–MK2019003, 2020.

[182] H. Ge, F. Tian, and Y. Wang, "Elastic and thermal properties of refractory high-entropy alloys from first-principles calculations," *Computational Materials Science*, vol. 128, pp. 185–190, 2017.

[183] O. Senkov, S. Rao, K. Chaput, and C. Woodward, "Compositional effect on microstructure and properties of nbtizr-based complex concentrated alloys," *Acta Materialia*, vol. 151, pp. 201–215, 2018.

[184] G. Dirras, L. Lilensten, P. Djemia, M. Laurent-Brocq, D. Tingaud, J.-P. Couzinié, L. Perrière, T. Chauveau, and I. Guillot, "Elastic and plastic properties of as-cast equimolar tihfzrtanb high-entropy alloy," *Materials Science and Engineering: A*, vol. 654, pp. 30–38, 2016.

[185] E. Fazakas, V. Zadorozhnyy, L. Varga, A. Inoue, D. Louzguine-Luzgin, F. Tian, and L. Vitos, "Experimental and theoretical study of ti20zr20hf20nb20x20 (x= v or cr) refractory high-entropy alloys," *International Journal of Refractory Metals and Hard Materials*, vol. 47, pp. 131–138, 2014.

[186] F. E. Stanke and G. S. Kino, "A unified theory for elastic wave propagation in polycrystalline materials," *The Journal of the Acoustical Society of America*, vol. 75, no. 3, pp. 665–681, 1984.

[187] A. I. Saville, S. C. Vogel, A. Creuziger, J. T. Benzing, A. L. Pilchak, P. Nandwana, J. Klemm-Toole, K. D. Clarke, S. L. Semiatin, and A. J. Clarke, "Texture evolution as a function of scan strategy and build height in electron beam melted ti-6al-4v," *Additive Manufacturing*, vol. 46, p. 102118, 2021.

[188] A. Pilchak and J. Williams, "Microstructure and texture evolution during friction stir processing of fully lamellar ti-6al-4v," *Metallurgical and Materials Transactions A*, vol. 42, no. 3, pp. 773–794, 2011.

[189] C. M. Kube, Z. Feng, R. A. Lebensohn, and M. Cherry, "Resonant ultrasound spectroscopy for crystalline samples containing initial strain," *Journal of Applied Physics*, vol. 131, no. 22, p. 225107, 2022.

[190] C.-S. Man and W. Lu, "Towards an acoustoelastic theory for measurement of residual stress," *Journal of Elasticity*, vol. 17, no. 2, pp. 159–182, 1987.

[191] Z.-C. Fang, Z.-L. Wu, C.-G. Huang, and C.-W. Wu, "Review on residual stress in selective laser melting additive manufacturing of alloy parts," *Optics & Laser Technology*, vol. 129, p. 106283, 2020.

[192] D. S. Hughes and J. Kelly, "Second-order elastic deformation of solids," *Physical review*, vol. 92, no. 5, p. 1145, 1953.

[193] J. D. Clayton, *Nonlinear mechanics of crystals*, vol. 177. Springer Science & Business Media, 2010.

[194] D. G. Isaak, J. D. Carnes, O. L. Anderson, and H. Oda, "Elasticity of fused silica spheres under pressure using resonant ultrasound spectroscopy," *The Journal of the Acoustical Society of America*, vol. 104, no. 4, pp. 2200–2206, 1998.

[195] J. Li and S. Rokhlin, "Propagation and scattering of ultrasonic waves in polycrystals with arbitrary crystallite and macroscopic texture symmetries," *Wave Motion*, vol. 58, pp. 145–164, 2015.

[196] A. Granato and K. Lücke, "Theory of mechanical damping due to dislocations," *Journal of applied physics*, vol. 27, no. 6, pp. 583–593, 1956.

[197] A. P. Arguelles and J. A. Turner, "Ultrasonic attenuation of polycrystalline materials with a distribution of grain sizes," *The Journal of the Acoustical Society of America*, vol. 141, no. 6, pp. 4347–4353, 2017.

[198] F. Shen, F. Fan, R. Wang, Q. Zhang, P. Laugier, and H. Niu, "Particle swarm optimization-based identification of the elastic properties in resonant ultrasound spectroscopy," *IEEE Transactions on Ultrasonics, Ferroelectrics, and Frequency Control*, vol. 67, no. 7, pp. 1412–1423, 2020.

[199] B. R. Goodlet, B. Bales, and T. M. Pollock, "A new elastic characterization method for anisotropic bilayer specimens via bayesian resonant ultrasound spectroscopy," *Ultrasonics*, vol. 115, p. 106455, 2021.

[200] H. Ogi, K. Sato, T. Asada, and M. Hirao, "Complete mode identification for resonance ultrasound spectroscopy," *The Journal of the Acoustical Society of America*, vol. 112, no. 6, pp. 2553–2557, 2002.

[201] K. Adachi, H. Ogi, N. Takeuchi, N. Nakamura, H. Watanabe, T. Ito, and Y. Ozaki, "Unusual elasticity of monoclinic β- ga 2 o 3," *Journal of Applied Physics*, vol. 124, no. 8, p. 085102, 2018.

[202] B. Goodlet, L. Rettberg, and T. Pollock, "Resonant ultrasound spectroscopy for defect detection in single crystal superalloy castings," *Superalloys*, 2016.